THERMAL INFRARED REMOTE SENSING OF ACTIVE BASALTIC VOLCANOES: A THERMAL AND SPECTRAL DECONVOLUTION APPROACH

by

SHELLIE R ROSE

B.S. Geology, Kent State University, Kent, Ohio 2001

M.S. Geological Sciences, Ohio University, Athens, Ohio 2004

Submitted to the Graduate Faculty of

Arts and Sciences in partial fulfillment

of the requirements for the degree of

Doctor of Philosophy

University of Pittsburgh

2010

UNIVERSITY OF PITTSBURGH

FACULTY OF ARTS AND SCIENCES

This dissertation was presented

by

SHELLIE R ROSE

It was defended on

December 1, 2010

and approved by

Ian P. Skilling, Assistant Professor, University of Pittsburgh

Thomas Anderson, Professor, University of Pittsburgh

William Harbert, Professor, University of Pittsburgh

Matthew Watson, Professor, University of Bristol, United Kingdom

Dissertation Advisor: Michael S. Ramsey, Associate Professor, University of Pittsburgh

THERMAL INFRARED REMOTE SENSING OF ACTIVE BASALTIC VOLCANOES: A THERMAL AND SPECTRAL DECONVOLUTION APPROACH

Shellie R Rose, PhD

University of Pittsburgh, 2010

The Advanced Spaceborne Thermal Emission and Reflection Radiometer (ASTER) was launched in December 1999 as one of five instruments on the NASA Earth Observing System's (EOS) Terra satellite, and has proven effective for the detection and monitoring of volcanic eruptions and their associated products (Ramsey and Dehn, 2004). However, continuous advancement in analytical remote sensing techniques remains essential. For example, features associated with active volcanism commonly 1) are below the spatial resolution of the instruments 2) are more indicative of the state of volcanic unrest 3) tend to saturate thermal infrared (TIR) sensors due to their high thermal output. In addition, compositional, textural, and thermal heterogeneities can vary greatly within one 90 m TIR pixel, making accurate analysis and interpretations almost impossible without advanced techniques. Previous studies have shown that the radiance of an isothermal surface can mix linearly with respect to composition and texture, whereby emitted or reflected energy (TIR) from a heterogeneous surface is a combination of the radiance from each component proportionally to its areal percentage. However, where thermal mixing of a target's surface is involved, this technique is no longer valid, requiring alternative approaches to the solution. A thermal deconvolution algorithm has been developed to identify thermally mixed pixels and separate them into their hot and cool thermal components using archival and Urgent Request Protocol (URP) data from the higher spatial resolution shortwave (SWIR) bands of ASTER. These datasets targeted three active basaltic volcanoes exhibiting various thermal states including high-temperature lava flows with minimal SWIR saturation (Kilauea, Hawaii), low-temperature fumarole fields (Cerro Negro, Nicaragua), and high-temperature flows with significant SWIR saturation (Kliuchevskoi, Kamchatka). The results of this study show that this algorithm provides more accurate temperature estimates and corrections to the emissivity for better compositional mapping of the surface where SWIR radiance values do not approach minimum and maximum thresholds within each TIR pixel. This approach also serves as a rapid means for accurately identifying sub-pixel temperatures and minimizes the processing time, therefore allowing critical information to be quickly disseminated on these processes and hazards, which are commonly obscured in low to medium-spatial resolution orbital datasets.

TABLE OF CONTENTS

LIST OF TABLES

LIST OF FIGURES

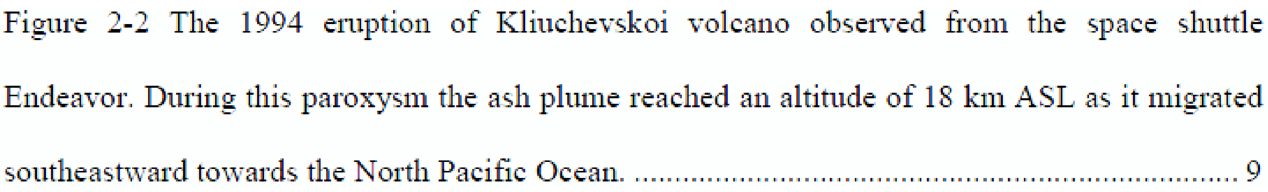

PREFACE

I would like to express my sincerest thanks to my advisor, Michael Ramsey for all of his academic, financial, and personal support throughout this very long process. Without Mike, I would have never traveled to the far reaches of the earth and met the most amazing people along the way. His strive for excellence in himself and his students has resulted in turning me into a more confident scientist, and for that, I am extremely grateful. THANKS MIKE!!!

A special thanks goes out to Matt Watson for taking a computer-illiterate schmuck like myself and turning me into an IDL machine. I may not be fluent, but his never-ending patience and ability to relate to my way of learning has been much appreciated. He has given me a newfound knowledge that I will forever use to become a more refined and efficient scientist. Oh no you didn't!

There are many organizations and people that I need to thank for their financial, scientific, and travel support including NASA, ASTER, AVO, Academy of Sciences in Petropavlovsk-Kamchatsky, INETER, the University of Pittsburgh, and my dissertation committee. They have provided travel grants, volcanic eruption updates, data, field assistance, laboratory data, and transportation that have all been essential for the completion of this project.

Last but not least, I'd like to thank my family and friends for their constant emotional support. I honestly could not have been successful without all of you pushing me to finish.

From the bottom of my heart, I love you all! Grandma, Mom, Dad, Nen, Rob, Ethan, Josh, Adam, Stephen, Topher, Rachel, Sarah, Bobby, James, Marion, Kevin, Alison, Amy, Tamara, and so many… many more. Yinz guys are the best!

1.0 INTRODUCTION

Volcanism can pose serious hazards such as lahars, earthquakes, and ash fall to nearby population centers. Similarly, larger explosive eruptions can impact more distant regions as well as interact with the approximate 200 aircraft and 20,000 people overflying the North Pacific region (Miller and Casadevall, 2000). For these reasons, it is critical to monitor and characterize eruptive activity in order to recognize the precursors of future behavior, and eventually predict eruptions to minimize risks.

The research presented here builds upon the foundation established in a previously-funded NASA Earth System Science project (NNG04G069G) entitled Automation of the ASTER Emergency Data Acquisition Protocol for Scientific Analyses, Disaster Monitoring and Preparedness, whereby an automated urgent request protocol (URP) was developed for the Advanced Spaceborne Thermal Emission and Reflection Radiometer (ASTER) to acquire emergency observations of natural disasters with minimal turn-around times for data processing. Collaboration of various institutions including the Alaska Volcano Observatory (AVO), Kamchatka Volcanic Eruption Response Team (KVERT), United States Geological Survey (USGS), Instituto Nicaragüense de Estudios Territoriales, and the University of Pittsburgh has been successful and will continue throughout the lifetime of the ASTER sensor. The goals of this research include: 1) Explore the errors associated with the presence of thermally mixed pixels in remotely sensed data; 2) Develop a thermal deconvolution algorithm that can identify and remediate the errors within each mixed pixel; and 3) Apply the algorithm to two volcanoes of similar composition. Each of the target volcanoes produce both low and high-temperature thermal features including fumaroles and incandescent lava flows. This range of activity provides a basis from which other volcanoes around the world may be similarly-monitored for potential eruptive behavior more efficiently.

Kliuchevskoi volcano, one of the most active volcanoes in the northern Pacific, is located on the Kamchatka Peninsula of far eastern Russia, at the junction between the Kurile-Kamchatka and Aleutian Island Arcs. Its location and diversity of eruption styles make satellite-based monitoring and characterization of its eruptive activity essential. The ASTER sensor has proven effective for the detection and monitoring of volcanic eruptions and their associated products including those of Kliuchevskoi. In 1994, Kliuchevskoi entered its largest eruptive phase in over 40 years (Miller et al., 1994), initiated by minor explosive activity within the summit crater that produced low-level ash clouds (< 9 km ASL). Within weeks, the eruption intensified to a paroxysmal state with large convecting columns that produced pyroclastic flows, as well as lahars and lava flows (~3.0×10^7 m^3; GVP, 2008). The largest explosive eruptions (VEI=3) during that time produced a significant ash column containing ~5.0×10^7 m^3 of material, which reached 18 km ASL and traveled approximately 1,000 km southeast into the North Pacific air traffic routes (Miller et al., 1994). This intense explosive stage of the eruption continued for roughly 36 hours. From that time, Kliuchevskoi has remained relatively active, producing smaller explosive eruptions (VEI=1-2) and effusive activity on a 1-2 year time scale (GVP, 2008) with the most recent eruptions occurring in 2005, 2007, 2008, 2009, and presently.

Conversely, the 250 m tall Cerro Negro volcano (12° 30'N, 86° 42'W) is located in northwestern Nicaragua, approximately 21 km east-northeast from the city of Leon, within the El

Hoyo-Las Pilas Volcanic Complex of the Marabios Range. This volcanic edifice is known as Central America's youngest volcano with its inception occurring in 1850 followed by >20 eruptions until 1995. Over time, Cerro Negro has produced an average of 1.6 km^3/k.y. of basaltic material since 1850 with an increase to 3.1 km^3/k.y. from 1947 until present (McKnight, 1995; McKnight and Williams, 1997) through activity ranging from strombolian to subplinian (VEI 3) style eruptions (GVP, 2008). This type of activity has produced a substantial lava flow field extending to the northeast as well as a vast blanket of tephra deposited to the southwest as a result of general weather patterns. The most recent subplinian eruptions have yielded column heights up to 9 km, resulting in tephra and ash fall in nearby population centers such as Telica and León. Cerro Negro was once thought to be a cinder cone for its relatively small size; however it is now referred to as a young stratovolcano due to its anomalously prolonged activity and eruption rates (McKnight, 1995; McKnight and Williams, 1997). Explosive activity at Cerro Negro has created an increased potential for volcanic hazards, necessitating constant monitoring and further investigations to predict future eruptions. Although Cerro Negro has been relatively quiet compared to Kliuchevskoi, it does provide information regarding precursory eruptive behavior and dormancy.

The thermal infrared (TIR) wavelength region has proven highly useful in extracting various components of volcanic activity. These components include composition, texture, and thermal anomalies of the surface that can vary greatly within one pixel of a remote sensing dataset. Where thermal heterogeneities occur, the associated emissivity spectrum for each of these pixels becomes less accurate. This study presents a new approach for deconvolving these thermally mixed pixels in a day/night pair of ASTER TIR scenes over Kilauea volcano, acquired during an active effusive phase in October 2006. This thermal deconvolution algorithm identifies thermally mixed pixels and separates them into their hot and cool thermal components using archival data from the higher spatial resolution short wave infrared (SWIR) bands of the Advanced Spaceborne Thermal Emission and Reflection Radiometer (ASTER). Effects of thermal mixing on derived compositional retrievals of the surface can be quantified using a spectral deconvolution approach for the original and thermally deconvolved data.

The purpose for studying Kliuchevskoi and Cerro Negro is to verify the efficacy of the proposed thermal deconvolution algorithm applied to a broad range of thermal features such as high-temperature lava flows (1100 ºC) and low-temperature fumaroles (300 ºC). Moreover, the locations of these two volcanoes allow us to validate the algorithm with respect to extreme variability in atmospheric conditions from extreme latitudes, which may also provide thresholds for viability. The success of the algorithm will lead to the ability to correct spectral errors associated with the presence of thermally mixed pixels and thereby result in more accurately constrained compositional, textural, and thermal characteristics of the observed targets where data has previously been considered futile.

2.0 THE 2005 ERUPTION OF KLIUCHEVSKOI VOLCANO: CHRONOLOGY AND PROCESSES DERIVED FROM ASTER SPACEBORNE AND FIELD-BASED DATA

2.1 INTRODUCTION

The Kamchatka Peninsula of eastern Russia is one of the most volcanically active regions in the world and eruptions there can pose hazards such as lahars, earthquakes, and ash fall to the sparse population centers. Larger ash-producing eruptions can also impact the greater northern Pacific region by way of interference with the approximately 200 aircraft and 20,000 people overflying the region daily (Miller and Casadevall, 2000), and ash-fall in nearby towns and cities. When aircraft engines come into contact with micron to submicron-sized glassy ash shards, catastrophic consequences such as severe abrasion to external surface components and welding of ash to mechanical elements has lead to engine failure (Casadevall, 1993; Self and Walker, 1994; Casadevall, 1994; Przedpelski and Casadevall, 1994; Searcy et al., 1998; Miller and Casadevall, 2000; Prata et al., 2010). For these reasons, it is critical to monitor and characterize eruptive activity of this region in order to better recognize the precursors of future behavior, and thus minimize risks.

Kliuchevskoi volcano (56º 11’N, 160º 47’E), located at the intersection of the Aleutian and Kurile-Kamchatka volcanic arcs, is the highest (4835 m) and one of the most restless of Kamchatka’s 29 active volcanoes (Figure 2-1). It produces and average 6.0×10^7 tons of erupted

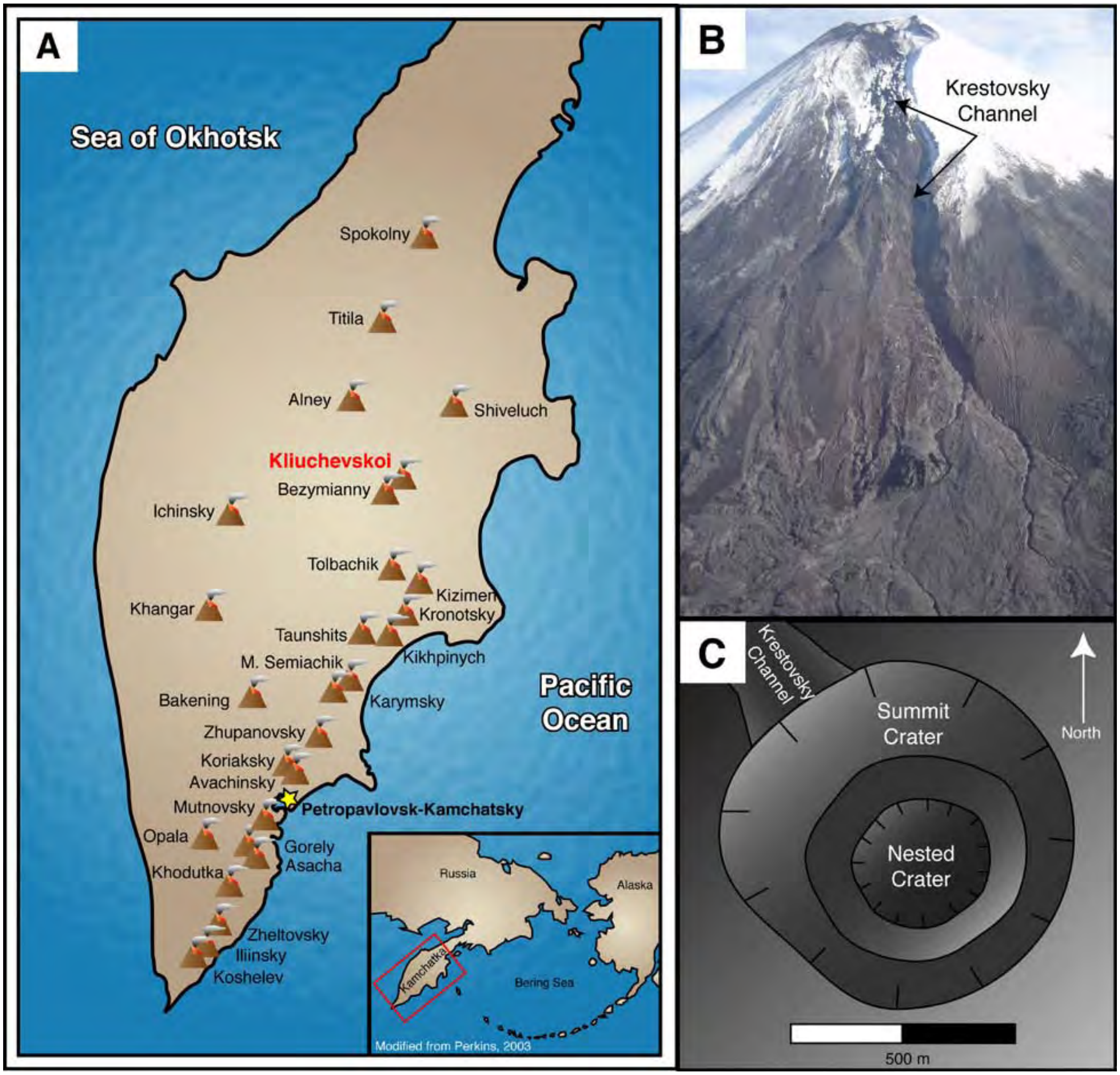

Modified from Perkins, 2003

Figure 2-1 (A) Location map of the Kamchatka Peninsula of far eastern Russia including the locations of the most active volcanoes in the region. Kliuchevskoi is highlighted in red. (B) A field photograph taken in August of 2005, approximately 3 months following the last data acquisition presented here. The view is looking toward the northwestern flank at the Krestovsky Channel. (C) A sketch map showing locations and extent of primary Kliuchevskoi features such as the summit crater, nested summit crater, and Krestovsky Channel from above.

material per year and contains over 250 km^3 of high-magnesian to high-aluminous basaltic-andesite material (51-54% SiO_2, 3-5% Na_2O+K_2O; Fedotov et al., 1987; 1991; Ozerov et al., 1997). The Kliuchevskoi eruptive dynamics can be separated into three distinct styles: flank, summit, and paroxysmal eruptions, with all of these having occurred in the last 21 years (Fedotov and Masurenkov, 1991; Smithsonian GVP, 2008; Rose and Ramsey, in review-b).

Sixteen historical flank eruptions have been documented from as early as 1907 (Smithsonian GVP, 2008) although a significant change in eruptive behavior, from summit to flank activity, has been noted following the 1932 eruption (Fedotov and Masurenkov, 1991). These types of eruptions typically start with the formation of radial linear fissures that produce explosive craters and explosive/effusive cinder cones at higher and lower elevations, respectively. The low elevation cinder cones have produced numerous blocky lava flows as large as 0.5 km^3 with eruption duration ranging from 5 days to 13 months (Fedotov and Masurenkov, 1991). The last recent flank eruption occurred during the 1984-1987 phase of activity with the opening of a fissure along the southeastern flank (3,800 to 3,400 m ASL) and the eruption of a lava flow down slope (Smithsonian GVP, 2008, Fedotov and Masurenkov, 1991). From that time, eruption activity has been constrained to the summit crater and lava flows emplaced from the summit (Smithsonian GVP, 2008).

Summit eruptions at Kliuchevskoi have been documented since 1697 and are characteristically Strombolian to Plinian in style, longer in duration than the flank eruptions, and occur approximately every 25 years (Gushchenko, 1979; Fedotov and Masurenkov, 1991). However in the last century, summit eruptions have increased significantly with one eruption occurring every 1 – 2 years (Smithsonian GVP, 2008). This suggests that the volcano may have entered a new phase of open-conduit heightened activity. Typically, summit eruptions at

Kliuchevskoi have started as increased fumarolic activity and phreatomagmatic/phreatic explosions within the central crater that are caused by rising lava interacting with melt water from the permanent snow/ice cover. Increased thermal activity near the summit, including the ejection of volcanic bombs, effusion of blocky lava flows, and hot avalanches of the lava flows from the unstable, steep slopes have commonly followed and produced lahars (derived from lava interaction with ice) tens of kilometers down the flanks into the nearby Kruten'kaya River (Fedotov and Masurenkov, 1991; GVP, 2008). Over the past 300 years, these types of eruptions have resulted in cyclical changes in the summit morphology (Fedotov et al., 1987), with lava infilling of the crater producing the overall conical shape, and paroxysmal eruptions destroying the summit edifice (Fedotov and Masurenkov, 1991).

The first historic paroxysmal summit eruption occurred in 1738 and the most recent in 1994. Descriptions of the 1738 eruption document a week of explosive activity that included incandescent, "audible" lava flows (most likely the result of interaction with snow/ice and avalanching down the steep slopes), notable seismic activity (trembling ground), and sizeable ash plumes (Krasheninnikov, 1949). These ash plumes were reported to have migrated (with the dominant wind direction) toward the sea, and produced little to no fallout locally, implying that the plume had reached the stratosphere (> 12 km at the latitude of Kliuchevskoi) where rapid transport occurred. Similarly, in 1994 Kliuchevskoi entered its largest eruptive phase in over 40 years (Miller et al., 1994). On 8 September this eruption initiated with minor explosive activity within the summit crater producing low-level ash clouds (< 9 km ASL), below the cruising altitude of aircraft. However, by 30 September the eruption intensified to a paroxysmal state with large convecting columns producing pyroclastic flows, as well as lahars and lava flows (~3.0×10^7 m^3) (GVP, 2008). The largest explosive eruptions (VEI=3) produced a significant

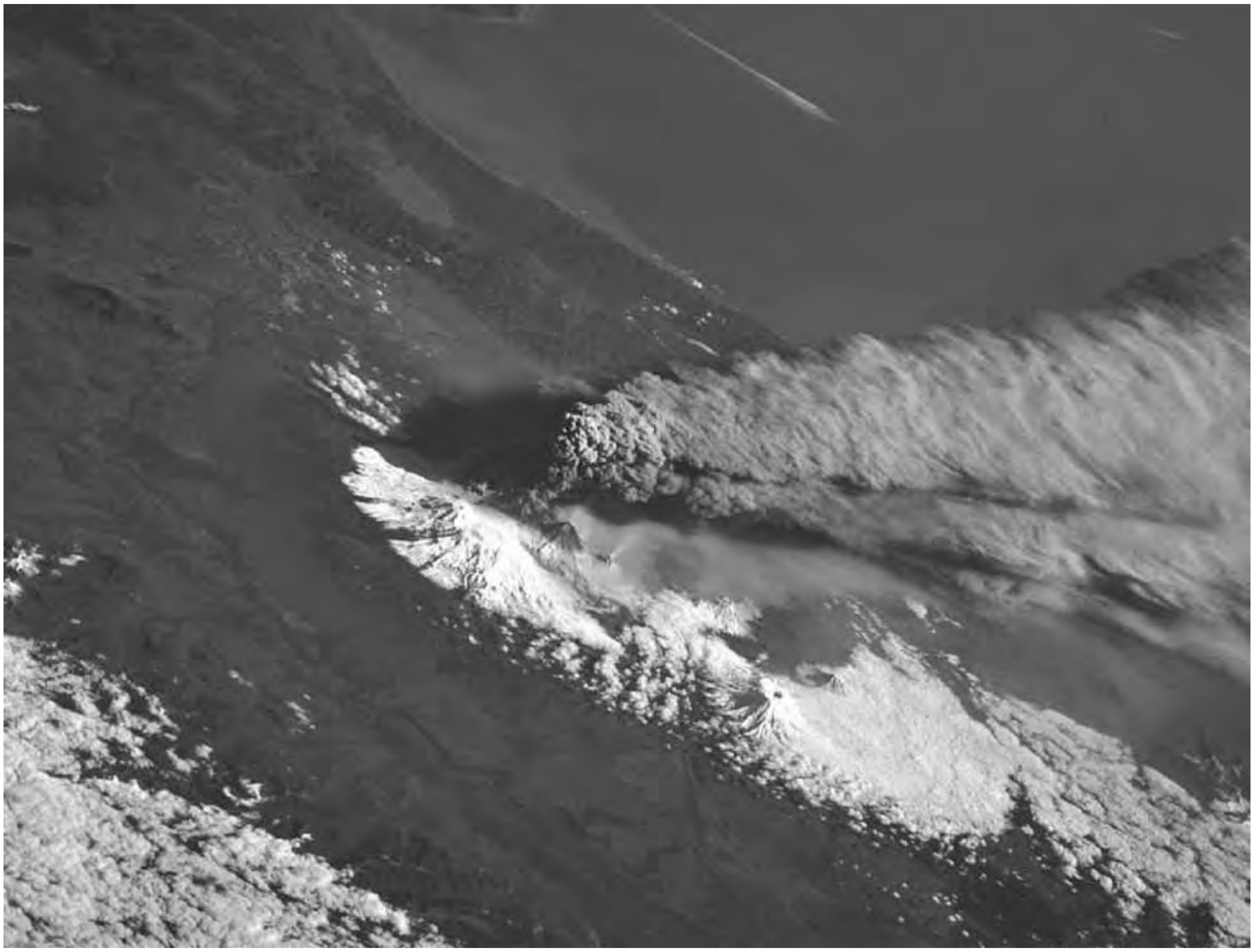

Figure 2-2 The 1994 eruption of Kliuchevskoi volcano observed from the space shuttle Endeavor. During this paroxysm the ash plume reached an altitude of 18 km ASL as it migrated southeastward towards the North Pacific Ocean.

ash column (Figure 2-2) containing ~5.0×10^7 m^3 of material, which reached 18 km ASL and traveled approximately 1,000 km southeast into the North Pacific air traffic routes (Miller et al., 1994). This intense explosive stage of the eruption continued for roughly 36 hours and eventually subsided by 2 October. From that time, Kliuchevskoi has remained relatively active, producing smaller explosive eruptions (VEI=1-2) and effusive activity on a 1-2 year time scale (GVP, 2008).

2.2 VOLCANO MONITORING OF THE NORTH PACIFIC

In 1993, a collaborative effort between scientists from the Alaska Volcano Observatory (AVO), the Russian Academy of Sciences Institute of Volcanic Geology and Geochemistry (IVGG), the Kamchatkan Experimental and Methodical Seismological Department (KEMSD), established the Kamchatkan Volcanic Eruption Response Team (KVERT) (Kirianov et al., 2002). This group was created from the existing Russian institutions and designed for rapid detection and response to volcanic activity on the Kamchatka Peninsula. The main function of KVERT is to provide eruption notices and status reports to local and international authorities in order to reduce associated risks to aircraft within the vicinity of drifting volcanic ash plumes (Heiken et al., 1992).

Presently, the principal methods for monitoring volcanic unrest in this region include seismic stations, ground-based visual observations, and low-spatial resolution (e.g., 1 km/pixel and larger) and high temporal resolution (e.g., 1-6 hours) satellite data. As of 2007, 33 remote seismic stations have been deployed throughout the most active volcanic areas on Kamchatka (Chebrov, 2008). In order to augment human observations and verify eruptive activity, a webbased video camera system was also installed in the town of Kliuchi in 2000 and trained on Kliuchevskoi. Periodic over flights are conducted to provide visual observations. These real time descriptions and images are compared to seismic data in order to scale visible plume heights to seismic energy (Roach et al., 2004). During periods of bad weather where visual observations are impossible, plume heights can therefore be estimated based solely on the seismic activity. More recently, visible and thermal infrared satellite-based instruments have been used to detect and model plume height, compositions, density, and temperature during an eruption (Rothery, 1989; Realmuto et al., 1994, 1997; Searcy et al., 1998; Dehn et al., 2002; Ramsey and Dehn, 2004; Vaughan et al., 2005). These instruments include the Geostationary Operational Environmental Satellites (GOES), the Advanced Very High Resolution Radiometer (AVHRR), and the Moderate Resolution Imaging Spectroradiometer (MODIS), which acquire data every 15 minutes to every 4-6 hours. Although ideal for detection and monitoring of hourly changes at an active volcano, high temporal/low spatial resolution can commonly miss smaller-scale observations. Thermally-anomalous pixels are only detectable if the erupted material is either very hot and/or covers a large percentage of the pixel. Furthermore, the inability to determine parameters such as composition, surface texture, and heat flux of small lava flows/fumaroles in sufficient detail makes these sensors non-ideal for small-scale mapping and monitoring.

The goal of this investigation is to determine how well data from a broad spectral range at spatial resolutions under 100 m per pixel can be used to document an ongoing eruption in a remote location during the harsh northern Pacific winter. This analysis allowed the assessment of the maximum temperature of the erupted products, the spatial extent of these products, the errors involved, and the overall usefulness of these data for extraction of the ongoing volcanological processes occurring during the 2005 eruption of Kliuchevskoi volcano.

2.3 2005 KLIUCHEVSKOI ERUPTION OBSERVATIONS AND DATA

2.3.1 KVERT Observations

During the 2005 eruption, KVERT disseminated multiple information releases, which summarized the latest observations (Table 2-1). On 12 January 2005, KVERT reported increased seismic and thermal activity at Kliuchevskoi. In addition, a weak gas-steam plume was observed emanating from the summit. Two days later, KVERT raised the color code from green to yellow and eventually, from yellow to orange on 16 January due to the increasing seismic activity as well as the incandescence observed above the crater. By the end of January, gas-water vapor plumes rose between 800-1500 m above the crater and Strombolian activity had initiated. Volcanic bombs were also observed being ejected 50-300 m above the crater on the evenings of 20-23 January and again on 27 January.

Throughout February and March, the eruption remained dynamic, with seismic activity well above background level. Gas-water vapor-ash plumes were more energetic, rising to >3,000 m above the summit and on 7 February produced ash fall that was observed on the flank of nearby Ushkovsky volcano (northwestern portion of the Kliuchevskaya group). Ash fall was also noted in the towns of Kliuchi and Kozyrevsk on 9 February and 11 March, respectively. In early February lava was first observed in the Krestovsky channel on the northwestern flank of Kliuchevskoi (Figure 2-3). The interaction of this flow with the summit glaciers and snow cover produced phreatic explosions and subsequent lahars. By 15 March, this flow became cooling limited and continued lava effusion from the summit produced a second flow. Strombolian explosions continued to become more vigorous throughout February and March, with ballistics

Table 2-1 Summary of KVERT information releases throughout the 2005 eruption (KVERT, 2005). ASTER acquisition dates are listed and the associated observations were released within several days. The level of concern color code is included to show relationships between the eruption characteristics and hazard level. EQ = earthquakes; T = volcanic tremor.

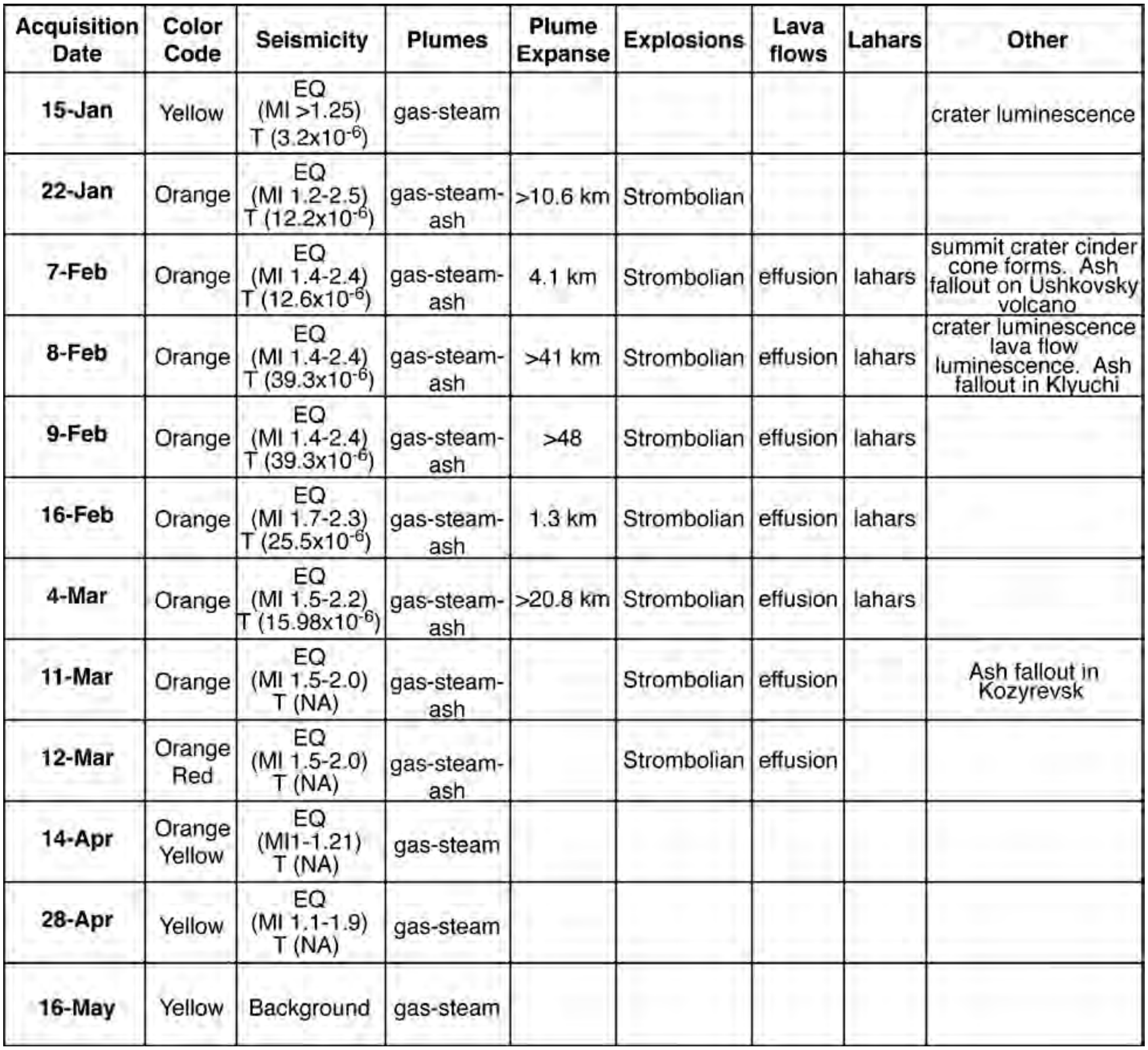

Acquisition Date	Color Code	Seismicity	Plumes	Plume Expanse	Explosions	Lava flows	Lahars	Other
15-Jan	Yellow	EQ (Ml >1.25) T (3.2x10^{-6})	gas-steam					crater luminescence
22-Jan	Orange	EQ (Ml 1.2-2.5) T (12.2x10^{-6})	gas-steam-ash	>10.6 km	Strombolian			
7-Feb	Orange	EQ (Ml 1.4-2.4) T (12.6x10^{-6})	gas-steam-ash	4.1 km	Strombolian	effusion	lahars	summit crater cinder cone forms. Ash fallout on Ushkovsky volcano
8-Feb	Orange	EQ (Ml 1.4-2.4) T (39.3x10^{-6})	gas-steam-ash	>41 km	Strombolian	effusion	lahars	crater luminescence lava flow luminescence. Ash fallout in Klyuchi
9-Feb	Orange	EQ (Ml 1.4-2.4) T (39.3x10^{-6})	gas-steam-ash	>48	Strombolian	effusion	lahars	
16-Feb	Orange	EQ (Ml 1.7-2.3) T (25.5x10^{-6})	gas-steam-ash	1.3 km	Strombolian	effusion	lahars	
4-Mar	Orange	EQ (Ml 1.5-2.2) T (15.98x10^{-6})	gas-steam-ash	>20.8 km	Strombolian	effusion	lahars	
11-Mar	Orange	EQ (Ml 1.5-2.0) T (NA)	gas-steam-ash		Strombolian	effusion		Ash fallout in Kozyrevsk
12-Mar	Orange Red	EQ (Ml 1.5-2.0) T (NA)	gas-steam-ash		Strombolian	effusion		
14-Apr	Orange Yellow	EQ (Ml1-1.21) T (NA)	gas-steam					
28-Apr	Yellow	EQ (Ml 1.1-1.9) T (NA)	gas-steam					
16-May	Yellow	Background	gas-steam					

observed as high as 1000 m above the crater (KVERT, 2005). The hazard level color code was raised from orange to red on 24 March and returned to orange four days later as seismic activity and volcanic tremor decreased.

The eruption activity began to lessen in April and throughout May. Both seismic activity and visual observations decreased, and the color code was reduced to yellow by 15 April. The lava flow was no longer advancing and although production of gas-water vapor-ash plumes continued, they rarely reached 1000 m above the summit. Strombolian activity ceased and seismic activity reached background levels by 29 April. Although seismic activity varied over the next few months, no significant volcanic changes were noted after 16 May and the hazard level color code was eventually reduced to green on 12 August, approximately one week prior to our field investigation. The ASTER data presented here span January through March, the most vigorous phase of the 2005 eruption.

2.3.2 ASTER Instrument and Data

The ASTER sensor was launched in December 1999 as one of five instruments on the Terra satellite, part of NASA’s Earth Observing System (EOS). Terra follows a sun-synchronous nearly polar orbit with an equator crossing time of ~10:30 am/pm. The ASTER instrument has a 60 km swath width, which allows any point on the surface to be imaged once every 16 days. At higher latitudes and with the capability of the sensor to point in the cross-track direction, this revisit time can be reduced to 1-5 days (Yamaguchi et al., 1998, Ramsey and Dehn, 2004). ASTER contains 14 spectral bands including three in the VNIR region (0.5 to 1.0 μm) with 15 m spatial resolution, six in the shortwave infrared (SWIR) region (1.0 to 2.5 μm) with 30 m spatial resolution, and five within the thermal infrared (TIR) region (8 to 12 μm) with 90 m spatial

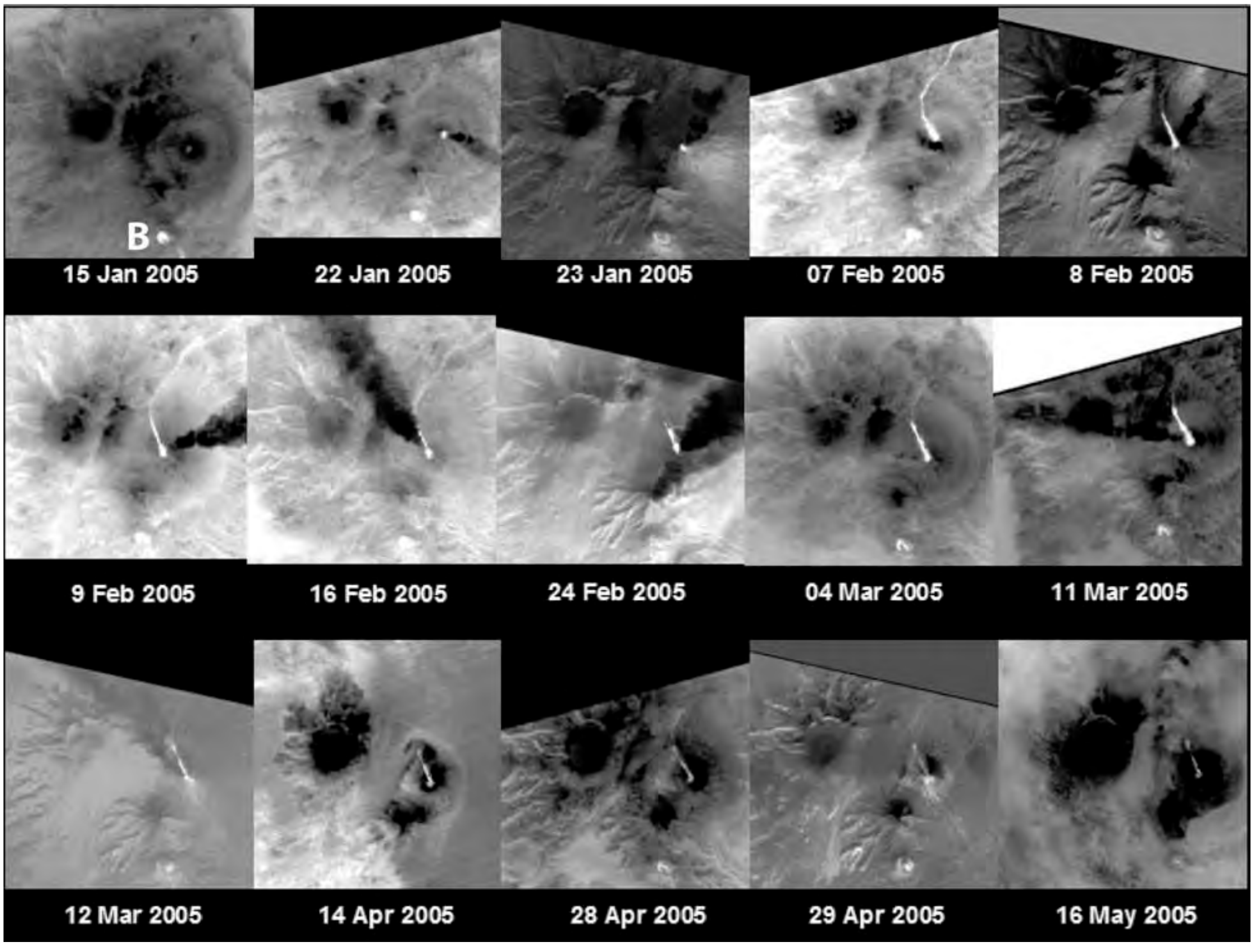

Figure 2-3 Time-series of ASTER TIR data of the 2005 eruption of Kliuchevskoi volcano, Russia. Data span from the initial thermal anomaly detected on 15 January to the cooling of the lava flow barely visible on 16 May. Also seen are the thermally elevated pixels of Bezymianny Volcano (B; south-southeast of Kliuchevskoi) in the early month of the year. Each image is ~50 km wide and rotated with north to the top.

resolution (Kahle et al., 1991). In conjunction with the nominal nadir viewing, an additional backward-looking telescope with the same spectral and spatial resolution as VNIR band 3 (0.807 µm), provides along-track stereographic imaging capability in order to produce digital elevation models (DEMs).

From its initial calibrated data release in March of 2000, ASTER has proven effective for the detection and monitoring of volcanic eruptions and their associated products. Ramsey and Dehn (2004) and Pieri and Abrams (2004) outlined five benefits of ASTER data where compared to other sensors used for volcanic monitoring. These include the ability to acquire nighttime TIR and SWIR data, variable spatial resolution for the different wavelength regions, image acquisition up to 85° latitude, DEM capabilities, as well as multiple bands in the TIR and SWIR regions, which allow for more precise composition, temperature, and surface property determination. Most importantly, ASTER can be pre-scheduled for various gain settings in the SWIR and VNIR in order to limit data saturation/loss for highly radiant targets (Pieri and Abrams, 2004). For example, a 'high' gain setting in SWIR Band 9 (2.40 µm) allows for greater sensitivity to targets with lower reflected radiance (~4.0 $W*m^{-2}*sr^{-1}*\mu m^{-1}$) or slightly warm emission (~86 °C); whereas a gain setting of 'Low2' for the same band allows unsaturated reflected radiance data to be collected up to ~73 W*m-2*sr-1*µm-1 or emission up to 329 °C. The TIR subsystem does not have gain settings but has 12-bit quantization, which maximizes the dynamic range and minimizes saturation for most targets. ASTER is the first orbital sensor with high spatial resolution to have more than two bands in the TIR region. These data provide the ability to develop new methods for extracting the small-scale compositional and temperature structure of the surface (Ramsey and Dehn, 2004).

ASTER is scheduled daily acquiring data for individual user requests, larger-scale global mapping campaigns, as well as emergency acquisitions for events such as volcanic unrest (Yamaguchi et al., 1998). Data can also be acquired in an expedited request mode and processed rapidly (< 4 hours), which is especially important for response to natural disasters. ASTER has been tasked numerous times in this mode to collect data of volcanic eruptions, forest fires, tsunami and hurricane aftermath, and flooding (Duda and Abrams, 2005; Morisette et al., 2005; Tralli et al., 2005; McAdoo et al., 2007; Carter et al., 2008). In order to utilize this system in the most efficient way possible for restless volcanoes in the north Pacific, a program is now in place whereby thermal anomalies detected by high temporal/low spectral resolution instruments (e.g., AVHRR) trigger an automatic ASTER expedited request (Ramsey and Dehn, 2004; Ramsey et al., 2004). This process has thus far been very successful, resulting in over 100 new ASTER acquisitions of erupting volcanoes since late 2006, including much of the data presented here.

2.4 RESULTS

2.4.1 ASTER response and urgent request data processing

The progression of the 2005 Kliuchevskoi eruption was captured with a time-series of ASTER urgent request observations, which spanned the first five months of 2005 (Figure 2-3). The first indication in ASTER data that Kliuchevskoi was in the initial stages of an eruption came during a nighttime overpass on 15 January 2005 at 10:55:55 GMT (21:55:55 local time). ASTER was targeted for the continual monitoring of the ongoing eruption of Bezymianny Volcano, 11 km to the south (Carter et al., 2007). Figure 2-4 shows both the ASTER TIR and SWIR images from the 15 January acquisition. The dome at Bezymianny is clearly visible in both datasets as is a weaker anomaly at the summit of Kliuchevskoi. ASTER band 9 (~ 2.4 μm) had saturated pixels, indicating maximum pixel-integrated brightness temperatures in excess of 97 ºC (ASTER saturation temperatures reported by Urai et al., 1999). However, this activity was not large or hot enough to have triggered a thermal anomaly in the routine monitoring using AVHRR data. It was not until the next day that the activity had increased to a level for an AVHRR band 3 anomalous pixels to be identified (Figure 2-4c). The ASTER detection on 15 January and the AVHRR detection the next day triggered a new series of ASTER urgent request observations that continued throughout the eruption, and are documented here.

ASTER level 2 (L2) data (i.e., calibrated, atmospherically-corrected, land-leaving radiance) have been examined in detail in order to determine the relationship of thermal anomalies seen in all three ASTER wavelength regions over time and how these relate to the eruption processes at Kliuchevskoi. Specific ASTER scenes were selected based on several criteria and processed into surface-leaving radiance (AST_09T and AST_09XT). The criteria used were: a low percentage of cloud cover, the presence of elevated pixel DN values (i.e., thermal anomalies), little to no noise/data loss, and the volcano being centrally-located within each image (Figure 2-3). Overall, the time range encompassed the onset of thermal activity at the summit (15 January) until the cessation of lava effusion (16 May), and are summarized in Table 2-2. As the eruption progressed and active lava flows were emplaced, the radiant temperature increased significantly allowing progressive detection by the TIR, the SWIR, and finally the VNIR subsystems, which provided a further constraint on the sub-pixel thermal features.

In total, 10 nighttime TIR datasets were used to extract the brightness temperature and composition of both the plumes and surface compositions. The AST_09T radiance data were used to produce decorrelation stretch (DCS) images, which enhanced the band-to-band emissivity variations, thus revealing the relative compositional differences of the surface units and eruption plumes. The same data were also separated into their temperature and emissivity components using a normalization approach (Gillespie, 1985; Realmuto, 1990; Gillespie et al., 1998; and Hook et al., 2005). The average seasonal background temperature was determined for each image by averaging a 40 x 40 TIR pixel (~13 km^2) area away from the volcanic activity. This value was subtracted from the brightness temperature image, which was then used to identify the location and number of thermally anomalous (>10 ºC above background) features, saturated pixels, and the maximum temperature in each image.

Nighttime data, with a lack of a solar reflected contribution, are typically ideal for SWIR temperature analysis. However, four daytime SWIR datasets and two VNIR datasets (acquired ~13 hours before the nighttime TIR) were also used for temperature analysis presented here. Furthermore the SWIR bands suffer from radiometric errors due to crosstalk contamination between the detectors, which can cause anomalies in the radiance products. The SWIR crosstalk effect can be corrected in the daytime (L2 XT) data products (Iwasaki and Tonooka, 2005). However, nighttime crosstalk corrected data are not available because of the lack of synchronous VNIR data, which are required in the current correction algorithm.

The average reflected radiance from a 30 x 30 pixel (1.2 km^2) non-volcanic area near the summit was calculated to determine the solar radiance contribution, which was then subtracted from the thermally–anomalous pixels. The solar corrected radiance images were separated into temperature and emissivity by applying the reference channel method (Kahle et al., 1980). The

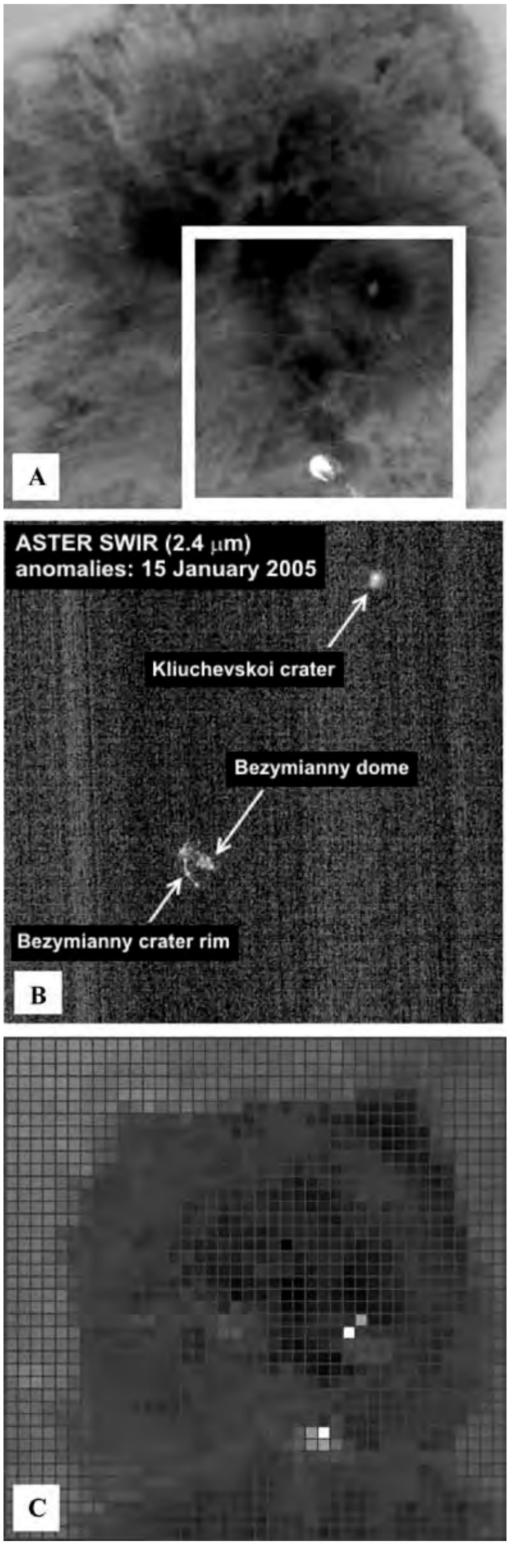

Figure 2-4 Time-series of ASTER TIR data of the 2005 eruption of Kliuchevskoi Volcano, Russia. Data span from the initial thermal anomaly detected on 15 January to the cooling of the lava flow barely visible on 16 May. Also seen are the thermally elevated pixels of Bezymianny Volcano in the early month of the year. Each image is ~ 50 km wide and rotated with north to the top

Table 2-2 Summary of the ASTER scenes used for this study. Mode: S/T= SWIR/TIR only, Full=VNIR/SWIR/TIR. SWIR Gain factor multipliers: High=2, Normal=1, Low1= 0.75, Low2=0.116–0.75). Level 2 (L2) product: AST_09T=ASTER TIR surface radiance, AST_09XT=ASTER SWIR surface radiance (crosstalk corrected).

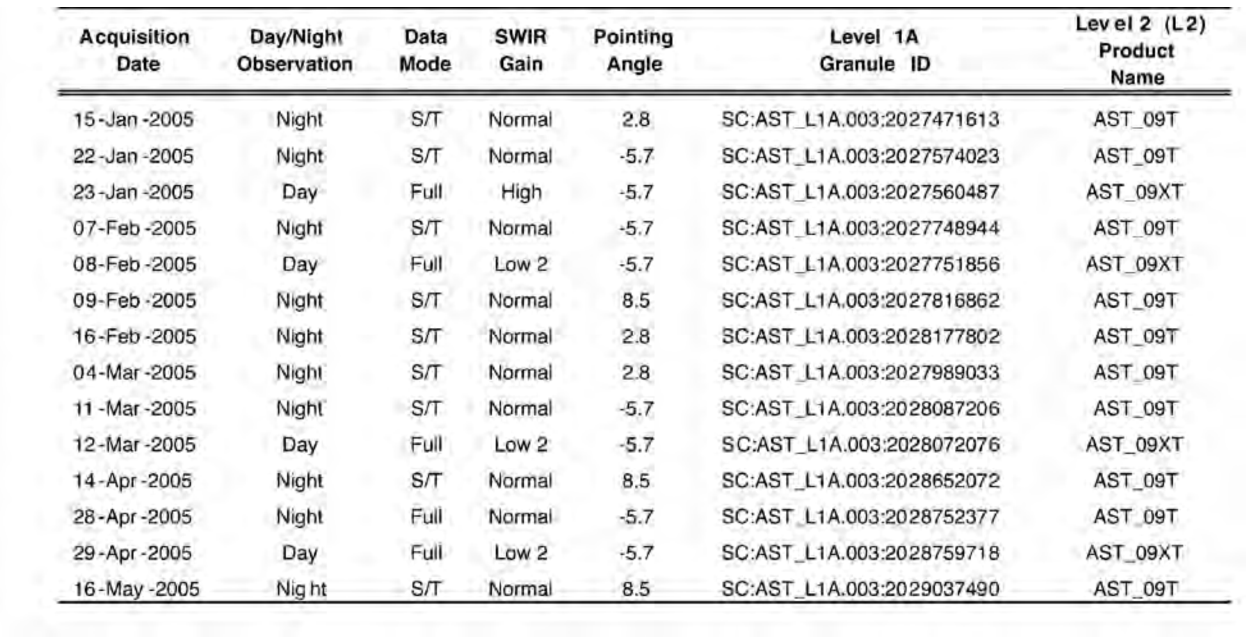

Acquisition Date	Day/Night Observation	Data Mode	SWIR Gain	Pointing Angle	Level 1A Granule ID	Level 2 (L2) Product Name
15-Jan-2005	Night	S/T	Normal	2.8	SC:AST_L1A.003:2027471613	AST_09T
22-Jan-2005	Night	S/T	Normal	-5.7	SC:AST_L1A.003:2027574023	AST_09T
23-Jan-2005	Day	Full	High	-5.7	SC:AST_L1A.003:2027560487	AST_09XT
07-Feb-2005	Night	S/T	Normal	-5.7	SC:AST_L1A.003:2027748944	AST_09T
08-Feb-2005	Day	Full	Low 2	-5.7	SC:AST_L1A.003:2027751856	AST_09XT
09-Feb-2005	Night	S/T	Normal	8.5	SC:AST_L1A.003:2027816862	AST_09T
16-Feb-2005	Night	S/T	Normal	2.8	SC:AST_L1A.003:2028177802	AST_09T
04-Mar-2005	Night	S/T	Normal	2.8	SC:AST_L1A.003:2027989033	AST_09T
11-Mar-2005	Night	S/T	Normal	-5.7	SC:AST_L1A.003:2028087206	AST_09T
12-Mar-2005	Day	Full	Low 2	-5.7	SC:AST_L1A.003:2028072076	AST_09XT
14-Apr-2005	Night	S/T	Normal	8.5	SC:AST_L1A.003:2028652072	AST_09T
28-Apr-2005	Night	Full	Normal	-5.7	SC:AST_L1A.003:2028752377	AST_09T
29-Apr-2005	Day	Full	Low 2	-5.7	SC:AST_L1A.003:2028759718	AST_09XT
16-May-2005	Night	S/T	Normal	8.5	SC:AST_L1A.003:2029037490	AST_09T

resulting temperature images were used to extract maximum temperatures of the thermal features. The stated geolocation accuracy of the ASTER subsystems (i.e., to within one VNIR pixel), together with the sensitivity of the SWIR data to higher temperatures and its greater spatial resolution, allow for an independent data set from which to extract the sub-pixel temperatures and their spatial distribution within the 90 m^2 TIR pixel (Figure 2-5). The emissivity spectra extracted from the TIR radiance of these pixels with significant sub-pixel thermal heterogeneities are commonly distorted due to the assumption of a single pixel brightness temperature during the emissivity/temperature separation stage (Ramsey and Kuhn, 2004). The ASTER SWIR subsystem with its higher spatial resolution provides for a new methodology, currently being developed, to correct a TIR pixel's distorted emissivity spectrum, which can then be used for accurate compositional analysis.

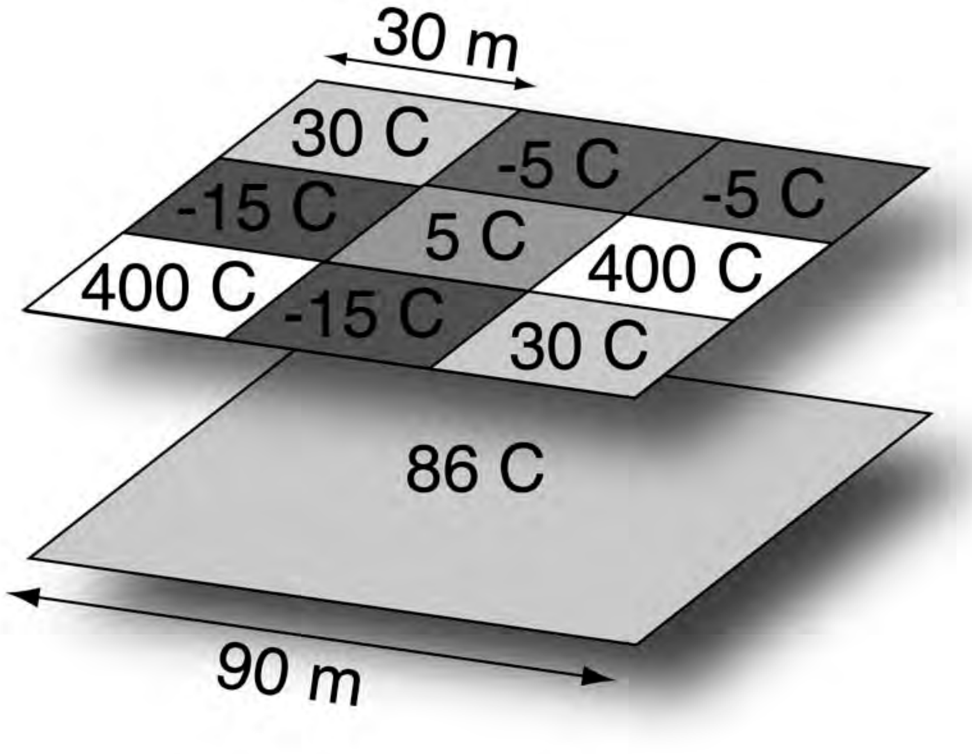

Figure 2-5 A simplified sketch demonstrating how the 30 m, high spatial resolution of the ASTER SWIR subsystem can be used to extract sub-pixel anomalies within one thermally anomalous, 90 m TIR pixel. Future work will include developing a deconvolution algorithm that will determine areal percentages of hot material within one TIR pixel

2.4.2 ASTER thermal observations

Volcanic activity at Kliuchevskoi was first reported by KVERT on 12 January 2005 as seismic activity increased substantially (Table 2-1). In addition, the first observations of an SO_2 gas and water vapor plume began just a few days prior, on 8 January. As previously mentioned, a nighttime ASTER image acquired on 15 January recorded a thermal anomaly that occupied one to three 90 m TIR pixels at the summit crater yielding temperatures between -24 and -22 °C, which were 7 to 9 °C above the average background temperature. A decorrelation stretch (DCS) was also performed on ASTER TIR bands 14, 13, and 11 placing them in R, G, B, respectively. A qualitative analysis of the plume can be performed on the resulting color image, with red to reddish-orange color indicating an ash-rich plume, a yellow to yellow-green plume being SO_2-rich, and blue to cyan plume being mostly H_2O-rich (Realmuto et al., 1994; Realmuto et al., 1997). For the 15 January data, the presence of a small water vapor plume within the summit crater was detected, which corresponded to the sparse ground-based visual observations from observers in Kliuchi.

One week later (22 January), ASTER recorded an increase in thermal output at the summit crater of Kliuchevskoi (Figure 2-3). Approximately 39 pixels were thermally elevated 10 °C or more above the average background temperature of -37 °C, and 7 of those pixels were now saturated (> 97 °C). Recovery pixels (i.e., pixels with no recorded values) were present "down-scan" from the saturated pixels in bands 11 and 12 of the AST_09T radiance data, and confirm a very high level of radiance was recorded in the adjacent pixels. A linear feature extending to the southeast from the summit crater was analyzed using the DCS approach and found to be a 1.8 km by >10.6 km long SO_2-rich plume containing ash near the summit, but primarily composed of water vapor. Daytime SWIR data, collected 12 hours later on 23 January, also revealed the presence of recovery pixels and 150 saturated pixels (temperatures > 410 °C) in band 4 that occupied an area 0.135 km^2. The gas-water vapor plume could be seen extending to the northeast from the summit crater. The saturated pixels present in the SWIR subsystem meant temperatures were now very high in the summit crater most likely from a small actively-overturning lava lake or vigorous Strombolian activity. A maximum pixel-integrated brightness temperature of 806 ºC was extracted from solar-corrected VNIR band 3 (0.807 µm) data.

On 7-9 February, a unique ASTER observational opportunity occurred. The high latitude of Kliuchevskoi, combined with the orbital configuration of the Terra satellite and the off-nadir pointing ability of the ASTER sensor, allowed for a consecutive night-day-night observation sequence. Two nighttime SWIR/TIR datasets and one daytime VNIR/SWIR/TIR dataset were collected. The 7 February nighttime TIR image had a large thermal anomaly along the NW flank, partially obstructed from view at the summit by a 4.1 km long plume that was composed of relatively equal amounts of ash and SO_2. The thermal feature consisted of hundreds of pixels thermally elevated at least 10 °C above background (-31 °C), 10 pixels at or above the TIR saturation temperature (97 °C), and an associated water vapor signature in the DCS image. The daytime SWIR temperatures extracted from the 8 February data had a maximum pixel-integrated brightness temperature at or above saturation (467 ºC in band 4). A linear stretch of the concomitant VNIR pixels shadowed by the upper portion of the volcano revealed incandescence within the Krestovsky channel. The thermally-elevated TIR and SWIR pixels were overlain onto the VNIR data for comparison and showed that the majority of saturated TIR and SWIR pixels were located on/near the incandescent pixels. The maximum VNIR brightness temperature was 807 ºC corresponding to the open-channel lava flow. On the night of 9 February, the eruption plume had the same composition observed previously, however it had shifted to the NE and extended > 40 km off the image (Figure 2-6). This shift allowed for an unobstructed view of the thermal anomaly at the summit region, which had a total of 35 TIR pixels above saturation. The prominent thermal feature was now ~ 600 to 900 m wide and extended ~ 2.0 km from the summit crater where it tapered to a width of 100 to 300 m. Below this feature a thin and much cooler (-25 ºC; ~ 10 ºC above background) linear feature (presumably a lahar deposit) extended ~27 km to the NW terminating in the Kruten‘kaya River.

On 16 February a decrease in saturated TIR pixels from 35 to 11 was observed within and near the summit crater along with one associated recovery pixel. The dimensions of the large thermal anomaly were ~670 m across near the summit and 100-350 m across, approximately 1 km down slope. A plume extended to the NW for > 48 km, and partially obstructed the view of the narrowest portion of the anomaly. The plume's composition had also changed from prior analyses becoming more ash-rich near the summit with a relatively increasing quantity of SO_2 distally. Similarly, smaller water vapor plumes were observed along the thermal anomalies on the NW flank and within the summit crater. The low-temperature, linear thermal anomaly was also visible with a consistent temperature from previous data of around –25 °C. Unfortunately, a daytime observation was not available around this time in order to produce a L2 SWIR and VNIR dataset.

The next successful nighttime ASTER acquisition was on 4 March and a significant change was noted with 373 TIR pixels being thermally-elevated over the background (-35°C). In total, there were 39 saturated pixels and 6 recovery pixels with the remainder of the prominent thermal feature temperatures ranging between –22 and 97 °C. Previously, the anomaly was measured at ~100 m across at the narrowest segment but had now increased to ~600 m. The

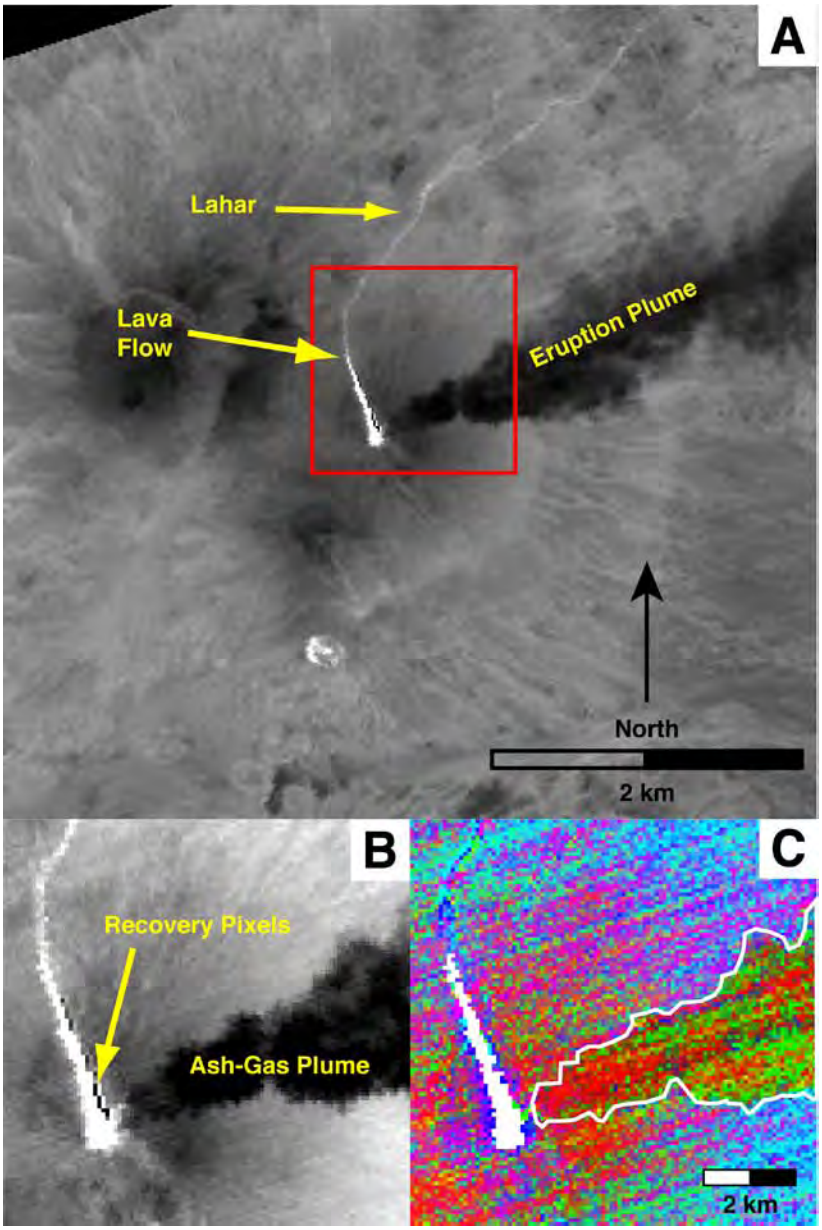

Figure 2-6 ASTER TIR data of Kliuchevskoi acquired on 9 February. (A) ASTER TIR band 10 radiance image. The lava flow, lahar, and cooler eruption plume are visible. The red box highlights the area in B and C. (B) Zoomed image showing the filled crater, lava flow and recovery pixels associated with adjacent saturated pixels. (C) A decorrelation stretch image of ASTER TIR bands 14, 13, 11 in R, G, B, respectively. Ash-rich portions of the plume are red, SO_2-rich portions are green/yellow, and water vapor is blue. This image shows a gradation from an ash-rich plume near the summit to prominently SO_2 distally as fallout occurs in addition to localized water vapor plumes along the perimeter of the thermally anomalous region (white)

length of the widest portion was 2.9 km with an additional 1 km segment exhibiting two tail-like features further down slope. The northern tail extends roughly 10 km, whereas the southern tail ends abruptly at 760 m. A continuous plume was no longer visible, however two small dark puffs (1.3 x 0.8 km) west of the summit and along the thermal anomaly were detected. The puffs contained a mixture of ash and SO_2, whereas the plumes along the flank appear to be a mix of ash and water vapor.

The thermal anomaly that had extended ~4.6 km NW of the summit began to decrease in temperature, but was still visible in the TIR and SWIR data acquired on 11 and 12 March, respectively. More than 100 pixels were > 10 °C above the background temperature (-16 °C; Figure 2-3) in the nighttime TIR data. In the summit crater area and upper elevations of the Krestovsky channel, 40 of those TIR pixels were at or above saturation. Most notably, the linear feature along the lower elevations was no longer visible except for a ~1.3 km tail-like portion at the terminus of the main anomaly. Daytime SWIR data acquired ~12 hours later showed 49 pixels greater than 378 °C (saturated band 6) over the summit and upper channel, similar to the 11 March data. However, a maximum VNIR temperature was not obtained and no visible incandescence was observed indicating that the lava had cooled significantly. Seismic data included within the KVERT information releases (Table 2-1) show decreasing volcanic tremor between 9 February and 12 March, and corresponds with a cessation in lava effusion by that time.

The remaining ASTER data showed a steady decrease in temperature of the thermal features. The dates of these datasets were 14 April, 28 and 29 April, and 16 May. It should be noted that a significant increase in volcanic tremor occurred on 23 March when it reached a maximum value of 6.2×10^7 µm/s and raised the level of concern color code from orange to red.

Over a 2-day period the volcanic tremor steadily decreased and the color code was dropped to orange by 28 March. Unfortunately, a cloud free ASTER acquisition was not available until 14 April to determine the true thermal response and eruptive processes at the surface during this time. By mid-April saturated TIR pixels were no longer present in the summit crater or along the flanks. Temperatures of the anomaly were much cooler than the two previous months ranging from –15 °C along the Krestovsky channel to 3.6 °C in the summit crater on 14 April. At this time, the total length was roughly 4.3 km and varied in width from 200 m near the base to 600 m at the summit. A nighttime TIR acquisition on 28 April had numerous pixels throughout the image at 10°C above background (-24°C). One pixel located within the summit crater area produced a maximum TIR temperature of 2.8 °C, whereas a daytime overpass on 29 April had a maximum SWIR temperature of 173.7 °C (band 6). Although the length of the anomaly remained relatively unchanged in the 16 May scene, the width steadily decreased to 470 m at its widest, and the temperatures ranged between –19.5 to -3.3 °C. These were beginning to approach equilibrium with seasonal background temperatures. Throughout the months of April and May no plume was detected in the TIR data (Figure 2-3).

2.4.3 Eruption Rate

In order to determine a proxy for lava effusion throughout the eruption, the number of saturated SWIR pixels (Band 4) for each daytime scene was recorded (Table 2-3). If one assumes that the saturated SWIR pixels correlate to lava flows with little to no crust, then the surface area of those flows can be easily extracted from the ASTER data. In order to calculate lava volume, an estimate of depth must be made. Ozerov et al., 1997 documented lava flow thicknesses for

Kliuchevskoi volcano ranging between 2 and 25 m (up to 4400 m ASL; near the summit) and the latter was used here to establish a maximum possible volume. Furthermore, to approximate the shape of the nested summit crater and Krestovsky channel, a disk and half elliptical tube cross-cut through the long axis were used.

Because the three SWIR datasets were acquired with different gain settings (and therefore a possibility of more or less saturated pixels), a correction factor was applied in order to scale between data collected. The 8 February and 12 March datasets were acquired in Low Gain 2 mode, whereas the 23 January dataset was in High gain. In order to normalize the difference between the Low2 and High gain settings, band 4 in each dataset was multiplied by its associated gain factor, and a common non-thermally elevated pixel for each scene was located. The difference in radiance values for this common pixel was used to scale the Low2 data into High gain. The corrected scenes were then divided by the new gain factor (High gain; 2) resulting in the same radiance value for the common non-thermally elevated pixel. Lastly, saturated pixels were counted for each dataset (Table 2-3). The newly determined saturated pixel count was used

Table 2-3 Summary of the saturated daytime SWIR pixels recorded by ASTER throughout the 2005 eruption of Kliuchevskoi volcano. This table shows the original pixel counts for each daytime acquisition under a High gain in January and Low2 gain for the remaining datasets as well as a corrected pixel count once the data was normalized to a High gain setting. A summary of the calculated lava volumes extracted from the normalized saturated SWIR pixels reveals a consistent decrease between 23 Jan and 12 Mar in spite of the initiation of effusion at the end of January.

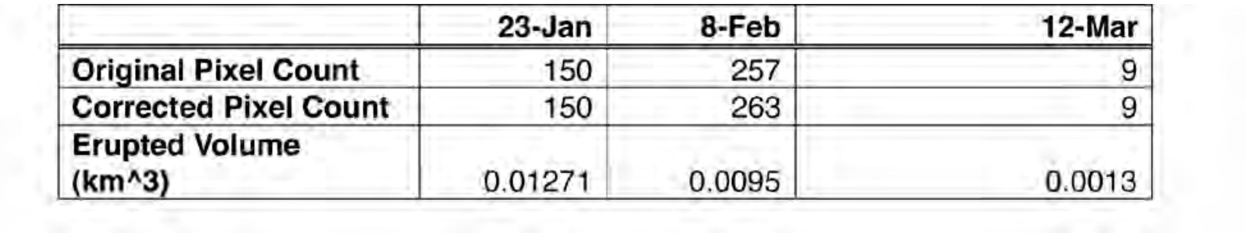

	23-Jan	8-Feb	12-Mar
Original Pixel Count	150	257	9
Corrected Pixel Count	150	263	9
Erupted Volume (km^3)	0.01271	0.0095	0.0013

to estimate the area of active lava within each SWIR scene. These areas were then converted into volumes by multiplying the assumed depths of the channel and summit crater. On 23 January, a total volume of 12.71 x 10^{-3} km^3 was present within the nested summit crater. Although effusion began shortly thereafter, the total volumes calculated for 8 February and 12 March decreased steadily to 9.5 x 10^{-3} km^3 and 1.30 x 10^{-3} km^3, respectively. In total, the ASTER data over this 3 month time period suggests approximately 23.51 x 10^{-3} km^3 of material was erupted at the summit of Kliuchevskoi.

2.4.4 ASTER Emissivity Observations

Emissivity spectra of two samples collected within the Krestovsky channel during the August 2005 field campaign were acquired in the IVIS laboratory at the University of Pittsburgh. These spectra were degraded to the spectral resolution of the ASTER TIR and compared to the TIR-derived emissivity spectra of an isothermal, non-thermally elevated pixel from the 9 February image (Figure 2-7). Sample Klyuch-01-05 is a blocky, massive non-vesicular basalt, whereas Klyuch-02-05 is a basaltic bread crust block. Sample Klyuch-01-05 produced a spectrum remarkably similar to the ASTER-derived data yielding a maximum emissivity difference ($\Delta\varepsilon$) of 0.023 in ASTER band 14. Although Klyuch-02-05 has a slight inversion between ASTER bands 11 and 12 (Figure 2-7), the maximum $\Delta\varepsilon$ compared to the isothermal ASTER pixel was also minimal (0.016) and indicates good agreement between the laboratory-derived and remotely sensed spectra.

A thermally-elevated ASTER pixel, located along the active lava flow on the northwestern flank was also chosen for comparison to the laboratory derived basalt spectra.

Although the overall spectral shape remains consistent with the lab spectra, especially in ASTER bands 10 and 11, a significant increase in $\Delta\varepsilon$ occurs in the ASTER spectrum as wavelength increases (Figure 2-7). A maximum $\Delta\varepsilon$ of 0.042 occurs at band 13 between the ASTER pixel and sample Klyuch-01-05, whereas the same band produces a maximum $\Delta\varepsilon$ of 0.036 for sample Klyuch-02-05. This error is the direct result of a TIR pixel with significant sub-pixel thermal heterogeneity being treated as isothermal during the separation of emissivity from temperature. Such an assumption is unavoidable and produces data that are easily identified as thermally-mixed. However, in order to correct these distorted emissivity spectra, further corrections and/or examination of the SWIR data is required. Collectively, comparisons between the lab derived and ASTER spectra exhibit good correlation with respect to composition, but clearly show errors commonly associated with thermally elevated features.

2.5 DISCUSSION

2.5.1 Thermal Data

During the 2005 eruption of Kliuchevskoi volcano, 6 saturated TIR pixels (0.05 km^2) were first observed on 22 January and increased to a maximum of 40 pixels (0.32 km^2) by 11 March (Figure 2-3). Similarly, the SWIR subsystem also saturated during this time, although the same pattern is not observed as in the TIR. A peak of 257 SWIR pixels (0.34 km^2) occurred in the 8 February dataset and decreased to 49 pixels (0.04 km^2) by 12 March. By utilizing the VNIR subsystem of ASTER, maximum temperatures of 808 and 806 ºC were extracted in the 22 January and 8 February data during which time incandescence was also reported by KVERT.

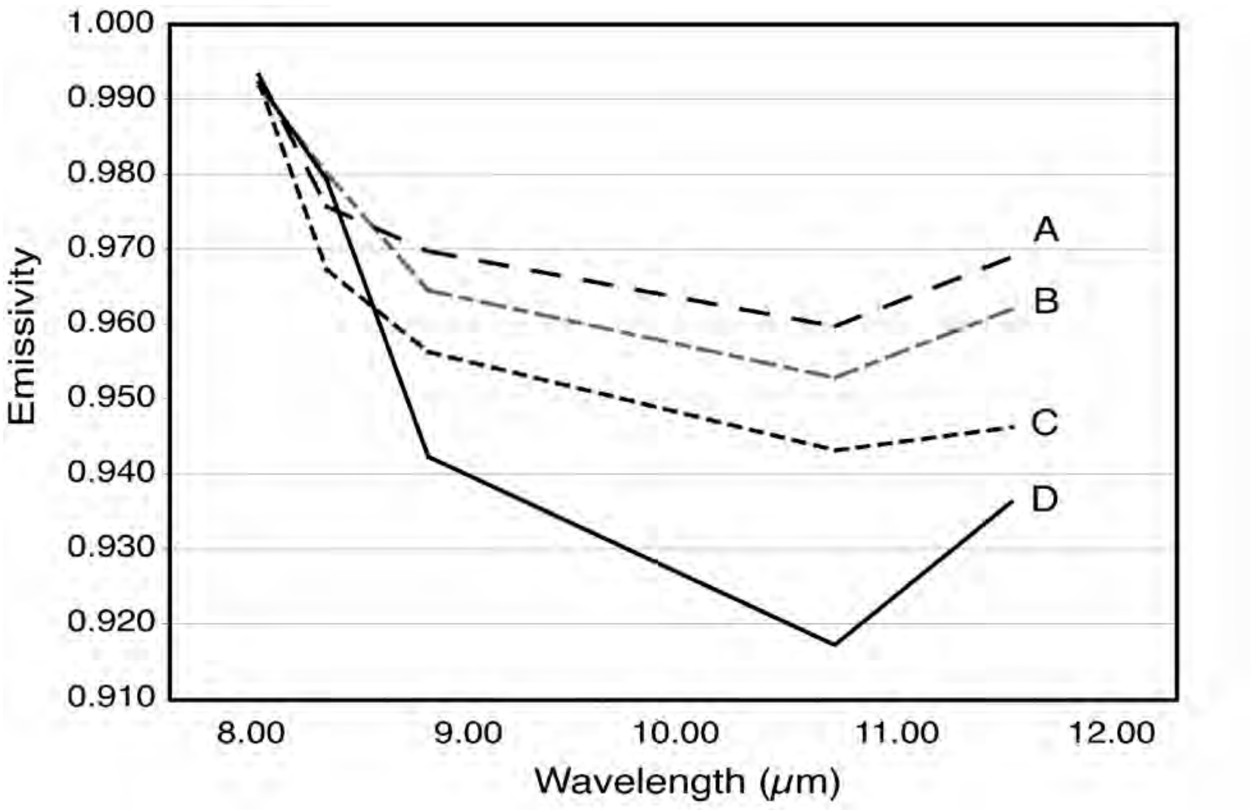

Figure 2-7 Summary of emissivity spectra obtained from two samples collected in the field in addition to spectra extracted from both thermally elevated and non-thermally elevated TIR ASTER pixels. A = Sample Klyuch-02-05 bread crust basalt; B = Sample Klyuch-01-05 blocky basalt; C = Non-thermally elevated, isothermal ASTER spectrum; D = Thermally elevated, non-isothermal ASTER spectrum. The data show how the presence of thermally mixed pixels result in large errors of emissivity spectra and support the development of a deconvolution algorithm.

Such high temperatures in conjunction with saturation of the TIR and SWIR suggest that the thermal anomalies within the summit crater and Krestovsky channel were produced by open-channel lava effusion rather than high temperature fumaroles.

The discrepancy between the timing of peak TIR and SWIR areas of saturation (Figure 2-8) is most likely the result of the lava flows simply being obscured by the shifting eruption plume. Moreover, the SWIR data may be recording peak open channel lava effusion during the 8 February acquisition and subsequent formation of a partial lava flow crust by 12 March. The VNIR data could not be used to determine temperatures subsequent to the 12 March acquisition due to the decreasing pixel-integrated brightness temperatures. We attribute this to the closing off of the open-channel and the formation of insulating lava tubes. These crusted surfaces were still hot enough to allow saturation of the SWIR pixels (467 ºC), but cooler than the lower limit of the VNIR detection (705 ºC). These results are in agreement with KVERT reports that document the presence of lava flows on 15 and 20 March, but do not specify if they are active (Table 2-1). Moreover, the information releases correspond well with our interpretations of the ASTER data as they first reported incandescence within the crater initiating on 16 January, strombolian activity on 20 January, and lava effusion from 31 January until 8 March.

The lava volumes calculated for the three daytime SWIR datasets indicate an overall decrease within a three-month period. However, the 8 February SWIR image shows the onset of an effusive stage of the eruption implying that an increase in lava volume should be expected. The decrease in lava volume from 23 January to 8 February may be the result of three possible factors: 1) The correction for the gain normalization between datasets may contain inherent errors whereby the solar azimuth, solar elevation, and seasonal variation between datasets could have resulted in an initial difference in radiance values for the pixels targeted; 2) Just prior to the

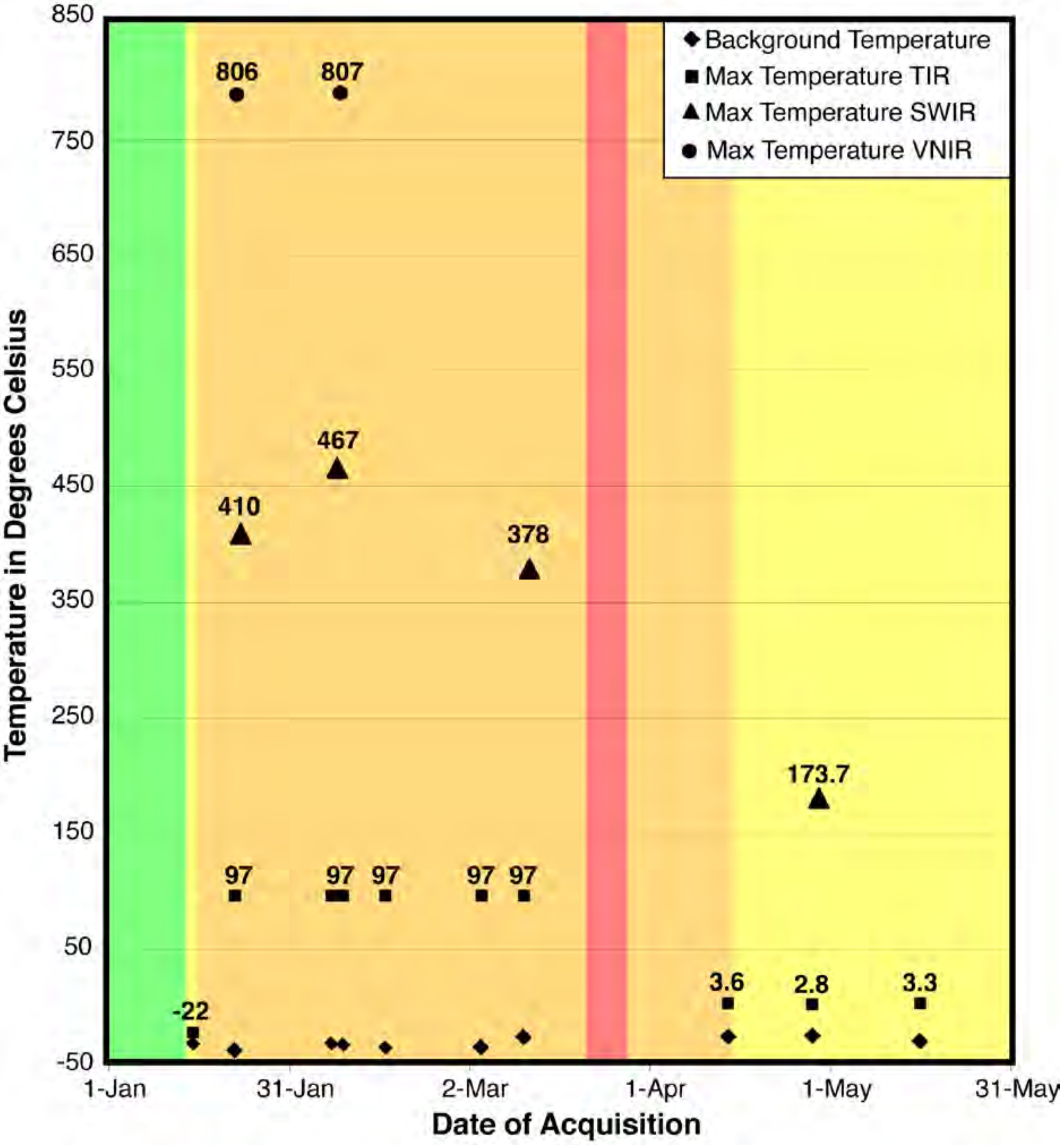

Figure 2-8 Summary of the 2005 Kliuchevskoi eruption pixel-integrated brightness temperatures derived from ASTER. Band 10 (TIR; squares), bands 4 and 6 (SWIR; triangles), and band 3 (VNIR; circles) from each subsystem were used. The data reveal a maximum temperature above saturation of both the TIR and SWIR subsystems starting on 8 Feb. Band 4 was used to determine maximum SWIR temperatures on 23 Jan and 8 Feb and variable saturation between acquisitions is a result of a High-gain and Low2 gain setting, respectively. Band 6 was used for the 12 Mar and 29 Apr acquisitions and also had a Low2 gain setting. The average background temperatures derived from the TIR (diamonds) are shown for reference, as is the KVERT color code in the background. A brief period of heightened seismicity (red) was reported by KVERT between 24 and 28 March.

8 February acquisition, a cooled-carapace and/or lava tubes may have formed on the surface of the lava flow that prevented saturation of the SWIR data, thereby minimizing the total surface area of the active flow; 3) In the 8 February SWIR image, the active lava within the summit crater appears to have reduced in size from 23 January and suggests that the lava lake has drained and/or cooled once effusion began in the Krestovsky channel.

Further examination of the saturated SWIR pixels in the 8 February dataset reveals a detachment between the nested summit crater lava pond and the lava flow within the Krestovsky crater, suggesting that the lava flow originated from a breakout point below the elevation of the nested summit crater. This may be due to a structurally weak zone at or near the summit, a feeder dike rooted from the main conduit, or development of a lava tube. During the August 2005 field investigation, a helicopter over flight and a Forward Looking Infrared (FLIR) camera were used to evaluate the thermal conditions of the volcano. This FLIR data (Figure 2-9) confirms the presence of a breakout point approximately 60 m below the rim of the nested summit crater, and does not reveal the presence of thermal anomalies within the main crater that would indicate a flow had breached the nested summit crater and traveled down the Krestovsky channel. Temperatures within the main summit crater remained at background levels (approximately -9 ºC +/- 5 ºC) whereas the lava flow and portions of the nested crater had maximum temperatures in excess of 100 ºC over 6 months following emplacement. These data in conjunction with volume change observations suggest that the lava lake within the summit crater drained either back into the main conduit, or into a weak fractured zone that rerouted the lava to the breakout point at the top of the Krestovsky channel.

2.5.2 Composition from the TIR

Gillespie et al., 1998 introduced a temperature and emissivity separation algorithm for ASTER data with the goals of determining surface temperatures and mineral compositions within 1.5 K and 0.015 errors, respectively. However, this algorithm (like all temperature/emissivity separation techniques) is constrained by assumptions of a homogeneous and isothermal Lambertian surface emitting equally at all angles over a 90 m by 90 m area. Previously, deconvolution or spectral unmixing algorithms have been developed and applied to the extracted emissivity for geologic applications (Adams et al., 1986; Gillespie, 1992; Johnson et al., 1992; Sabol et al., 1992; Ramsey and Christensen, 1998; Ramsey and Fink, 1999; Zorn and Ramsey, 2002) in order to determine mineral and textural abundances in spectrally-mixed TIR pixels. These approaches fail however where non-isothermal conditions are present (Ramsey and Dehn, 2004; Ramsey and Kuhn, 2004). Unlike ASTER pixels with varying compositions that produce linearly mixed emissivity spectra, the non-isothermal pixels behave non-linearly producing large errors in slope of emissivity versus wavelength plots (Figure 2-7). The conditions on Kliuchevskoi that produced the slope in the emissivity spectra are related to one of the following: 1) A portion of the pixel contains active lava as well as ambient surface material; 2) Hot cracks may have formed on a cooling carapace of the lava flow; and/or 3) Hot fumaroles may be scattered across the northwestern flank. Future work will attempt to utilize data from all three subsystems of ASTER in order to develop a thermal deconvolution algorithm capable of extracting the temperatures and areal percentage of hot material in mixed TIR ASTER pixels for the purpose of correcting the emissivity spectra.

Information extracted from the decorrelation stretch of the ASTER TIR data also allowed

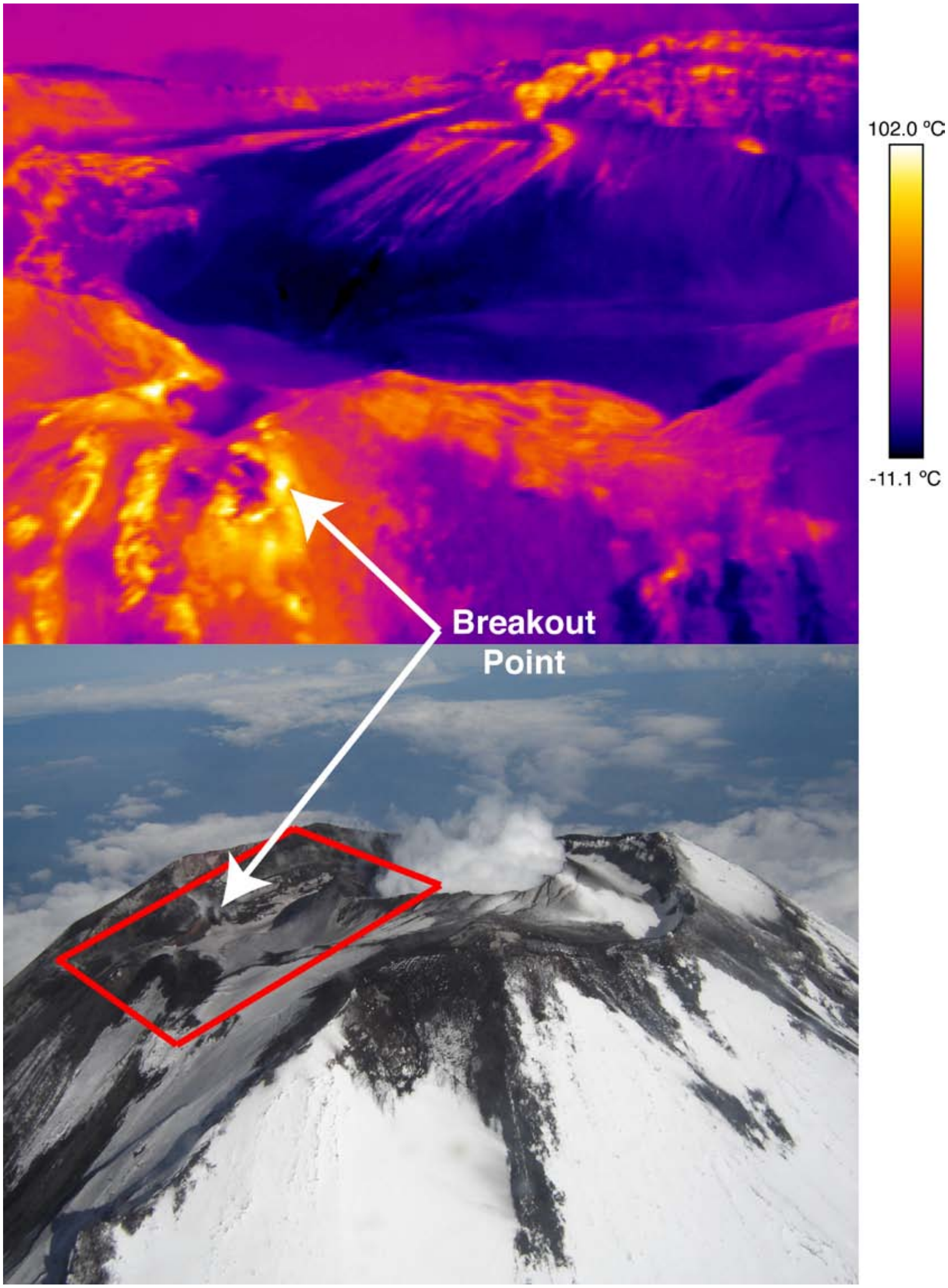

Figure 2-9 A comparison between a Forward Looking Infrared (FLIR) image and a digital photo of the summit of Kliuchevskoi, taken during a post-eruption over flight in August 2005. Red box shows coverage of the FLIR image with the breakout point highlighted by white arrows. The high-spatial resolution of the FLIR data reveals a breakout point for the effusion of lava on the top northwestern flank in the Krestovsky channel, possibly due to a structurally weak zone in the summit region. White/Yellow = hot pixels; Black/Blue = cold pixels.

for compositional discrimination of the plumes throughout the 2005 eruption. Water vapor plumes were present in each acquisition and were typically located within the summit crater and along the lava flows in the Krestovsky channel. Water vapor plumes within the summit crater appear to be persistent throughout the eruption and are probably related to degassing of magma, fumarolic activity, and the melting of snow and ice during heating events. During effusive activity, KVERT reported phreatic explosions and lahar production within the Krestovsky channel as a result of lava interaction with snow and ice. This activity supports the interpretation of the presence of water-rich plumes along the lava flows.

Based upon information releases by KVERT, ash fallout occurred on 7 February on the southwest flank of nearby Ushkovsky volcano, in the town of Kliuchi on 9 February, and in the town of Kozyrevsk on 11 March (Table 2-1). The ASTER TIR data agrees with these reports and showed an ash depletion signature of the eruption plume as it migrated away from the summit crater. Additionally, the 22 January and 16 February ASTER data had a similar ash fallout signature. The 4 March acquisition does not exhibit this type of plume activity. However, it does reveal a series of isolated ash/SO_2 puffs commonly associated with Strombolian explosions during gas-rich magma resupply (Ripepe et al., 2002). This interpretation is also consistent with the KVERT seismic data that showed a dramatic increase in activity at this time.

2.5.3 Limitations

This study has produced results, which are in agreement with the observations documented by KVERT. However, some limitations of extracting critical information were identified. First, the extreme topographic relief of Kliuchevskoi combined with varying look angles between the day and night ASTER acquisitions (Table 2-2) resulted in a parallax error at the highest elevations even following geometric correction and using orthorectified data. This error prevented precise pixel-to-pixel comparisons between the VNIR, SWIR, and TIR data thereby limiting certainty of spatial comparisons to within one 90 m TIR pixel as opposed to the standard 15 m registration error for regions of little topographic relief.

In order to minimize this problem in the future, two approaches may be used: 1) Use only daytime or nighttime acquisitions, such that the look angle remains constant between the subsystems; 2) Collect a well-distributed series of ground control points on or near the summit and the surrounding plain so that images can be geolocated to compensate for parallax and geometric distortions; and/or 3) Concentrate on determining sub-pixel temperature extraction where relief and distortion is minimal. Of these, the first appears to be most feasible although it does limit the amount of data available for analysis. Collecting ground control points in such a remote and topographically-extreme area includes numerous logistic issues, and applying sub-pixel temperature extraction on volcanic areas of little relief seems relatively simplistic. Therefore in order to characterize the eruptive behavior of large, dangerous volcanoes such as Kliuchevskoi using all possible ASTER data, future work must include a more robust topographic and data geolocation approach.

Other limitations are present in the ASTER data. The daytime SWIR and VNIR data contain a mixture of emitted radiance from the lava flows and solar reflected radiance, but are able to have the cross-talk error removed from the SWIR data. Conversely, the nighttime SWIR data are free of solar contamination, but remain uncorrected for the cross-talk error. The contributions of solar reflected radiance to the maximum derived brightness temperatures is only an approximation and can have associated errors due to over or under-correcting for this variable. In this study, over-compensating for solar reflected radiance results from subtracting an average background value that is higher than the true radiance and ultimately produces maximum brightness temperatures that are too low (for what is expected for these active lava flows as well as the detection thresholds of ASTER). The opposite is true for instances of under-correcting as well, and suggests that a logical correction of solar reflectance will result in relatively small errors (as little as 0.3 ºC) in the derived pixel-integrated brightness temperatures of highly-radiant targets approaching saturation. However, as surface temperatures decrease, errors in resultant brightness temperatures of the SWIR also increase significantly (up to 130 ºC). Ultimately, the errors associated with solar correction, geolocation, and crosstalk correction all propagate into the derived brightness temperature calculations and introduces future obstacles in the precise and accurate deconvolution of thermally mixed pixels in order to extract accurate surface compositional/textural information of hot targets.

Previous work has compared two primary methods developed to minimize errors associated with solar reflected radiance: a mean background subtraction and per-pixel correction (Wooster and Kaneko, 2001). Although that study found the per-pixel method to be more robust, the results were for a dacitic surface with much cooler carapace temperatures. Dacite rocks require higher surface temperatures (>30 ºC) than basaltic rocks in order to isolate their thermal signal from the solar reflected signal, essentially making surfaces with basaltic compositions less susceptible to errors associated with solar reflectance in general (Wooster and Kaneko, 2001). The maximum temperatures of the basalt lava flows presented here are in excess of 30 ºC, suggesting that the solar corrections applied to the daytime datasets had minimal affect on the resulting brightness temperatures of the hot pixels.

To minimize the errors associated with solar reflected surface radiance, the use of nighttime data is preferred. However, these data present the aforementioned issues of crosstalk as well as larger geolocation errors due to the lack of the VNIR data and inability to know precisely the amount of error involved in geolocating the SWIR and the TIR images. Future work will continue attempts to acquire nighttime data in addition to utilizing the “per-pixel” approach to correct for reflected solar radiance in daytime SWIR and VNIR data. In addition, an error analysis of using the daytime versus the nighttime SWIR/TIR data will be needed, incorporating all the errors from crosstalk to geolocation to solar reflection.

2.6 CONCLUSIONS

The behaviors described here for the 2005 Kliuchevskoi eruption are analogous to those observed in previously documented summit eruptions such that this summit eruption included strombolian activity, lahars, and phreatic explosions along the flanks. Large ash plumes produced during this event and extending more than 300 km from the volcano corroborate why monitoring of Kliuchevskoi is essential for aircraft safety. The 2005 eruption of Kliuchevskoi volcano was monitored and observed using the ASTER instrument and supplemented by information releases provided by KVERT. Collectively, these data revealed three phases of activity, including a precursory, explosive, and explosive-effusive phase as the eruption progressed over a five month long period (Figure 2-10). On 12 January, seismic activity increased above background levels followed by gas-water vapor emission and the onset of a summit thermal anomaly within the main crater by 15 January. We interpret this activity as a precursory signal for an impending eruption.

Over the course of five days, the precursory phase transitioned into a vigorous explosive phase of activity associated with Strombolian explosions within the summit crater as well as a continued increase in seismic signals. This explosive phase of the eruption monitored by the ASTER instrument is characterized by the presence of saturated TIR and subsequently SWIR pixels as magma began to rise to shallower levels. Decorrelation stretch images performed on the TIR radiance datasets reveal that explosive activity is associated with a transition from gas-water vapor plumes to ash-bearing plumes (Figure 2-11). Furthermore, the ASTER instrument allowed for identification of explosive activity by recording the presence of incandescence within the summit crater, which was also concurrent with a strong seismic signal reported by KVERT.

The final explosive-effusive stage of eruptive activity is distinguished by a significant increase in the number of saturated ASTER TIR and SWIR pixels. In addition, a peak in seismic signal intensity related to the initiation of lava effusion from the summit crater is also observed (Table 2-1). Visible incandescence within the summit crater (Figure 2-11) and within the area of TIR and SWIR saturation is observed in the VNIR datasets as maximum temperatures of the basalts are in excess of 800 ºC. Moreover, the lava effusion likely melted snow cover and produced water vapor plumes along the flows, an SO_2 plume extending from the summit crater, and cooler lahar signals emanating from the toes of the flows.

Collectively, the thermal and seismic data show a correlation between the color code advisory and maximum temperatures recorded by the ASTER instrument, whereby the highest temperatures occurred during lava effusion and elevated seismic activity. The first thermal anomaly recorded by ASTER occurred on 15 January, and the following day the color code was raised to orange. Between the 14 April and 16 May acquisitions, the general pattern of maximum

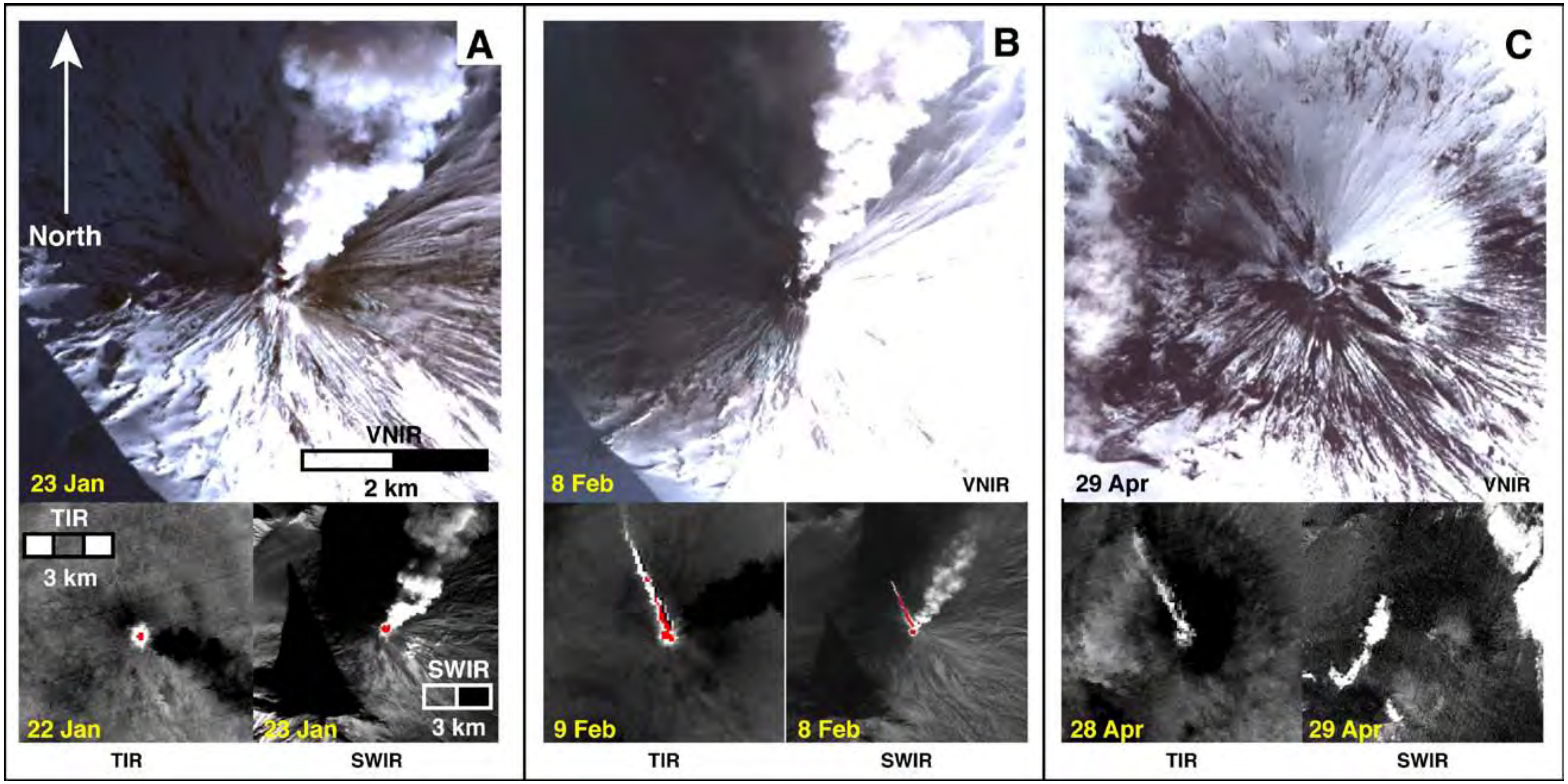

Figure 2-10 An eruptive phase summary of the 2005 Kliuchevskoi eruption as observed by the 3 subsystems of the ASTER instrument. These datasets reveal an A) explosive B) explosive-effusive and C) cooling phase. Saturated TIR and SWIR pixels are shown in red in addition to the associated recovery pixels shown in black along the flows. Spatial scale is consistent between each phase and subsystem.

temperatures of the eruption suggest steady cooling of the lava flows as well as decreased thermal activity within the crater, as the areal expanse of the anomalies decreases. Furthermore, KVERT information releases report decreased seismic activity and a cessation of Strombolian activity by the end of April, also in agreement with the ASTER observations presented here.

Field observations including a high-spatial resolution forward looking infrared (FLIR) camera, conducted in August 2005 and 2007 will be used to supplement results presented here in order to further elucidate compositional and thermal variables below the inherent spatial resolution of the ASTER instrument. Although, further image processing is needed in order to correct the thermally-mixed data, extract accurate compositional and temporal information, and precisely characterize the inherent radiometric and geometric errors, this work provides a foundation for similar thermal/compositional monitoring of ongoing eruptions around the world using ASTER or future instruments with similar characteristics.

3.0 ACCURATE RETRIEVAL OF MULTISPECTRAL INFRARED EMISSIVITY FROM THERMALLY-MIXED VOLCANIC SURFACES

3.1 INTRODUCTION

The goal of many terrestrial remote sensing studies of volcanoes has been to understand global and/or localized impacts on the natural and human environment. This evolving science takes advantage of the atmospheric windows throughout the electromagnetic spectrum, including the thermal infrared (TIR), providing unique information for a given science objective. Previous accomplishments in thermal remote sensing of volcanoes have resulted in: 1) minimizing the time between detection and response of eruptions, especially in remote areas (Dehn et al., 2000; Wright et al., 2004); 2) establishing a detailed chronology of volcanic activity via archival data to predict future behavior (Wright et al., 2005; Carter et al., 2008; Rose and Ramsey, 2009); 3) interpreting rapidly changing surficial characteristics where accessibility is limited due to hazardous eruption processes (Realmuto et al., 1992; Wooster and Rothery, 1997; Carter et al., 2009); and 4) the derivation of thermal flux (Rothery et al., 1988; Pieri et al., 1990; Oppenheimer and Rothery, 1991; and Harris et al., 1998).

One important benefit of advancing analytical techniques includes the development of algorithms to extract additional information that may exist in complimentary wavelength regions and/or below the spatial scale of the data (e.g., Hughes and Ramsey, 2010), such that the full potential of the datasets is possible. These algorithms also act as a proxy for data reduction that can minimize the amount of time required for processing, therefore allowing critical information of volcanic eruptions to be disseminated quickly and accurately. More importantly, these techniques can be modified for application to future missions and their associated datasets. Spectral deconvolution of data is one such technique for extracting information below the inherent spatial or spectral resolution of a remote sensing dataset by using a library of compositional spectra and assumptions about the processes of spectral mixing (e.g., Ramsey and Christensen, 1998). It can be an invaluable tool for understanding many volcanological processes and hazards that can be obscured in low to medium spatial resolution datasets. For example, this technique has been used to detect volcanic unrest and understand variations in volcanic variables such as surface chemistry (Ramsey, 2002; Christensen et al., 2005) and lava texture (Ramsey and Fink, 1999; Carter et al., 2009).

Previous models (e.g., Thomson and Salisbury, 1993; Ramsey, 1996; Hamilton et al., 1997; Ramsey and Christensen, 1998) have used the TIR with a linear mixing approach to conduct compositional mixture analyses. Linear mixing is based on the assumption that TIR emissivity from a multi-component surface is a combination of the radiant energy from each component in proportion to its areal percentage (Lyon, 1964; Singer and McCord, 1979; Adams et al., 1986; Ramsey and Christensen, 1998). Therefore, spectral absorption features of each component (e.g., mineral) end-member are present in the composite spectrum in proportion to their areal percentage exposed on the surface. Composite spectra are deconvolved using library or image derived end-member spectra and a linear least squares minimization algorithm to fit the data. This process results in a percentage of each component in addition to measurements of the model's quality by way of the root-mean-squared (RMS) error. The assumptions that affect the overall accuracy of the results for this type of model include: the spectral resolution of the instrument, the number of end-members chosen, and to a lesser degree, the particle size of the surface materials and the pixel-integrated brightness temperature (Ramsey and Christensen, 1998; Ramsey and Dehn, 2004). The maximum number of end-members mathematically allowed is determined by the number of spectral bands (plus one) of the instrument. Generally, only three to four end-members are used because Earth-orbiting TIR instruments have very limited spectral resolution and because most geologic surfaces rarely contain a great number of mineral end-members in percentages greater than the detection limit for the model (~5%) (Gillespie, 1992; Ramsey et al., 1993). Particle sizes less than ~60 µm can also impart non-linear spectral effects that must be taken into account using more complex scattering models or appropriate spectral libraries (Hapke, 1993; Ramsey and Christensen, 1998). Moreover, the particle size, maximum emissivity, and pixel-integrated temperature are limited by a priori knowledge of the surface in question. Despite these complexities, the linear quantitative deconvolution approach of thermal emission spectra is relatively straightforward and has become an important tool for interpreting TIR data for Earth and Mars-based studies over the past 20 years.

However, if thermal mixing of a target is also occurring, the linear deconvolution approach of surface radiance and emissivity is no longer valid and requires alternative approaches to the solution. Deconvolving TIR data into its sub-pixel temperature components was first introduced by Dozier, 1981 and Matson and Dozier, 1981. In these studies, they use the two atmospherically corrected TIR wavelength bands of the Advanced Very High Resolution Radiometer (AVHRR) at 1 km spatial resolution and an assumption about the background temperature to solve for the unknown high temperature and its areal percentage within each pixel. However, because of the limited spatial and spectral resolution of the data, they did not take variations in the high temperature component nor the surface emissivity into account. As with all deconvolution approaches, the accuracy of this “dual band” method depends upon initial assumptions, which must not violate the mathematics involved (See Figure 5 in Dozier, 1981).

Previous studies that applied the dual band approach to volcanic processes used the AVHRR and Landsat Thematic Mapper (TM) sensors to produce a relatively-accurate estimation of temperature, radiant flux, and the behavior of volcanic features such as lava flows and fumaroles (Rothery et al., 1988; Glaze et al., 1989; Pieri et al., 1990; Abrams et al., 1991; Oppenheimer and Rothery, 1991; Oppenheimer 1993, Oppenheimer et al., 1993, Flynn et al., 1994; and Harris et al., 1998). Because, active volcanic features such as high temperature fumaroles and lava flows can reach temperatures capable of affecting and eventually saturating most TIR sensors, Rothery et al., 1988 followed by Oppenheimer, 1991, applied the dual band technique to short wave infrared (SWIR) data (2 bands at 30 m spatial resolution) of Landsat Thematic Mapper TM and summarized the errors in volcanic settings. In order to determine the size and temperature of the hot portions of a TM pixel, a temperature for the cool background is typically assumed. If the hot portion of the pixel is equal within two spectral bands, then the percentages of hot and cool portions can be determined where the derived temperatures are set equal in each band. However, inherent errors such as daytime solar reflected radiance, the presence of steam and gas plumes, precipitate minerals accumulated on the surface, topography relative to the viewing angle, and the width of each spectral band of the instrument make thermal deconvolution difficult. These errors can affect the resulting temperatures from 5 to 30 ºC and emissivity by up to 20% (Rothery et al., 1988). Despite these complications, Rothery et al., 1988 demonstrated the effectiveness of the dual band approach for a more accurate understanding of the data acquired over volcanic surfaces.

For the past 10 years, the ASTER sensor has proven effective for the detection and monitoring of volcanic eruptions. However, continuous advancement of analytical techniques remains essential to better understand the infrared data acquired from surfaces with high radiant temperatures, because these thermal features are indicative of the active state of the volcano. With the increase in spectral and spatial resolution of the TIR and SWIR sensors of the ASTER instrument, the ability to determine sub-pixel temperature and compositional distributions within a mixed pixel has increased. However, a more complex methodology than the dual-band model is required to accurately deconvolve these data. We present such an approach using the multispectral TIR and SWIR capabilities of ASTER to automatically identify thermally mixed pixels, deconvolve them into their thermal components, and use that information to correct the emissivity errors in these pixels.

3.2 BACKGROUND

3.2.1 ASTER and Data Products

The ASTER instrument, on the Terra Satellite, was launched in December 1999, as part of NASA’s Earth Observing System (EOS). ASTER acquires data over a 60 km swath width in 14 spectral bands including three in the visible near-infrared (VNIR) region (0.5 to 0.9 µm) with 15 m spatial resolution, six in the SWIR region (1.6 to 2.4 µm) with 30 m spatial resolution, and five in the TIR (8.1 to 11.6 µm) with 90 m spatial resolution. The instrument has outlived its initial design life of five years. Unfortunately, the first and only major failure occurred in 2009 when the SWIR subsystem cryocooler ceased operation producing saturated (and unusable) data. However, nine years of archived SWIR data are available and the methodology presented here is easily adapted to future TIR/SWIR sensors such as the Landsat Data Continuity Mission (LCDM) and the Hyperspectral Infrared Imager (HyspIRI). Unlike previous broadband TIR sensors, ASTER's multispectral and moderately-high spatial resolution TIR capabilities with a high radiometric resolution ≤ 0.2 ºC allows for compositional analysis in the 8 to 12 µm region (Adams et al., 1986; Kahle et al., 1991; Gillespie, 1992; Johnson et al., 1992; Sabol et al., 1992; Ramsey and Christensen, 1998; Ramsey and Fink, 1999; Zorn and Ramsey, 2002; Rose and Ramsey, 2009).

Various standard data products are generated in a hierarchical data format (HDF), ranging from Level 0 (unprocessed data at full resolution) to Level L1B (geometrically and radiometrically calibrated radiance-at-sensor). Higher-level data products such as Level 2 (L2; e.g. atmospherically-corrected at-ground radiance/reflectance, surface temperature and emissivity; Abrams, 2000) can also be generated on demand through the Land Processes Distributed Active Archive Center (LPDAAC). For this investigation, L1B and L2 products including surface TIR radiance (AST_09T), surface emissivity (AST_05), and crosstalk corrected SWIR radiance (AST_09XT) products were utilized. These data products are described in detail below.

3.2.2 Test Locale

Kilauea volcano is located on the island of Hawaii, and is the most active volcano in the world. The most recent eruption of Kilauea volcano began on January 3, 1983, continuing to the present day. The primary activity of this eruption has been concentrated between the Pu'u O'o and Kupaianaha vents along the eastern rift zone, and has produced more than 3.1 x 10^9 m^3 meters of material (Smithsonian GVP, 2010). Since the launch of ASTER, the Kupaianaha activity has waned and an extensive network of lava tubes and breakouts has formed from the Pu'u O'o vent, extending approximately 10 km to the coast. In addition, lava fountaining, a'a channels, and explosions have also been documented during this time (Smithsonian GVP, 2010). Previous studies have reported maximum surface temperatures of the lava tube system to reach 1411K with internal lava temperatures reaching 1426K (e.g. Pinkerton et al., 2002). Although these temperatures result in saturation of the TIR and SWIR subsystems of ASTER, pixels located adjacent to the active flows will be the primary target, as they are most likely to contain portions of the active flow in addition to the surrounding ambient material.

The 2006 Kilauea effusive flank eruption (Prince Kuhio Kalaniana`ole 'PKK' lava tubes; HVO, 2008) was chosen for this study due to its continuous production of lava flows extending from the Pu'u'O'o crater to the breakout points along the lava tube system, the availability of archived cloud-free ASTER day and night data over the past 10 years, in addition to minimal topographic relief that may complicate the atmospheric correction for the upwelling radiance at the sensor. Although the climate of the test area is located in a humid environment that can commonly produce significant cloud cover and atmospheric attenuation of surface radiance, the very high level of emitted radiance from exposed basalt flows dominates the overall signal.

3.2.3 Data Products and Image Preprocessing

Two ASTER datasets chosen for the thermal deconvolution process were acquired on 12 October and 14 October 2006. The processing applied to each dataset is outlined in Figure 3-1. These respective daytime and nighttime datasets (Table 3-1) were used not only to validate the algorithm, but to also determine the sensitivity to solar reflected radiance and the crosstalk calibration error seen in the ASTER SWIR subsystem. The SWIR crosstalk phenomenon occurs because the energy detected in band 4 is not completely isolated and some amount of stray light reflects into the other SWIR bands causing excess detected radiance [Iwasaki and Tonooka, 2005]. The excess radiance from the crosstalk contamination can be corrected to a large degree, but only using daytime data (Iwasaki and Tonooka, 2005).

The daytime SWIR data of high temperature targets must also be corrected to separate the solar reflected radiance component from the thermally emitted component. In order to do this, the "per pixel" method outlined by Oppenheimer, 1991 and Wooster and Kaneko, 2001 was applied to the L2 AST_09XT data. Nighttime L2 SWIR atmospherically and crosstalk corrected surface radiance data are not standard products because of the lack of synchronous VNIR data, which are required in both correction algorithms (LPDAAC, 2009). This was not a factor for the nighttime data; however an ad hoc crosstalk correction must still be made. The same process used to correct the solar reflected radiance component in the daytime data was used for this correction and the errors explored.

ASTER L2 data are generally well registered (to within 2 VNIR pixels) between the VNIR, SWIR and TIR subsystems (Iwasaki and Fujisada, 2005). However, more precise registration can only be achieved using ground control points, which were not available for this study. Therefore, dataset registration between the SWIR and TIR was performed using the coastline in the 12 October VNIR image as a reference vector. The SWIR and TIR datasets were shifted slightly for precise alignment using this vector. The accuracy of this method is limited to the spatial resolution of the TIR, where the error of registration is within one 90 m area.

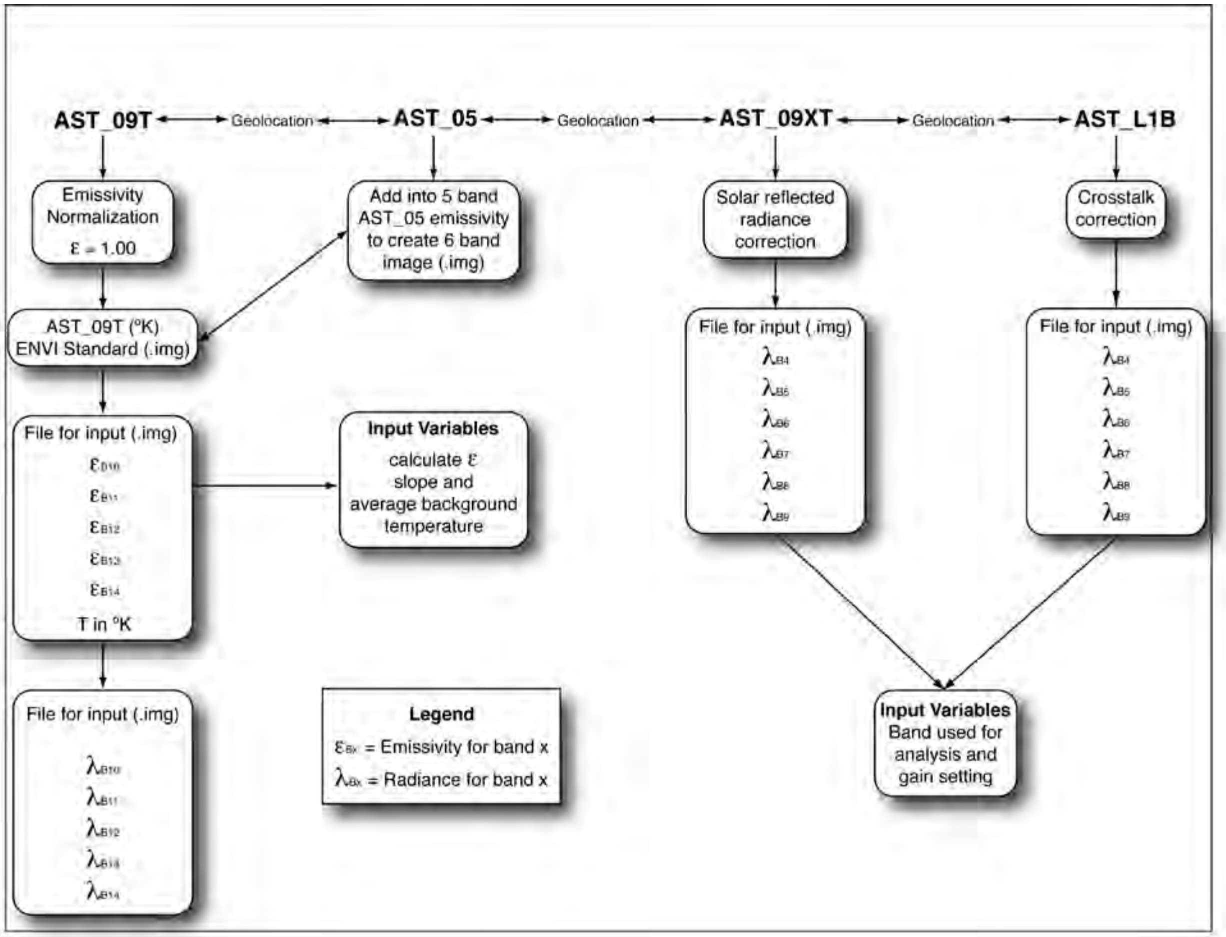

Figure 3-1 The data processing flow chart outlining the steps applied to each dataset prior to thermal deconvolution. Input variables are required before running the algorithm in addition to deciding which SWIR band will be used.

Table 3-1 Summary of ASTER datasets used for input into the thermal deconvolution algorithm.

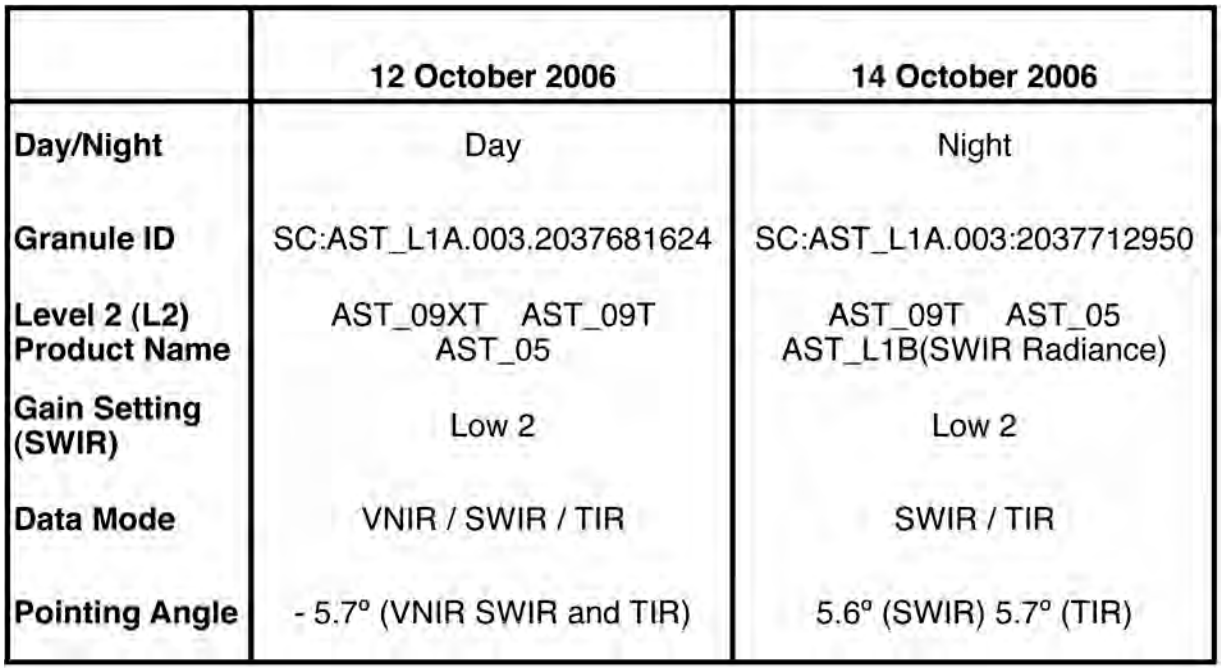

	12 October 2006	14 October 2006
Day/Night	Day	Night
Granule ID	SC:AST_L1A.003.2037681624	SC:AST_L1A.003:2037712950
Level 2 (L2) Product Name	AST_09XT AST_09T AST_05	AST_09T AST_05 AST_L1B(SWIR Radiance)
Gain Setting (SWIR)	Low 2	Low 2
Data Mode	VNIR / SWIR / TIR	SWIR / TIR
Pointing Angle	- 5.7° (VNIR SWIR and TIR)	5.6° (SWIR) 5.7° (TIR)

Essentially, when the geolocation process was complete, the high-resolution vector fell squarely within the low-resolution coastline of the SWIR and TIR datasets. Collectively, each of these datasets can be processed into the necessary variables needed as input for the deconvolution process, such as pixel-integrated brightness temperature, radiance at the surface, and emissivity.

The L2 AST_09T data were used to produce pixel integrated brightness temperatures, whereas the L2 AST_05 product was used to extract surface emissivity. The AST_09T product was processed to extract the wavelength independent pixel-integrated brightness temperature using the emissivity normalization process outlined by Gillespie, 1985; and Li et al. 1999 and applied by Realmuto, 1990; and Gillespie et al., 1998. A maximum emissivity of 1.0 was assumed for this method. The five TIR emissivity bands in the AST_05 product were extracted using the temperature emissivity separation (TES) algorithm (Gillespie, et al., 1998), and combined with the pixel-integrated brightness temperature band to create a six-band dataset for use in the thermal deconvolution algorithm. The TES derived AST_08 surface kinetic temperature product was not used in this study, because the calculations involved in the deconvolution algorithm modeling are based upon blackbody radiance/intensities and the associated temperatures at particular wavelengths. Kinetic temperatures are wavelength independent and therefore do not provide the required radiance values for blackbodies exhibiting non-isothermal conditions.

3.3 METHODOLOGY

3.3.1 Modeling Mixed Planck Functions

The TIR radiance recorded by spaceborne instruments is a function of the surface temperature, emissivity, as well as the interaction of that emitted energy with, and upwelling radiation from, the overlying atmosphere. For a theoretical surface at a constant temperature, with no emissivity variations (i.e., blackbody) and no overlying atmosphere, the directional spectral radiance (in W / m^2 sr µm) would be defined by Planck's Law:

$$L_{bb}(\lambda,T_{bb}) = \varepsilon_{\lambda}*(c_1 / \{\lambda^5[\exp(c_2 / \lambda T_{bb}) - 1]\})/\pi \qquad (3\text{-}1)$$

where, ε_{λ}= emissivity, c_1 = first Planck constant = 3.74 x 10^{-16} W m^2, c_2 = second Planck constant = 0.0144 mK, T = temperature in Kelvin, and λ = wavelength in µm. Solving for the temperature of the blackbody surface:

$$T_{bb} = c_2 / [\lambda \ln (c_1 / \lambda L_{bb})+1] \qquad (3\text{-}2)$$

However, if non-isothermal conditions are present, a simple assumption of two temperature components (hot and cool) can be made. In order to model the contribution of each component, equation (1) can be rewritten:

$$L_{mix}(\lambda,T) = \{f_h\,[L_h(\lambda,T_h)]\} + \{(1 - f_h)\,[L_c(\lambda,T_c)]\} \qquad (3\text{-}3)$$

where, f_h = the fraction of the hot surface (subscripts h and c = hot and cool, respectively). However, this approximation begins to break down if the pixel area is composed of fractional areas of multiple high temperatures. This situation has been shown by Wright and Flynn, 2003 to occur on Hawaiian lava flows and is easily detected by examining the extracted multi-spectral emissivity spectrum, which is commonly depressed at longer wavelengths where thermal mixing occurs.

Prior to constructing the thermal deconvolution algorithm, Planck curves were mathematically mixed model the behavior. This allowed for a better determination and understanding of the temperature thresholds particular to real world scenarios imaged by ASTER. For example, assuming 0.10% of a surface with a temperature of 1000 ºC is mixed with a cooler background temperature of 25 ºC, the resulting Planck curves of the hot, background, and thermally mixed areas can be derived (Figure 3-2). Clearly, the addition of a very small percentage of hot material can significantly alter the shape of a Planck curve, which begins to take on features of both the hot and cool components.

Wien's Law states that as an object's temperature increases, the peak emitted energy of the Planck curve will shift to shorter wavelengths. However, in non-isothermal conditions, as the average surface temperature increases, the Planck curve will undergo a transition from an isothermal appearance, to a non-linear mix of both components, and ultimately become dominated by the average hot temperature Planck curve (Figure 3-2). In this example, the shift

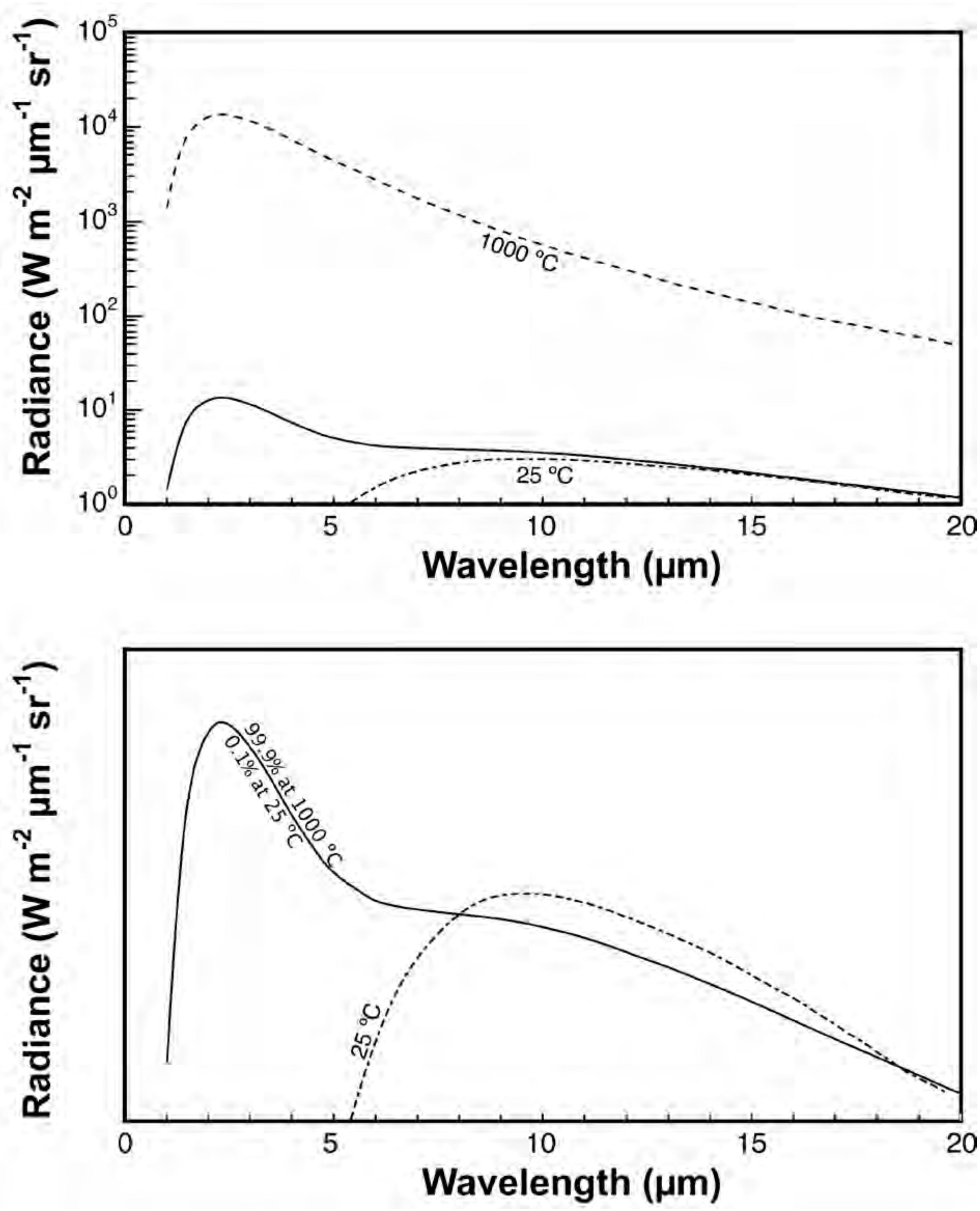

Figure 3-2 Plank curves at various temperatures and mixing percentages. Top) The relationship between hot and cold isothermal Planck curves (dashed curves) at 1273 and 298K to that of a mixed Planck curve of 99.9% 25 °C and 0.1% 1000 °C temperatures. Bottom) The non- isothermal and cool Planck curves normalized at 8 µm. The mixed Planck curve exhibits features of both components and has characteristically steeper slopes compared to the isothermal Planck curve as the wavelength increases in the 8-12 µm region.

of the peak radiance occurs rapidly where the percentage of the hot component increases from 0.02 to 0.03%. In the 8 to 12 µm region the thermally mixed Planck curve will decrease more rapidly toward the longer wavelengths than that of the cooler isothermal Planck curve where the two are normalized against one another at 8 µm (Figure 3-2B). For this reason, a distinct negative slope (most noticeable as the wavelength increases) will be imparted in the emissivity spectrum once it has been extracted from the mixed Planck curve.

Previously, the two-component assumption used by Rothery et al., 1988 was limited to two mid infrared spectral bands of the TM sensor, and an assumption of one of the unknown temperatures was required to deconvolve thermally mixed pixels. In contrast, the hyperspectral Hyperion instrument was used to deconvolve non-isothermal areas into as many as 5 to 7 temperature components (Wright and Flynn, 2003) using 9 to 13 spectral bands. However, Hyperion coverage is relatively sparse and has a swath width of only 7 km; which limits full coverage of extensive lava flows, pyroclastic flows, and lahars. Although, ASTER has considerably fewer thermal bands than Hyperion, the greater spectral range in multiple wavelength regions and wider spatial coverage of ASTER allows the maximum temperature and areal distributions of hot and cool thermal features (as small as 11% of a 90 m area based upon the 30 m resolution of the SWIR data used in this investigation) to be determined. In addition, determining an average background radiance of non-thermally elevated basalt in the TIR eliminates the ambient temperature variable required in the previous studies.

The objective of the approach presented here is to quantitatively determine the average, relative hot and cold temperature components within a thermally mixed TIR pixel, and assess the effect on the emitted radiance and extracted emissivity of basalt. In order to accomplish this, artificial temperature mixtures were first created using laboratory emissivity data. An emissivity spectrum for a previously collected basalt sample from Kliuchevskoi volcano, Russia (51 to 54% SiO_2) was created in the laboratory using a Nicolet Nexus 670 FTIR spectrometer, which is capable of collecting high-resolution (~2 wavenumber) data between 5 and 22 µm (Figure 3-3). Although the sample was not Hawaiian in origin, it is only used as a model for the response of a thermally mixed basaltic surface and bears no weight on the actual thermal deconvolution process on the Hawaiian ASTER datasets. The emissivity spectrum was convolved with artificial mixtures of Planck radiance curves corresponding to 33.3% at 25 ºC and 66.7% at 122 ºC, which resulted in an average brightness temperature of 363K. This brightness temperature was used because it both lies below the ASTER TIR saturation threshold of 97 ºC, and the temperature of the hot component is large enough to be detected by the SWIR subsystem (minimum detectable temperature in the SWIR is 86 ºC in band 9 in High gain mode). The chosen percentages were also combined to reflect a simple areal mixing of the nine SWIR pixels that would occupy the area of one TIR pixel (e.g., 3 cool pixels and 6 warm pixels).

The goal is to model the Planck curves such that they mimic what is expected in actual ASTER data of basaltic lava flows (Figure 3-4). Figure 3-4A shows three Planck curves; with the top and bottom curves (dashed) representing the isothermal Planck curves, whereas the middle (dashed) curves show the result where the isothermal curves are mixed using the quantities mentioned above. A laboratory measured basalt radiance curve has been overlain onto each Planck curve to show the spectral properties of a non-blackbody material under the same thermal conditions of each blackbody, and to resemble radiance spectra of the basalts acquired by ASTER, used for this study. Figure 3-4B shows only the mixed and cool radiance curves to highlight the difference between the two. The hot radiance curve (122.5 ºC) is not shown in this example because it is above the saturation level for the ASTER TIR subsystem. In these cases,

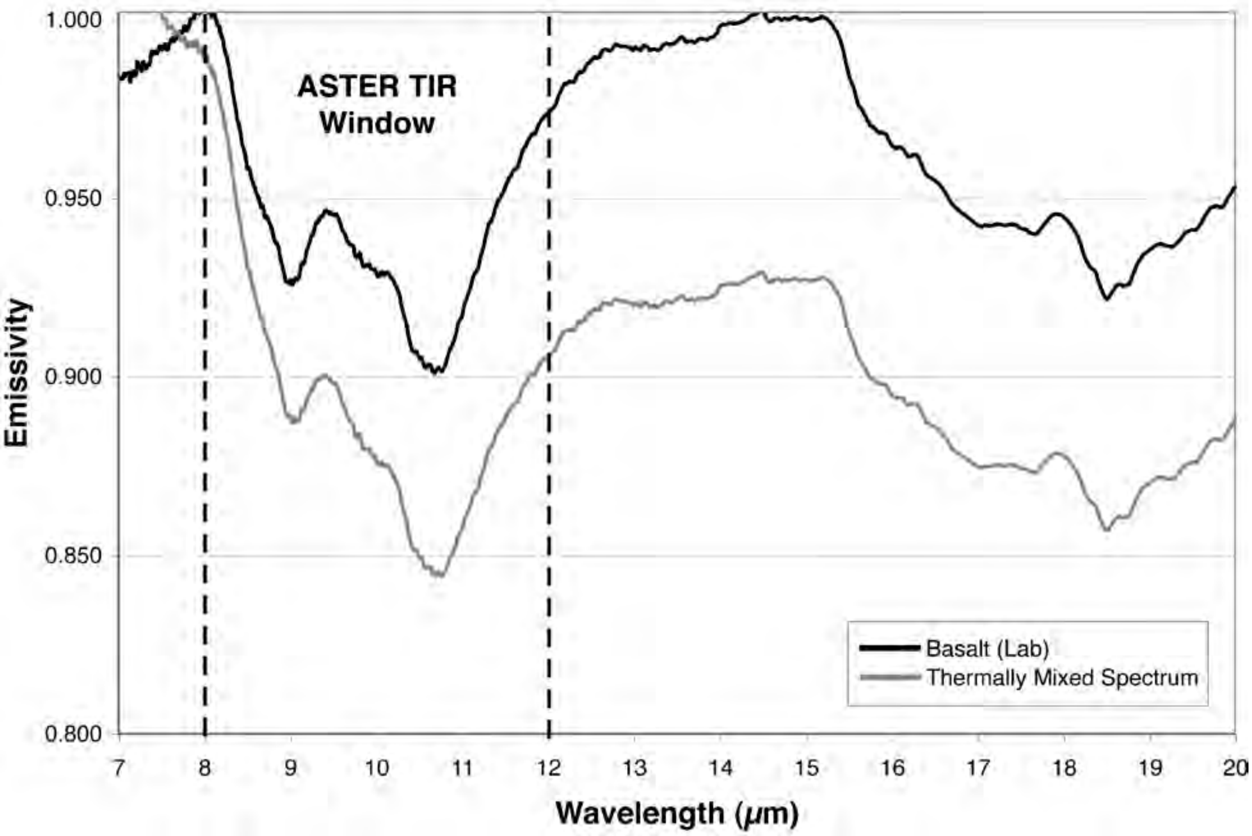

Figure 3-3 Laboratory TIR emissivity spectrum of a basalt sample (black line). The primary absorption feature occurs within the TIR wavelength region of the ASTER instrument. This emissivity spectrum was converted to radiance using the Planck equation and manipulated using various mixtures of hot and cool component percentages in order to model the associated effects (gray line). The minimum detectable slope in the ASTER data was determined to be -0.015, indicating possible thermal mixing effects.

the SWIR data would be used to extract Planck curves for the hot components (> 97 ºC) of a mixed pixel.

After the basalt radiance is degraded to the spectral resolution of the ASTER sensor, the behavior in actual ASTER data can be simulated (e.g., Figures 3-4C and 3-4E). If the mixed Planck curve is normalized to the cool component (Figure 3-4D and 3-4E), it becomes clear that the mixed Planck curves of both the blackbody and basalt spectra exhibit a greater slope with increasing wavelength compared to the isothermal curves. This phenomenon has been observed previously in ASTER emissivity data, especially in active volcanic settings (Ramsey and Dehn, 2004; Rose and Ramsey, 2009). Figure 3-4F shows how the thermal mixing impacts the extracted emissivity spectrum by imparting the negative slope. Given that the slope is more dramatic in the emissivity spectra, it is crucial to correct for thermal mixing to avoid misinterpretation of the surface composition, thermal flux, and micron-scale texture of targets, which all rely on accurate emissivity spectra.

Lastly, the laboratory derived basalt spectrum (Figure 3-3) was used to model the effect of thermal mixing of a surface analogous to that of Kilauea basalts. The isothermal laboratory emissivity spectrum yielded no negative slope between 8.3 and 11.3 µm. Similarly, the emissivity values of a 400 pixel area of non-thermally elevated TIR pixels from the AST_05 (12 Oct 2006; daytime) dataset also showed no negative slope. These pixels were also used to extract the average background temperature. The ASTER AST_05 emissivity product has an absolute accuracy of 0.1, or 10% [ASTER, 2001], and therefore under ideal circumstances, the minimum slope that could be used to detect a non-isothermal ASTER TIR pixel is -0.05. The process for identifying and deconvolving thermally heterogeneous pixels is described in detail below.

3.3.2 Thermal Deconvolution Algorithm

Because of the unique design of the ASTER instrument with non-uniform spatial resolution and temperature sensitivities across the wavelength regions, the TIR, SWIR, and VNIR subsystems can be used simultaneously to extract temperature distributions over each 90 m^2 TIR pixel surface. This process does not require any assumptions of the background temperature, hot target temperature, or the areal percentage occupied by each, as these components can be measured directly from the datasets. The premise of the algorithm includes a set of pre-determined thresholds to identify pixels that are thermally mixed based upon the pixel-integrated brightness temperatures and the associated magnitude of negative slope in the emissivity spectrum. In order to determine the minimum temperature threshold, the AST_09T dataset was utilized to calculate an average background temperature of non-active basaltic lava flows using a 400-pixel average in both the day and nighttime scenes. The same 400-pixel area was also used to determine the average slope in the emissivity spectra of these surfaces. Thermally anomalous pixels were defined as those with pixel-integrated brightness temperatures 10K above background. An upper threshold was set at 96 ºC in order to preclude saturated TIR pixels because the emissivity spectra from these pixels would contain no useful information. The values for the temperature thresholds, emissivity slope threshold, and average background temperature are entered prior to analysis and can be varied by the user.

The theory behind the thermal deconvolution procedure is illustrated in Figure 3-5. The emissivity and pixel-integrated brightness temperature images are initially scanned, and number of TIR pixels that meet the mixed criteria (10K above background and an emissivity slope greater than -0.015) are identified. Subsequently, the AST_09XT (crosstalk corrected SWIR

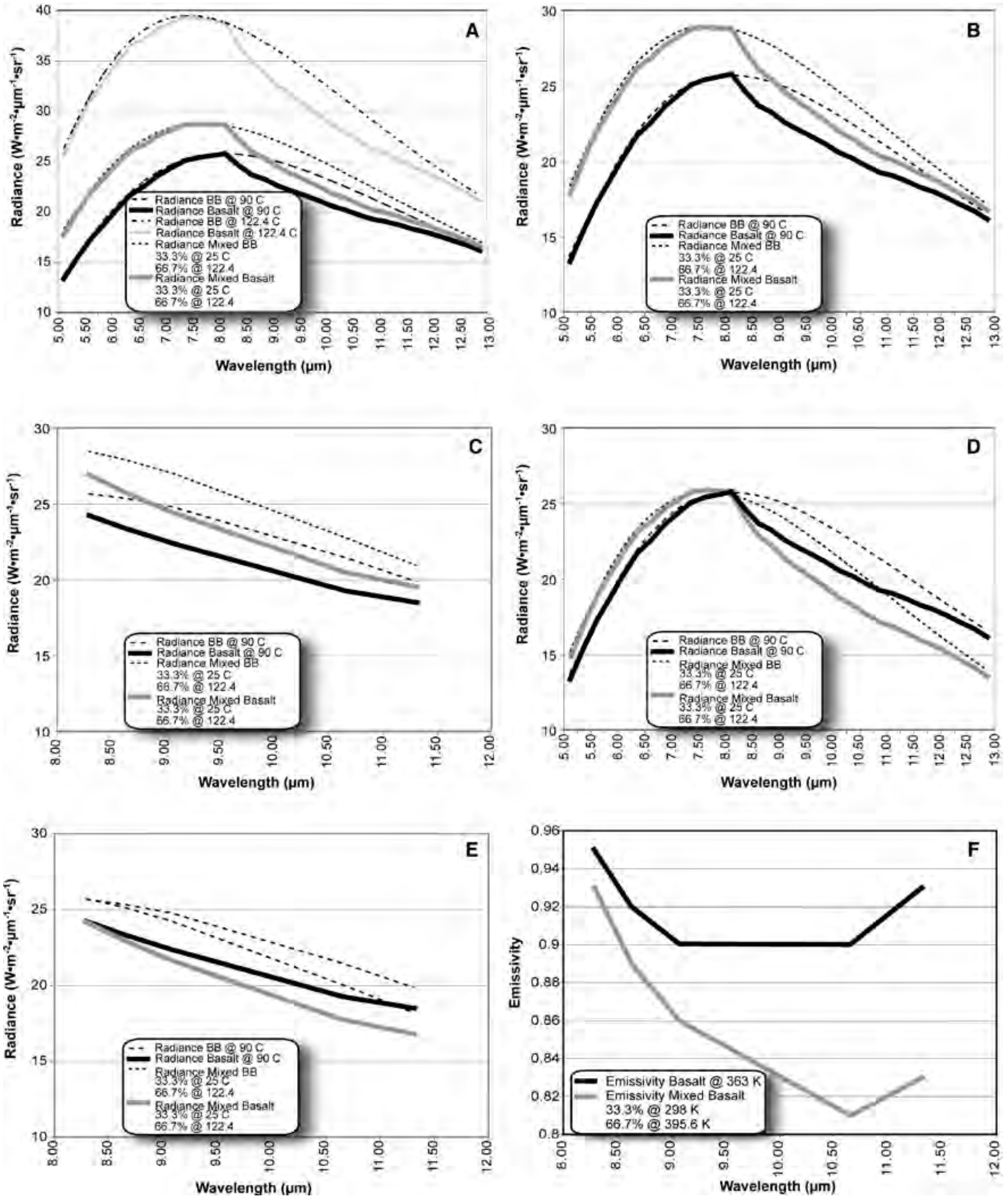

Figure 3-4 Thermal conditions expected in typical ASTER data of thermally-mixed surfaces. A) Two isothermal Planck curves and a thermally mixed curve with a laboratory-derived radiance spectra of a basalt overlain for each. B) An enlarged version of the bottom curves in (A) to show the difference in slope associated with thermally mixed Planck curves. C) The same Planck curves shown in (B) and degraded to the same spectral resolution of the ASTER TIR subsystem. The steeper slope in the non-isothermal curve is still preserved regardless of the spectral resolution. D) Where normalized to 8 µm, the radiance slopes show an increased difference toward longer wavelengths. E) Normalized curves degraded to ASTER TIR resolution. F) Where the wavelength independent temperature component is removed, the ASTER resolved emissivity spectra of the basalt clearly show large errors that may lead to misinterpretation of composition and texture of the surface.

radiance at ground) and AST_09 (SWIR radiance at ground), and the AST_09T (TIR radiance at ground) files are read into memory. Only one SWIR band, chosen by the user, is used to determine the radiance of the nine pixels corresponding to each thermally-mixed TIR pixel. In this study, all six of the SWIR bands were compared in order to determine which one produces the most robust results.

The nine SWIR radiance values for each 90 m area are analyzed according to six criteria: 1) if none of the pixels have a detectable radiance in the SWIR band chosen, the corresponding TIR pixel is removed from the list of thermally mixed pixels and the original emissivity values are retained; 2) if at least one SWIR pixel is detected, the radiance of the remaining pixels with radiance values ≤ the minimum detectable radiance is set to that of the background radiance determined earlier in the TIR data; 3) in the event that some of the pixels contain negative values as a result of the solar correction applied or nighttime crosstalk correction described earlier, these pixel values are also set to the background radiance and the areal percent is calculated accordingly; 4) the hot pixels (those with detectable radiance values for the band and gain setting specified) are averaged, thus determining the average hot radiance and hot area percentage, as well as the corresponding cool radiance, and cool area percentage; 5) if all nine SWIR pixels are detectable in the SWIR, do not reach saturation values, and are all equal to one another, then the 90 m area is considered isothermal and the original TIR emissivity values are retained; 6) in the instance where there are SWIR pixels with radiance values greater than the maximum detectable radiance for the band and gain setting chosen (i.e., saturation), the thermal deconvolution algorithm is no longer valid and the original TIR emissivity values are retained. In the next modification of the algorithm the same methodology will be applied to one band of the VNIR data of ASTER. This would allow further identification of the hot components corresponding to the saturated or thermally mixed SWIR pixels at the 15-meter scale.

For the instances where the criteria above are met then a thermally-mixed pixel is identified. The average hot and cool radiance values are used to solve the Planck equation (eqn. 2) for the associated hot and cool temperatures (assuming an emissivity of 1.00). Once these temperatures are known, the mixed Planck equation (eqn. 3) can be calculated to determine the predicted radiance values in the TIR region. The correction ratio for each band is calculated by dividing the originally measured TIR radiance by the newly determined mixed TIR radiance (based on the SWIR values). This ratio is then used to correct the emissivity for that particular thermally mixed TIR pixel. The new emissivity will have the correct shape, however it can be significantly lower, relative to the original emissivity, due to the iterative TES normalization process outlined in [Gillespie et al., 1998] and used to derive the AST_05 data product. Essentially, the TES algorithm estimates values for the maximum emissivity of a spectrum during the normalized emissivity method (NEM) module and also scales relative emissivities (β) to actual emissivity values during the minimum-maximum differencing (MMD) module. Again, this method preserves the spectral shape but scales each spectrum to fit realistic emissivity values. For this reason, the new emissivity spectrum produced by the thermal deconvolution algorithm must be renormalized to the original spectrum for direct comparison. In order to accomplish this, a ratio of each TIR band's original AST_05 emissivity and the corrected emissivity must be determined using the following equation:

$$R_\lambda = \varepsilon_{o\lambda} / \varepsilon_{n\lambda} \qquad (4)$$

where, R = emissivity ratio for each band, ε_o = original emissivity for each band, and ε_n = corrected emissivity for each band. The five calculated emissivity ratios are multiplied by the

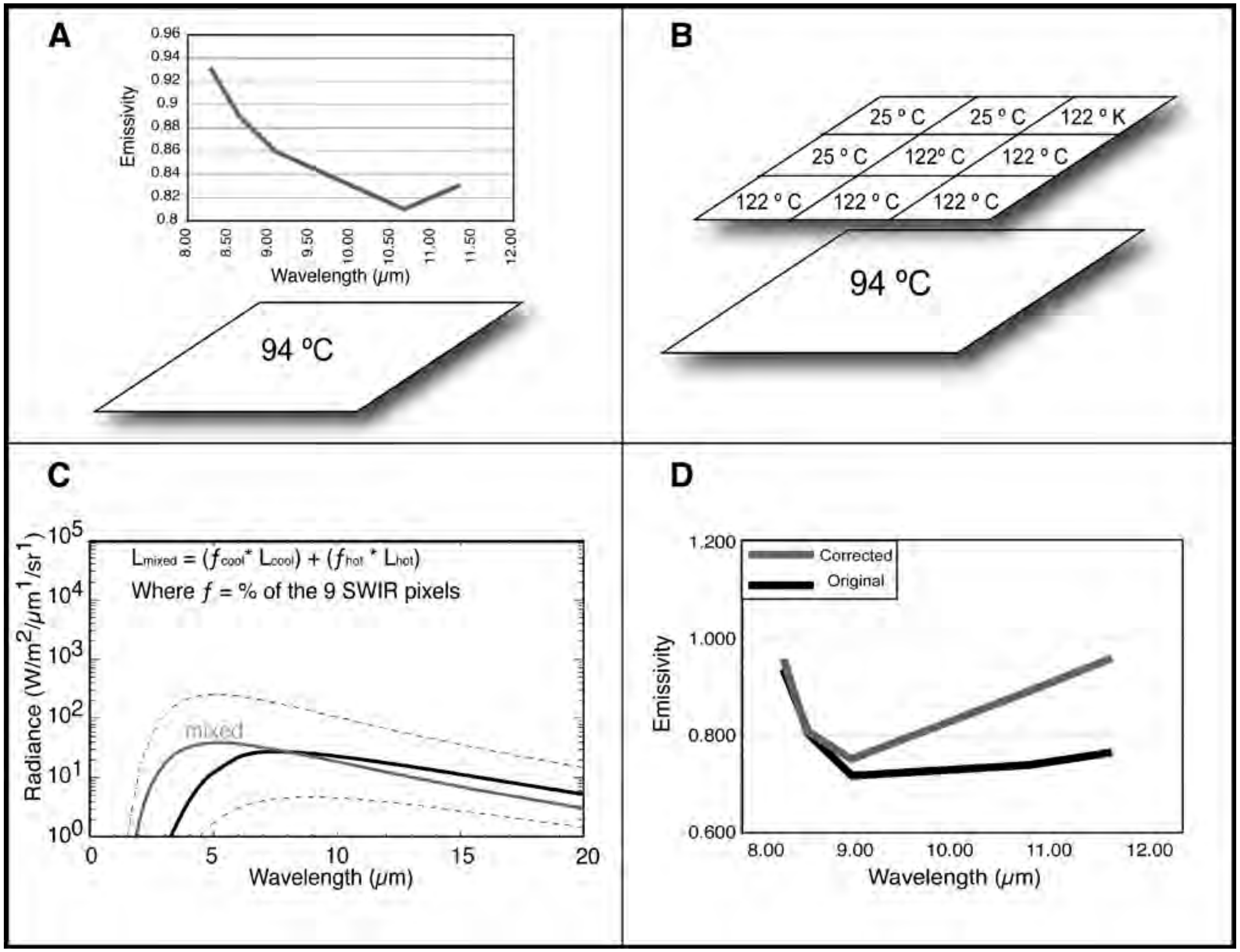

Figure 3-5 The thermal deconvolution concept. A) A non-saturated TIR pixel > 10K above background and with an emissivity slope < -0.015 is identified as potentially mixed. B) The 9 SWIR temperatures values within the mixed TIR pixel are derived and an average hot and cool temperature and areal percentage is determined. C) The percentage of hot and cool temperatures and the radiance values are used to derive a mixed Planck curve and calculate the mixed radiance values in each TIR band. The ratio between the original and newly calculated radiance values now equals the corrected emissivity. D) The corrected emissivity spectrum after the removal of the TES algorithm effects compared to the original spectrum.

corrected emissivity spectrum, which yields five potential emissivity spectra per pixel. The final corrected emissivity spectrum is chosen based upon the maximum emissivity value such that the maximum value cannot be greater than an arbitrary value of 1.005. In the case that all of the five spectra have maximum emissivity values > 1.005, then the spectra with the lowest maximum is chosen. Ultimately, this process both corrects the spectral shape and preserves the magnitude thereby resulting in the most accurate emissivity spectrum possible. The thermal deconvolution process results in the generation of three new image files, which include a TIR unmixed radiance file and a TIR unmixed emissivity file. Only the thermally mixed pixels will have new values, otherwise all original values remain unchanged. In order to easily determine which TIR pixels were thermally mixed, a binary masked image is also produced highlighting the location of the thermally deconvolved pixels.

3.4 RESULTS

3.4.1 Daytime/Nighttime Algorithm Results

The results of the algorithm vary depending on the acquisition (daytime vs. nighttime) and which SWIR band was chosen to correct the mixed TIR pixels. Each of these variables must therefore be analyzed. The thermal deconvolution results for both the daytime and nighttime ASTER datasets are reported in Table 3-2 and the main points are described below. The 12 October 2006 daytime dataset initially yielded 240 potentially mixed pixels based solely upon the magnitude of the emissivity slope (< -0.015) and the pixel integrated brightness temperature (larger than 10 degrees above the background temperature of 52.4 ºC) in the AST_05 and AST_09T datasets.

Once the crosstalk corrected SWIR surface radiance (AST_09XT) data was used, the number of thermally mixed pixels decreased from 240 to as few as 20 (using SWIR band 5) to as many as 57 (using SWIR bands 4 and 8). The resulting mask images created from the analyses of each SWIR band were overlain onto the associated corrected emissivity and pixel integrated brightness temperature datasets. This revealed that the corrected pixels were in expected locations - primarily adjacent to saturated TIR pixels and along the most active and hottest portions of the lava flows. This spatial distribution gave confidence that the chosen thresholds and applied methodology was working well. The slopes of emissivity spectra for each of these thermally mixed pixels were calculated and resulted in values ranging from -0.072 (using SWIR band 7) to as much as 0.085 (using SWIR band 6; Table 3-2). By comparison, the original slopes in the uncorrected data were -0.103 and -0.018, respectively thereby indicating that the algorithm successfully removed/minimized the negative emissivity slope and in some cases may have overcorrected it. The SWIR band that produced the highest number of ideal emissivity spectral slopes (-0.015 > x < 0.015) was SWIR Band 9, with 20 out of 50 corrected TIR pixels falling into this category. The minimum number of ideal spectra was produced using SWIR band 4, which only produced 5 out of 57 corrected TIR pixels.

Using the nighttime data, the thermal deconvolution algorithm identified 424 TIR pixels as potentially mixed in the 14 October 2006 AST_05 and AST_09T combined dataset (emissivity slopes < -0.015 and pixel integrated brightness temperatures greater than 10 degrees above the background temperature of 21.1 ºC). However, once the ad hoc crosstalk correction was applied, the number of thermally mixed TIR pixels was reduced to a minimum of 44 using SWIR band 4 to a maximum of 61 using SWIR band 8. The locations of the thermally mixed pixels were also adjacent to the saturated TIR pixels and along the hottest portions of the flow.

Table 3-2 Results of the thermal deconvolution algorithm daytime analysis (top) and nighttime analysis (bottom).

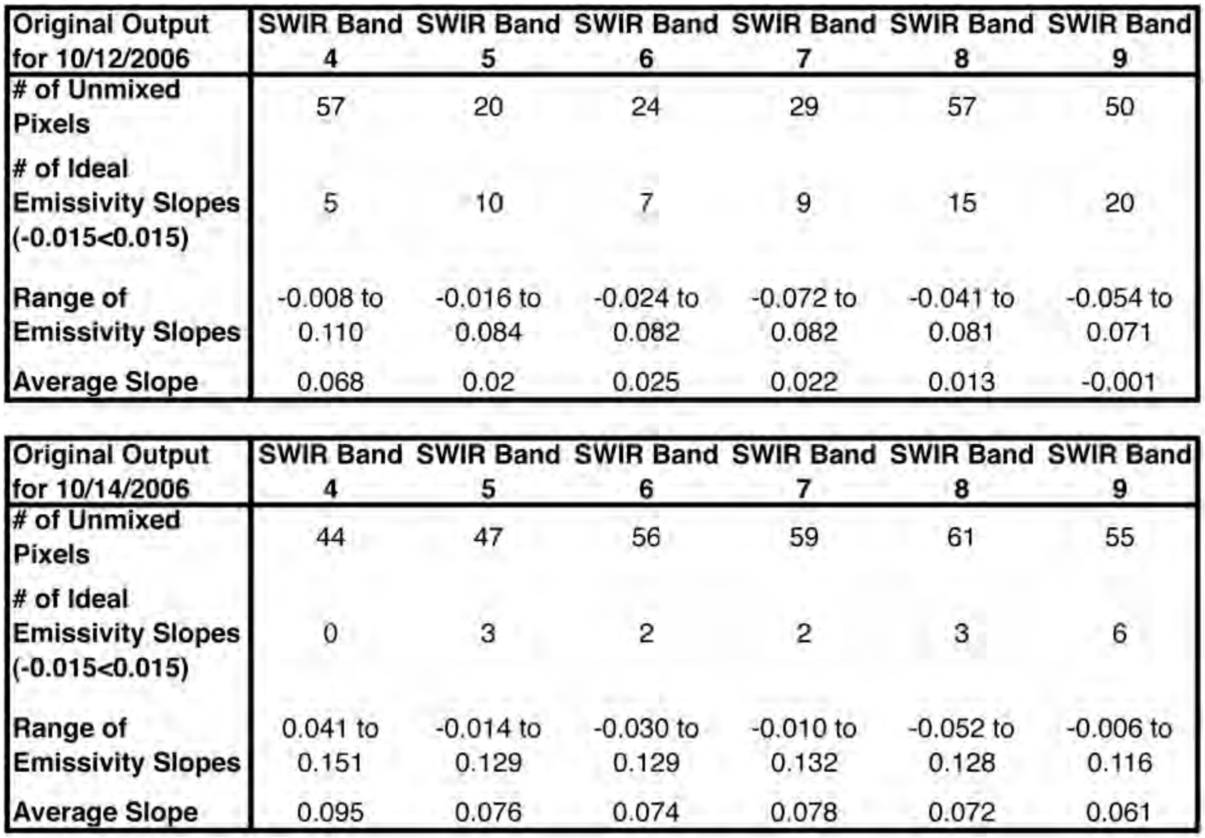

Original Output for 10/12/2006	SWIR Band 4	SWIR Band 5	SWIR Band 6	SWIR Band 7	SWIR Band 8	SWIR Band 9
# of Unmixed Pixels	57	20	24	29	57	50
# of Ideal Emissivity Slopes (-0.015<0.015)	5	10	7	9	15	20
Range of Emissivity Slopes	-0.008 to 0.110	-0.016 to 0.084	-0.024 to 0.082	-0.072 to 0.082	-0.041 to 0.081	-0.054 to 0.071
Average Slope	0.068	0.02	0.025	0.022	0.013	-0.001

Original Output for 10/14/2006	SWIR Band 4	SWIR Band 5	SWIR Band 6	SWIR Band 7	SWIR Band 8	SWIR Band 9
# of Unmixed Pixels	44	47	56	59	61	55
# of Ideal Emissivity Slopes (-0.015<0.015)	0	3	2	2	3	6
Range of Emissivity Slopes	0.041 to 0.151	-0.014 to 0.129	-0.030 to 0.129	-0.010 to 0.132	-0.052 to 0.128	-0.006 to 0.116
Average Slope	0.095	0.076	0.074	0.078	0.072	0.061

Table 3-2 lists the values of the corrected emissivity spectra slopes, which ranged from a minimum of -0.052 (SWIR band 8) to 0.151 (SWIR band 4) and had similar magnitudes as those in the daytime data. However, the uncorrected emissivity slopes for these particular pixels were -0.052 and -0.021, respectively, thereby indicating that the slope was preserved in the first example and minimized in the latter of the two. The SWIR band that produced the largest number of ideal corrected emissivity spectral slopes was band 9 (6 of 55 corrected TIR pixels; Table 3-2). The smallest number of corrections occurred where using band 4, which did not produce any ideal emissivity slopes for the corrected pixels.

3.4.2 Error Analysis for Daytime Dataset

In order to determine the effect of inherent errors within the ASTER data products on the thermal deconvolution process presented here, the original datasets used in the analysis were manipulated by adding and subtracting the absolute error listed in the ASTER Level-1 Users Guide (v. 5.1, 2007) and the ASTER Higher-Level Product User Guide (v. 2.0, 2001) for each product. However, the absolute error for the crosstalk corrected data has never been established (Iwasaki, personal communication). Therefore, the standard deviation of radiance values for the pixels along the boundaries of the hot flows (identified by the crosstalk "halos" or energy bleeding) were calculated from the AST_09XT daytime product in order to estimate the magnitude of the associated errors (Table 3-3). Once the associated errors of each data product were added to and subtracted from the original datasets used in the analysis above, the algorithm was run six times (once per SWIR band) for each error scenario to quantify the amount of change produced from each error per band. Therefore, only one product with the error applied was used at a time such that its associated errors could be distinguished from the other errors. The final corrected emissivity values were compared to the original output data in order to quantify the amount of change that had taken place using only the mixed pixels that were located at the same coordinates as the original results described previously. Ultimately, the purpose of the error analysis was to determine if a preferential SWIR band could be established for the thermal deconvolution process by determining which band was least affected by all other errors. The SWIR bands that produced the smallest errors in the corrected emissivity spectra were compared to the original output regardless of how noisy or erroneous the data products were initially. This same process was also used in the nighttime dataset error analysis. The values reported below represent maximum values and best-case scenarios (minimum values) of the error bars established using each band of the SWIR during analysis.

Table 3-3 The absolute errors calculate for each SWIR band used for the error analysis of the AST_09XT product. This product currently does not have an absolute error value and the standard deviation derived from the "halo" areas around the thermal anomalies was used. Additional analyses are required to better constrain these values.

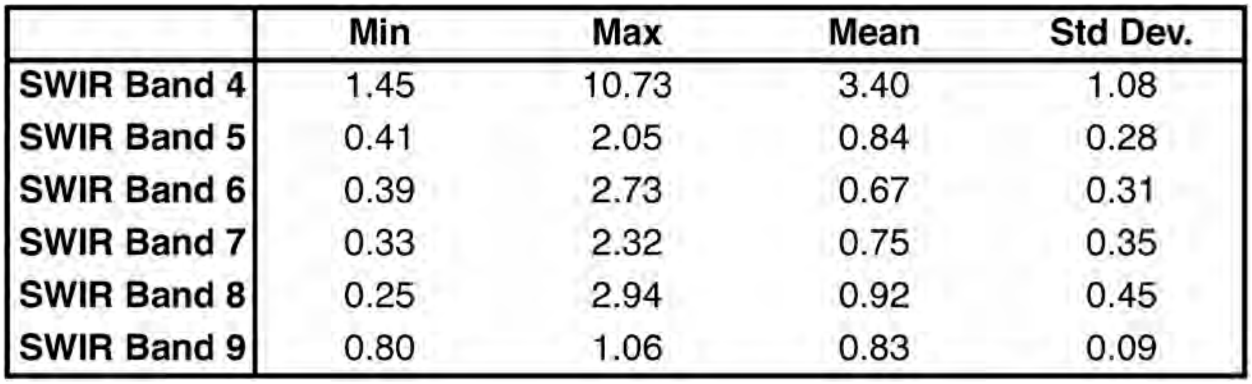

	Min	Max	Mean	Std Dev.
SWIR Band 4	1.45	10.73	3.40	1.08
SWIR Band 5	0.41	2.05	0.84	0.28
SWIR Band 6	0.39	2.73	0.67	0.31
SWIR Band 7	0.33	2.32	0.75	0.35
SWIR Band 8	0.25	2.94	0.92	0.45
SWIR Band 9	0.80	1.06	0.83	0.09

The first error analysis was run using the daytime AST_09T data product and identified 224 (+1% temperature error) and 252 (-1% temperature error) potentially non-isothermal pixels. The number of pixels (16 to 57) identified as truly thermally mixed was compared to those located in the same coordinates (80 to 100%) produced in the original algorithm output. The largest errors in the corrected emissivities were +0.028 (SWIR band 7) and -0.062 (SWIR band 9). Conversely, the smallest emissivity errors were 0.0 (did not change from the original results), as a result of using bands 4, 5, 6, and 7 for the upper error bar and bands 4, 5, and 6 for the lower error bar. The average errors for each TIR band (see Table 3-4) reveal that a +/- 1% temperature error associated with the AST_09T product resulted in a maximum algorithm error of ~2% (Figure 3-6). Overall, SWIR band 4 yielded the most desirable results with a upper emissivity error bar of 0.002 and lower emissivity error bar of 0.001.

An absolute error of +/- 0.05 applied to the AST_05 emissivity product resulted in the identification of 240 potentially non-isothermal TIR pixels. Introducing the SWIR AST_09XT product into the algorithm reduced this number, and provided between 20 and 57 pixels (same as the original locations) per each SWIR band analysis. As previously observed in the mask images, the locations of the thermally mixed pixels were adjacent to the saturated TIR pixels occurring at the hottest portions of the lava flows, which was also observed in the remaining error analyses. Where SWIR band 4 was used in the analysis, maximum emissivity error bars of +0.118 and -0.189 were calculated. The smallest errors determined were +0.028 (SWIR band 5) and -0.051 (SWIR band 4). Overall, the maximum average error per each TIR emissivity band was +0.100 and -0.131, suggesting that in a worst-case scenario, the absolute error associated with the AST_05 product could produce a maximum error of 13% in the thermal deconvolution process (Table 3-4 and Figure 3-6). Based upon the results produced by each SWIR band, band 5 yielded the smallest overall emissivity errors with a maximum emissivity error of +0.028 and -0.067.

The absolute errors for the AST_09XT crosstalk corrected product were applied to each band and the values used are listed in Table 3-3. This resulted in identifying 20 to 57 thermally mixed pixels (49 to 100% of the original pixels). The use of SWIR band 4 in the algorithm resulted in maximum emissivity errors of +0.297 and -0.237. The smallest error determined was +/- 0.001, produced using SWIR band 9. The maximum average error per each TIR emissivity band was +0.162 and -0.119 (TIR band 10), suggesting that in a worst-case scenario, the absolute error associated with the AST_05 product inherently produces a maximum error of 16.2% in the thermal deconvolution process (Table 3-4 and Figure 3-6). Overall, SWIR Band 9 yielded the most desirable results with an error of +/- 0.001.

Collectively, the error analysis of the daytime data reveals that the crosstalk errors (max = 16.2%) are the most influential in terms of accurately deconvolving thermally-mixed emissivity spectra. The errors associated with the AST_05 product (max = 13.1%) are not as prominent as the crosstalk, but still remain significant. And the errors associated with the AST_09T product produced a negligible impact on the final results (max = 2.3%; Figure 3-6). These are the maximum possible errors based on the reported accuracies in the ASTER L2 data. We do not expect these maximum errors to be encountered routinely nor are these errors interdependent on the other datasets thereby reducing any possibility that these errors are additive. Furthermore, the range of these errors (2 – 16%) is a similar magnitude to compositional deconvolution of isothermal emissivity spectra found by Ramsey and Christensen, 1998 and Ramsey et al., 1999.

3.4.3 Nighttime Results for Error Analysis

A similar error analysis procedure was applied to the nighttime datasets using the associated error specifications for the L2 datasets. It should be noted that due to the lack of a crosstalk correction for the nighttime data, the absolute error for the SWIR surface radiance could be as large as 4% (ASTER, 2001). The absolute error values for the AST_09T and AST_05 products remained the same as the daytime analysis.

The thermal deconvolution algorithm identified 501 (+1% temperature error) and 368 (-1% temperature error) potentially non-isothermal pixels in the AST_09T nighttime data product, which is nearly 100 more than the daytime data reflecting the lower background temperatures. Of these, 44 to 61 pixels (96 to 100% of the nighttime algorithm results) were located at the same coordinates for direct comparison to the nighttime algorithm results. The errors associated with the AST_09T product did not change the final emissivity values in the error regardless of the SWIR band used, therefore suggesting that the errors associated with the nighttime AST_09T product are negligible in the thermal deconvolution process. In comparison with the daytime analysis, the nighttime data yields a 2.3% smaller average TIR emissivity error (Table 3-4 and Figure 3-6). Based upon the results produced by using each SWIR band, bands 4 through 9 all produce little to no impact on the outcome of the thermally deconvolved data.

A +/- 5% absolute error value for the AST_05 nighttime dataset identified 430 (+5%) and 420 (-5%) potentially non-isothermal TIR pixels. Similar to the AST_09T nighttime error analysis, 44 to 61 pixels (the same locations as the original output) were used to determine errors. The largest differences in emissivity compared to the original nighttime data output were +0.213 (SWIR band 6) and -0.241 (SWIR band 7). The smallest of the errors was +0.094 (SWIR

Table 3-4 The minimum and maximum deconvolution errors from the data products used to correct the emissivity errors in each TIR band. The AST_05 and AST_L1B data affect the outcomes the most, whereas the AST_09T product imparts no to minimal error. Errors associated with the daytime data products (top). Errors associated with the nighttime data products (bottom).

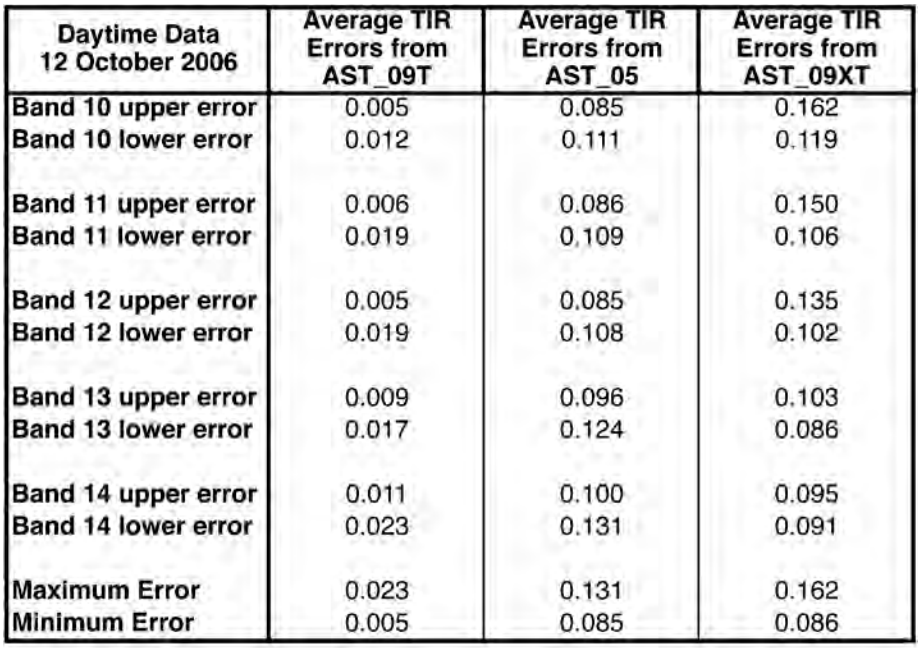

Daytime Data 12 October 2006	Average TIR Errors from AST_09T	Average TIR Errors from AST_05	Average TIR Errors from AST_09XT
Band 10 upper error	0.005	0.085	0.162
Band 10 lower error	0.012	0.111	0.119
Band 11 upper error	0.006	0.086	0.150
Band 11 lower error	0.019	0.109	0.106
Band 12 upper error	0.005	0.085	0.135
Band 12 lower error	0.019	0.108	0.102
Band 13 upper error	0.009	0.096	0.103
Band 13 lower error	0.017	0.124	0.086
Band 14 upper error	0.011	0.100	0.095
Band 14 lower error	0.023	0.131	0.091
Maximum Error	0.023	0.131	0.162
Minimum Error	0.005	0.085	0.086

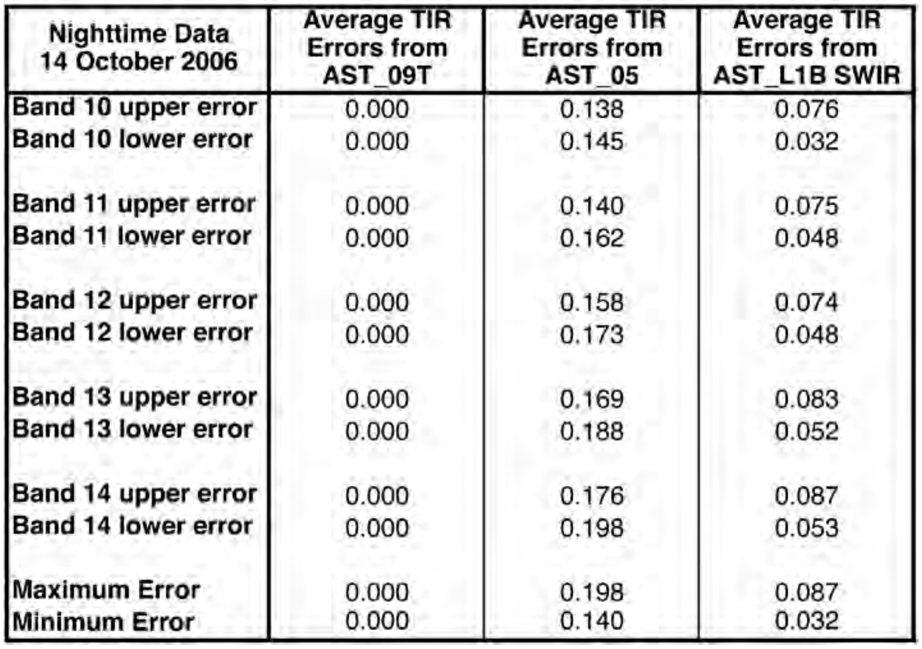

Nighttime Data 14 October 2006	Average TIR Errors from AST_09T	Average TIR Errors from AST_05	Average TIR Errors from AST_L1B SWIR
Band 10 upper error	0.000	0.138	0.076
Band 10 lower error	0.000	0.145	0.032
Band 11 upper error	0.000	0.140	0.075
Band 11 lower error	0.000	0.162	0.048
Band 12 upper error	0.000	0.158	0.074
Band 12 lower error	0.000	0.173	0.048
Band 13 upper error	0.000	0.169	0.083
Band 13 lower error	0.000	0.188	0.052
Band 14 upper error	0.000	0.176	0.087
Band 14 lower error	0.000	0.198	0.053
Maximum Error	0.000	0.198	0.087
Minimum Error	0.000	0.140	0.032

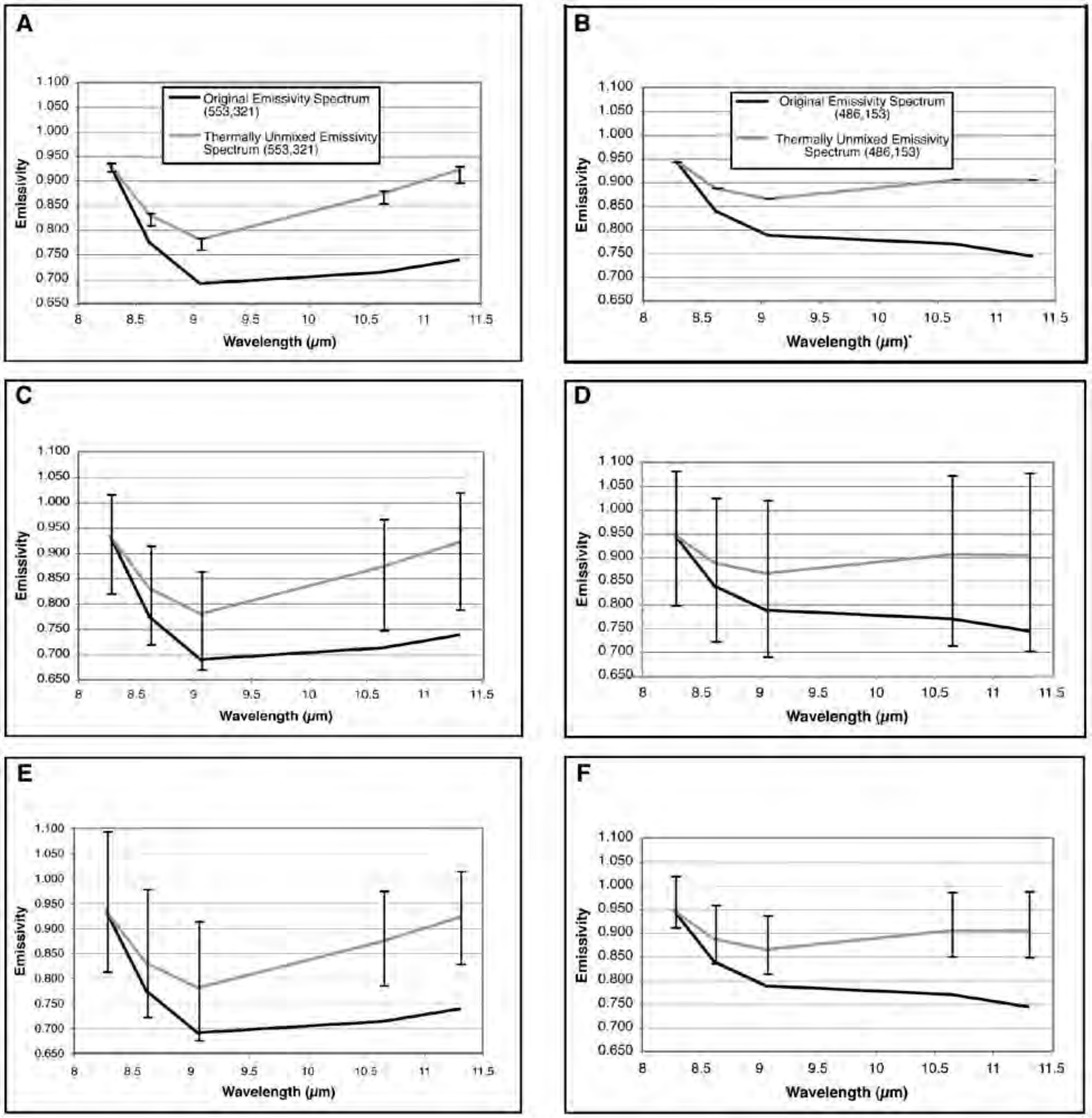

Figure 3-6 Examples of a corrected emissivity spectrum from the daytime (left) and nighttime data (right). The pixel coordinates for the daytime and nighttime datasets are listed. A) The correction of a daytime emissivity spectrum with the associated AST_09T error bars for each TIR band. B) As shown in (A), but for the nighttime data. C) The correction of a daytime emissivity spectrum with the associated AST_05 error bars for each TIR band . D) As shown in (C), but for the nighttime data. E) The correction of a daytime emissivity spectrum with the associated AST_09XT error bars for each TIR band. F) Established errors resulting from the AST_L1B nighttime SWIR surface radiance product.

band 7) and -0.118 (SWIR band 9). The maximum average errors of the corrected TIR emissivity values were +0.176 and -0.198 for the upper and lower error bars, respectively (Table 3-4 and Figure 3-6). In comparison with the daytime error analysis of the AST_05 product, the nighttime dataset resulted in a 6.7% higher, maximum error. SWIR band 9 yielded the most desirable results with a maximum emissivity error of +0.176 and -0.118.

Lastly, the AST_L1B SWIR surface radiance product was analyzed to determine the errors associated with atmospheric attenuation and the crosstalk phenomenon. Out of the 424 potentially non-isothermal TIR pixels identified, 44 to 61 (the same locations as the original output) were used in the error analysis. The largest emissivity error was +0.215 (SWIR band 9) and -0.202 (SWIR band 5). Most notably, the smallest emissivity errors of ±0.001 were produced using SWIR bands 4, 6, and 7. Collectively, the errors associated with each SWIR band resulted in maximum average TIR emissivity errors of +0.087 and -0.053 (Table 3-4 and Figure 3-6). These errors are 4.4% lower than those calculated in the daytime error analysis. Based upon the results produced by each SWIR band, band 4 yielded the smallest overall emissivity errors with maximum emissivity errors of +0.002 and -0.001.

The AST_09T product yielded the smallest inherent errors in the nighttime data which were even smaller than those observed in the daytime scene (Table 3-4 and Figure 3-6). However, the absolute errors related to the AST_05 product reveal the most significant influence on the final corrected emissivity values with a maximum average error value of 19.8% whereas the AST_09XT product imparted the most significant errors on the daytime error analysis. The nighttime data error analysis also shows that the maximum average emissivity error on the TIR bands was 8.7% using the AST_L1B, which is almost 50% of the inherent crosstalk errors observed in the daytime data.

3.4.4 Impact on Spectral Analysis

In order to quantify the effects of thermal mixing on derived compositional retrievals of the surface, the spectral deconvolution approach of Ramsey and Christensen, 1998 was applied to the emissivity spectrum shown in Figure 3-6A for both the original and thermally deconvolved data (Table 3-5). The absolute error in derived end-member percentages using the spectral deconvolution approach is no better than 5% for laboratory data and 10% for multispectral image-based data, and therefore detected end-members below this level are not considered significant (Ramsey and Christensen, 1998; Ramsey and Fink, 1999). In both the thermally-mixed and corrected datasets, the spectral end-members identified by the deconvolution approach (olivine, pyroxene, basaltic glass and vesicles) are consistent with a fresh Kilauea basalt. The actual values of these end-members are not consistent with the percentages derived from petrologic analysis, but this is expected considering the low spectral resolution of the ASTER data and the small size of the mineral phenocrysts in the fresh basalt. Data at higher spectral resolution (e.g., laboratory spectra) than the five ASTER TIR channels would yield more accurate end-member mineral percentages. The high percentage of glass and relatively low vesicularity detected is consistent with the upper surface of pahoehoe lava flow crusts (Byrnes et al., 2004). The upper millimeters of pahoehoe crusts are dominated by glass with minimal vesicles present at the surface. Over time, flows tend to lose this glassy surface due to flow inflation, spalling, and weathering. However, the formation time of the flows in this study was recent enough that these factors would have not had sufficient time to expose the underlying vesicular core of the flow (Ramsey and Fink, 1997; Byrnes et al., 2004).

The compositional analysis on both the original and post thermal deconvolution datasets produced good and nearly similar model fits. The root mean squared (RMS) error improved from 0.879 to 0.813 after the thermal deconvolution was applied. However, the end-member percentages changed significantly with the most notable change found in the glass and vesicularity end-member. The glass and vesicle end-members changed from 70.2% to 49.3% and from 0.7% to 16.3%, respectively. These new values are much closer to those derived by Ramsey and Fink, 1997 and Byrnes et al., 2004 and are similar to the values derived from the basalt flows that were not influenced by thermal mixing. The application of the thermal mixing correction can be judged qualitatively successful based upon the visible change in the spectra as well as quantitatively successful based upon the derivation of accurate detection and estimation of surface composition and micron-scale textures.

Table 3-5 Compositional derivation before and after the thermal deconvolution algorithm. The RMS error decreased slightly after the thermal deconvolution correction and a much better estimation of glass and vesicle percentages was found.

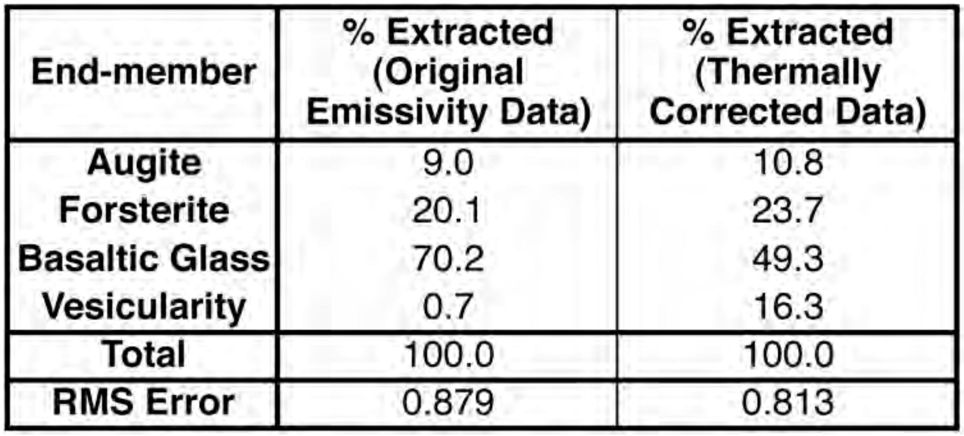

End-member	% Extracted (Original Emissivity Data)	% Extracted (Thermally Corrected Data)
Augite	9.0	10.8
Forsterite	20.1	23.7
Basaltic Glass	70.2	49.3
Vesicularity	0.7	16.3
Total	100.0	100.0
RMS Error	0.879	0.813

3.5 DISCUSSION

The thermal deconvolution model presented here provides a methodology for identifying and correcting pixels influenced by the mixing of multiple temperature components at the surface. It correctly identifies these pixels in areas expected to be the most influenced by temperature mixing and provides a methodology for the extraction of accurate pixel integrated brightness temperature and emissivity. However, the results are clearly influenced by the inherent errors present in each input dataset. Because these datasets are independent, the errors are not expected to be additive in the final model results, however each was explored in order to ascertain their individual impacts.

The daytime AST_09XT SWIR product produced the highest errors (7.5% more for the daytime dataset) in the thermal deconvolution process. By contrast, the nighttime SWIR crosstalk error is not visibly obvious, nor is it consistently located in the same area for each band, making the ad hoc correction somewhat problematic. Due to a lack of a reported crosstalk absolute error, the values reported in this investigation for the daytime data were determined by taking a 2 pixel wide area surrounding the thermally anomalous features in each band of the AST_09XT dataset and calculating the standard deviation of those pixels. The standard deviation of the radiance values for each SWIR band (both with and without the ad hoc crosstalk correction) was used as the upper and lower error limits prior to the application of the algorithm. This would be considered a maximum error estimation and the actual errors are likely less than these values. The resulting errors in the uncorrected nighttime data were almost twice as high as those for the data corrected for crosstalk. Therefore, the results suggest that the SWIR data contributes a significant amount of error in the outcome of the thermal deconvolution process, thereby supporting the notions that absolute error values need to be established for the

AST_09XT product, and a crosstalk correction for nighttime data would be crucial to obtain the most accurate results.

The L2 TIR radiance product (AST_09T) produced the smallest errors on the final outcome (+/- 2.3%) suggesting that the lack of an atmospheric correction or errors in the derived pixel integrated brightness temperatures had a negligible impact. Therefore, no additional corrections to the AST_09T product are necessary for the thermal deconvolution of either day or nighttime ASTER data. Similarly, the inherent errors present in the AST_05 data do not affect the model output by more than 2%. The inherent errors associated with the solar reflected radiance present in the SWIR daytime data is more significant than those associated with the pixel integrated brightness temperatures or the emissivity derived from the AST_09T and AST_05 products, respectively. Ultimately, the solar reflected radiance component present in the daytime data was not fully eliminated by the correction discussed in this investigation, which led to a maximum 2.3% error on the emissivity spectra compared to the 0.0% error for the nighttime error analysis.

Upon application of the model, a small percentage of the thermally-mixed emissivity spectra were overcorrected, having their spectral slope changed from negative to positive (average slope of 0.180 daytime; 0.154 nighttime). Ideally, there should be no slope in the data after the model has been applied. The overcorrection is likely due to unaccounted for, excess radiant energy within the 30 m SWIR pixels that decreases the emissivity of the shorter wavelength TIR bands and increases the emissivity of the longer wavelength bands during the radiance ratio calculations (Figure 3-5C). In essence, this can occur under two circumstances: 1) the percentage of the hot component may have been higher than the true aerial distribution due to contributions of solar reflected radiance or residual crosstalk components that were not fully corrected, and thereby caused an “apparent” size increase of the thermal feature; and/or 2) the aerial distribution of the hot component may have been accurate but the average calculated new radiance was too high as a result of highly radiant energy bleeding into adjacent pixels, crosstalk components, and/or solar reflected radiance causing an “apparent” intensity increase. It should be noted that “energy bleeding” may occur when energy emitted from a thermal feature may be scattered and/or reflected due to surface variability in texture, topography, etc, whereas crosstalk is sensor induced. Presently, there are no studies that have reported the extent to which the energy bleeding occurs.

Other improvements could be made in order to further increase the accuracy of the thermal deconvolution approach, but these would involve more detailed analyses and code refinements in the ASTER L2 datasets. Such an undertaking is well beyond the scope of this work, but is suggested for the ASTER Science Team and/or future TIR/SWIR instrument teams. The larger error value recorded for the nighttime data appears to be affected primarily due to the rough approximation and correction of the crosstalk contribution. However, the contribution of atmospheric attenuation to the overall error appears not to be significant. The errors associated with the AST_05 datasets may be minimized by developing a crosstalk correction algorithm that can be uniformly applied to the nighttime data. Furthermore, by correcting the nighttime data for atmospheric attenuation, the additional radiance could be removed and provide more accurate SWIR radiance values. In order for this model to produce the most accurate results, the validity of the daytime crosstalk correction algorithm should be independently established for the AST_09XT product. Finally, additional modeling and/or a level 2 product corrected for crosstalk and for the solar reflected components of various volcanic surfaces would be ideal in order to minimize their influence in the deconvolution algorithm. This corrected product may also be useful in additional studies where significantly hot / radiant bodies are priorities such as wildfires, geothermal features, and lava flows.

In order to determine the most accurate radiance values and areal percentages for the highest temperature features that produce saturation in the SWIR data, the VNIR data could be integrated into the analysis in a similar approach as the SWIR data. The VNIR is capable of detecting significantly higher temperatures (> 700 ºC) at 15 m spatial resolution. This integration would provide better estimates of thermal distributions on the surface (e.g. 36 independent temperature measurements per 90 m TIR pixel as opposed to 9 measurements using only the SWIR) and alleviate the over-correction of the emissivity slopes observed here (i.e. minimizing the occurrence of positive values for corrected emissivity slopes). This may also assist in further defining a preferential SWIR band for use in the thermal deconvolution process, by limiting the number of corrected emissivity slopes above the ideal limit (+0.015). Integration of the ASTER VNIR data will be the next phase of this work.

3.6 CONCLUSIONS

For this study, a thermal deconvolution algorithm was developed and extensively tested on laboratory TIR data as well as ASTER SWIR and TIR datasets in order to implement a means for accurately correcting the negative emissivity slope commonly observed in spectra of non-isothermal surfaces. Previous thermal deconvolution techniques have concentrated primarily on determining the aerial distributions and intensities of thermal features smaller than the spatial resolution of various remote sensing instruments by using linear fractional modeling. The algorithm presented in this study provides another approach that calculates these variables using direct measurements across the wavelength regions and then corrects spectral signatures in the TIR for better composition and texture estimates. Throughout this process, the original emissivity spectral shapes are preserved and the negative slopes corrected to an acceptable range ($0.70 < \varepsilon < 1.0$; Prabhakara and Dalu, 1976; Gillespie et al., 1998), indicating that the thermal deconvolution algorithm is a successful and valid approach. Overall, the results produced by this algorithm do not show preference toward daytime or nighttime analysis and indicate that the effect of atmosphere for the nighttime datasets appears to be minimal. The thermal deconvolution algorithm, therefore, can provide useful and accurate information under a variety of conditions. This is especially critical when equatorial (humid) or the high-latitude (dry) volcanic regions require frequent monitoring and assessment.

The results have shown that there are errors inherent in using this approach and that improvements could be made. The ASTER data products associated with the SWIR subsystem appear to be the most significant factor in producing the largest errors for the following reasons: 1) there is no nighttime crosstalk corrected data available; 2) solar reflected radiance for the daytime data is corrected using an ad hoc approach similar to the crosstalk correction applied to the nighttime AST_09SWIR data; and 3) the absolute errors established in this study for the AST_09XT daytime data product appear to be overestimated. The impact of these factors could be reduced if more accurate data products were available. However, there are preferred ASTER SWIR bands (bands 4 and 9) that produce the smallest errors in the thermal deconvolution results. The application of SWIR Band 9 in the algorithm produces minimal errors where used in the daytime analysis, but produced the largest errors for the nighttime AST_L1B error analysis. However, the use of Band 4 is suggested because it is least influenced by the crosstalk component and has the highest temperature sensitivity, thereby limiting the number of saturated

SWIR pixels. This is supported by the very low error bars produced in the nighttime error analysis presented here.

Considerations for improving the results of the thermal deconvolution algorithm would include using the VNIR data, with its higher 15 m spatial resolution to more accurately determine temperature distributions on the surface as well as pixel integrated brightness temperatures for the hot components within a 90 m area. By including the VNIR data, it will also be possible to thermally deconvolve a TIR pixel where a very small area of one SWIR pixel causes one of the nine SWIR pixels to saturate; a common condition in active volcanic settings that produce incandescent lava flows. Because precise pixel registration between instrument subsystems is required by the algorithm, the geo-registration accuracy is also critical for the validity of this approach. Typically, the registration provided by the standard ASTER L2 processing is within 1 to 2 TIR pixels. However, ground control points should be used if possible in order to provide the most accurate alignment within the same 90 m area. However, even with these limitations, the work presented here validates the thermal deconvolution approach as an independent means to correct the emissivity spectra of non-isothermal ASTER pixels.

Accuracy of the model should be ultimately judged on how well the new emissivity spectra could be used for volcanological studies (e.g. deriving surface composition, texture, cooling rates, and eruption rates). Previous studies quantified errors for the compositional deconvolution technique for both laboratory and multispectral TIR data, respectively (Ramsey and Christensen, 1998; Feely and Christensen, 1999; Ramsey et al., 1999). These studies report an average error of 5% for high-spectral resolution laboratory data of mineral detection and up to 10% for rocks as well as multispectral TIR data. Those studies did not perform the level of error analysis presented here with no attempt made to quantify errors associated with the instruments and/or the data correction as we have done here. Therefore, the errors reported in previous studies are likely underestimated by some amount. The average errors associated with the ASTER L2 data used for the thermal deconvolution process are slightly (but not significantly) higher than the previous compositional studies. And with the establishment of a more accurate correction for the crosstalk data, the thermal deconvolution algorithm would in fact have errors of similar magnitude to those associated with the linear spectral algorithm.

The necessity of applying linear and non-linear deconvolution techniques to remote sensing studies has been evident through the continued development of new TIR sensors. Although the SWIR subsystem of the ASTER instrument is no longer collecting data, the thermal deconvolution algorithm is applicable to the nine year ASTER archive containing thousands of scenes with hot targets. It is also easily applied to future missions with SWIR and TIR sensors. The approach presented here provides an accurate mechanism for quickly understanding the surface temperature, composition, and texture in an expeditious manner as well as from a safe distance. Such data are critical for scientific analyses and monitoring of volcanic eruptions or potentially, wild fires hazards.

4.0 COMPOSITIONAL VARIATIONS AND RELATIVE DATES OF THE RECENT BASALTIC LAVA FLOWS AT CERRO NEGRO VOLCANO, NICARAGUA USING SPACEBORNE TIR DATA

4.1 INTRODUCTION

The process of relative dating of basaltic lava flows using TIR remote sensing/spectroscopy data has been examined over the past two decades (e.g. Kahle et al., 1988; Crisp et al., 1990; Abrams et al., 1996). These studies have shown that over time, the exposure of the glassy surfaces to the chemical and mechanical weathering produces a relatively consistent change in the spectral signatures of the basalts. In the 8 to 12 µm region of the TIR, silicate minerals and volcanic glasses exhibit fundamental absorption features that are produced by the molecular vibrations of Al-Si-O bonds unique to each mineral. Following emplacement of the lava flows, physical and chemical weathering of the minerals leads to the oxidation of iron, polymerization of glass, and the development of silica-rich coatings from windblown tephra and soil (Farr and Adams, 1984; Curtiss et al., 1985). As a result, the associated spectral features have been observed to change in a specific pattern that can be related to these processes (Kahle et al., 1988; Crisp et al., 1990). These changes in spectral morphology have been used to relatively date century old to recent basaltic lava flows at Mauna Loa and Pu'u O'o, Hawaii (Kahle et al., 1988; Crisp et al., 1990) and Etna, Sicily (Abrams et al., 1996). However, the rate of spectral change has not been addressed. Additionally, these studies have employed high-spatial resolution multispectral airborne data, which can be costly if acquisitions are required frequently or for very remote volcanoes.

This investigation attempts to use both laboratory TIR emission spectroscopy and spaceborne multispectral TIR imagery from the Advanced Spaceborne Thermal Emission and Reflection Radiometer (ASTER) to relatively date a series of recent (< 76 years old) lava flows from multiple effusive eruptions of Cerro Negro volcano in northwestern Nicaragua. Although the spatial resolution of the ASTER TIR subsystem (90 m) is much lower compared to TIMS (5 to 15 m; Kahle et al., 1988), it can image a target once every 16 days, resulting in an extensive data archive since its launch in December 1999. For this study, a priori knowledge of the absolute ages of the lava flows allows a rate of weathering to be established. The findings could also lead to relative dating methodology of unknown lava flows for volcanoes of similar composition and located in similar climate regions around the world. Age dating of lava flows, whether absolute or relative, is critical to determine the frequency of volcanic eruptions, how volcanoes behave over time, and aid in predicting future eruptions, especially where access is limited. Although Cerro Negro has remained relatively quiet since it's last eruption in 1999, passive degassing through fumarolic activity provides an exceptional thermally-mixed environment, at relatively low temperatures (<400 ºC), for further testing the efficacy of the thermal deconvolution algorithm (Rose et al., in preparation-c) in basaltic volcanic environments in order to extract more accurate compositional information over the lifetime of the volcano.

4.2 CERRO NEGRO

The Nicaraguan Depression in Northwestern Nicaragua is an extensive graben trending north-northwest and parallel to the Middle American Trench. It lies between the subducting Cocos plate and the terrane of continental crust known as the Chortis Block on the overriding Caribbean plate. Within the center of the graben is a chain of volcanoes known as the Maribios Range that includes the volcanic complexes of Rota, El Hoyo, and Momotombo. The El Hoyo-Las Pilas volcanic complex consists of several eruptive centers such as cinder cones, explosion craters, maars, and young composite cones. Most notably, Cerro Negro volcano is located on the northwest flank of this complex, 21 km northeast of the city of León (Figure 4-1).

Cerro Negro is approximately 726 m high, with a basal elevation of 475 m above sea level. The 250 m tall volcanic edifice is composed of basalts erupted from strombolian to subplinian style explosions, commonly accompanied by effusive activity. Both the ash and lava flows are phenocryst-rich composed of plagioclase (An_{96-85}), clinopyroxene (En_{45} Wo_{38} Fs_{16}-En_{41} Wo_{45} Fs_{14}), and to a lesser extent, titanium magnetite (Usp_{16-20}) (Walker and Carr, 1986). Sedimentary xenoliths are also common. Generally, any variability observed in the lavas produced by Cerro Negro have been attributed to gravity-driven settling of olivine and clinopyroxene phenocryst during their ascent to the surface from a closed, homogeneous magma chamber (Walker and Carr, 1986). Although its morphology resembles that of a monogenetic cinder cone, Cerro Negro has been reclassified as a young composite cone, as it maintains an eruptive rate similar to those of nearby stratovolcanoes ($1.6 - 3.1$ km^3/k.y), which is far less than the average for cinder cones (McKnight and Williams, 1997; Femina et al., 2004).

Since its initial appearance in 1850, Cerro Negro has erupted more than 20 times with the

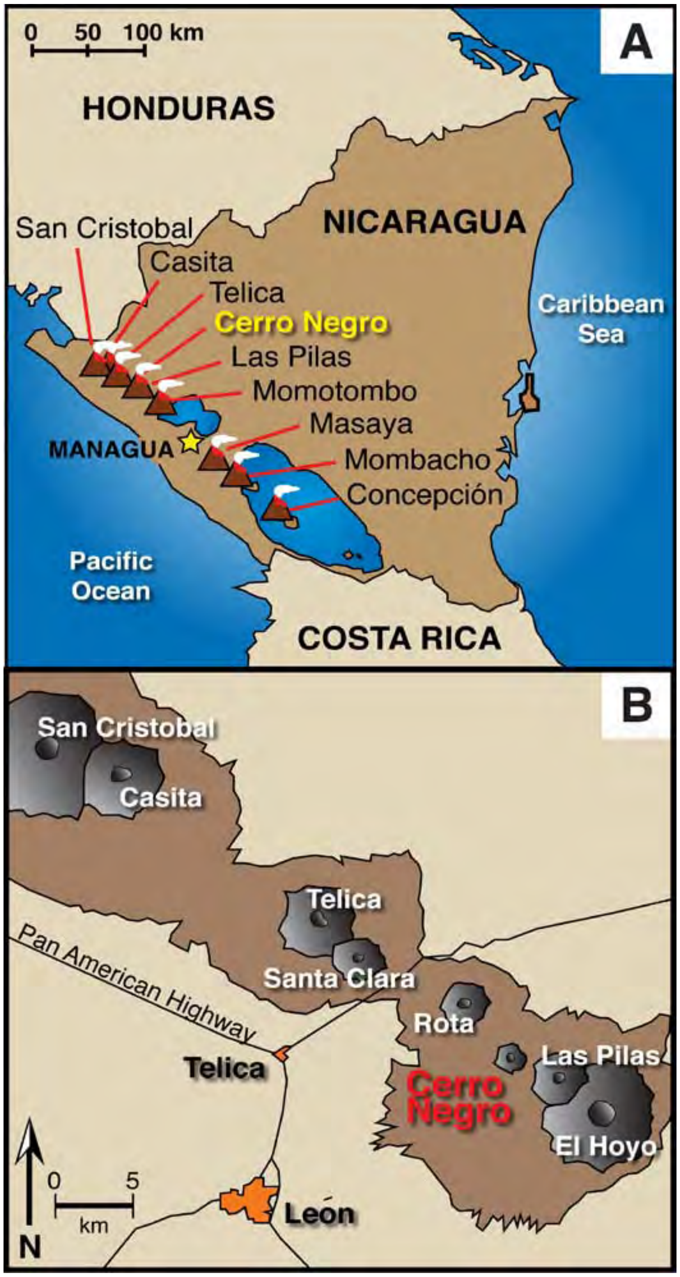

Figure 4-1 A) Simplified map of the Central American Volcanic Belt (CAVB) in Nicaragua. The CAVB is a 1,100 km long chain of 41 active volcanoes spanning from Guatemala in the north to Panama in the south. Nine volcanoes are represented here including Cerro Negro Volcano, located in the Marabios Range of northwestern Nicaragua near the El Hoyo-Las Pilas volcanic complex. B) A detailed map of the Marabios Range, associated volcanoes, and nearby towns. Cerro Negro Volcano is located approximately 21 km from the city of León.

Table 4-1 Summary of eruptive activity at Cerro Negro from its inception in 1850 (modified from INETER, 2005).

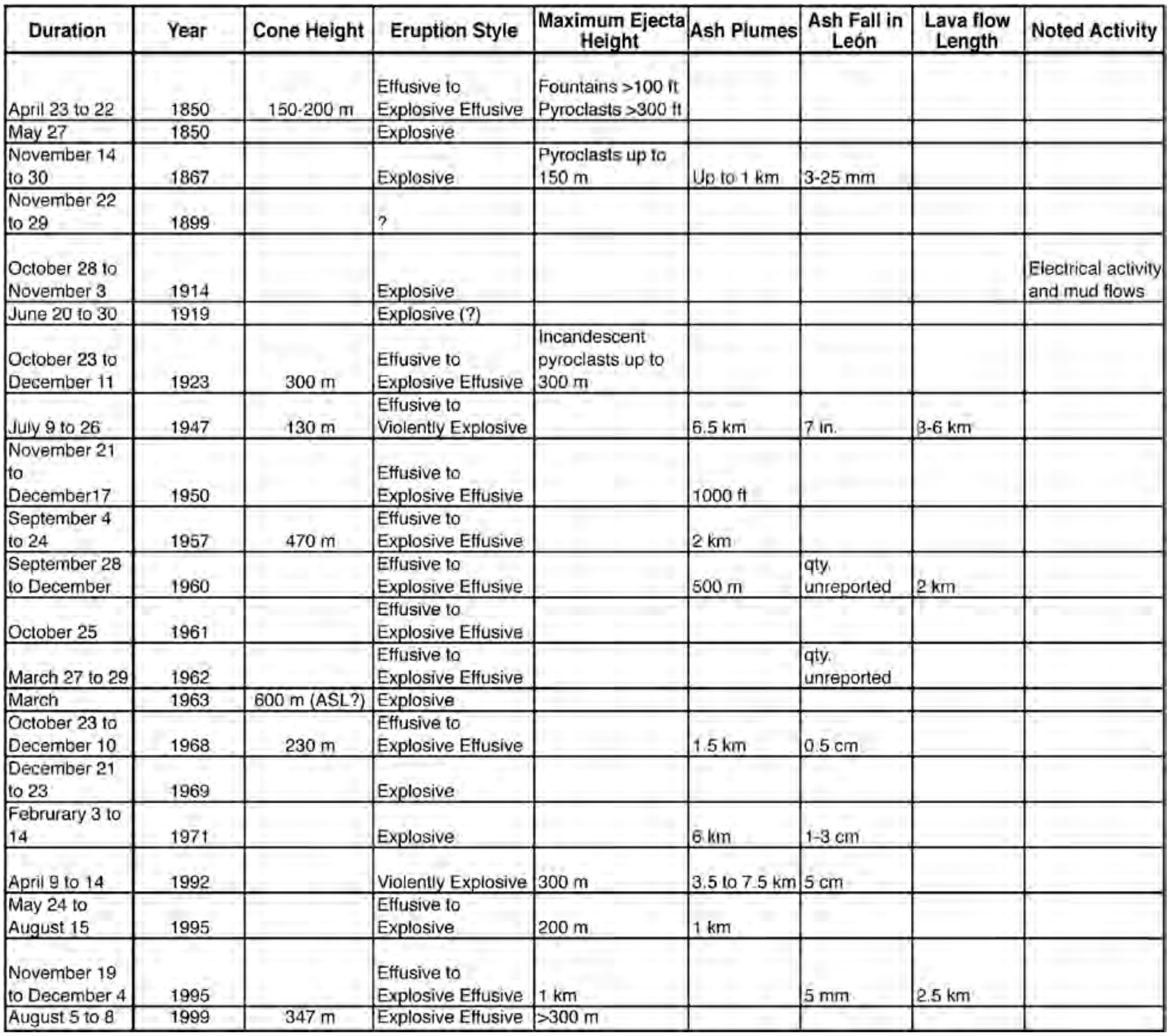

Duration	Year	Cone Height	Eruption Style	Maximum Ejecta Height	Ash Plumes	Ash Fall in León	Lava flow Length	Noted Activity
April 23 to 22	1850	150-200 m	Effusive to Explosive Effusive	Fountains >100 ft Pyroclasts >300 ft				
May 27	1850		Explosive					
November 14 to 30	1867		Explosive	Pyroclasts up to 150 m	Up to 1 km	3-25 mm		
November 22 to 29	1899		?					
October 28 to November 3	1914		Explosive					Electrical activity and mud flows
June 20 to 30	1919		Explosive (?)					
October 23 to December 11	1923	300 m	Effusive to Explosive Effusive	Incandescent pyroclasts up to 300 m				
July 9 to 26	1947	130 m	Effusive to Violently Explosive		6.5 km	7 in.	3-6 km	
November 21 to December17	1950		Effusive to Explosive Effusive		1000 ft			
September 4 to 24	1957	470 m	Effusive to Explosive Effusive		2 km			
September 28 to December	1960		Effusive to Explosive Effusive		500 m	qty. unreported	2 km	
October 25	1961		Effusive to Explosive Effusive					
March 27 to 29	1962		Effusive to Explosive Effusive			qty. unreported		
March	1963	600 m (ASL?)	Explosive					
October 23 to December 10	1968	230 m	Effusive to Explosive Effusive		1.5 km	0.5 cm		
December 21 to 23	1969		Explosive					
Februrary 3 to 14	1971		Explosive		6 km	1-3 cm		
April 9 to 14	1992		Violently Explosive	300 m	3.5 to 7.5 km	5 cm		
May 24 to August 15	1995		Effusive to Explosive	200 m	1 km			
November 19 to December 4	1995		Effusive to Explosive Effusive	1 km		5 mm	2.5 km	
August 5 to 8	1999	347 m	Explosive Effusive	>300 m				

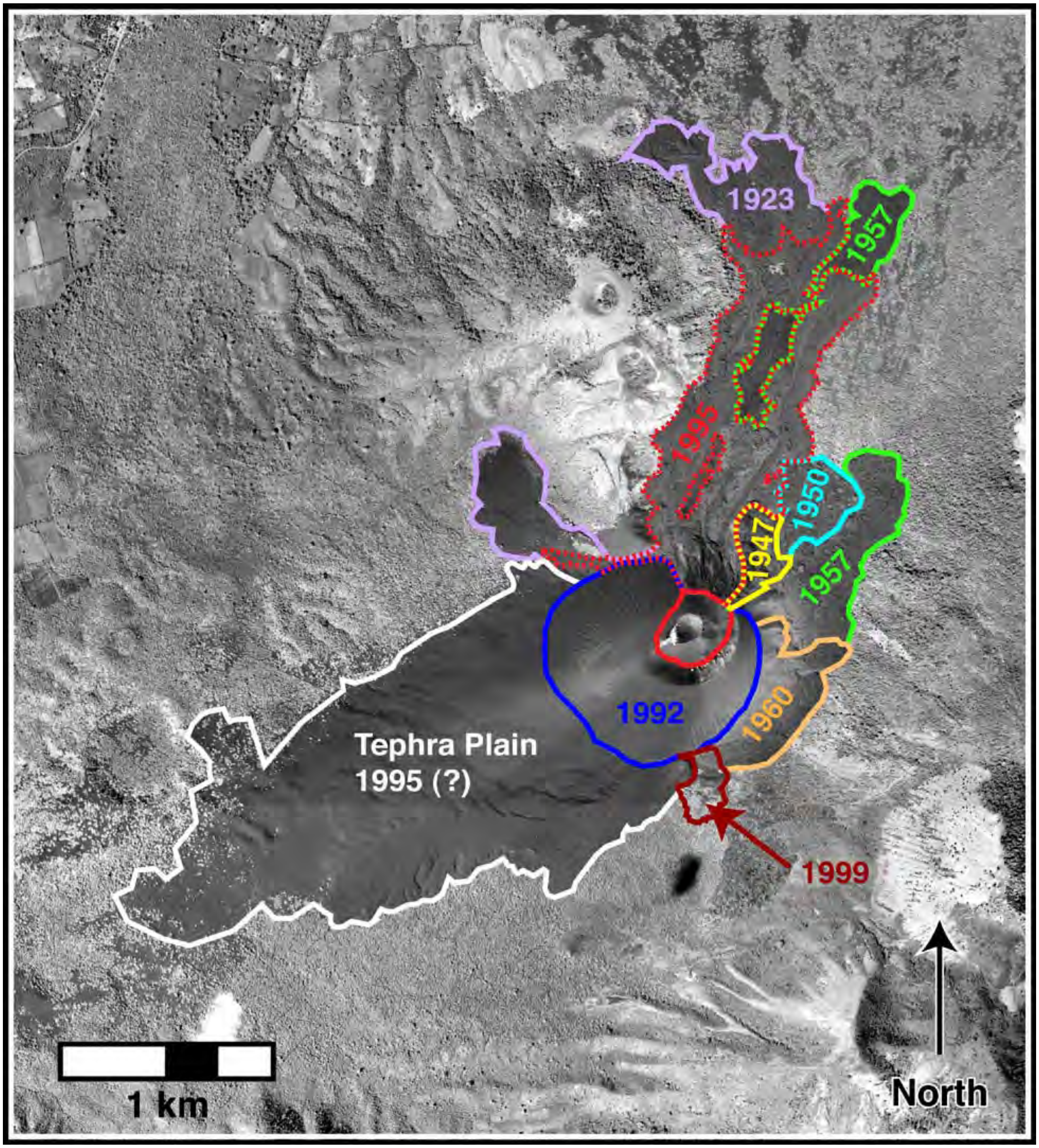

Figure 4-2 Aerial photo acquired in 1996 provided by INETER. The complex pattern of lava flows for 6 effusive events (modified from McKnight, 1995; Viramonte and Di Scala, 1970) are outlined to the north and the extensive tephra plain containing surface material from the 1995 event is labeled to the south. The extent of the 1968 flow is somewhat apparent within the tephra plain. The 1995 lava flows have not been formally mapped (hence the dotted pattern). The 1947 and 1950 lava flows were also combined into one unit for the analyses due to the ambiguity of the boundary between them. The parasitic cinder cones from 1999 are not present in the photograph. The periphery of these features was mapped for this study using GPS data.

most recent occurring in August of 1999 (Table 4-1). The most recent subplinian eruptions (1947 and 1992) have produced ash column up to 9 km high, resulting in tephra and ash fall in the city of León (Table 4-1; Figure 4-1) and surrounding farming communities. Moreover, these more intense eruptions have produced an extensive tephra plain as a result of the prevailing winds in that area, which extends to the south and west of the main edifice. Passive activity has produced multiple a'a lava flows from the main edifice that extend as far as 6 km to the north and north-northeast (Table 4-1; Figure 4-2). A complicated pattern of exposed lava flows exists, which were emplaced during the 1923, 1947, 1957, 1960, 1995, and 1999 events (Figure 4-2). This investigation attempts to determine bulk composition, phenocryst assemblages and the relative age of these flows using spaceborne and laboratory TIR spectroscopic techniques. Since its last eruption in 1999, Cerro Negro has remained relatively quiescent and continues to passively degas SO_2, H_2O and H_2S (Lopez, 2006) through several fumarole fields within the two main craters (Figure 4-3F). The past eruptive history at Cerro Negro creates an increased potential of hazards to nearby populous centers, which necessitates continued monitoring to characterize eruptive activity/products and forecast future behavior.

Cerro Negro is exposed to a similar average rainfall (125-150 cm/yr; Taylor, 1963) as Mauna Loa (150-600 cm/yr; Crisp et al., 1990) and Etna (130 cm/yr; Giammanco et al., 1996). However, the rainfall at Cerro Negro occurs dominantly during the wet season that occurs between May and November. Therefore, the process of relative age dating of lava flow surfaces using the TIR spectral changes should be viable at this location. A visible amount of oxidation and chemical alteration is easily identified on the lava flow surfaces. However, the tephra plain, which is not a target in the investigation, has remained relatively unaltered. It is assumed that the exposed layer of tephra is continually abraded due to eolian processes and therefore chemical

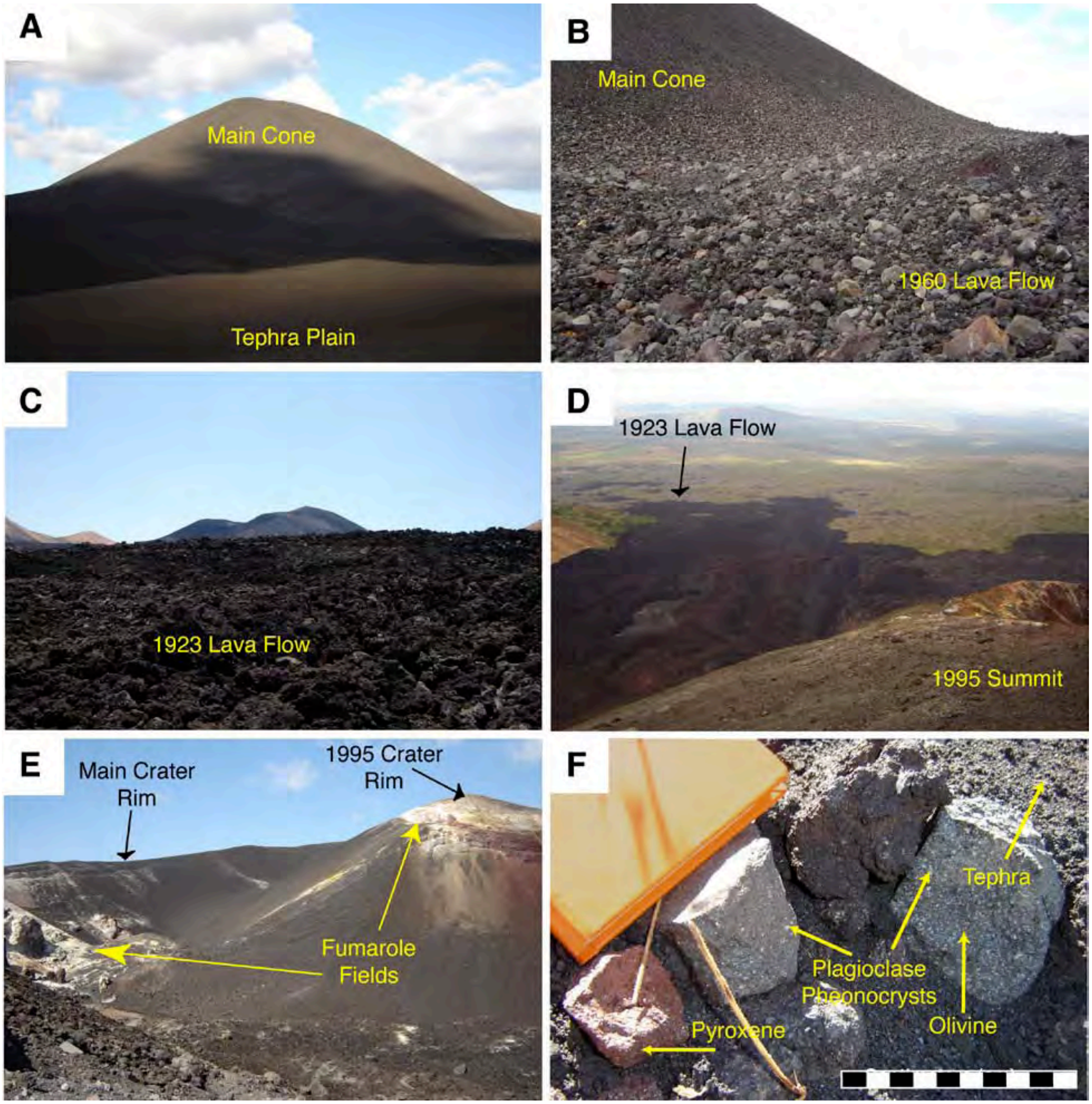

Figure 4-3 Field photographs of Cerro Negro. A) a view of the main cone and tephra plain from the southwest; B) the eastern flank of the cone and the 1960 lava flow in the foreground, which is composed of a mixture of lava compositions and textures; C) a view of the main cone from the 1923 lava flow to the far north; D) the lava flow field from the summit of the 1995 cone with the 1923 flow labeled for reference; E) panoramic view within the main crater showing the 1995 cone and the two main fumarole fields; F) various compositions and textures of the lavas.

weathering of the surface is minimized. Furthermore, this tephra is some of the newest material exposed, being emplaced during the 1995 eruption.

4.3 METHODOLOGY

4.3.1 Sample Collection and Descriptions

A comprehensive lava flow map was constructed by combining those created by Viramontee and Di Scala (1970) and McKnight (1995) (Figure 4-2) and used to determine sample collection locations. The lava flows associated with the 1995 eruption were mapped in the field based upon the shapes of the older flows in the previous maps and whether those flows appear to have superimposed termini or an obvious color/textural change in the 1996 aerial photo (courtesy of INETER). Similarly, the 1947 and 1950 flow boundaries were complexly mixed and therefore these flows were combined into a single 1947-50 event for the purpose of this study. During the field campaigns of January 2006 and March 2009, 23 representative a’a lava samples were collected from each of the 6 visible flows outlined in Figure 4-2. These were located using a Trimble differential GPS Pathfinder Pro XRS unit to verify that the collection sites were within the boundaries of each lava flow. At some locations, multiple samples were collected because the lava flows contained a considerable mixture of basalts, secondary volcanics of varying composition (Figure 4-3F), and/or degrees of vesicularity. A detailed list of sample descriptions can be found in Table 4-2.

Table 4-2 Summary of each sample collected and used for the linear deconvolution process. The most abundant phenocryst is listed first. Note how the 1960 lava flow consists of a variety of samples in color, oxidation, and texture.

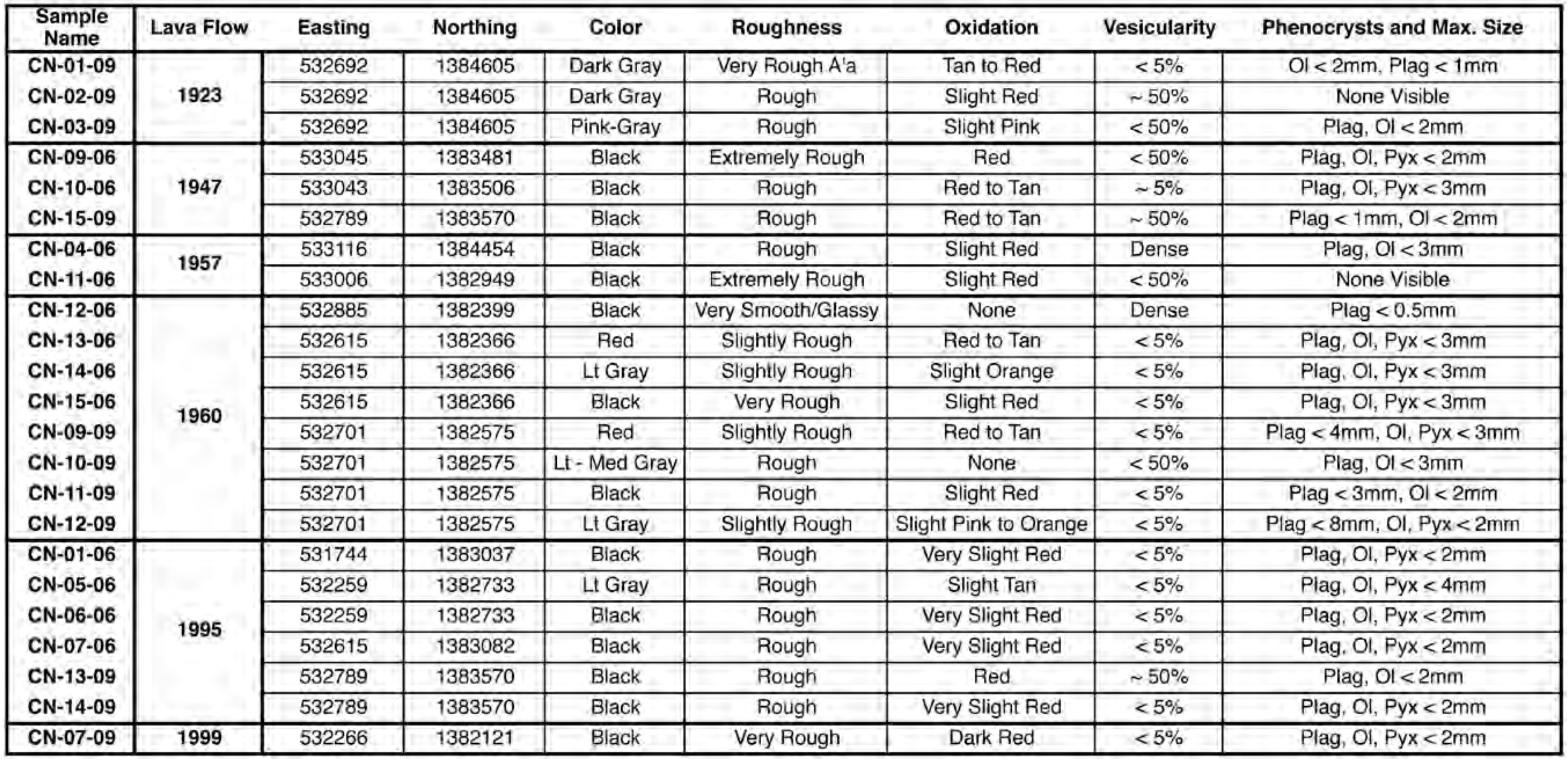

Sample Name	Lava Flow	Easting	Northing	Color	Roughness	Oxidation	Vesicularity	Phenocrysts and Max. Size
CN-01-09	1923	532692	1384605	Dark Gray	Very Rough A'a	Tan to Red	< 5%	Ol < 2mm, Plag < 1mm
CN-02-09		532692	1384605	Dark Gray	Rough	Slight Red	~ 50%	None Visible
CN-03-09		532692	1384605	Pink-Gray	Rough	Slight Pink	< 50%	Plag, Ol < 2mm
CN-09-06	1947	533045	1383481	Black	Extremely Rough	Red	< 50%	Plag, Ol, Pyx < 2mm
CN-10-06		533043	1383506	Black	Rough	Red to Tan	~ 5%	Plag, Ol, Pyx < 3mm
CN-15-09		532789	1383570	Black	Rough	Red to Tan	~ 50%	Plag < 1mm, Ol < 2mm
CN-04-06	1957	533116	1384454	Black	Rough	Slight Red	Dense	Plag, Ol < 3mm
CN-11-06		533006	1382949	Black	Extremely Rough	Slight Red	< 50%	None Visible
CN-12-06	1960	532885	1382399	Black	Very Smooth/Glassy	None	Dense	Plag < 0.5mm
CN-13-06		532615	1382366	Red	Slightly Rough	Red to Tan	< 5%	Plag, Ol, Pyx < 3mm
CN-14-06		532615	1382366	Lt Gray	Slightly Rough	Slight Orange	< 5%	Plag, Ol, Pyx < 3mm
CN-15-06		532615	1382366	Black	Very Rough	Slight Red	< 5%	Plag, Ol, Pyx < 3mm
CN-09-09		532701	1382575	Red	Slightly Rough	Red to Tan	< 5%	Plag < 4mm, Ol, Pyx < 3mm
CN-10-09		532701	1382575	Lt - Med Gray	Rough	None	< 50%	Plag, Ol < 3mm
CN-11-09		532701	1382575	Black	Rough	Slight Red	< 5%	Plag < 3mm, Ol < 2mm
CN-12-09		532701	1382575	Lt Gray	Slightly Rough	Slight Pink to Orange	< 5%	Plag < 8mm, Ol, Pyx < 2mm
CN-01-06	1995	531744	1383037	Black	Rough	Very Slight Red	< 5%	Plag, Ol, Pyx < 2mm
CN-05-06		532259	1382733	Lt Gray	Rough	Slight Tan	< 5%	Plag, Ol, Pyx < 4mm
CN-06-06		532259	1382733	Black	Rough	Very Slight Red	< 5%	Plag, Ol, Pyx < 2mm
CN-07-06		532615	1383082	Black	Rough	Very Slight Red	< 5%	Plag, Ol, Pyx < 2mm
CN-13-09		532789	1383570	Black	Rough	Red	~ 50%	Plag, Ol < 2mm
CN-14-09		532789	1383570	Black	Rough	Very Slight Red	< 5%	Plag, Ol, Pyx < 2mm
CN-07-09	1999	532266	1382121	Black	Very Rough	Dark Red	< 5%	Plag, Ol, Pyx < 2mm

4.3.2 Thermal Infrared Spectroscopy Background

The TIR radiance emitted of a surface per unit area and per unit solid angle is a function of both the wavelength-dependent emissivity and the surface brightness temperature. It is expressed by the Planck equation (Equation 3-1). In order to solve for the emissivity from radiance data, it must be separated from the temperature using one of several temperature emissivity separation (TES) approximations such as the emissivity normalization approach described in Realmuto, 1990 and Gillespie et al., 1998. Depending upon the number of wavelength bands (n) for the instrument used, the set of Planck radiance equations is under-determined, such that there will be n+1 unknowns. This requires an assumption of either one of the n emissivity values or the temperature. The resulting emissivity spectrum can then be used to determine the composition (Lyon, 1965; Ramsey and Christensen, 1998, Gillespie et al., 1998), texture (Byrnes et al., 2004, Carter et al., 2009), and/or degree of weathering (Kahle et al., 1988; Crisp et al., 1990; Abrams et al., 1996) of the surface. However, most lithologic surfaces of the Earth contain a mixture of components and the emitted energy is further averaged over the spatial resolution of the instrument. Therefore, a mixing model of emitted energy is needed in order to deconvolve this complex mixing of mineralogy, surface texture, and temperature. One commonly-used and well-tested approach is that of a linear deconvolution, used in combination with a spectral library of mineral end-members.

Linear mixing is based on the assumption that TIR emissivity from a multi-component surface is a combination of the radiant energy from each component in proportion to its areal percentage (Lyon, 1964; Singer and McCord, 1979; Adams et al., 1986; Ramsey and Christensen, 1998). Therefore, spectral absorption features of each end-member (e.g., mineral) are present in the composite spectrum in proportion to their areal percentage exposed on the surface. Mixed spectra are deconvolved into their end-member percentages using a linear least squares minimization algorithm to fit the data. This process results in a percentage of each component in addition to measurements of the model's quality by way of the residual (measured minus modeled emissivity at each wavelength) and root-mean-squared (RMS) errors. The RMS error is a singular value for each model spectrum fit over the entire wavelength.

The assumptions that affect the overall accuracy of the results for this type of model include: the spectral resolution and signal to noise of the instrument, the number of end-members chosen, and to a lesser degree, the particle size of the surface materials and the pixel-integrated brightness temperature (Ramsey and Christensen, 1998; Ramsey and Dehn, 2004). The maximum number of end-members mathematically allowed is determined by the number of spectral bands of the instrument. Generally, only three to four end-members are used for ASTER data because of the limited spectral resolution. Furthermore, most geologic surfaces rarely contain more mineral end-members than that in percentages greater than the detection limit for the model (~5%) (Gillespie, 1992; Ramsey et al., 1993). Particle sizes less than ~60 µm can also impart non-linear spectral effects that must be taken into account using more complex scattering models or appropriate spectral libraries (Hapke, 1993; Ramsey and Christensen, 1998). Moreover, the particle size, maximum emissivity, and pixel-integrated temperature are limited by a priori knowledge of the surface in question. Despite these complexities, the linear quantitative deconvolution approach of thermal emission spectra is relatively straightforward and has become an important tool for interpreting TIR data for Earth and Mars-based studies over the past 20 years (Bandfield et al., 2000; Ramsey et al., 1999; Hamilton et al., 2001; Wright and Ramsey, 2006).

4.3.3 Laboratory Spectral Analysis

Lava flow compositions were determined by collecting calibrated, absolute TIR emissivity spectra of the 23 field samples (collected from the 6 exposed lava flows), using a Nicolet Nexus 670 FTIR spectrometer and the calibration approach outlined in Ruff et al., (1997). The spectrometer is equipped with a potassium bromide (KBr) beamsplitter in combination with a temperature-stabilized Deuterated Triglycine Sulfate (DTGS) nitrogen-cooled detector. It detects emitted energy from the sample over the range of 2000 – 500 cm^{-1} (2.5 to 22 µm) at a spectral resolution of 4 cm^{-1} and a variable spot size of between 1 – 10 cm. However, due to noise at longer wavelengths, a spectral range of 7 to 18 µm was used in this study. Emission data of the samples, as well as the temperature-controlled blackbodies ($\varepsilon = 1.0$) used to determine the instrument response function (e.g. Ruff et al., 1997) are acquired in a nitrogen-purged environment to minimize the influence of water vapor and carbon dioxide on the emission spectrum. Once these calibrated spectra were processed, a representative emissivity spectrum from each of the exposed lava flows was examined to determine how the spectral features change over the 76 year time period. And more importantly, these changes were assessed for their significance for relative dating of the basalt flows in an environment different from the previous studies in Hawaii and Italy.

The linear spectral deconvolution algorithm described previously was applied to the laboratory spectra of the weathered surfaces of each sample. Spectral mineral end-members from the Arizona State University Spectral Library (Christensen, 2000) were chosen based upon the most abundant minerals of Cerro Negro lavas reported in Roggensack, (2001) in addition to the weathering products most common to basalts (Eggleton et al., 1987). These end-members are reported in Table 4-3. Spectra of a basaltic glass (sample CN-12-06) and blackbody were also included because most of the spectra displayed a morphology consistent with glass (Lee et al, 2010; Ramsey and Fink, 1997). Once the end-member compositions were determined, the results for all samples from each lava flow were first normalized to remove the percentage of blackbody, which is a proxy for vesicularity/surface roughness (Ramsey and Fink, 1999). The blackbody-normalized end-member percentages were then grouped according to each of the six eruptive events and averaged together for a final, overall composition for each flow. These values resulted in compositional trends over time. A standard error of 5% was used for all laboratory deconvolution model results following the results of Ramsey and Christensen (1998) and Feely and Christensen (1999) for the laboratory analyses.

Table 4-3 A list of the end-members used in the linear deconvolution approach. Noted that the Saponite, Nontronite, and Halloysite end-members were added together to produce the Total Clays end-member, as each of these minerals fell within or close to the error limit of the linear deconvolution technique for laboratory spectra (5%).

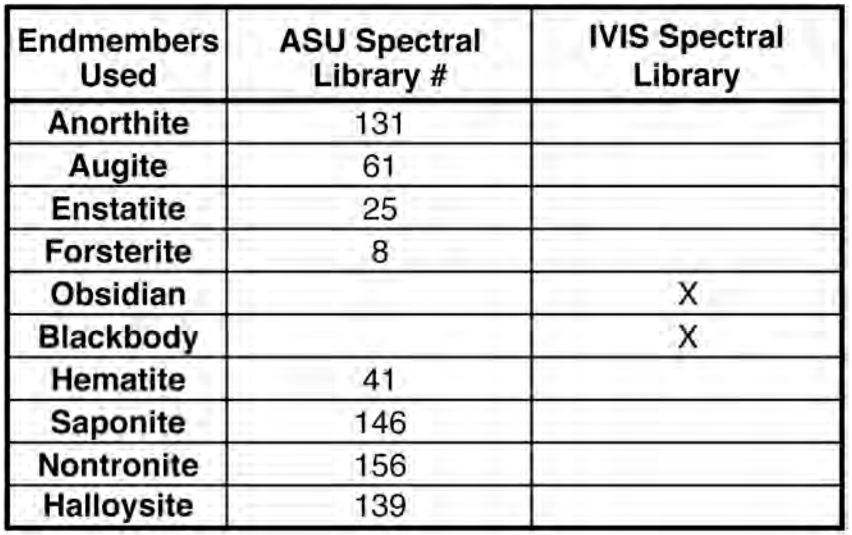

Endmembers Used	ASU Spectral Library #	IVIS Spectral Library
Anorthite	131	
Augite	61	
Enstatite	25	
Forsterite	8	
Obsidian		X
Blackbody		X
Hematite	41	
Saponite	146	
Nontronite	156	
Halloysite	139	

4.3.4 ASTER Data Acquisition and Data Processing

The Advanced Spaceborne Thermal Emission and Reflection Radiometer (ASTER) instrument is a moderately-high spatial resolution, multispectral imager on the Terra spacecraft. It consists of three subsystems: visible near infrared (VNIR; 0.56 – 0.81 µm) with three channels, shortwave infrared (SWIR; 1.65 – 2.40 µm), and thermal infrared (TIR; 8.29 – 11.318 µm) with five channels. The spatial resolution varies from 15 m (VNIR) to 30 m (SWIR) to 90 m (TIR) (Kahle et al., 1991). The raw image data collected by ASTER are corrected for geometric distortion and image registration, and later processed into level 2 (L2) on-demand products processed with the latest calibration coefficients. For this investigation, a L1B surface leaving SWIR and TIR radiance dataset was used for the preliminary thermal deconvolution process, described below, and L2 TIR surface emissivity and L2 brightness temperature were used for the compositional deconvolution portion of the study. The purpose for using the L1B SWIR data is due to a lack of correction available for the crosstalk error in L2 nighttime data (Iwasaki and Tanooka, 2005).

Unlike the relatively small spot size and thermally stable environment of the laboratory spectrometer, the ASTER TIR subsystem integrates a variety of thermal features, such as cold rocks, sunlit slopes and fumaroles over a 90 m^2 pixel, resulting in non-isothermal emitted radiance, which is easily identified by emissivity spectra that slope toward longer wavelengths (Ramsey and Dehn, 2004; Rose and Ramsey, 2009; Rose et al., in review-a). Therefore, a thermal deconvolution correction (Rose et al., in review-a) is required, especially where accurate surface compositional information is the goal. The non-isothermal effects on the emissivity spectra are corrected by identifying pixels that have a combination of an anomalously-high pixel-integrated brightness temperatures compared to the average background temperature of the scene together with an emissivity spectral slope of < -0.015. The higher spatial resolution and radiance detection limit of the SWIR subsystem is then used to subdivide the spatial distribution of the thermal heterogeneities within each 90 m TIR pixel to produce a more accurate and thermally mixed Planck curve that can be used to correct the measured emissivity spectrum (Eq. 1). Once the negative emissivity slopes have been corrected, the compositional analysis is much more accurate (Rose et al., in review-a).

ASTER data were acquired during both field campaigns, on 18 January 2006 and 30 March 2009. The L1B data acquired on 18 January 2006 was required in order to determine whether the extensive fumarole fields within the two main craters contributed a significant amount of thermal radiance, which would affect the emissivity spectra extracted from the associated ASTER TIR pixels. The ability of ASTER to detect highly-radiant features on a smaller spatial scale in the SWIR allows for a better constraint of spatial distribution of these thermal heterogeneities (if present). Unfortunately, the first and only major failure of the ASTER instrument occurred in January 2009 when the SWIR subsystem cryo-cooler ceased operation. Therefore, only the January 2006 L1B dataset (SWIR + TIR) could be used to identify thermally-mixed pixels and correct their associated emissivity slopes, whereas only the TIR data from 30 March 2009 could be used to identify potentially non-isothermal pixels, with no way of correcting the spectra. In order to validate the locations of thermally-mixed TIR pixel locations in the ASTER datasets, the locations of the fumaroles within the two main craters were mapped by GPS prior to both of the ASTER over flights in 2006 and 2009.

Once the emissivity correction process was completed, the L2 TIR emissivity data from the 30 March 2009 over flight was linearly deconvolved using the five most abundant end-members determined from the laboratory analyses. Due to the reduced spectral resolution of ASTER (5 bands) in the TIR compared to the laboratory spectrometer, the number of end-members was limited further. The outlines of each lava flow were overlaid on the ASTER emissivity images and regions of interest were created in known areas from each flow. It should be noted that the 1995 flow that dominates the surface to the north has not been mapped by previous investigators and the boundaries presented here are inferred based on our field studies (Figure 4-2). Also, due to the absence of the 1999 parasitic cinder cones and lava flows on the southeastern flank of Cerro Negro in Figure 4-2, the extent of these features was mapped using the GPS during the 2009 field campaign and overlain as a vector and region of interest on the aerial photo and ASTER data. A representative emissivity spectrum for each flow was extracted from the regions of interest and used to compare to the laboratory data, as well as examine their spectral pattern(s) over. Similar to the laboratory compositional analysis, the results were also normalized using a blackbody end-member to account for variations in band depth between the laboratory end-members and the ASTER emissivity data. A standard assumed detection limit of 15% (Feely and Christensen, 1999) was used to establish the error range because the results are obtained from a multispectral instrument as opposed to the hyperspectral laboratory data. Overall, the wide range of volcanic features present at Cerro Negro, ranging from small clusters of fumaroles (varying temperatures) on a meter scale to extensive kilometer-scale lava flows (varying compositions) provided a challenging setting to test these deconvolution approach over the relatively brief (76 years) period of time.

4.4 RESULTS

4.4.1 Laboratory Spectroscopy and Compositional Deconvolution

Emissivity spectra of the weathered surfaces for representative samples from each flow were acquired and plotted (Figure 4-4). The emissivity spectra reveal three prominent spectral features: A (8.1 – 8.2 µm), B (9.2 µm), and C (10.5 – 10.8 µm), which change as the flows age. Features A and B increase in spectral contrast (deepen), whereas C begins to decrease (shallow) as the lava flows age over a period of 76 years. Feature A is only slightly visible in the relatively recent (oxidized) 1999 lava flow, but reappears in samples from flows older than 1957. However, feature B tends to dominate every spectrum, regardless of age, and increases in spectral contrast as the flows become older. Feature C is obvious in the most recent effusive events dating back to 1957 with the highest spectral contrast (deepest) occurring in 1995. In addition, the 1999 flow reveals a slight shift in feature C toward 12 µm. Overall, the laboratory emissivity spectra show a definite progression in spectral morphology with time.

The spectral linear deconvolution algorithm was applied to the laboratory emissivity spectra from each year, using the mineral end-members listed in Table 4-3. For this approach, an RMS of < 1.0% indicates a relatively good fit (Ramsey and Christensen, 1998). The RMS errors associated with these deconvolution results range from a best fit of 0.32% to a worst fit of 1.58%. The representative spectra of the best and worst RMS values are shown in Figure 4-6. Sample CN-11-06, collected from the 1957 lava flow, shows a poor model fit occurred particularly in the areas of spectral features A and B. However, sample CN-15-06 from the 1960 lava flow produced the best overall fit of the end-members with a slight misfit between 9 – 11 µm and toward longer wavelengths of 15 to 17 µm, which was uncharacteristically distorted by

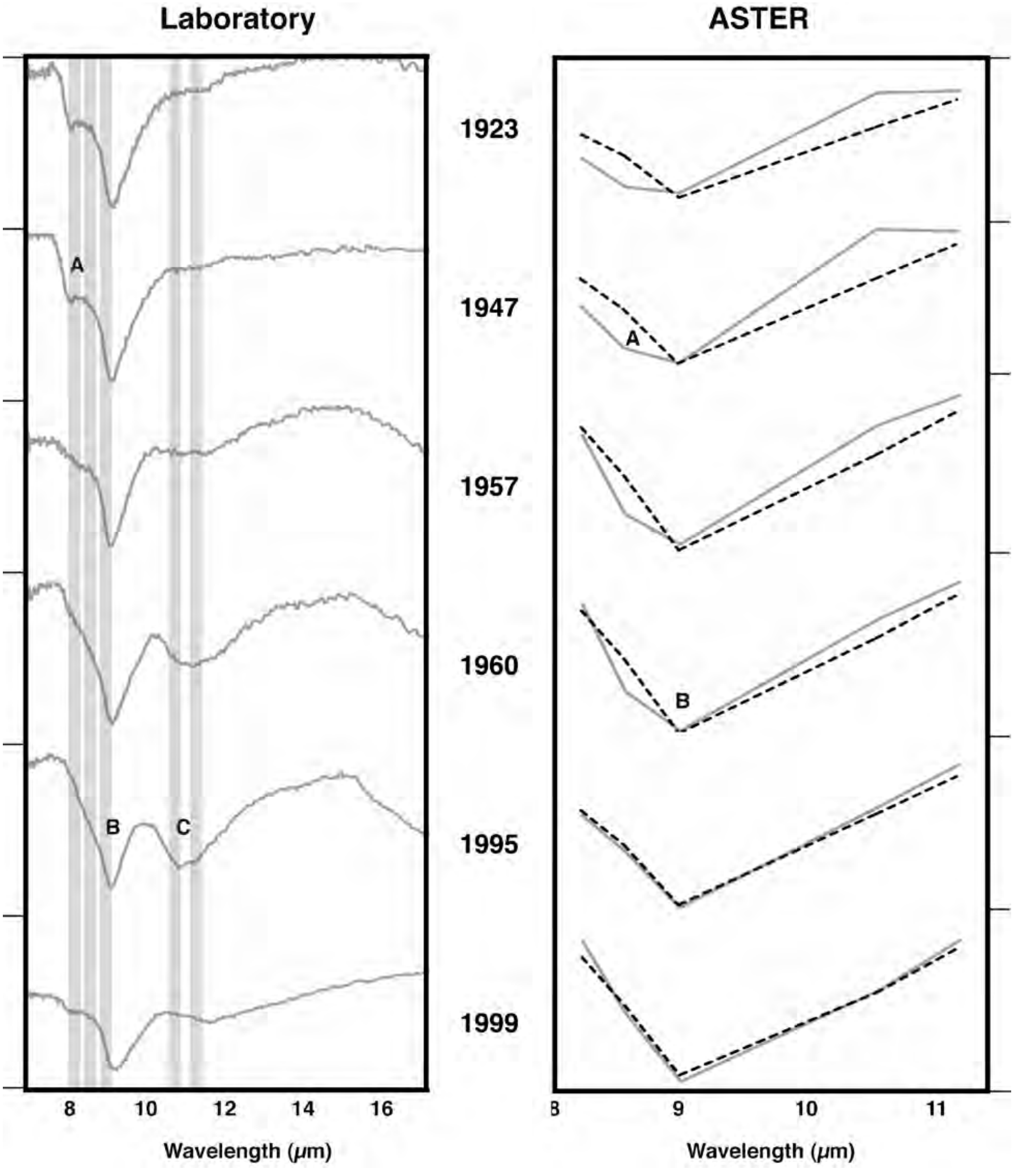

Figure 4-4 Linear deconvolution results obtained from both the laboratory (left) and ASTER (right) arranged in the order of decreasing age. Both datasets reveal a change in spectral features A, B, and C and agree with those features discussed in Kahle et al., 1988 and Crisp et al., 1990. The gray vertical lines on the laboratory spectra represent the spectral bands available on the ASTER instrument.

noise in the detector during these particular analyses.

The percentage of each mineral end-member was averaged for each of the lava flows to show the overall compositional changes (Figure 4-7). Because all the clay end-member weathering products (sapronite, halloysite, and nontronite) were detected close to the detection limit (~ 5%) using the linear deconvolution algorithm, these end-members were added together into a Total Clay fraction in order to show their cumulative effect. It should be noted that the lava flows contained sporadic locations of previous fumarolic activity, with no active lava flow fumaroles, and that any clay end-member detections are derived from deuteric weathering. The most abundant mineral percentages (anorthite, forsterite, and enstatite) were previously reported by Roggensack (2001) using major element analysis of melt inclusions and bulk ash analyses. That work also reported results for tephra sample from 1867, which have been included here in order to extend the time series and validate the spectral results from earlier flows. However, it should be noted that there is no 1867 lava flow exposed at the surface.

The spectral end-members anorthite, enstatite, and hematite reveal an obvious increasing percentage with time, whereas the augite, forsterite, and total clays show the opposite trend. The quantity of glass on the surface, however, appears to be relatively constant over time, only slightly increase (<5%) as the flows become younger. The 1867 data points for the anorthite, enstatite, and forsterite retrieved from the analysis of Roggensack, 2001 are in agreement with the results reported here (Figure 4-7). The enstatite abundance of that study was ~13% whereas the maximum value reported here was ~5%. However, the general trend of the data was consistent over time. The anorthite, augite, total clays, and glass produced the highest average abundances. A linear regression was applied to each of the mineral results over time with a specific focus on the hematite and glass end-members. Although the data contains a considerable amount of scatter, the regression resulted in an average rate of formation for the hematite and glass of +20.3% and -1.1%, respectively over the 76-year period. Moreover, by not including the oldest and youngest data points, the R^2 values will decrease to < 5%.

4.4.2 ASTER Thermal Deconvolution

The thermal deconvolution process was first applied to the 17 January 2006 L1B ASTER data in order to determine if the fumarole fields were of significantly-high thermal radiance to affect the associated TIR emissivity spectra. An inspection of the SWIR dataset revealed that there were no detectable radiant pixels, which eliminated the possibility of using the thermal deconvolution algorithm in its present configuration. Furthermore, the failed cryo-cooler rendered SWIR data unusable after mid-2009 and therefore precluded the use of the thermal deconvolution approach on the second dataset acquired on 30 March 2009. However, a manual inspection of the L2 emissivity and pixel-integrated brightness temperature data was performed to identify pixels that could potentially be non-isothermal. An average background temperature of 26.8 ºC was calculated and therefore temperatures above this value (in combination with an emissivity slope < -0.0001) could be considered thermally-heterogeneous. Only three potentially non-isothermal pixels were identified within the two craters of Cerro Negro in the 2009 data. Two of these were located within the larger fumarole field of the main crater, whereas the third non-isothermal pixel was located within the 1995 (smaller) summit crater (Figure 4-3F; Figure 4-8). Field-based GPS locations of these fumarole fields were overlain onto the ASTER datasets and confirmed that these warmer pixels corresponded to the hottest fumarole locations.

4.4.3 ASTER Compositional Deconvolution

Emissivity spectra of representative ASTER pixels from each flow were extracted, plotted and compared to the results obtained in the laboratory (Figure 4-4). The emissivity spectra also show the presence of the three spectral features (A, B, and C) and how they vary with time. Feature A reveals an increase in spectral contrast (deepen), whereas C begins to invert from an apex to a trough as the lava flow become younger in age. Although feature A (8.1 to 8.2 µm), appears briefly in the relatively recent (oxidized) 1999 lava flow, it does not reappear until 1960 and thereafter. However, feature B (9.2 µm) tends to dominate the overall spectra, regardless of age, but unlike the laboratory spectral progression, becomes more muted as the lava flows become older. Feature C (10.7 µm) is less obvious in the 1995 spectrum with the inversion from an apex to a trough occurring within the 1995 spectrum. Despite the decrease in spectral resolution from the laboratory emissivity data, the ASTER spectra also show the definite progression in the spectral changes over time with a slight variation compared to the laboratory results.

The spectral linear deconvolution algorithm was applied to the ASTER emissivity spectra, using the mineral end-members listed in Table 4-3. However, the total clay end-member was not used because of the small percentages of this end-member identified in the laboratory analysis and the limited number of end-members allowed for the five-point ASTER emissivity spectra. The RMS errors associated with these deconvolution results range from a best fit of 0.07% to a worst fit of 2.29% within the lava flows only. The emissivity and modeled spectra of the best and worst ASTER RMS values are shown in Figure 4-9. The highest RMS ASTER pixel was located along the western perimeter of the 1995 lava flow and possibly could contain some fraction of vegetation, and shows that a poor fit occurred in the areas of spectral features A

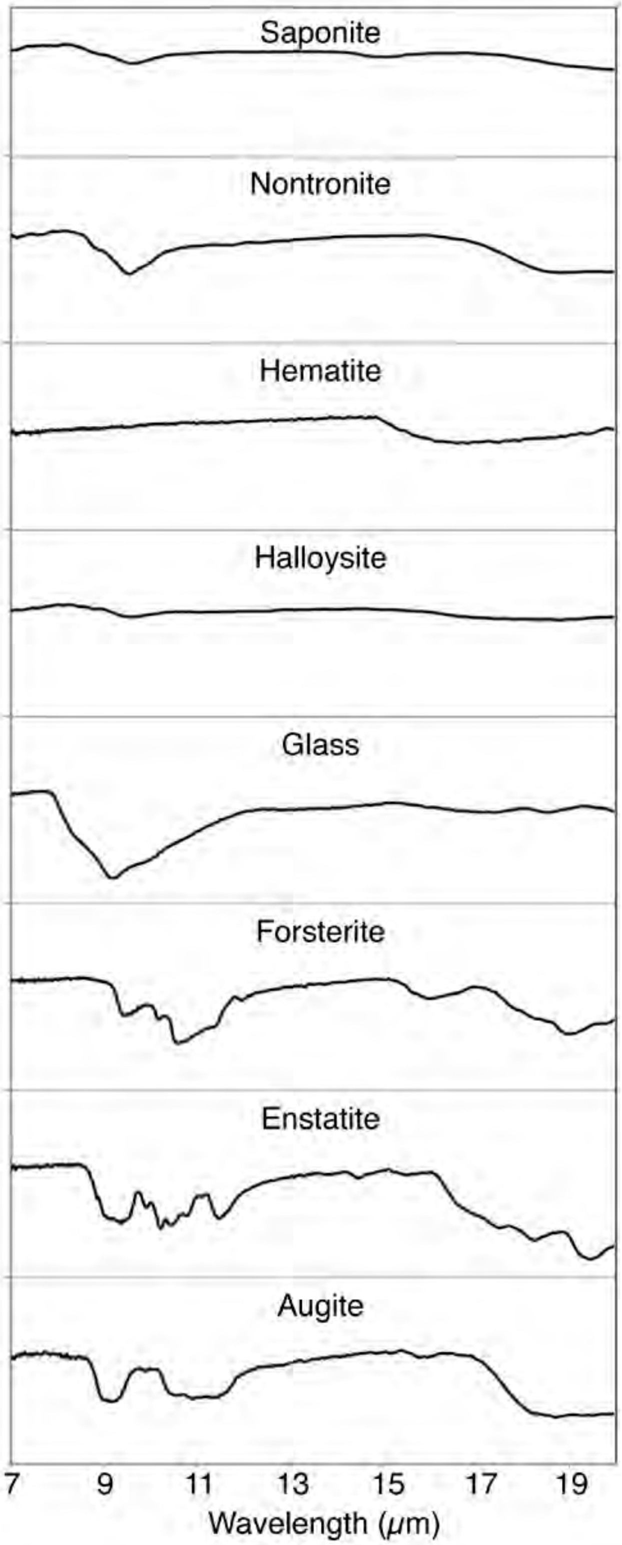

Figure 4-5 Emissivity spectra for each mineral end-member used in the linear deconvolution algorithm. Halloysite, Nontronite, and Saponite are grouped together as a "Total Clays."

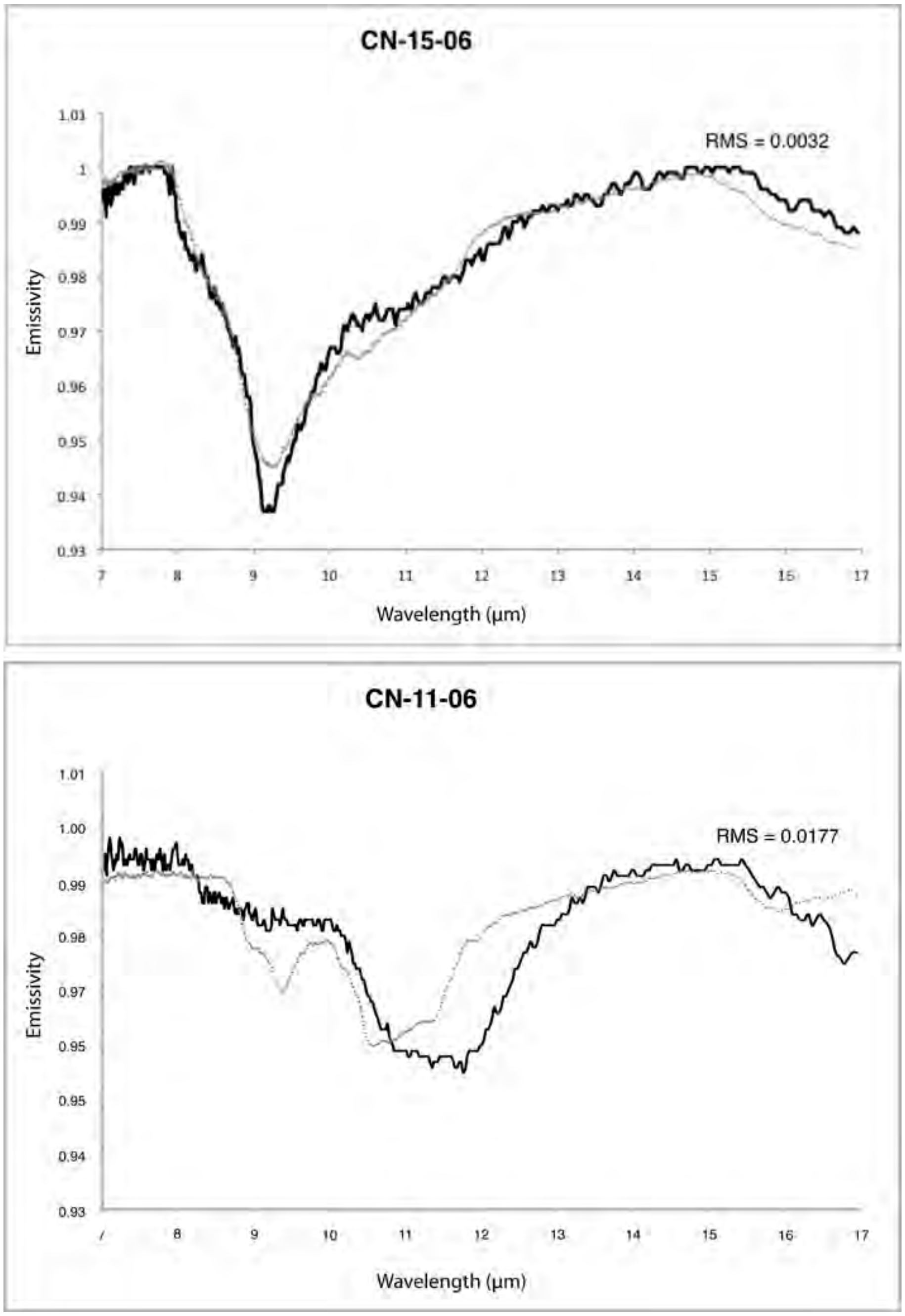

Figure 4-6 Sample emissivity spectra and the associated deconvolution model fit of the lowest and highest RMS errors. (A) The highly glassy sample (CN-15-06) produced the lowest RMS error. However, the slight discrepancy between the two spectra at 10 to 11 µm, 12 to 13 µm, and 15 to 17 µm indicate that additional end-members may be needed to better fit the data. (B) Sample CN-11-06 clearly shows a less glassy signature than (A) and the end-members used for the linear deconvolution produced a poor fit.

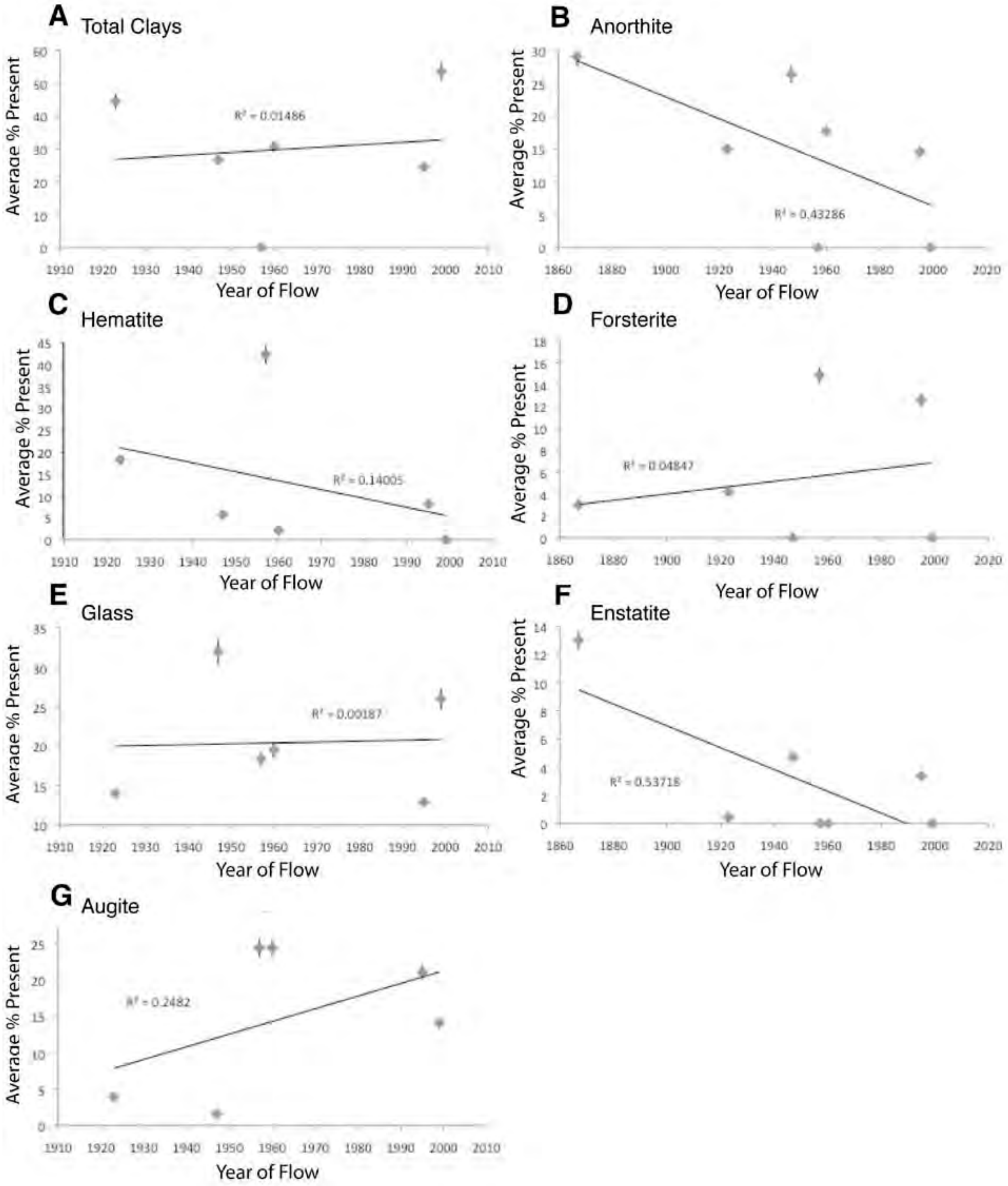

Figure 4-7 The linear deconvolution results of the laboratory TIR emissivity data showing the change of end-members over time. The saponite, nontronite, and halloysite end-members have been summed into the total clays category because each of these values fell within or close to the error of the algorithm.

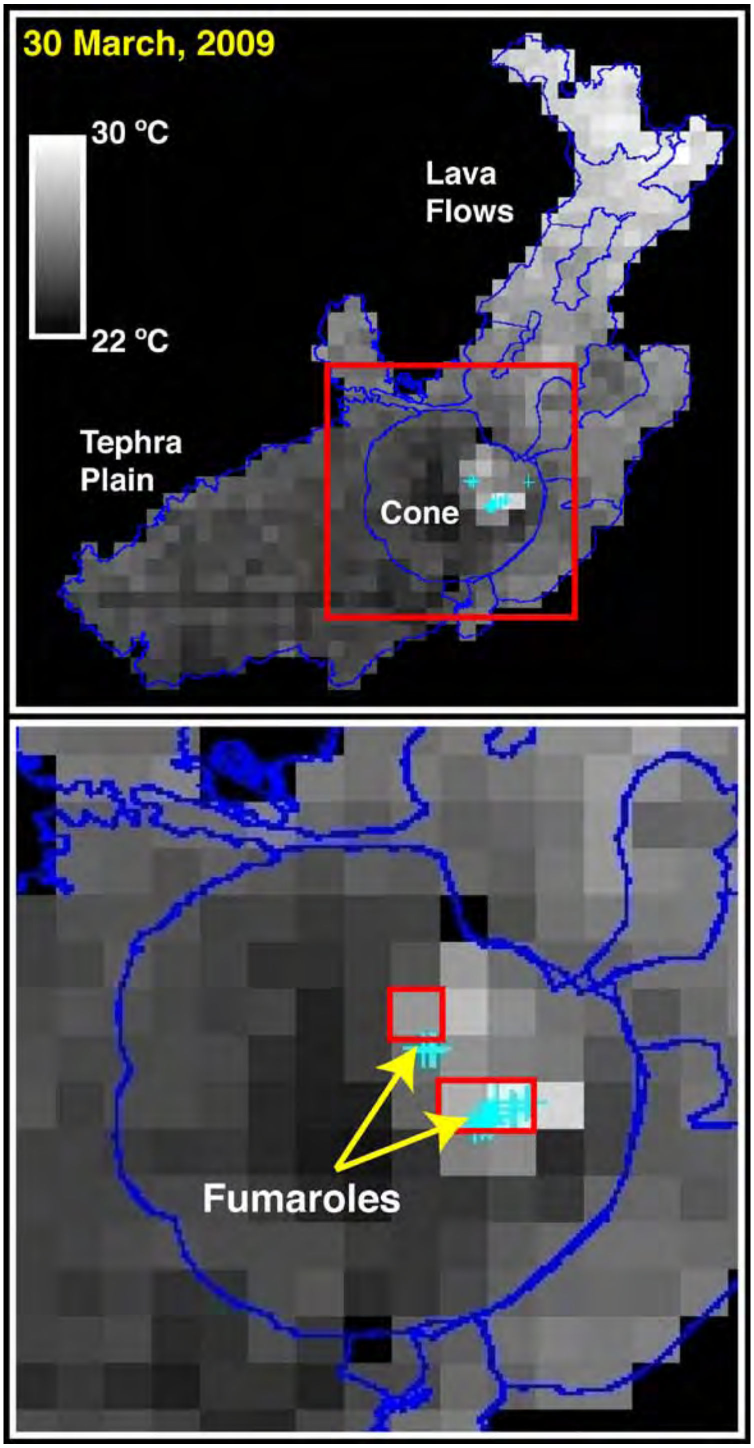

Figure 4-8 Nighttime (30 March 2009) temperature image showing the warm areas of Cerro Negro. (A) The lava flows to the north are warm due to remnant solar heating combined with the relatively high thermal inertia of these flows. The red square is the area shown in (B). (B) The area of the crater with the locations of fumaroles is denoted by the cyan crosses. Solar heating combined with a high thermal inertia results in the slightly warm lava flows relative to the tephra plain.

and C. The poor fit at the shortest wavelength (ASTER TIR band 10) could also be due to a poor atmospheric correction of water vapor. However, the lowest RMS value was located from a pixel well within the 1995 lava flow. The model produced the best overall fit of the end-members with only a very slight misfit between 10 and 11 µm (Figure 4-9). The misfits in the modeled and original ASTER data are consistent with the same areas of misfit between the modeled and original laboratory data indicating that one or more spectral end-members may be missing from the spectral library used for the analysis.

Outside of the main, 1992 crater, the lava flows occupy 272 ASTER TIR pixels. From these, 266 were used to construct the regions of interest in order to determine the compositions of the flows (Table 4-4). The final results of the ASTER linear deconvolution show that the quantity of hematite present on the surface increases as the lava flows become older, whereas the quantity of glass and anorthite decrease (Figure 4-10). The augite shows a slight decrease with age of the flow, although its appearance in the data is relatively sporadic. Overall, the glass and hematite are the most abundant of the identified end-members and the anorthite and augite are slightly above the ~10% error associated with linear deconvolution for multispectral data. Similar to the results obtained from the laboratory data, a linear regression was applied to the results for each of the end-members, with a specific focus again on the hematite and glass end-members. These ASTER-derived results produced an average rate of formation for the hematite and glass of +9.1% and -8.8%, respectively over the 76-year period. These weathering rates are slightly above to within the 10% uncertainty range of the deconvolution results between laboratory and multispectral image data. A difference of 11.2% and 7.7% was found between the ASTER and laboratory results for the hematite (+9.1% versus +20.3%) and glass (-8.8% versus -1.1%) formation/weathering rates, respectively.

4.5 DISCUSSION

The observed spectral transitions of basaltic lava flows from Hawaii, presented in Kahle, et al., 1988 and Crisp et al., 1998 have been compared to the results obtained here using both the laboratory and ASTER image datasets. The previous studies utilized the airborne TIMS instrument to test its applicability in relatively dating basaltic flows. That instrument provides high spatial resolution image data (~5 m) with 6 band TIR channels. However, airborne TIR data requires a significant amount of pre-planning and is not cost effective for obtaining this type of data for remote volcanoes. For this reason, the ASTER spaceborne instrument with its lower spatial and spectral resolution was used to test and validate its applicability for relative age dating of basaltic flows of Cerro Negro, and similar basalts of this climate.

The laboratory and ASTER emissivity spectra for each lava flow clearly show the presence of the spectral features (A, B, and C) varying in a similar progression to those presented in Kahle et al., 1988 and Crisp et al., 1990 (Figure 4-4). These three spectral features are the most important for distinguishing the surfaces of glassy, basaltic lava flows. Kahle et al., 1988 document the first occurrence of feature A after ~100 years, whereas Crisp et al., 1990 report the development of this feature as early as 3 years after emplacement in wet climates (250 cm/yr) with more common time of 50 years after emplacement. This particular feature is associated with the formation of a silica-rich rind, composed of opal or hydrated SiO_2 glass, which forms due to the addition of material (tephra and dust) to the surface of the lava flows (Crisp et al., 1990). In both the laboratory and ASTER data presented here, feature A can be first identified in the 1999 lava flow, and then reappears in the spectra of flows older than 1960. The disappearance of feature A on the 1995 flow may be explained by its recent emplacement and

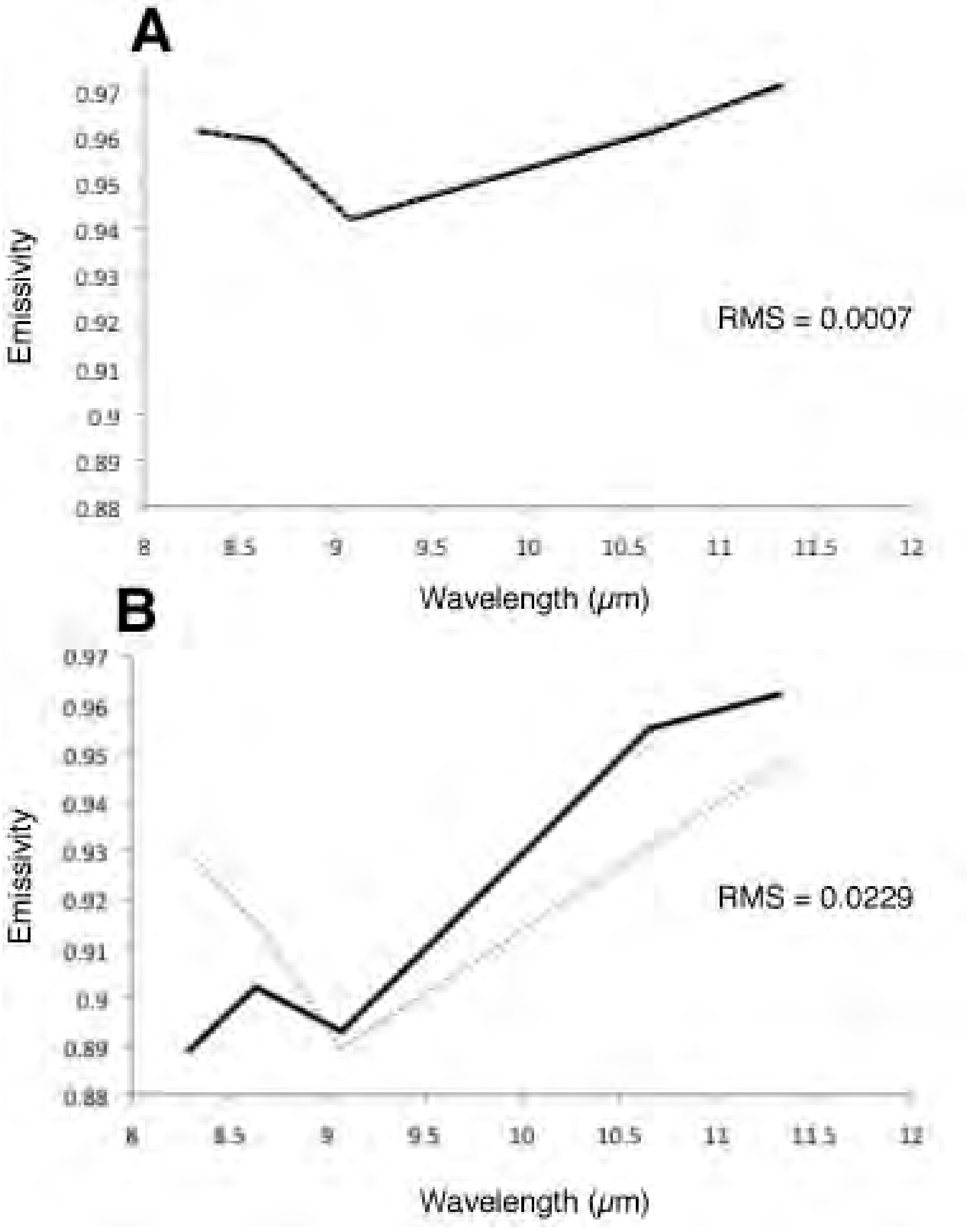

Figure 4-9 Model results for the lowest and highest RMS value for pixels subjected to the deconvolution algorithm. A) The lowest RMS error was from a pixel located within the 1995 lava flow and shows a near-perfect fit (compared to the results obtained for sample CN-15-06 in Figure 5). B) The highest RMS error was located along the lateral margin of the 1995 flow and most likely contains a mix of vegetation within the pixel as well as a poor atmospheric correction.

Table 4-4 The average composition of each lava flow derived from the ASTER TIR linear deconvolution results. A total of 266 pixels were used from the 272 pixels that fell within the lava flows.

End-members	Lava Flow Year					
	1923	**1947-50**	**1957**	**1960**	**1995**	**1999**
Anorthite	0.1	0	0.4	0.1	0.2	0.4
Augite	0	0.1	0.3	0.1	0.2	0
Blackbody	0	12.2	5.1	9.0	5.7	9.1
Hematite	61.0	41.8	61.0	46.7	52.3	42.9
Glass	38.9	45.9	40.2	44.1	41.7	47.7
RMS	0.016	0.012	0.014	0.011	0.015	0.015
# of Pixels	38	21	63	32	107	5

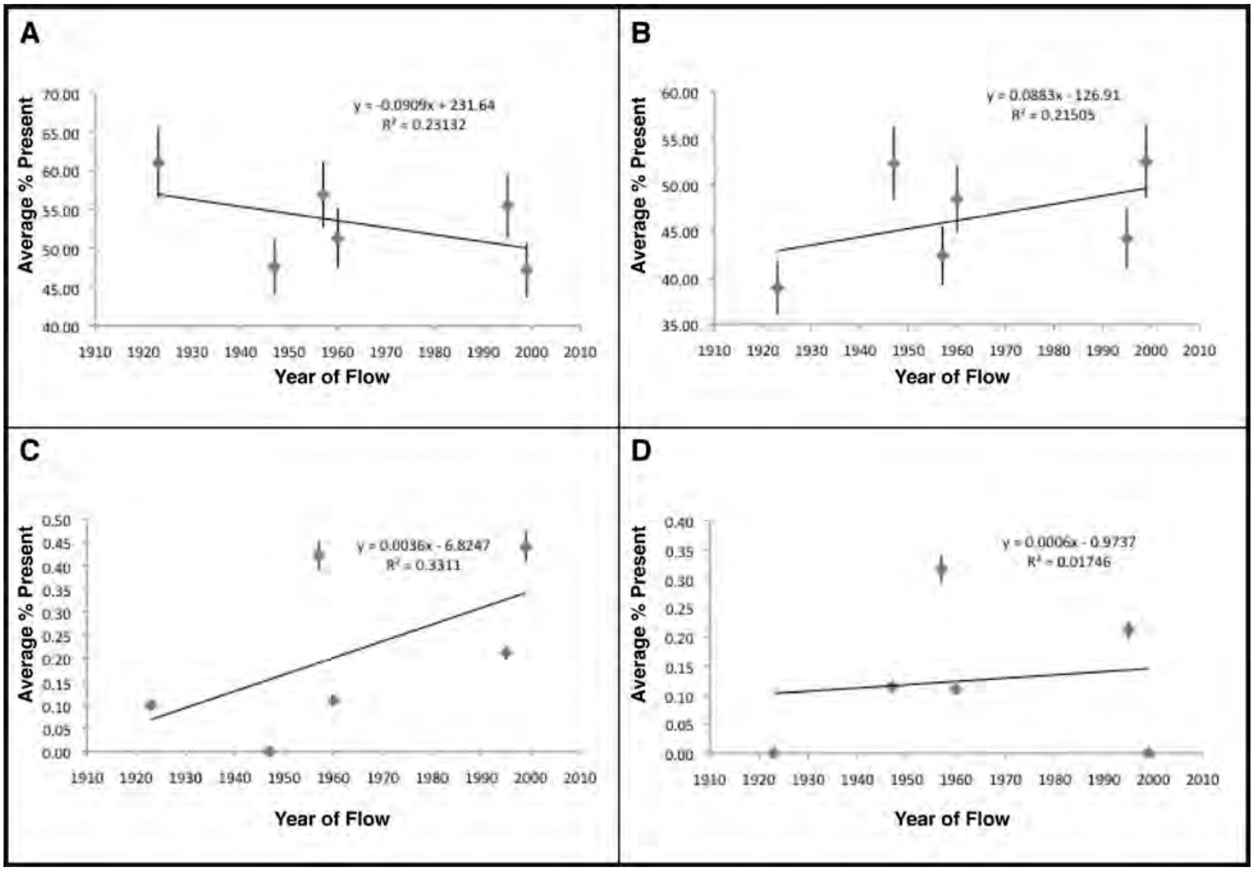

Figure 4-10 The linear deconvolution results of the ASTER TIR emissivity data over time. The degradation in spectral resolution of the ASTER instrument prevents the same number of end-members used in the laboratory analysis. The end-members chosen were the most abundant identified in the laboratory analysis. Results do show how ASTER data can be used to relatively date each flow based upon the amount of weathering products versus glass are present on the surface.

large expanse, covering a significant portion of the older weathered lava flows to the north, in conjunction with the prevailing winds to the southwest preventing the transport of loose materials, tephra, and dust onto the flow. Conversely, the A feature observed in the 1999 lava spectra could be explained due to its juxtaposition to the main, tephra covered cone and the eastern lava/debris field. Below the silicate-rich rind is a very small coating of opaque minerals including hematite and magnetite, which would lead to the positive identification of the hematite end-member in the linear deconvolution process, in addition to explaining the ubiquitous nature of the glass and hematite end-members shown in Figure 4-11, as the surfaces of lava flows rarely remain pristine and the thickness of the rind is uneven (Crisp et al., 1990). This allows for a slight basaltic signature within the associated spectra.

Spectral feature B has been shown to occur due to the Si-O and Al-O vibrations of sheet silicates, and primarily comes from the uppermost surface (10-100 µm) of the flows, in contrast to spectral feature A that is derived from the top 1 to 10 µm (Crisp et al., 1990). Although not observed in the spectra presented here, feature B has been reported to split in the spectra from feature C within 3 years of emplacement. Throughout all of the spectra presented in this study, feature B appears to be the most dominant in both the laboratory and ASTER spectra, and as previously stated by Kahle et al., 1988 and Crisp et al., 1990, tends to develop a deep spectral contrast as the lava flows age (Figure 4-4). This spectral contrast of feature B tends to be diminished in the ASTER data due to the development of feature A and a decreased spectral resolution of the instrument. However, the spectra maintain a unique shape over time, which is necessary for relatively dating basaltic lava flows using a five band multispectral spaceborne instrument.

In extremely young, glassy basaltic flows, a strong spectral feature C in relation to feature B is typically observed (Crisp et al., 1990). There have also been some cases where a strong C feature, relative to B, can still be observed in ~50 year old lava flows exposed to less rainfall (60-100 cm/yr; Crisp et al., 1990). However, the most recent flows of Cerro Negro were between 7 to 10 years of age when sampled for analyses and do not display this phenomenon even though the climate is generally dryer compared to that of Hawaii. This may be the result of the bimodal climate in Nicaragua, which is marked by 6 months of a dry season, followed by a 6 month long wet season that may contribute to inhibiting a strong C feature due to possible hydration of the basalt (Crisp et al., 1990). The gradual disappearance of feature C over time has been attributed to the glassy surface becoming more polymerized (ordered) over time without chemical changes taking place (Crisp et al., 1990). Based upon the results obtained by ASTER, the spectral feature C can be used to constrain the lava flows from 1957 and older (Figure 4-4). Moreover, the most recent flow from 1999 may also be constrained from the other flows based upon the inversion of feature C relative to those older flows (Figure 4-4). Overall, the ability to detect spectral features A, B, and C using the ASTER instrument clearly shows that it can be an effective tool for relatively dating the basaltic lava flows of Cerro Negro.

The thermal deconvolution technique was applied to the ASTER data and identified three potentially mixed pixels within the main crater and the smaller, 1995 crater (Figure 4-8). These three pixels correspond to the locations of the largest fumarole fields mapped during the 2009 field campaign and indicate that the relatively-small (< 1m) but hot (25 to > 350 ºC) fumaroles can affect the pixel-integrated emissivity and temperature of a 90 m^2 pixel. A small error in the geo-location of the image is revealed where the fumaroles within the 1995 crater lie in the adjacent pixel just to the south of the one marked as thermally mixed. However, the sub-meter

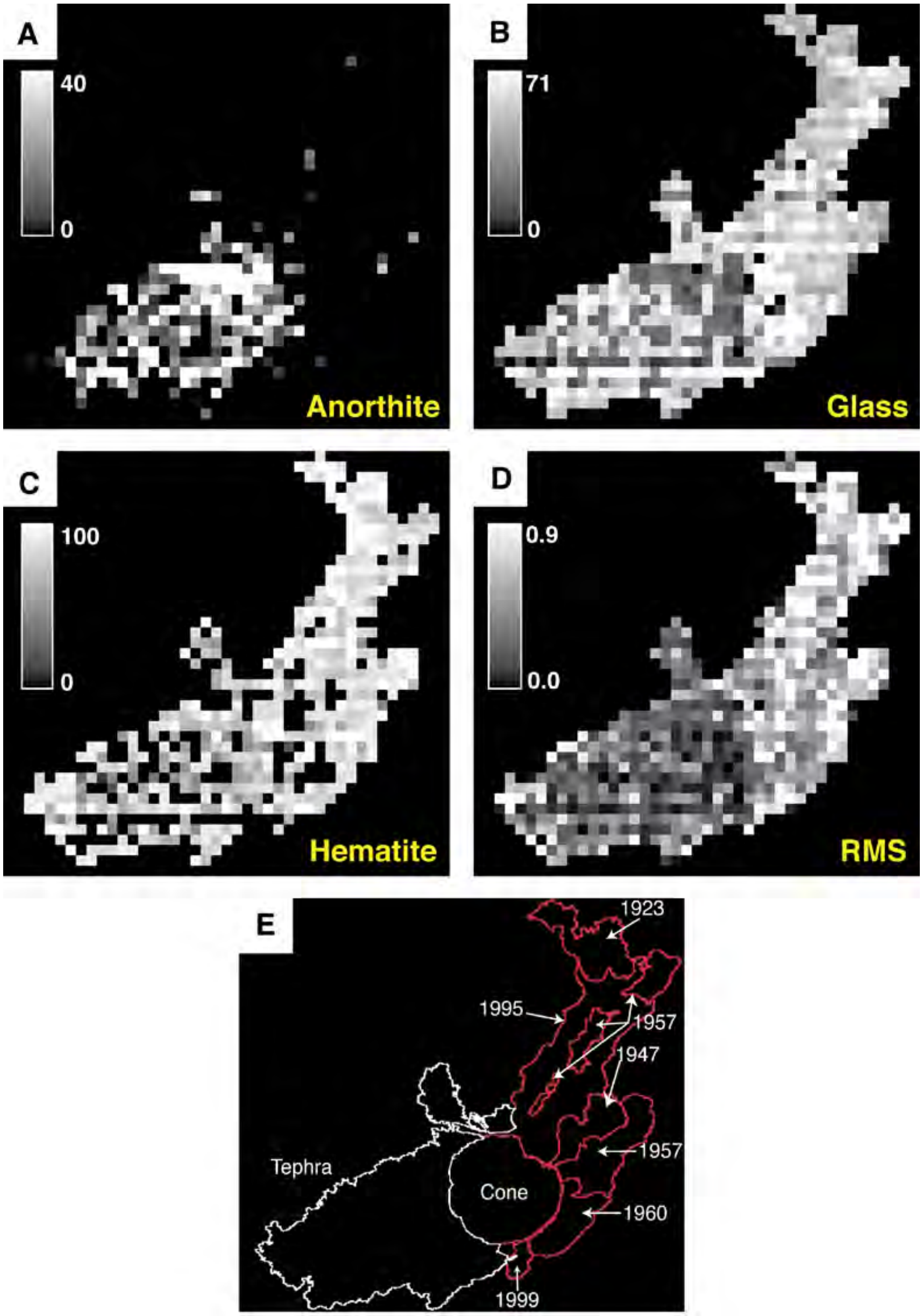

Figure 4-11 Spectral end-member maps derived from ASTER data of Cerro Negro volcano. A) a large concentration for anorthite on the southwestern flank of the main cone shows a general decrease distally on the tephra plain most likely due to wind winnowing; B) the glass end-member shows a relatively ubiquitous concentrations except for the area of high anorthite concentrations; C) hematite shows a large concentration along the lava flows and to some extent within the crater and tephra plain; D) the RMS errors appear to be lower within the tephra plain and slightly higher in the lava flows suggesting that alternative end-members may be needed; E) the lava flows and their ages are shown for reference.

resolution of the GPS fumarole locations indicates that the absolute geolocation of ASTER TIR data is within 45 m, thereby validating the registration process to within a preferred error of one 90 m TIR pixel (< 50 m; Iwasaki and Fujisada, 2005). Although the thermally mixed pixels are located in the predicted areas, there are still warm pixels within the craters that have not been identified as thermally mixed. This is likely the result of more uniform heating from deeper levels or from solar heating, which produce a relatively isothermal surface temperature for the pixel.

The linear deconvolution results obtained from the laboratory and ASTER data show a good correlation in the trends of the augite and hematite, whereas the anorthite end-member does not follow a similar pattern between the two datasets (Figures 4-6 and 4-9). The average percentages of the anorthite and augite end-members are below the error of the linear deconvolution algorithm and therefore the results cannot be considered reliable. However, the highest anorthite detections on Cerro Negro tend to fall within the southwestern tephra plain and the main cone, with minimal detection on the lava flows. During the field campaigns of 2006 and 2009, it was noted that the tephra plain and southwestern flank of the cone consisted of mm to cm sized, vesicular, and glassy tephra that appeared to be relatively un-weathered. The tephra also contained loose, mm-scale anorthite crystals mixed throughout and commonly exposed on the surface. Due to the relatively recent emplacement of the tephra (1995), it is unlikely that these crystals have been weathered out, but instead were erupted as crystal fragments during explosive activity and also sorted by wind winnowing. The quantity of these crystals, exposed on the surface, reached up to 40% on the southwestern flank of the cone, and appears to decrease distally (Figure 4-11) based on the results here.

The laboratory and ASTER data also support the formation of the silica-rich rind on the surface of the flows as shown in Figure 4-4. The presence of the rind in conjunction with the lower layer hematite results in a strong detection of these two end-members in the ASTER linear deconvolution process (Figure 4-11). Overall, the glass appears to be the dominant constituent of the lava flow and tephra surface whereas the hematite appears to be more abundant on the lava flows, and is probably the result of oxidation of magnetite within the lava. The quantity of the hematite end-member is lower on the tephra plain and lends support to the hypothesis of the eolian transport of the smaller particles producing some abrasion. The dominant presence of the hematite and glass on the lava flow can be attributed to the formation of the glassy rind and opaque mineral layers previously mentioned. The uneven formation of the glassy rind allows for the detection of the other minerals. This can also be observed on the surfaces of the lava flows with the presence of red to tan oxidation products. The maximum RMS error produced from the linear deconvolution of the ASTER data was 0.9 from one pixel in the crater located within the fumarole field; an area known for significant precipitate deposits (Figure 4-3F). However, it should be noted that the average RMS error was 1.3%. In general the RMS errors for the lava flows were much better than those of the cone where significant sulfur deposits cover a large portion of the crater. The generally low RMS in the tephra plain may be related to exposed anorthite and augite crystals as opposed to those that are weathered on the lava flows, and also tend to be covered by the glassy rind and hematite/opaque mineral layer. Moreover, the lower RMS in the tephra plain may be the result of significantly less variability in the texture of the surface, compared to the rough a'a flows to the north.

The mineral end-member images were displayed with hematite, anorthite, and glass in red, green, blue, respectively (Figure 4-12). The lava flows, cone, and tephra plain were then overlain as vectors for reference. From this image it is apparent that the anorthite dominates over the glass and hematite in the tephra plain and the southwestern portion of the cone most likely due to wind winnowing of particles along the southeastern flank of the cone and during explosive eruptions. The fumarole covered portions of the cone tend to show a mixture of glass and anorthite, but this is probably a result of a poor model fit due to the lack of a sulfur mineral end-member in the model. However, the end-member images do reveal how the deconvolution approach can be used to relatively date the flows. In general, the older 1923 flow to the far north is dominantly red due to a high quantity of hematite, whereas the relatively recent flows are more blue, enriched in glassy relative to the other end-members. The older flows may be exhibiting some distribution of hematite due to clastic, oxidized material being transported off of the flows and down the slopes. The flows that were emplaced between the 1923 and 1999 exhibit a variety of mixing conditions, but an overall magenta color indicated an approximate equal mix of hematite and glass. This can be seen specifically on the 1957 flow to the far north and 1947-50 flow northeast of the cone. Due to the frequency of the effusive events during a small window of time (~76 years), and the relatively large pixel size of the ASTER TIR instrument, constraining emplacement times in between the oldest and youngest events can be challenging but does appear possible. However, it is important to note that additional variables such as magnetite sorting during emplacement, porosity, permeability, and emplacement temperatures may also be factors in the hematite variability of the surface.

4.6 SUMMARY AND CONCLUSIONS

This study demonstrated that spaceborne image-derived multispectral analyses of relatively-recent glassy basalts from Cerro Negro volcano correlate well with the observed changes in the high-spectral resolution laboratory emissivity data in addition to those reported in Kahle et al., 1988; and Crisp et al., 1990. These results, along with the end-member maps validate the use of ASTER TIR data to map and relatively-date young lava flows based upon their TIR emissivity spectral signatures. However, there was poor agreement between the laboratory and image derived average compositional trend of the anorthite end-member, most likely as a result of: the relatively large (90 m) footprint of an ASTER TIR pixel compared to the < 1 cm spot size of the spectrometer, as well as the larger error (~10%) associated with the linear deconvolution process of multispectral image data. The weathering rate estimates of the lava flows derived from the ASTER TIR data indicate that the iron oxide constituents of the basaltic flows chemically weather to hematite on/near the surface at a rate of approximately 9 - 20%, whereas the breakdown of glass, whether by devitrification or spalling, occurs at a slower rate of approximately 1 - 9% over 76 years.

The results of this study also show that the automated thermal deconvolution algorithm presented in Rose et al., 2010 is limited in its applicability to volcanoes with low-temperature thermal features such as fumaroles because these temperatures are not large enough to be detected in the SWIR. The thermally mixed pixels were identified here solely based upon their temperature relative to the background in addition to the negative slope observed in their emissivity spectra. It can be inferred based upon this study that the minimum requirement for applying the thermal deconvolution algorithm to ASTER datasets is the presence of a thermally elevated pixel in the TIR data together with a slope of -0.0001.

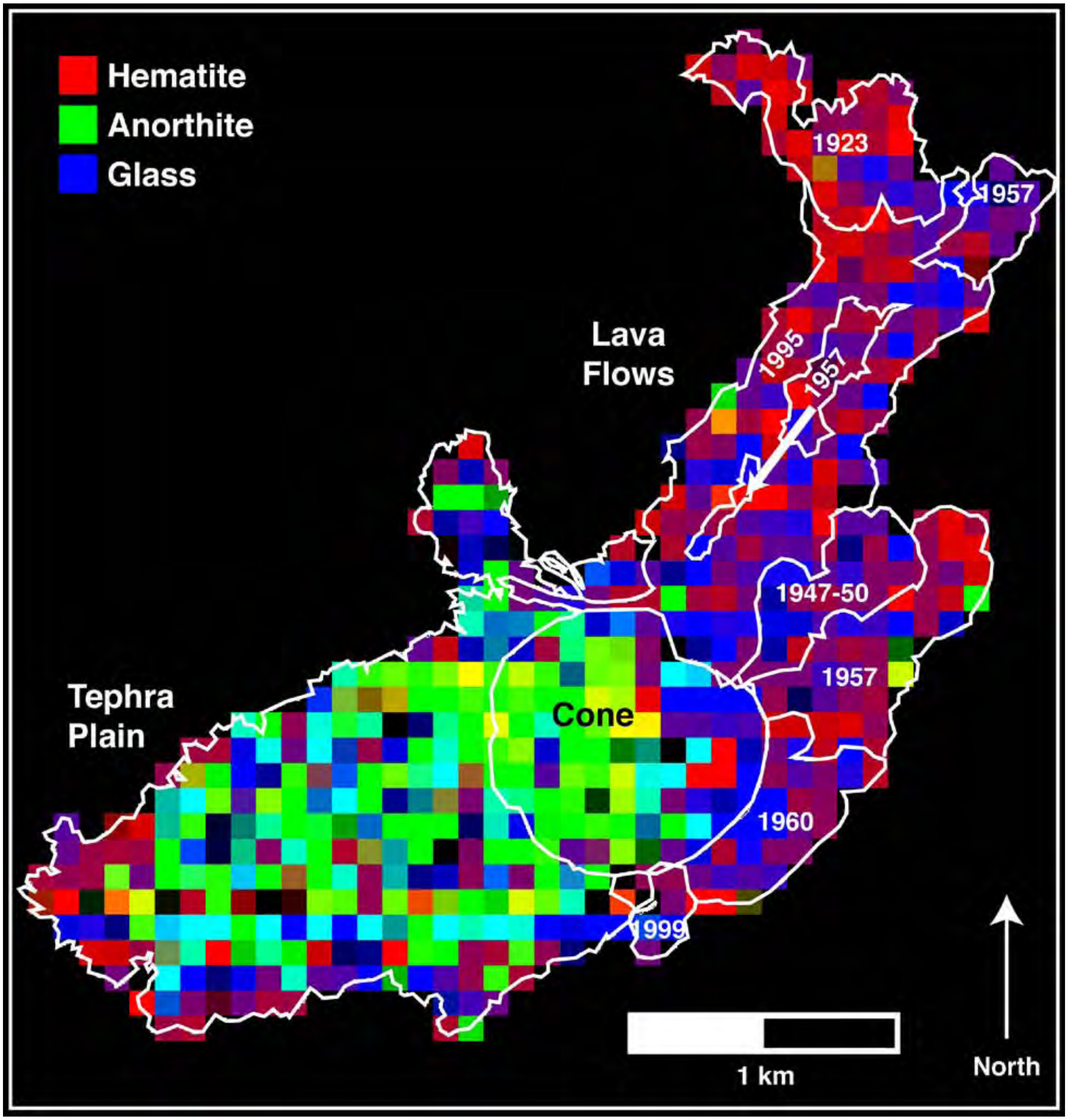

Figure 4-12 Color composite of the end-members hematite, anorthite, and glass in the R, G, B, respectively. The lava flows can be grouped into three general age classes: oldest, intermediate, and young, based on their color appearance.

We have shown for the first time that spaceborne multispectral TIR data can be used to efficiently map and relatively date young basaltic lava flows in a similar climate to that of Hawaii and Sicily. Although constraining flows very close in age remains a challenge, these flows on Cerro Negro can be characterized into three general age groups: oldest, intermediate and youngest. The results of this investigation reveal that the original techniques developed by Kahle et al., 1988 can be applied to new sensors in order to study volcanoes in a more cost and time efficient manner, and also lend support for applications to future sensors.

5.0 THERMAL AND COMPOSITIONAL ANALYSES OF THE 2005 AND 2007 ERUPTIONS OF KLIUCHEVSKOI VOLCANO

5.1 INTRODUCTION

5.1.1 Kliuchevskoi Volcano

Kliuchevskoi volcano is located on the Kamchatka peninsula of far-eastern Russia, and is the largest stratovolcano in Eurasia. The volcano, lying within the Central Kamchatka Depression, is a member of the Klyuchevskaya group, which also includes nearby Kamen and Bezymianny volcanoes (Figure 5-1). Since its formation approximately 6000 years ago, a nearly perfect symmetrical edifice approximately 4835 m tall has formed. During the last 3000 years, activity has been concentrated within the 750 m wide summit crater, resulting in frequent modifications in its size and shape (Smithsonian GVP, 2008). Historically, eruptions have originated from the summit crater, but have also included explosive and effusive eruptions from the flanks and its 80 parasitic cinder cones. Kliuchevskoi is known for producing large quantities of calc-alkaline high-magnesian basalt to basaltic andesite each year (6.0 x 10^7 tons; Fedotov and Masurenkov, 1991), that commonly reach temperatures above 1000 ºC (Ozerov, 1997). The most recent eruptive activity included strombolian explosions within the main summit crater, effusive lava flows from the summit and down the flanks, and occasional subplinian explosions producing large ash plumes >12 km above sea level.

Because of its eruption frequency of once every 1 to 2 years and its common production of expansive ash plumes, Kliuchevskoi is an important target for volcano monitoring in the north Pacific. As a result, the Alaska Volcano Observatory (AVO), in conjunction with the Kamchatka Volcano Emergency Response Team (KVERT), and the United States Geological Survey (USGS) have developed an Urgent Request Protocol (URP) System for the Advanced Spaceborne Thermal Emission and Reflection Radiometer (ASTER) to acquire remote emergency observations of natural disasters with minimal turn-around times for data processing.

5.1.2 2007 Kliuchevskoi Eruption

The 2007 eruption of Kliuchevskoi volcano began on 15 February, when a thermal anomaly of elevated pixels appeared in ASTER thermal infrared (TIR) datasets, within the summit crater, and continued for the next 5-months. During this time, the Urgent Request Protocol (URP; discussed in Chapter 2) acquired 21 data acquisitions (manual and automatic requests), many of which were day/night pairs. In mid-April, the summit crater thermal anomaly began to enlarge and change shape as lava erupted down the northern flank of the volcano in an explosive-effusive phase similar to that of the 2005 eruption (Rose and Ramsey, 2009). Unlike the 2005 eruption, the 2007 eruption produced multiple lava flows, forming a radial pattern around the summit crater, commonly saturating the thermal infrared (TIR) and shortwave infrared (SWIR) ASTER subsystems. Saturation of the sensor is noted by the presence of black (recovery) pixels adjacent to the bright thermal anomalies of the lava flows (Figure 5-2). Because Kliuchevskoi is

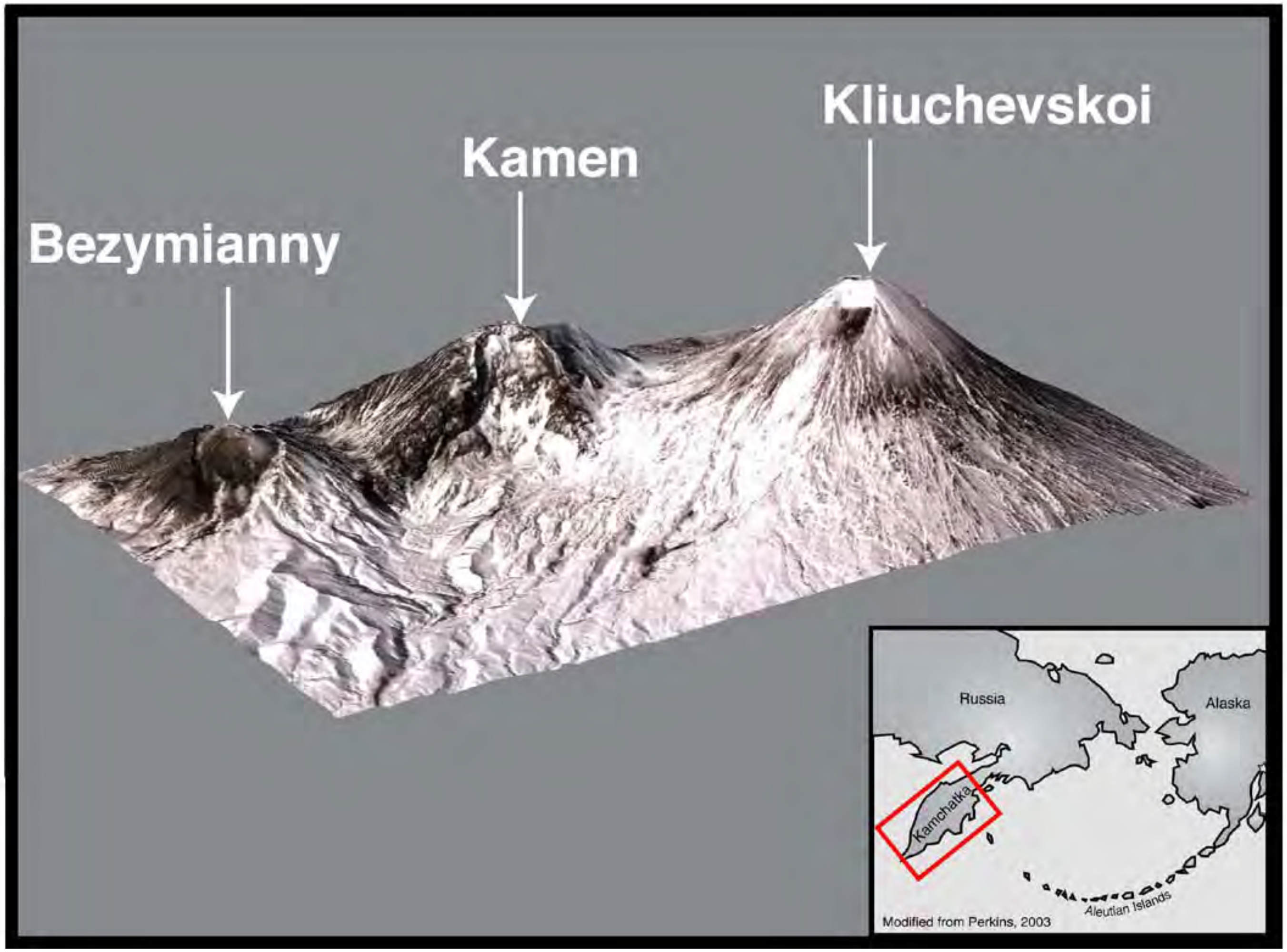

Figure 5-1 A VNIR ASTER image overlain onto a digital elevation (DEM) of Kliuchevskoi volcano and nearby Kamen and Bezymianny volcanoes revealing its relative size and shape with respect to other volcanoes within the Kliuchevskaya group. These volcanoes are located within the Kamchatka peninsula near the junction of the Aleutian Islands and the Kurile Kamchatka volcanic arcs (red box; inset).

covered by snow year-round, the interaction between snow and ice commonly resulted in phreatic explosions and associated steam plumes along the flanks of the volcano. Moreover, strombolian to vulcanian activity in the summit crater often produces thick gas-steam-ash plumes resulting in ash fall in the nearby towns of Kliuchi and Kozyrevsk, and extending 1000's of kilometers into the north Pacific and beyond. At the beginning of June, the URP acquisition frequency decreased when activity diminished, but monitoring of the volcano continued via the Kamchatka Volcanic Emergency Response Team (KVERT), Alaska Volcano Observatory (AVO), and the University of Pittsburgh's Image Visualization and Infrared Spectroscopy (IVIS) Laboratory. A time series of the activity captured by ASTER can be found in Figure 5-2, and a correlative summary of the KVERT information releases is shown in Table 5-1. The explosive activity within the main summit crater began to subside at the end of June, and subsequent cooling of the surface flows ensued. By mid-October KVERT reduced the color code of concern back to green as the seismicity and tremor returned to background levels (Table 5-1).

5.1.3 Goals of the Study

Kliuchevskoi provides a tremendous opportunity for studying active volcanism because of the eruption frequency and high-latitude of the volcano, which allows for frequent observations by polar orbiting sensors such as ASTER. Furthermore, Kliuchevskoi is known for incandescent lava flows during its eruptions, thereby providing excellent test material for remote sensing thermal studies across multiple wavelength regions such as the TIR, SWIR, and visible near infrared (VNIR) (Rose and Ramsey, 2009). The goals of this investigation are to: 1) test the thermal deconvolution algorithm on steep terrain (Rose et al., in review-a) where these

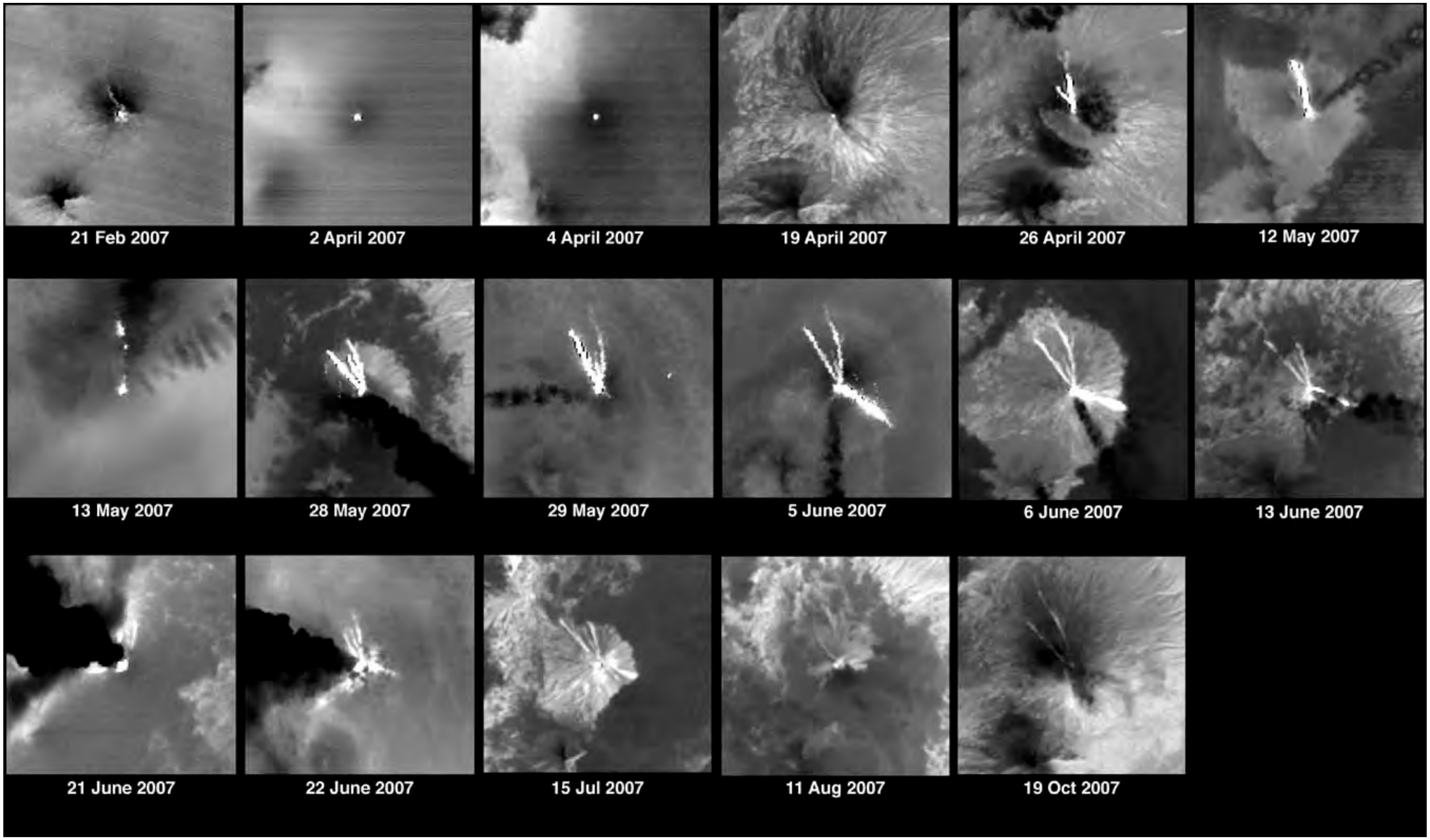

Figure 5-2 Time-series of ASTER TIR data of the 2007 eruption of Kliuchevskoi volcano, Russia. Data span from the initial thermal anomaly detected on 21 February to the cooling of the lava flow barely visible on 19 October. Each image is ~10 km wide and rotated with north to the top.

Table 5-1 Summary of KVERT information releases throughout the 2007 eruption (KVERT, 2010). ASTER acquisition dates are listed and the associated observations were released within several days. The level of concern color code is included to show relationships between the eruption characteristics and hazard level.

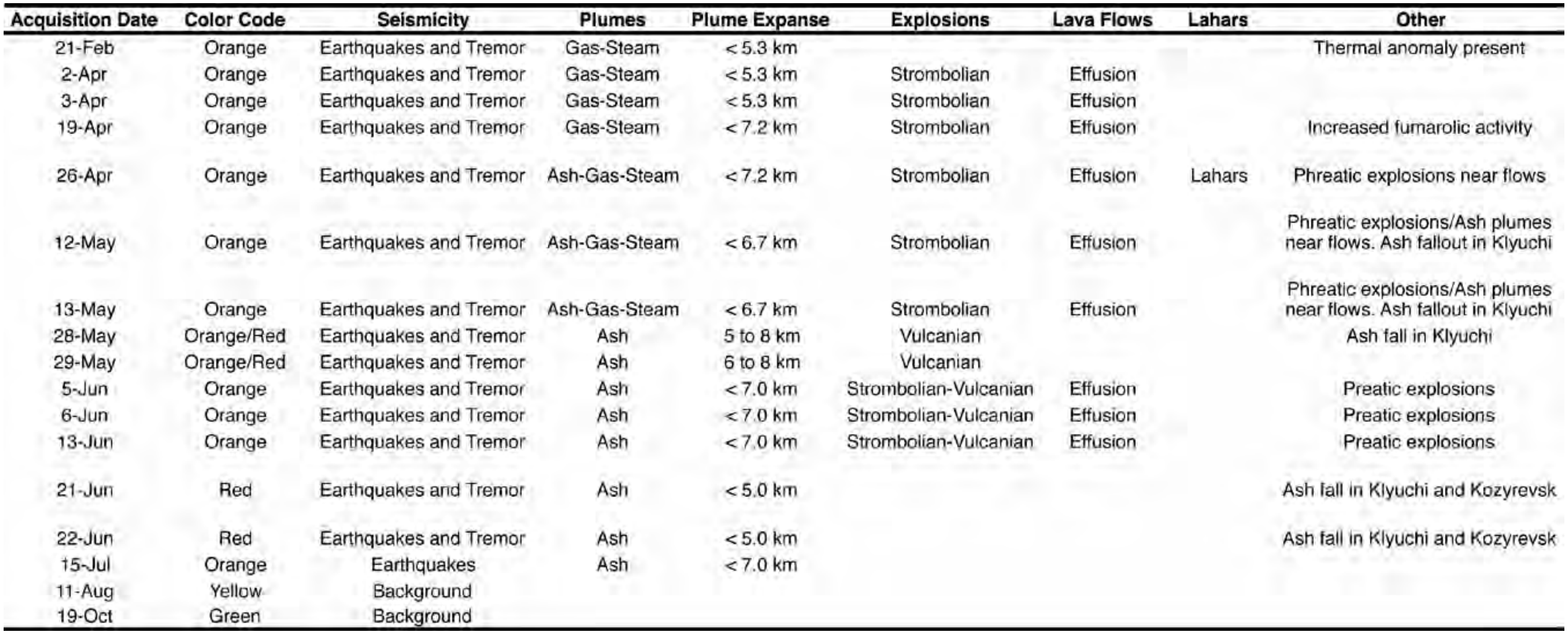

Acquisition Date	Color Code	Seismicity	Plumes	Plume Expanse	Explosions	Lava Flows	Lahars	Other
21-Feb	Orange	Earthquakes and Tremor	Gas-Steam	< 5.3 km				Thermal anomaly present
2-Apr	Orange	Earthquakes and Tremor	Gas-Steam	< 5.3 km	Strombolian	Effusion		
3-Apr	Orange	Earthquakes and Tremor	Gas-Steam	< 5.3 km	Strombolian	Effusion		
19-Apr	Orange	Earthquakes and Tremor	Gas-Steam	< 7.2 km	Strombolian	Effusion		Increased fumarolic activity
26-Apr	Orange	Earthquakes and Tremor	Ash-Gas-Steam	< 7.2 km	Strombolian	Effusion	Lahars	Phreatic explosions near flows
12-May	Orange	Earthquakes and Tremor	Ash-Gas-Steam	< 6.7 km	Strombolian	Effusion		Phreatic explosions/Ash plumes near flows. Ash fallout in Klyuchi
13-May	Orange	Earthquakes and Tremor	Ash-Gas-Steam	< 6.7 km	Strombolian	Effusion		Phreatic explosions/Ash plumes near flows. Ash fallout in Klyuchi
28-May	Orange/Red	Earthquakes and Tremor	Ash	5 to 8 km	Vulcanian			Ash fall in Klyuchi
29-May	Orange/Red	Earthquakes and Tremor	Ash	6 to 8 km	Vulcanian			
5-Jun	Orange	Earthquakes and Tremor	Ash	< 7.0 km	Strombolian-Vulcanian	Effusion		Preatic explosions
6-Jun	Orange	Earthquakes and Tremor	Ash	< 7.0 km	Strombolian-Vulcanian	Effusion		Preatic explosions
13-Jun	Orange	Earthquakes and Tremor	Ash	< 7.0 km	Strombolian-Vulcanian	Effusion		Preatic explosions
21-Jun	Red	Earthquakes and Tremor	Ash	< 5.0 km				Ash fall in Klyuchi and Kozyrevsk
22-Jun	Red	Earthquakes and Tremor	Ash	< 5.0 km				Ash fall in Klyuchi and Kozyrevsk
15-Jul	Orange	Earthquakes	Ash	< 7.0 km				
11-Aug	Yellow	Background						
19-Oct	Green	Background						

hot volcanic targets exist; 2) compositionally deconvolve the ASTER TIR pixels associated with the lava flows of the 2005 and 2007 eruptions; and 3) conduct a comparative analysis of the lava flows and eruption mechanisms between these two eruptions.

The thermal deconvolution algorithm (Rose et al., in review-a) was originally tested on the basaltic flows of the 2006 eruption phase of Kilauea. Rose et al., in preparation also applied the thermal deconvolution algorithm to low-temperature thermal anomalies such as the fumarole fields of Cerro Negro volcano in Nicaragua. The temperatures of these thermal sources proved to be to low for applying that technique as shown by the lack of thermal anomalies in the SWIR ASTER datasets. This work applies the algorithm to incandescent flows that reach saturation levels in the SWIR and are located within an area of high relief. Although saturation of the SWIR results in unusable data, the non-saturated adjacent pixels of the lava flows can be used in the deconvolution process to extract compositional and textural information. The results obtained by the study presented here will help to understand how the algorithm reacts to various conditions exhibited by basaltic volcanoes, and where improvements may be needed.

A linear spectral deconvolution algorithm, developed by Ramsey, 1996 and first applied in Ramsey and Christensen, 1998 will be used to extract compositional information of the lava flows produced in the 2005 and 2007 eruptions. As previously mentioned, Kliuchevskoi commonly produces a range in volcanic products including high-magnesian basalt and basaltic andesite. For this reason, compositional analyses are needed to determine the current trends of the volcano and if they are changing in a relatively fast (2 yr) rate. By understanding the compositional trends, a broader picture of the magmatic evolution can be established.

Rose and Ramsey, 2009 identified a new mechanism for lava effusion at Kliuchevskoi in ASTER TIR data as well as hand-held thermal data acquired in the field. Within these datasets, a separation was noted between the hot lava flows and summit crater. This suggested that during the explosive-effusive phase and cooling phase, a breakout point was located within the Krestovsky channel, similar to the mechanism of effusion observed at Pacaya volcano in Guatemala. As noted, the 2007 eruption produced flows on the northwestern, northern, and southeastern flanks, providing an excellent environment for studying the effusion mechanisms at other points surrounding the summit. Again, by comparing the two eruption mechanisms present in 2005 and 2007, this investigation will provide insight into the overall behavior of the volcano and potentially aid in forecasting future eruptive behaviors.

5.2 METHODOLOGY

5.2.1 Field Methods and Sample Collection

Two field campaigns were carried out to Kliuchevskoi volcano in August of 2005 and 2007, shortly after the cessation of the explosive and effusive activity of both eruptions. Thermal images of the summit of Kliuchevskoi were captured by a Forward Looking Infrared (FLIR) Camera from multiple helicopter over flights. The FLIR ThermaCAM^{TM} S40 camera has a 24 x 18 degree instantaneous field of view (IFOV) and a spatial resolution of approximately 1.3 mrad. It is capable of detecting thermal features with a precision of 0.1 ºC along the 7.5 to 13 µm region, with multiple gain setting options in order to prevent saturation. The FLIR images were used to target sampling locations based upon their thermally elevated signature. However, due to poor field conditions and minimal access to the lava flows during the 2007 campaign, sample collection was not possible. Therefore, only three representative lava flow samples were collected from the 2005 flows for laboratory TIR spectral analyses, which were used to validate results obtained in the ASTER datasets for both eruptions.

5.2.2 TIR Laboratory Spectral Analysis and Linear Deconvolution

Field campaigns to Kliuchevskoi volcano were conducted in August of 2005, and 2007, shortly after the cessation of the explosive and effusive activity of the eruptions. Images captured by a Forward Looking Infrared (FLIR) Camera from helicopter over flights revealed the presence of the 2005 and 2007 lava flows on the flanks of the volcano, as shown by still-elevated temperatures. These images were used to target sampling locations. However, due to poor field conditions (rain and wind) and minimal access to the lava flows during the 2007 campaign, sample collection was not possible. Therefore, only three representative lava flow samples were collected only from the 2005 flows for laboratory TIR spectral analyses, which were used to validate results obtained in the ASTER datasets for both eruptions. Lava flow compositions were determined by collecting calibrated, absolute TIR emissivity spectra of the three samples, using a Nicolet Nexus 670 FTIR spectrometer (described in detail in Chapter 4) and the calibration approach outlined in Ruff et al., (1997). During the analysis of the sample TIR spectra, the environmental temperature and down welling radiance remains relatively stable and therefore the sample remains thermally homogeneous. Basalts by nature tend to have an inherent emissivity spectral slope between the 8 to 12 µm region, due to a large absorption feature at these wavelengths. The slope can change based upon the density, glass content, and/or micron-scale roughness of the surface analyzed. Therefore, the average slope of the three samples was determined and later used in the thermal deconvolution process.

The linear spectral deconvolution algorithm (Ramsey, 1996; Ramsey and Christensen, 1998) was applied to the laboratory spectra of the surfaces of each of the three samples. Spectral mineral end-members from the Arizona State University Spectral Library (Christensen, 2000) were chosen based upon the most abundant minerals from a suite of Kliuchevskoi lavas, reported in Ozerov, 2000. A spectrum of a basaltic glass, collected and immediately quenched from an active Hawaiian flow, was also included as some of the laboratory spectra displayed morphologies consistent with glass (Lee et al., 2010; Ramsey and Fink, 1997). The inclusion of glass accounts for the glassy component of the samples as well as the interaction between lava and ice at Kliuchevskoi.

5.2.3 Image Acquisition and Data Processing

Throughout the 2005 and 2007 eruptions, the automated urgent request protocol (URP; described in Rose and Ramsey, 2009) was tasked in acquiring ASTER imagery of the events. As a result of these requests, 27 scenes have been used to document the eruptive behavior of Kliuchevskoi in great detail during these two events (Rose and Ramsey, 2009; Rose and Ramsey, in review-b; Rose and Ramsey, 2008). For this investigation, 3 ASTER datasets acquired on 8 Feb, 2005; 28 May, 2007; and 6 June, 2007 were used to represent climactic effusive activity in both eruptions. Due to the numerous flows produced during the 2007 eruptions, two scenes were required in order to compare how the deconvolution algorithms performed on the cooling flows to the northwest, and the active hot flows on the southeast flank. The 2005 flows were all concentrated within the Krestovsky channel on the northwestern flank, thereby requiring only one dataset.

ASTER data are available and distributed though the National Aeronautics and Space Administration (NASA) and the Warehouse Inventory Search Tool (WIST). Various standard data products are generated in a hierarchical data format (HDF), ranging from Level 0 (unprocessed data at full resolution) to Level L1B (geometrically and radiometrically calibrated radiance-at-sensor). Higher-level data products such as atmospherically-corrected Level 2 (L2; Abrams, 2000) products can also be generated. The at-ground TIR radiance (AST_09T), SWIR at-ground radiance corrected for crosstalk errors (AST_09XT), and surface emissivity (AST_05) products were used to thermally deconvolve and compositionally deconvolve pixels within the three image datasets. The reasons for choosing these data products include: 1) The L2 AST_08 surface kinetic temperature product was not used in this study because the calculations involved in the deconvolution algorithm modeling are based upon blackbody radiance/intensities and the associated temperatures at particular wavelengths. Kinetic temperatures are wavelength independent and therefore do not provide the required radiance values for blackbodies exhibiting non-isothermal conditions. 2) The AST_05 products are corrected for down-welling radiance and therefore preserve the spectral contrast in the pixel spectra. The accuracy of these L2 data products range from ± 1% for the AST_09T to ± 5% for the AST_05 product. The absolute accuracy for the crosstalk corrected SWIR AST_09XT product has not been documented and its validity has only been established for scenes with low-temperature contrasts (e.g. coastlines; Iwasaki and Tanooka, 2005).

5.2.4 Thermal Deconvolution of ASTER Spectra

Pixels composed of non-isothermal surfaces within each of the three ASTER scenes were characterized based upon their pixel-integrated brightness temperatures and the negative slope present in their derived emissivity spectra. As previously stated, basalt spectra tend to have an inherent negative slope toward longer wavelengths, and this phenomenon must be taken into account during the process. Therefore, the spectral slopes of the Kliuchevskoi basalts were measured in the laboratory data and ranged from -0.0087 to -0.0196 between the wavelengths of 8 and 12 µm, which is the range of the TIR subsystem of ASTER. For comparison, the average slope of isothermal basalts on Kliuchevskoi was obtained using 40 non-thermally elevated ASTER pixels, which produced a value of -0.0069. In order to ensure that all thermally mixed basalt pixels would be identified in the deconvolution process, an average was used that lies between the smallest laboratory value and the ASTER slope value.. Therefore, pixels exhibiting slopes less than -0.0077 and 10 ºK above background levels were considered thermally mixed. In order to determine if these pixels were indeed mixed, the higher spatial resolution AST_09XT SWIR data (30 m) was examined and used in the algorithm. The results were then assessed for radiance distributions. Pixels recorded in the previous step, and their associated SWIR pixels that did not exceed saturation levels (> 73.3 W/m^2/µm/sr), were identified as truly mixed. An average hot and cool temperature for each 90 m area were calculated from the nine SWIR radiance values using the Planck Equation (Eq. 1; Rose et al., in review-a) and then mixed according to the fraction of the 90 m area they occupied, to create a hypothetical thermally-mixed Planck curve. The rationale for this method stems from the assumption that each 90 m TIR pixel of ASTER is thermally homogeneous. By calculating a ratio of the original radiance of each thermally mixed TIR pixel to the newly determined mixed radiance at the same wavelength, this method can now provide an accurate means for deriving emissivity values, and spectra, without the affects of heterogeneous thermal conditions of the surface. Overall, this correction in emissivity spectra should aid in providing more accurate compositional analyses of the ASTER data.

5.2.5 Linear Deconvolution of ASTER Spectra

The linear deconvolution of ASTER spectra was conducted in order to determine the compositional variability within the lava flows. This is crucial in understanding how the lava flows are changing between and during eruptions. Once the emissivity correction process was completed, the L2 TIR emissivity data from the 8 Feb, 2005; 28 May, 2007; and 6 Jun, 2007 over flights were linearly deconvolved using the four most abundant end-members determined from the laboratory analyses in addition to a blackbody end-member that was used as a proxy for micron-scale surface roughness (Carter, 2009). Compared to the laboratory spectrometer analyses, the number of end-members here was limited to the spectral resolution of the ASTER instrument (5 bands; Ramsey, 1998). For the resulting images, the outlines of each lava flow were overlaid on the ASTER emissivity images and regions of interest were created from each flow. An average composition for the lava flows was calculated based upon the end-member statistics for the thermally deconvolved linearly unmixed data in addition to the linearly unmixed data without the thermal deconvolution correction. Overall, the wide range of thermal conditions of the lava flows present at Kliuchevskoi, ranging from high-temperature active effusive flows, cooling flows, and even lava flow breakouts on the cooled flows, proved to be a challenging setting to test these deconvolution approaches to determine lava flow composition for extremely hot targets. Previous studies (Rose et al., in review-a; Rose et al., in preparation) concentrated on less-complex areas that lacked incandescent lava flows and had limited thermal intensities (e.g., no saturation in the SWIR).

5.3 RESULTS

5.3.1 Linear Deconvolution of Laboratory Spectra

Three hand samples of basalt were analyzed with the laboratory spectrometer in order to provide a comparison with the spectral results derived from analyses of data from the ASTER instrument. Sample Klyuch-01-05: A dense, micro-crystalline rock containing plagioclase phenocrysts, <1 mm and a rough breadcrust-type surface texture. Glassy shards <1 mm in diameter are also visible on the surface, although they are sparse. The surface is red to tan, suggesting iron oxidation. Sample Klyuch-02-05: A basalt rock with an amalgamation of smooth, dense and rough, breadcrust textures on the surface. Sporadically located plagioclase crystals within the matrix are < 1 mm in diameter, whereas a glassy coating can be observed over much of the sample's surface in conjunction with a tan alteration product. Sample Klyuch-04-05: A vesicular (vesicles 1 to 7 mm in diameter) basalt exhibiting numerous 1 mm plagioclase phenocrysts and occasional olivine crystals up to 1.5 mm in diameter. Glassy shards are also present along the surface in addition to a slight coating of tan-colored alteration product(s).

Emissivity spectra of the sample surfaces for the 2005 lava flow were acquired and plotted (Figure 5-3). The emissivity spectra reveal prominent spectral absorption features at 9.7 µm and 20.4 to 25 µm. The spectral signatures of samples Klyuch-01-05 and Klyuch-04-05 appear to be very similar with respect to the feature shapes throughout the wavelength region. Sample Klyuch-02-05, however, appears to have a significantly different spectral shape than the other two samples, whereby the primary absorption feature at 9.7 µm is much narrower and deeper. Moreover, the deepest absorption feature at 21.5 µm for sample Klyuch-02-05 is muted in sample Klyuch-04-05 and only slightly recognizable in sample Klyuch-01-05.

The spectral linear deconvolution algorithm was applied to the laboratory emissivity spectra from each sample, using the most abundant mineral end-members of previous Kliuchevskoi eruptions, listed in Ozerov, 1997. In addition, the spectral deconvolution process was conducted many times in order to determine which clay and alteration minerals were most abundant. The RMS errors, or measure of how well each modeled end-member fits the sample spectra, associated with these deconvolution results range from a best fit of 0.21% to a worst fit of 0.79%. In general, an RMS of < 1.0% indicates a relatively good fit (Ramsey and Christensen, 1998). The linear deconvolution results for all three samples, and the associated RMS values are shown in Figure 5-3 and Table 5-2. Generally, all three samples show a good model fit for the absorption feature at 9.7 µm. However, toward longer wavelengths a slight misfit between the modeled and sample spectra becomes apparent between 19 and 25 µm.

5.3.2 Thermal Deconvolution

The thermal deconvolution process was applied to the ASTER datasets listed in Table 5-3, in order to determine if the lava flows were thermally mixed, and therefore affecting the associated TIR emissivity spectra. Inspection of the SWIR datasets reveals numerous saturated pixels located within the saturated TIR pixel locations and validated the geo-location of the datasets for each acquisition, whereby saturated SWIR pixels were geo-located to those of the TIR data. An average background temperature was calculated for each TIR scene using a 20 x 20 pixel area, and resulted in temperatures of -19.9 ºC for 8 Feb, 2005; 2.4 ºC for 28 May, 2007; and 3.63 ºC for 6 June, 2007. Pixel integrated brightness temperatures above these values (in combination with an emissivity slope < -0.0077) were considered potentially thermally-heterogeneous,

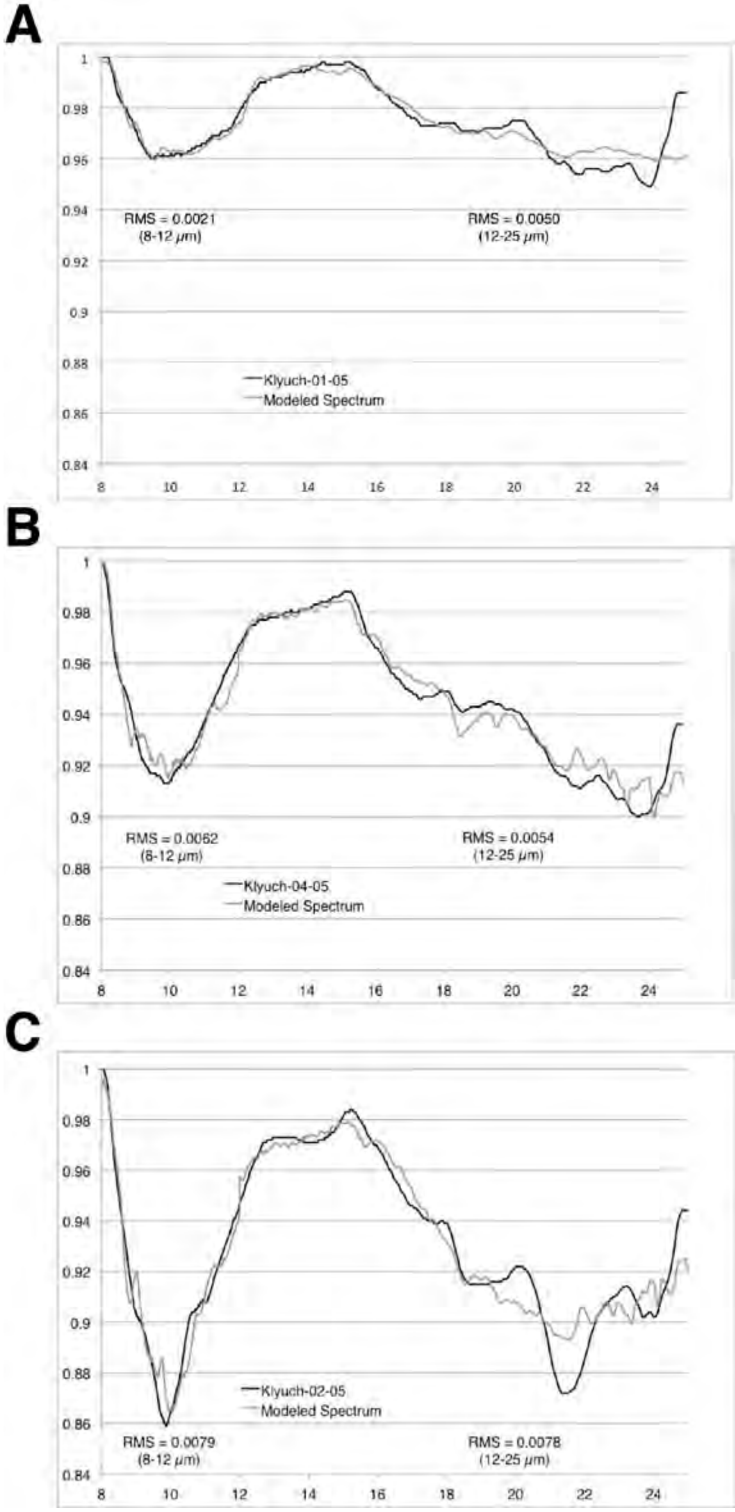

Figure 5-3 Original and modeled results of the linear deconvolution of laboratory samples collected from the 2005 Kliuchevskoi lava flows. The deconvolution process was conducted on each spectrum for the 8-12 and 12-25 μm wavelength regions and thereby results in two RMS values for each modeled spectrum. Mineral end-members were initially chosen by the most abundant minerals reported in Ozerov, 1997.

Table 5-2 End-member results for the linear deconvolution of the laboratory derived emissivity spectra (Figure 5-3)

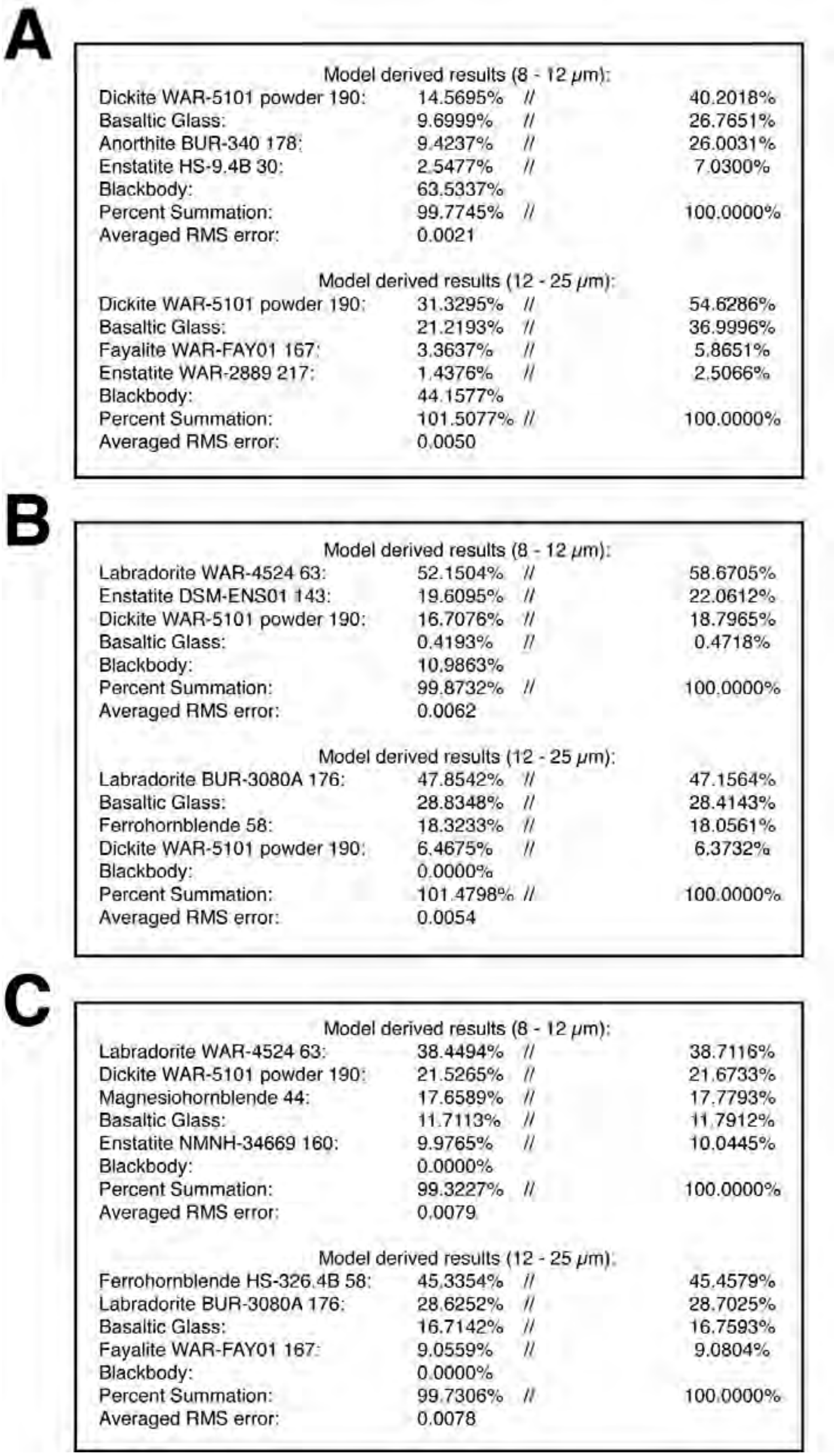

A

```
                          Model derived results (8 - 12 μm):
Dickite WAR-5101 powder 190:      14.5695%   //              40.2018%
Basaltic Glass:                   9.6999%    //              26.7651%
Anorthite BUR-340 178:            9.4237%    //              26.0031%
Enstatite HS-9.4B 30:             2.5477%    //               7.0300%
Blackbody:                        63.5337%
Percent Summation:                99.7745%   //             100.0000%
Averaged RMS error:               0.0021

                          Model derived results (12 - 25 μm):
Dickite WAR-5101 powder 190:      31.3295%   //              54.6286%
Basaltic Glass:                   21.2193%   //              36.9996%
Fayalite WAR-FAY01 167:           3.3637%    //               5.8651%
Enstatite WAR-2889 217:           1.4376%    //               2.5066%
Blackbody:                        44.1577%
Percent Summation:                101.5077%  //             100.0000%
Averaged RMS error:               0.0050
```

B

```
                          Model derived results (8 - 12 μm):
Labradorite WAR-4524 63:          52.1504%   //              58.6705%
Enstatite DSM-ENS01 143:          19.6095%   //              22.0612%
Dickite WAR-5101 powder 190:      16.7076%   //              18.7965%
Basaltic Glass:                   0.4193%    //               0.4718%
Blackbody:                        10.9863%
Percent Summation:                99.8732%   //             100.0000%
Averaged RMS error:               0.0062

                          Model derived results (12 - 25 μm):
Labradorite BUR-3080A 176:        47.8542%   //              47.1564%
Basaltic Glass:                   28.8348%   //              28.4143%
Ferrohornblende 58:               18.3233%   //              18.0561%
Dickite WAR-5101 powder 190:      6.4675%    //               6.3732%
Blackbody:                        0.0000%
Percent Summation:                101.4798%  //             100.0000%
Averaged RMS error:               0.0054
```

C

```
                          Model derived results (8 - 12 μm):
Labradorite WAR-4524 63:          38.4494%   //              38.7116%
Dickite WAR-5101 powder 190:      21.5265%   //              21.6733%
Magnesiohornblende 44:            17.6589%   //              17.7793%
Basaltic Glass:                   11.7113%   //              11.7912%
Enstatite NMNH-34669 160:         9.9765%    //              10.0445%
Blackbody:                        0.0000%
Percent Summation:                99.3227%   //             100.0000%
Averaged RMS error:               0.0079

                          Model derived results (12 - 25 μm):
Ferrohornblende HS-326.4B 58:     45.3354%   //              45.4579%
Labradorite BUR-3080A 176:        28.6252%   //              28.7025%
Basaltic Glass:                   16.7142%   //              16.7593%
Fayalite WAR-FAY01 167:           9.0559%    //               9.0804%
Blackbody:                        0.0000%
Percent Summation:                99.7306%   //             100.0000%
Averaged RMS error:               0.0078
```

requiring the input of the SWIR radiance data in order to identify the truly thermally mixed pixels. Although the saturated SWIR pixels could not be used for the thermal deconvolution portion of the study, they were still valuable in the calculation of the erupted volumes (Table 5-4) in both the 2005 and 2007 eruptions (Rose and Ramsey, 2008), as it was assumed that these saturated pixels record active lava. The 2007 eruption produced multiple flows on various flanks of the volcano. However, that eruption produced 23% less material than in 2005.

Table 5-3 Summary of the ASTER scenes used for this study. Mode: Full = VNIR/SWIR/TIR. Level 2 (L2) product: AST_09T = ASTER TIR surface radiance, AST_09XT = ASTER SWIR surface radiance (cross-talk-corrected).

Acquisition Date	Day/Night Observation	Data Mode	SWIR Gain	Level 1A Granule ID	L2 Products Used
8-Feb-05	Day	Full	Low 2	SC:AST_L1A.003:2027751856	AST_05; AST_09T; AST_09XT
28-May-07	Day	Full	Low 2	SC:AST_L1A.003:2043462012	AST_05; AST_09T; AST_09XT
6-Jun-07	Day	Full	Low 2	SC:AST_L1A.003:2043591979	AST_05; AST_09T; AST_09XT

Table 5-4 A summary of calculated lava volumes produced during the explosive-effusive phases of the 2005 and 2007 eruptions.

	23-Jan	**8-Feb**	**12-Mar**	NA	NA	**Total Volume**
Erupted Volume (km^3) 2005	0.01271	0.0095	0.0013	0	0	0.0235 km^3
Erupted Volume (km^3) 2007	0.0001	0.0031	0.0044	0.0045	0.0061	0.0182 km^3
	18-Mar	**26-Apr**	**12-May**	**28-May**	**6-Jun**	**Total Volume**

Forty-one saturated TIR pixels were identified in the 8 Feb, 2005 dataset, and excluded from the thermal deconvolution process. However, 149 TIR pixels within the summit crater and the lava flows within the northwest Krestovsky channel were thermally anomalous. Out of those, only 35 pixels were corrected for their negative emissivity slopes. The 28 May, 2007 dataset yielded 67 saturated TIR pixels, and 152 pixels that were thermally anomalous, located along the lava flows, and within the summit crater. In total, 115 TIR pixels were thermally deconvolved and their emissivity spectra corrected. Finally, the 6 June, 2007 data exhibited 68 saturated TIR pixels, and 441 pixels that were 10 ºC above background. Out of these, 168 pixels were corrected.

The thermal deconvolution algorithm produced three types of corrected emissivity spectra (Figure 5-4). In the first class, the original spectral shapes were preserved, shifted upward in the longer wavelengths, and produced acceptable emissivity values ($0.70 < \varepsilon < 1.0$; Prabhakara and Dalu, 1976; Gillespie et al., 1998). Pixels showing this type of behavior appear to be located along the lateral margins of the active flows, away from the summit, and not within the areas of the associated gas-steam plumes. In some circumstances (Figure 5-4B) the spectral shapes were preserved, but the longer wavelengths were shifted significantly upward, which imposed a positive slope on the emissivity spectra. This result also produced emissivity values that were anomalously low (0.4 or less). Pixels exhibiting this result were generally located along the active flows and more proximal to the hotter portions up-flow from the previous pixels described in the first outcome. Lastly, the corrected pixels that did not exhibit these scenarios fell within the class shown in Figure 5-4C. In this situation, the original spectral shape was not preserved during the correction process, the longer wavelengths were shifted significantly up with respect to the shorter wavelengths, and emissivity values were anomalously low. Notably, these types of emissivity spectra were present in the pixels located within areas affected by the gas-steam plumes of the summit crater and higher elevations of the lava flows where temperatures were higher.

5.3.3 Linear Un-mixing of ASTER Data

In order to assess the affect of the three resulting scenarios of the thermal deconvolution algorithm described above, the linear spectral un-mixing was performed on the non-thermally and thermally deconvolved datasets using the most abundant end-members identified in the laboratory spectral un-mixing results (Table 5-2). The 8 February, 2005 results reveal a significant difference in the quantity of glass and labradorite in the original and thermally deconvolved data (Table 5-5). The enstatite and dickite end-members fall at or within the error of the linear un-mixing process and do not fluctuate regardless of the changes produced during the thermal correction process. However, the thermally deconvolved data yield a lower end-member total of 94.3% (5.7% could not be modeled by the end-members chosen) and much higher RMS error of 109%, compared to the original end-member total of 99.9% and an RMS of 16%.

A similar trend was also observed in the 28 May 2007 results whereby the glass and labradorite values changed significantly. Before applying the thermal deconvolution algorithm, the linear deconvolution algorithm resulted in the glass end-member as the primary component of the lava flows, and enstatite as the secondary end-member. However, the thermally corrected data resulted in no glass present on the lava flows and the primary end-member being identified as labradorite; enstatite decreased almost entirely between the original and thermally corrected results (Table 5-5). Again, the thermally deconvolved data produced a lower end-member total of 98.2% and a higher RMS error of 120%, whereas the original data produced an end-member total of 100.0% and an RMS of 14.3%.

The primary and secondary end-members (glass and enstatite) disappeared in the 6 June,

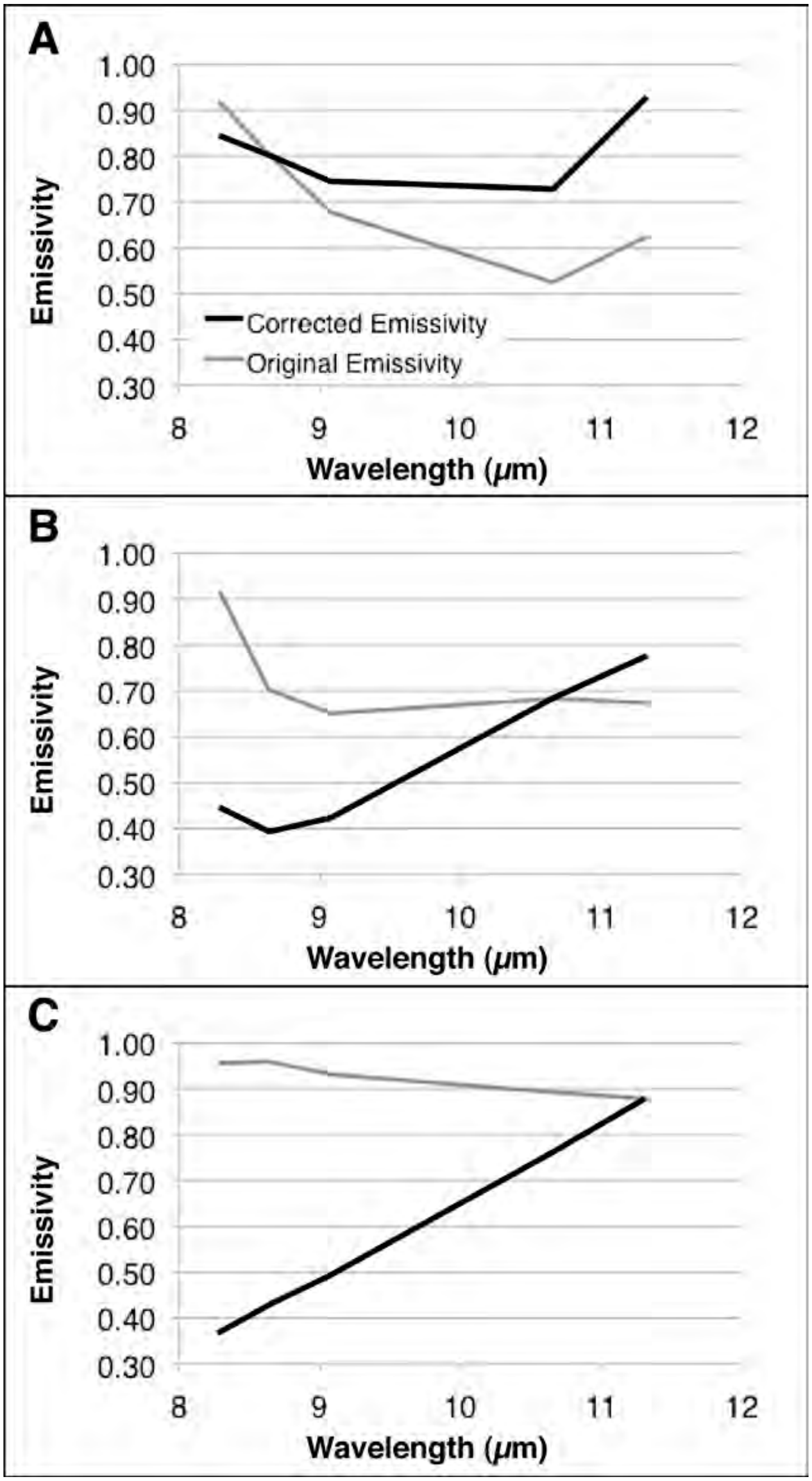

Figure 5-4 Results of the thermal deconvolution algorithm applied to the ASTER data of the 2005 and 2007 eruptions. Three general outcomes were produced: A) the corrected emissivity values were well within reasonable values (expected) B) moderately-high positive slope and moderately-low emissivity values in the corrected spectra C) significantly-large positive slope with minimized and/or eliminated spectral features.

Table 5-5 The average composition of each lava flow derived from the ASTER TIR linear un-mixing and thermal deconvolution results.

Endmembers	8-Feb-05		28-May-07		6-Jun-07	
	Original ASTER Composition (%)	Thermally Deconvolved ASTER Composition (%)	Original ASTER Composition (%)	Thermally Deconvolved ASTER Composition (%)	Original ASTER Composition (%)	Thermally Deconvolved ASTER Composition (%)
Glass	80.5	0.0	58.1	0.0	52.5	0.0
Labradorite	2.3	87.5	12.3	94.2	17.2	97.3
Enstatite	15.8	6.1	21.9	0.2	18.4	0.0
Dickite	1.3	0.7	7.7	3.8	11.9	1.5
Total	99.9	94.3	100.0	98.2	100.0	98.8
RMS	0.1600	1.0939	0.1430	1.2000	0.1270	1.4104

2007 datasets from the original and thermally deconvolved results, respectively. As observed in the results of all of the datasets, dickite fell to within the error of the linear un-mixing process and labradorite was the dominant end-member in the thermally deconvolved results. Notably, the labradorite end-member peaked in the thermally deconvolved data where compared to the other acquisition results. The thermally deconvolved dataset produced the highest RMS error for each of the acquisitions, with a value of 141.0%, even though the total of end-members was the highest of the three (98.8%). Conversely, the original data for 6 June produced the lowest overall RMS of 12.7%.

Based upon the compositions extracted by the linear and thermal deconvolutions on the three ASTER datasets used in this study, the lavas have become enriched in labradorite (~15%) and enstatite (~6%) since 2005 (Table 5-5). This is evident in the original and thermally deconvolved datasets. Conversely, the quantity of glass has decreased by almost 30% in the original data, but remains obscured in the thermally deconvolved data. Although the dickite end-member is within the margin of error for the linear un-mixing process, the original data shows indications of an increase over time.

5.4 DISCUSSION AND CONCLUSIONS

Preliminary results from the spectral linear deconvolution process reveal a poor fit of the laboratory emissivity spectra using the selected end-members from 12 to 25 µm regardless of the end-members chosen. The main absorption feature at 9.7 µm however, produced a generally good fit to the modeled emissivity spectra. This phenomenon may be due to differential sensitivity with depth as function of wavelength. A general rule of thumb is that the depth of emission is approximately ten time the wavelength and therefore spectral features at 25 microns may be coming from twice the depth as those from 10 microns. For this reason and in order to better-fit the entire spectral range, each laboratory spectra was split in half (8-12 µm and 12-25 µm). Linear deconvolved was performed on each segment independently with the same library end-members. Using this approach, the modeled spectra fit more closely to the original spectra, although the fits were not exact. This may be the result of two possibilities: 1) additional end-members are present in the samples (perhaps at greater depths) that were not selected/available; 2) the analyzed spot may have contained a phenocryst/end-member that was not included within the most abundant minerals listed in Ozerov, 1997 due to a change in lava composition from the those results were reported; there have been 8 eruptions between the time those data were reported and the 2005 eruption.

The thermal deconvolution algorithm was used in this study in order to test its ability to correct emissivity spectra for extremely hot targets such as the Kliuchevskoi lava flows in 2005 and 2007. The results presented here show three types of emissivity correction scenarios. In the first outcome, the spectral shape is preserved and the longer wavelength values were corrected upward thereby producing acceptable and expected emissivity results. However, the natural negative slope associated with isothermal basalts appears to have disappeared altogether, and a slight positive slope has been created (Figure 5-4). This positive slope is also observed in the remaining two outcomes of the thermal deconvolution algorithm. The pixels exhibiting this behavior appear to be located down-slope, near to the toe of the flow as opposed to the summit crater. The correlation between the location and the positive emissivity slope suggests that the thermal deconvolution algorithm is most accurate for slightly cooler pixels, which are not affected by the plume. However, steam plumes produced by lava/snow interactions, along the lateral margins of the lava flows and near the summit, appear to play some a role in the magnitude of the positive slope.

The second outcome produced an over-enhancement of the positive slope with the spectral shape being preserved and the emissivity values being lowered significantly. It should be noted that the original emissivity spectrum shown in Figure 5-4B indicates that the emissivities were already lower than acceptable (< 0.70) before the emissivity corrections were made, suggesting that pre-existing errors were carried through the thermal un-mixing process. The effects of errors associated with the thermal deconvolution algorithm (Rose et al., in review-a) most likely enhanced those original errors. However, the locations of the pixels exhibiting this type of spectral behavior after correction were in areas of the hottest pixels (~27 ºC) and/or adjacent to the saturated TIR pixels, suggesting that the recovery time required for the ASTER TIR detector to equilibrate following an observation of extremely high radiance (and saturation), may take more than the one pixel.

In the last scenario, a loss of the spectral shape, the largest enhancement on the positive slope, and the creation of very low emissivity values (< 0.3) occurred. The original spectra tended to have very minimal contrast, but unlike the previous outcome, the original spectra did have acceptable emissivity values (> 0.7). Pixels that displayed this type of behavior tended to be located within areas adjacent to or within the main ash-gas-steam eruption plume. The general blackbody nature of water vapor may explain this minimal spectral contrast. The steam plume would contain minor quantities of ash or be optically-thin resulting in spectra with very minimal spectral contrast and an absorption feature indicative of a basaltic composition at 9.1 µm.

A positive emissivity slope of the thermally corrected pixel spectra is present if the integrated brightness temperatures are close to saturation and/or where steam plumes are located near the thermally-mixed pixels. Abtahi (2002) showed that molten basaltic lava flows from the 1984 Mauna Loa eruption produce much lower broadband emissivity values (0.55) compared to those of cooler flows (0.85). This result was confirmed by Ramsey (2006) using a FLIR camera and thermocouple measurements of pahoehoe flows from the ongoing eruption of Kilauea. This lends some credence to the resultant ASTER emissivity values that were < 0.7 (Figure 5-4) following the thermal deconvolution process, and for pixels whose original integrated brightness temperatures are close to saturation. An increase in the slope also occurs if the steam plume becomes more concentrated, or optically thick. Although the TIR wavelength region of ASTER is capable of penetrating optically thin plumes, it is likely that the pixels exhibiting this behavior were located over much thicker plumes. Furthermore, ASTER SWIR data are more affected by ground-leaving radiance as well as solar reflected radiance. The datasets used in the study are corrected for this excessive radiance factor using the per-pixel method described in Wooster and Kaneko, 2001. However, based on these results, it appears that there is still excessive radiance remaining in the SWIR corrected pixels. This may be due to the crosstalk radiance that has not been fully accounted for in the crosstalk corrected datasets. The AST_09XT product has been validated for low thermal contrast targets such as bodies of water (cool) vs. adjacent shore temperatures (warm; Iwasaki and Tanooka, 2005), but not for instances where hot features (e.g. lava flows and wildfires) are adjacent to very cold background temperatures (e.g. snow and ice). Based upon the results presented here, it is important that the crosstalk phenomenon be subject to additional analyses in order to determine if the current correction is indeed valid under these circumstances.

Linear deconvolution of ASTER data revealed a decrease in the quantity of glass, and an increase in labradorite before and after the thermal deconvolution algorithm was applied. These results suggest that the thermally corrected pixels may contain high temperature components or active lava flows. The movement of the lava down the significant slopes of the summit region and an extreme temperature differential during interactions with the snow/ice may be causing abrasion and/or removal of the glassy coating due to spalling, fragmentation, and overturning of the flow. Moreover, overturning of the flow may expose material that contains more crystallized lava rather than glass, and explains the significantly higher labradorite quantity in the thermally deconvolved data. A consistent effusion of fresh, hot lava may also inhibit the formation of glass on the surface by providing sufficient heat to slow the cooling/quenching process required for glass formation.

Figure 5-5 shows the areas of the highest concentrations for each of the end-members found on the active lava flows. The uncorrected ASTER datasets resulted in significantly-high percentages of glass on the active flows, whereas the cooling flows had some surface alteration with the presence of clay mineralogy (with the best fit being dickite). Although the slopes of Kliuchevskoi are perpetually covered in snow year round, it seems unlikely for the cooling flows to be dominated by dickite, however. The data indicate that the cooling flows appear more glassy than altered, possibly due to rapid quenching from the cold air temperature and decreased flow velocity (Figure 5-6). The portions of the cooled flows, dominated by dickite are located toward the distal margins of the flows where melt water is most likely to come into contact and facilitate alteration. It should be noted that the results in Figure 5-5G and 5-7G have been stretched relative to the thermally corrected pixels. Therefore the non-corrected pixels maintain the original values shown in Figure 5-5.

Overall, the thermal deconvolution algorithm shows potential for applications to pixels with significantly hot targets. However, future work will be needed in order to assess the true effects of the crosstalk errors on the data and potentially minimize/remove the positive slope commonly observed in the corrected data. Modeling the behavior of emissivity spectra where phase changes occur (Lee et al., 2010) is also critical in determining the applicability of the algorithm to active volcanic areas and potentially wildfires, and quantifying the accuracy of this method. Thin section analyses will also allow for the determination of the most appropriate end-members for these particular samples where applying the linear unmixing process. Collectively, these will provide more accurate results and increase our understanding of flow emplacement using TIR remote sensing at these potentially dangerous volcanoes.

During analyses of the 2005 FLIR thermal data, explained in detail in Rose and Ramsey, 2009, a distinctive discontinuity was observed between the summit crater and northwestern lava flow thermal anomalies. This phenomenon was explained by a breakout point for lava effusion approximately 90 m below the crater rim, most likely as the result of the formation of a lava tube or fractures within the summit region. SWIR and FLIR data acquired during the 2007 eruption also indicate that this process continued as exhibited in Figure 5-7. Airborne FLIR data collected in 2007 reveal that the lava flows and summit crater have remained hot in August of 2007 (several month after the eruption had ceased). However, the separation between the crater and

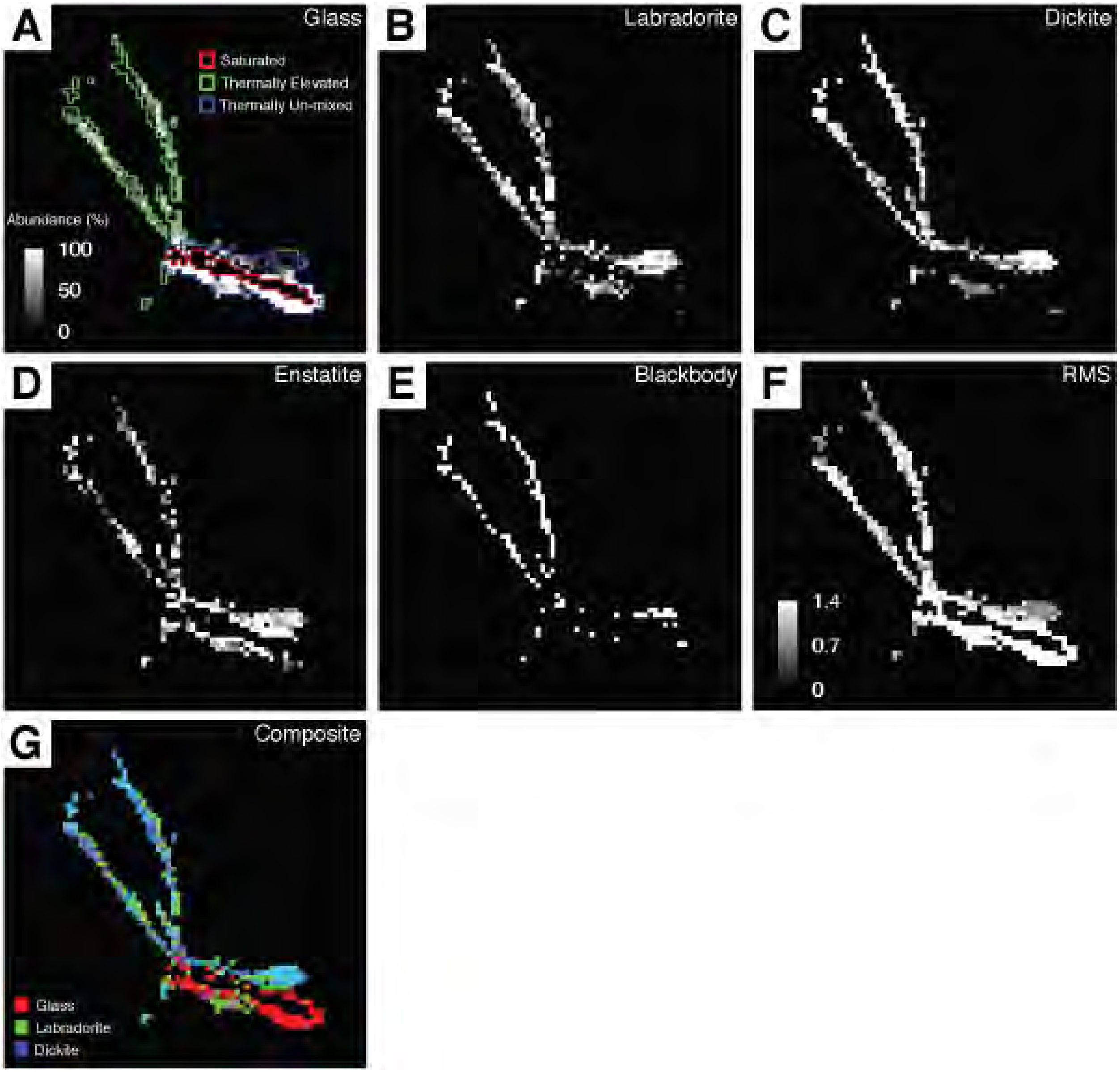

Figure 5-5 Results of the linear un-mixing algorithm applied to the uncorrected 6 June 2007 ASTER TIR data. Each end-member has been stretched according the glass abundance in (A). The blackbody end-member is used as a proxy for surface roughness. The composite image (G) shows the areas of the most abundant mineral end-members of glass, labradorite, and dickite in RGB channels, respectively.

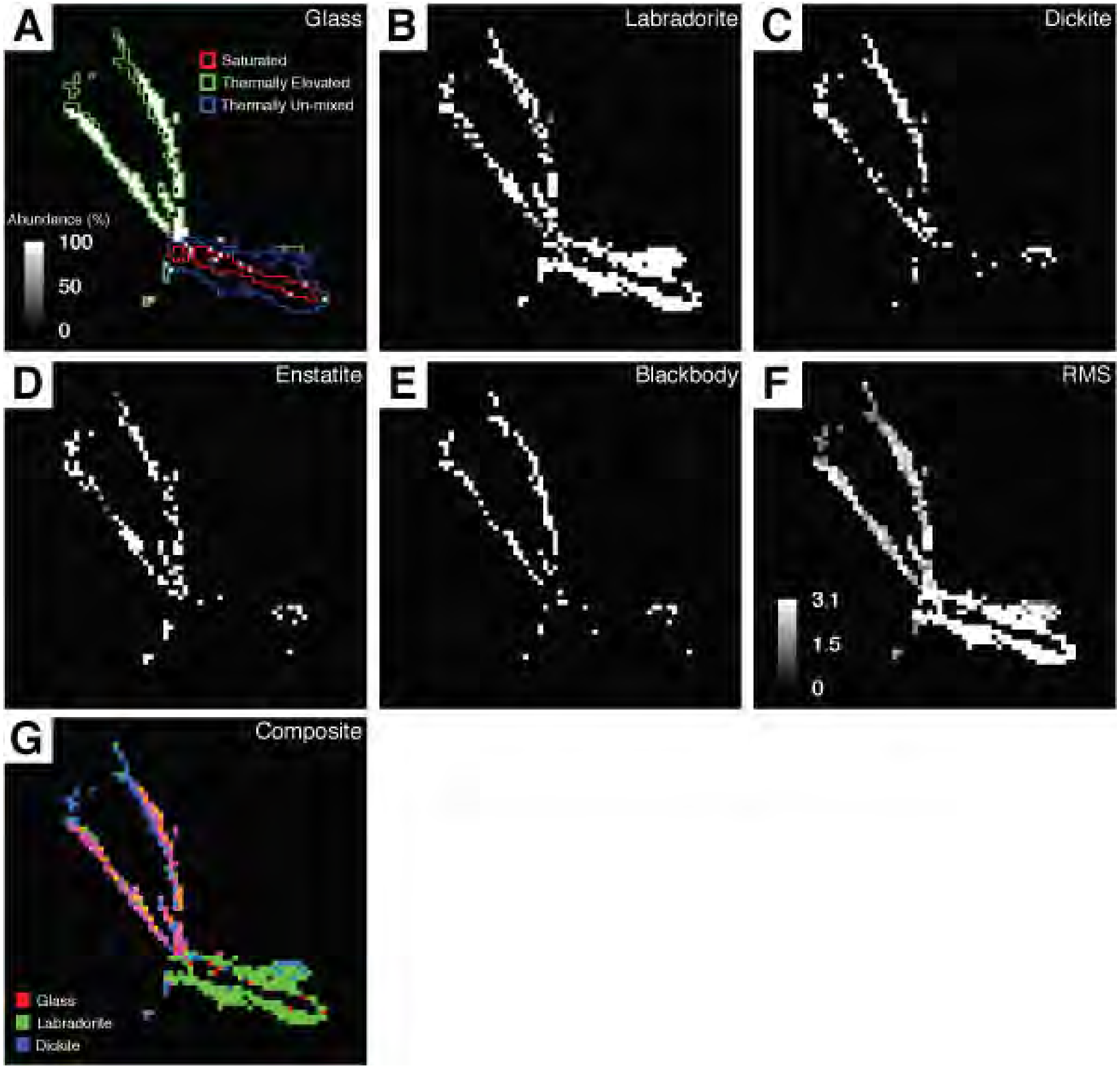

Figure 5-6 Results of the linear un-mixing algorithm applied to the 6 June 2007 ASTER TIR data following the thermal deconvolution algorithm. Each end-member has been stretched similar to those represented in Figure 5-5 and the blackbody end-member presented here is also a proxy for surface roughness.

flows can still be seen near the summit, similar to what was reported using ASTER data from the 2005 eruption. This similarity in eruption behavior suggests something fundamental about the structure of Kliuchevskoi's summit region as well as the emplacement process for flows emanating from the summit. All lava flow breakout points initiate approximately 60 m below the summit crater rim, and is most likely the result of a series of fractures near the summit (Figure 5-8), and not due to the formation of lava tubes, as the initiation of the southeastern flows displayed the disconnect early into their formation and no apparent thermal anomalies within the separation support existence of lava tubes. Based upon the shear height of Kliuchevskoi, and the instabilities of the steep slopes, it is likely that the magma within the conduit is under a high hydraulic pressure, thereby preventing lava from breeching the summit crater and breaking out at a slightly lower elevation.

This study demonstrated that spaceborne image-derived multispectral analyses of very-recent basalts from Kliuchevskoi volcano correlate well with the high-spectral resolution laboratory emissivity data in addition to those reported in Ozerov, 1997. However, after the thermal deconvolution algorithm was applied, the results produced were significantly different with respect to the glass and labradorite end-members, suggesting that additional work is necessary on the algorithm when applied to very hot targets such as incandescent lava flows. Future work will include the addition of higher-spatial resolution VNIR data, capable of detecting much higher temperatures, in order to calculate more accurate thermal distributions and maximum temperatures where the SWIR subsystem has saturated. This may also aid in reducing or eliminating the positive emissivity slopes observed in the corrected pixels, by bypassing the attributions of the crosstalk phenomenon, commonly occurring in large temperature differentials in the SWIR data.

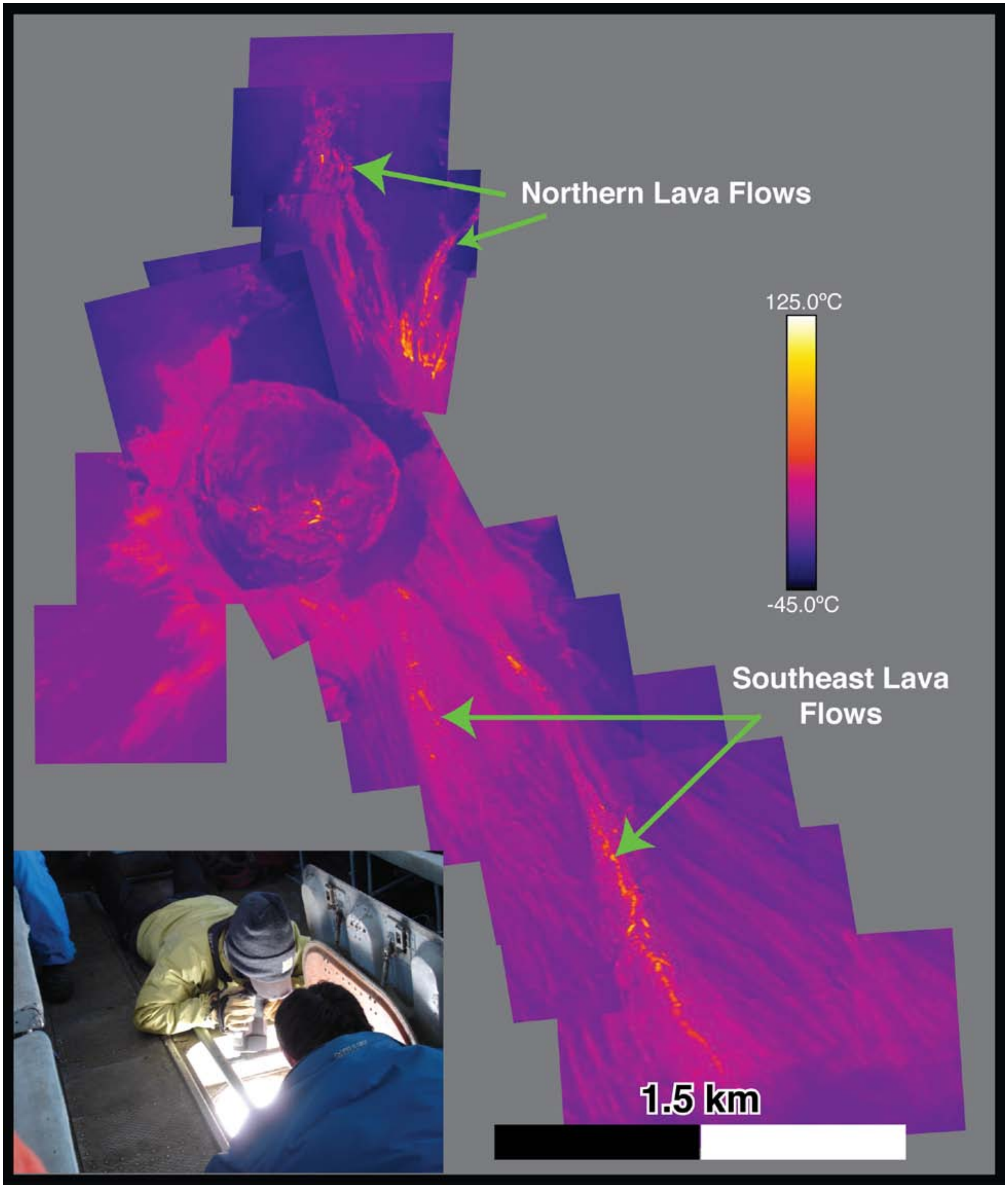

Figure 5-7 A thermal mosaic of the 2007 lava flows acquired via a helicopter over flight (inset) in August. The lava flows on the southeast and northern flanks were still hot and a clear discontinuity of the flows with the summit crater thermal anomaly is observed just as the 2005 eruption.

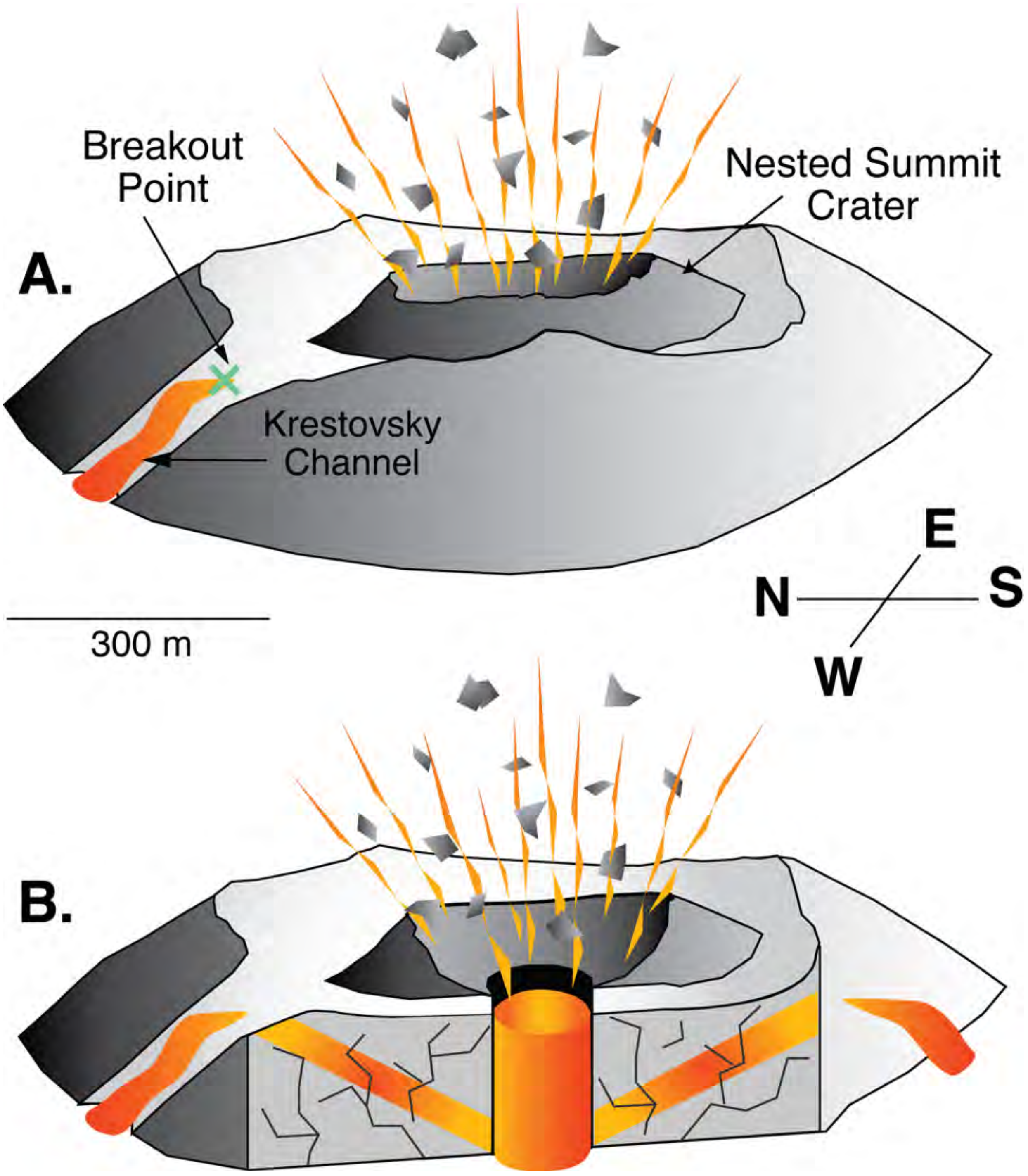

Figure 5-8 **Proposed mechanisms for producing the observed breakout point identified in the ASTER and FLIR images. A) Lava is channeled up through the main conduit to the surface where Strombolian to Vulcanian activity occurs. Effusion into the Krestovsky Channel initiates at a breakout point just below the summit of the nested crater. B) Structural weakness in the summit may allow for the formation of feeder dikes off of the main conduit from depth in addition to hydraulic pressures within the conduit.**

6.0 CONCLUDING REMARKS

By utilizing the ASTER TIR and SWIR subsystems simultaneously, a more accurate determination of the areal percentage of hot and cool surface temperatures has been made for thermal features of active basaltic volcanoes in Russia, Hawaii, and Nicaragua. The results presented here reveal that the negative slope commonly associated with thermally mixed emissivity spectra has been corrected using the thermal deconvolution algorithm. More importantly, the overall spectral shapes of the corrected emissivity spectra are preserved where interference from gas-steam plumes is negligible, and lead to increased accuracy in compositional extraction of the eruptive products. These results also provide a framework from which thermal characteristics and eruptive behavior of active basaltic volcanoes can be identified and modeled such as the eruptive phases and lava breakout point at Kliuchevskoi volcano.

Although the ASTER SWIR subystem has expired within the last year, the extensive archive of data provides an excellent opportunity to study previous eruptions. By doing so, volcanic precursory and eruptive behavior can be better understood and used to predict future behavior. Moreover, the thermal deconvolution algorithm can also be applied to these datasets in order to study a variety of basaltic volcanoes, commonly overlooked due to their remote location or inaccessibility. Ideally, further testing and application of the algorithm to intermediate and felsic volcanoes can provide valuable information into additional behavior, as these types of volcanoes tend to create more hazardous conditions for field measurements during eruptions.

Throughout the testing and application of the thermal deconvolution algorithm to high and low-temperatures targets, limitations were noted, that can be used to help develop future sensors. For instance, during daytime acquisitions, the SWIR datasets of ASTER contain two components that are not present in the nighttime SWIR datasets, including solar reflected and crosstalk radiance. These components tend to introduce significant errors into the results of the thermal deconvolution algorithm by minimizing spectral contrast and imparting a positive emissivity slope toward longer wavelengths in the TIR. The most significant errors were caused by bright steam plumes due to phreatomagmatic explosions at Kilauea and Kliuchevskoi volcanoes. It is suggested that a more accurate daytime SWIR radiance product, corrected for the solar reflected radiance component, should be developed to aid in minimizing excess energy. In addition a mask should also be developed in order to prevent gas-steam plumes from affecting the results. Lastly, in order for this algorithm to be applied to future sensors, the concept of increased spatial resolutions towards shorter wavelength subsystems is crucial for determining spatial distributions of thermal features on the surface. Currently, the algorithm uses 90 m TIR and 30 m SWIR spatial resolutions specific to ASTER. The proposed Hyperspectral-Infrared Imager (HyspIRI) includes 60 m TIR and (Visible near infrared and SWIR) VSWIR resolutions, thereby requiring additional algorithms to be developed. However, by using a 30 m resolution, similar to ASTER, minimal changes will be required and more accurate analyses will be possible due to the increased resolution of the TIR (with respect to ASTER). By using the thermal deconvolution algorithm with ASTER data as a proxy for future sensors, efficiency in instrument development and cost effectiveness will increase.

APPENDIX A

(THERMAL DECONVOLUTION ALGORITHM FOR IDL)

The information provided in this appendix includes the thermal deconvolution algorithm, written in the Interactive Data Language (IDL), and shows the step-by-step procedures for correcting the negative emissivity slope associated with thermally heterogeneous ASTER pixels. Each appendix subsection is arranged according to the order the procedures are called throughout the program. Comments, noted by semi-colons, are included for clarification of each step. It should be noted that the functions for reading the ASTER images throughout the procedures were written by Vince Realmuto, 1997. For a detailed explanation of the algorithm and how it can be used, please refer to Rose et al., in review-a.

A.1 MIXPIX.PRO

```
Pro MixPix

;controller hub for thermal mixed pixel retrieval.  It calls the other 12 procedures/functions
;to determine the true emissivity and radiance of thermally mixed pixels.

print, "
print, "
```

```
print, 'Welcome to the Thermal Deconvolution Algorithm for ASTER image data!"
print, "
print, "
print, 'Please refer to the user prompts at the bottom of the screen to'
print, 'guide you through the process.'
print, "
print, "
print, 'Before using this program, please be sure to have the following'
print, 'information ready, as input variables are required throughout the'
print, 'deconvolution process.  You will need:'
print, "
print, "
print, 'The maximum emissivity slope (-0.015 is suggested as the default).'
print, 'The minimum background temperature (10 ºK above the average background temp is
suggested)'
print, 'The SWIR band to be used for analysis'
print, 'The gain setting for the SWIR dataset.'
print, "
print, "
print, 'Let us begin!'
wait, 2.0
print, "------------------------------------------------------------------------"
print, 'Please select the emissivity and temperature image you would like to use.'
print, "------------------------------------------------------------------------"
;;;;;;;;;;;;;;;;;;;;;;;;;;;;;;;;;;;;;;;;;;;;;;;;;;;;;;;;;;;;;;;;;;;;;;;;;;;;;;;;;;;;;;;;;;;;;;;;;;;;;;;;;;;;;;;;;;;;;;;;;;;;;;;;;;;;;;;;;;;;;;;;;;;;;;
;Everything in this portion of mixpix.pro is selecting the datasets for use in the deconvolution
algorithm

;prompt user for TIR emissivity and temperature image and return no. of hot pixels
mixel_locator_E, temp_thresh, bkd_temp, hot_pixel_count, hot_pixel_info,
emis_spectrum_array, emis_img ;This calls the mixel_locator_E function that

;goes through five emissivity bands of a TIR image. A temperature band in Kelvin (band 6) is
also used to calculate the
;emissivity spectrum slope.  Pixels are identified as mixed if the slope is < a pre-determined
value and the integrated
;brightness temperature exceeds 10º above the pre-determined background temperature.

print, "------------------------------------------------------------------------"
print, 'Please select the SWIR radiance dataset you would like to use.'
print, "------------------------------------------------------------------------"

;prompt user for SWIR image
swir_reader, SWIR_img ;Once the mixed pixels have been identified on the above criteria, this
line calls the associated SWIR image
```

```
print, "--------------------------------------------------------------"

print,'Please enter the information in the prompt below'

print, "--------------------------------------------------------------"
SWIR_length=''
read, band_no, prompt='Enter the SWIR band used for analysis (4, 5, 6, 7, 8, or 9):'

print, "--------------------------------------------------------------"

print,'Please enter the information in the prompt below'

print, "--------------------------------------------------------------"
gain_setting=''
read, gain_setting, prompt='Enter the gain setting noted by L2, L1, N, or H (case sensitive)'

;make mixed_radiance_array
mixed_rad_array=fltarr(5, hot_pixel_count) ;newly calculated mixed TIR radiance array for
each TIR band
TIR_rad_array=fltarr(5, hot_pixel_count) ;original TIR radiance array for each TIR band
rad_array=fltarr(5, hot_pixel_count);newly calculated mixed TIR radiance array for each TIR
band

;create a new array to track the number of mixed pixels in the TIR.
true_mixed = fltarr(hot_pixel_count)
print, "--------------------------------------------------------------"
print, 'Please select the TIR radiance image you would like to use.'
print, "--------------------------------------------------------------"
;go get original TIR radiances
ASTER_img_reader_TIRrad, img, dims
;All images have been selected by this point.

;;;;;;;;;;;;;;;;;;;;;;;;;;;;;;;;;;;;;;;;;;;;;;;;;;;;;;;;;;;;;;;;;;;;;;;;;;;;;;;;;;;;;;;;;;;;;;;;;;;;;;;;;;;;;;;;;;;;;;;;;;;;;;;;
;The following loop goes through the nine SWIR pixels within the identified TIR pixel to
determine its radiance mixture properties
;find underlying pixels in SWIR one at a time
for i= 0, hot_pixel_count-1 do begin
   ;define hot_pixel
   hot_pixel = round(hot_pixel_info(0:1, i))
   true_mix = 0
   swir_pixel_retriever, temp_thresh, band_no, gain_setting, hot_pixel, swir_img,
mixed_radiance, wavelen, radiance, true_mix, img ;calls the SWIR_pixel_retriever to
   ;calculate radiance values of 9 SWIR pixels within the one TIR pixel identified earlier.
   true_mixed(i)=true_mix ;true_mixed(i) is the number of TIR pixels that are mixed based on
the TIR temperature and emissivity values.
   mixed_rad_array(*,i)=mixed_radiance
```

```
    rad_array(*,i)=radiance
endfor

;We are going to eliminate hot, unmixed pixels where all of the 9 SWIR pixels are hot and not
truly mixed.
hot_pixel_count=size(where(true_mixed eq 1));This is the number of TIR pixels actually
corrected in the algorithm
hot_pixel_count=hot_pixel_count[1] ;hot_pixel_count is the number of TIR pixels that are truly
mixed based on the SWIR radiance values.
hot_pixel_info=hot_pixel_info[*,where(true_mixed eq 1)]

;resize these to the correct subset
subset=where(true_mixed eq 1)
TIR_rad_array  = TIR_rad_array(*, subset)
mixed_rad_array= mixed_rad_array(*, subset)

;This part makes a mask image to show which pixels were determined to be thermally mixed in
the TIR emiss/temp dataset.
mask_img=img(*,*,0)
mask_img(*)=0

;A window size is designated in case the user would like to preview the mask ahead of time.
window, 0, ysize=850
!p.multi=[0,1,2]

;The following FOR loop creates two plots in order to illustrate the original radiance,
;new radiance, and new emissivity for each thermall mixed pixel.
print, "--------------------------------------------------------------"

print,'Planck curves are shown in the top graph'
print,'Thermally unmixed emissivity spectra are below!!!'

print, "--------------------------------------------------------------"
corrected_emissivity=fltarr(dims.ns, dims.nl, dims.nb)
for i=0, hot_pixel_count-1 do begin
  TIR_rad_array(*,i)=img(hot_pixel_info(0,i), hot_pixel_info(1,i), *)
  wavelen=[8.291, 8.634, 9.075, 10.657, 11.318]
  plot, wavelen,(mixed_rad_array(*,i)), yrange=[0,40], charsize=2,$  ;This plots the original
radiance
  xtitle='wavelength in microns', ytitle='radiance in W m^-2 um^-1 sr^-1',$
  psym=-7, thick=2
  oplot, wavelen,(TIR_rad_array(*,i)),psym=-1, thick=2,color=255  ;This plots the corrected
radiance

  plot, wavelen, TIR_rad_array(*,i)/mixed_rad_array(*,i), yrange=[0,1],$  ;This plots the new
emissivity spectrum
```

```
  xtitle='wavelength in microns', ytitle='emissivity', charsize=2

  ;replace old values in radiance image with new ones for only the thermally mixed pixels.
  img(hot_pixel_info(0,i), hot_pixel_info(1,i), *)=mixed_rad_array(*,i)
  ;mixed_rad_array(*,i) = mixed_rad_array(*,i) > 0.00

  ;replace old values in emissivity image with new ones for only the thermally mixed pixels
  corrected_emissivity[hot_pixel_info[0,i], hot_pixel_info[1,i],
*]=TIR_rad_array[*,i]/mixed_rad_array[*,i]
  ratio=fltarr(1,1, dims.nb)
  ratio= emis_img[hot_pixel_info[0,i], hot_pixel_info[1,i],
*]/corrected_emissivity[hot_pixel_info[0,i], hot_pixel_info[1,i], *]
  unTES_emissivity=fltarr(5,5)
  for band_for_ratio=0, dims.nb-1,1 do begin  ;where to start, where to end, how many to
increment
    unTES_emissivity[band_for_ratio,*]=ratio[0,0,band_for_ratio] *
corrected_emissivity[hot_pixel_info[0,i], hot_pixel_info[1,i], *]
  endfor



  emiss_possibility = -1.0
  max_emis_possible = -1.0
  for final_emis=0, 4, 1 do begin
    ;find the max emissivity in the first spectrum
    if (max(unTES_emissivity[final_emis,*]) gt 1.005) then continue
    if (max(unTES_emissivity[final_emis,*]) gt max_emis_possible) then begin
      max_emis_possible = max(unTES_emissivity[final_emis,*])
      emiss_possibility = final_emis
    endif
  endfor

  if (emiss_possibility eq -1.0) then begin  ;if all emissivity maximums are gt 1.005 this will
choose which array to use for the final unTESsed emissivity spectrum for the pixel
    max_emis_possible = 200.0
    for final_emis=0, 4, 1 do begin
      if (max(unTES_emissivity[final_emis,*]) lt max_emis_possible) then begin
        max_emis_possible = max(unTES_emissivity[final_emis,*])
        emiss_possibility = final_emis
      endif
    endfor
  endif

emis_img(hot_pixel_info(0,i), hot_pixel_info(1,i), 0:4)= unTES_emissivity[emiss_possibility,*]

  ;make mask (placeholder)
```

```
  mask_img(hot_pixel_info(0,i), hot_pixel_info(1,i), *)=1
  wait, 0.1
endfor

print, "------------------------------------------------------------"
print, 'The number of true thermally mixed pixels:'
print, TOTAL(true_mixed)
print, "------------------------------------------------------------"


;;;;;;;;;;;;;;;;;;;;;;;;;;;;;;;;;;;;;;;;;;;;;;;;;;;;;;;;;;;;;;;;;;;;;;;;;;;;;;;;;;;;;;;;;;;;;;;;;;;;;;;;;;;;;;;;;;;;;;;;;;;;
print, "------------------------------------------------------------"
print, 'Let us now save our new files!'
print, "------------------------------------------------------------"


print, "------------------------------------------------------------"
print, 'Please select a destination and file name for the unmixed TIR radiance file.'
print, "------------------------------------------------------------";This portion writes out the final
corrected images
;Final TIR radiance file with the new TIR mixed radiances inserted for the corrected pixels
rad_file=dialog_pickfile(Title='Please select destination for new TIR radiance file',
path='/Users/shellierose/Desktop')
vjr_write_envi, dims, rad_file+'.hdr' ;Calls the vjr_write_envi procedure to write an ENVI
compatible radiance image file
vjr_write_image, dims, img, rad_file  ;Calls the vjr_write_envi procedure to write the radiance
image file
print, "------------------------------------------------------------"
print, 'Please select a destination and file name for the unmixed emissivity file.'
print, "------------------------------------------------------------"
;Final emissivity file with the new values inserted for the corrected pixels
emis_file=dialog_pickfile(Title='Please select destination for new Emissivity file',
path='/Users/shellierose/Desktop')
;change number of bands (5 for emissivity and 1 for the temperature)
dims.nb=6
vjr_write_envi, dims, emis_file+'.hdr'  ;Calls the vjr_write_envi procedure to write an ENVI
compatible radiance image file
vjr_write_image, dims, emis_img, emis_file ;Calls the vjr_write_envi procedure to write the
radiance image file

print, "------------------------------------------------------------"
print, 'Please select a destination and file name for the masked file.'
print, "------------------------------------------------------------"

;This produces the mask file that shows which TIR pixels have been corrected
mask_file=dialog_pickfile(Title='Please select destination for new masked image',
```

```
path='/Users/shellierose/Desktop')
;change number of bands (again)
dims.nb=1
vjr_write_envi, dims, mask_file+'.hdr' ;Calls the vjr_write_envi procedure to write the ENVI
compatible masked image file
vjr_write_image, dims, mask_img, mask_file ;Calls the vjr_write_image procedure to write the
masked image file


print, "-----------------------------------------------------------"
print, 'Hooray!  You have successfully completed this program.'
print, "-----------------------------------------------------------"

stop
END
```

A.2 MIXEL_LOCATOR_E.PRO

```
PRO Mixel_Locator_E, temp_thresh, bkd_temp, hot_pixel_count, hot_pixel_info,
emis_spectrum_array, img

; This program locates and identifies thermally
; mixed pixels in an ASTER image based upon the
; spectral signature and temperature.
; The input image should be set up as follows:

        ; 5 emissivity bands in the TIR with the
        ; associated brightness temperature image
        ; as band 6 (i.e. stack the two files).
;;;;;;;;;;;;;;;;;;;;;;;;;;;;;;;;;;;;;;;;;;;;;;;;;;;;;;;;;;;;;;;;;;;;;;;;;;;;;;;;;;;;;;;;;;;;;;;;;;;;;;;;;;;;;;;;;;;;


ASTER_img_reader, img, dims                     ;calls the img reader program

                                                ;so that emissivity
                                                ;values can be read in
;Define variables
print, '     reading aster file'
x= dims.ns                                      ;number of columns in a TIR image
                                                ;in the x direction
y= dims.nl                                      ;number of columns in a TIR image
                                                ;in the y direction
```

```
z= dims.nb                                               ;number of bands in a TIR image
lambda= [8.291, 8.634, 9.075, 10.657, 11.318]            ;wavelength values for TIR
print, "-------------------------------------------------------------"

print,'Please enter the information in the prompt below'

print, "-------------------------------------------------------------"
read, thresh, prompt='Enter an emissivity threshold:'
print, "-------------------------------------------------------------"

print,'Please enter the information in the prompt below'

print, "-------------------------------------------------------------"
read, temp_thresh, prompt='Enter the minimum temp threshold (ºK):'
bkgd_temp = temp_thresh-10.0

;thresh= -0.015                      ;this is the upper limit of slope for mixed pixels
hot_pixel_count=0                    ;number of pixels identified as thermally mixed
placeholder_image=fltarr(x,y)        ;used to create a resultant image
placeholder_image(*,*)=0.1           ;creates a transparency to highlight thermally mixed
                                     ;pixels
hot_pixel_info=fltarr(4, x*y)        ;make info array
emis_spectrum_array=fltarr(5, x*y)   ;make emissivity array

;;;;;;;;;;;;;;;;;;;;;;;;;;;;;;;;;;;;;;;;;;;;;;;;;;;;;;;;;;;;;;;;;;;;;;;;;;;;;;;;;;;;;;;;;;;;;;;;;;;;;;;;;;;;;;;;;;;;;;;;;

; The following loops works its way across and down
; the image.  Outer loop = x direction and
; inner loop = y direction.
print,"
print, "-------------------------------------------------------------"
print,'Please wait while we look for mixed pixels using an emissivity threshold =' +
string(thresh)
print, 'And a minimum temperature threshold of:' + string(temp_thresh)
print, "-------------------------------------------------------------"
print, "

FOR i=0, x-1 DO BEGIN                ;For every pixel in the x direction do the following:
 for j=0, y-1 do begin               ;For every pixel in the y direction do the following;
 emis_spectrum = img(i,j,0:4)        ;set the emissivity spectrum to the x and y pixel

;coordinates with z values equal to the 5 emissivity
;bands in the image

 pixel_temp= img(i,j,5)              ;set the temperature to the x and y pixel coordinate
                                     ;as the value in band 6.
```

```
 b_and_m=LINFIT(lambda, emis_spectrum)           ;Makes a best fit line, and calculates slope
                                                 ;and y intercept
        if b_and_m(1) lt thresh and b_and_m(1) gt -0.1 and pixel_temp ge temp_thresh and
pixel_temp lt 370.15 then begin

                  ;******************
   hot_pixel_info(*,hot_pixel_count) = [i,j,b_and_m(1),pixel_temp]
   emis_spectrum_array(*, hot_pixel_count)=emis_spectrum

   hot_pixel_count=hot_pixel_count+1             ;counts the number of hot pixels
   placeholder_image(i,j)=1.0                    ;creates a mask for isothermal pixels
        endif
 endfor
ENDFOR

;remove extra points
hot_pixel_info=hot_pixel_info(*,0:hot_pixel_count-1)
emis_spectrum_array=emis_spectrum_array(*,0:hot_pixel_count-1)

;;;;;;;;;;;;;;;;;;;;;;;;;;;;;;;;;;;;;;;;;;;;;;;;;;;;;;;;;;;;;;;;;;;;;;;;;;;;;;;;;;;;;;;;;;;;;;;;;;;;;;;;;;;;;;;;;

;This portion will plot an emissivity spectrum from one pixel as well
;as the line of the slope calculated above.
PRINT,' '+ string(hot_pixel_count) + '  mixed pixels found'
                  ;prints the number of hot pixels on the screen
PRINT, hot_pixel_info

END
```

A.3 ASTER_IMAGE_READER.PRO

```
PRO ASTER_img_reader, img, dims

;reads in aster IMG data and returns an array

;read in the hdr file
hdr_file=dialog_pickfile(title='Select the Emissivity and Temp file', filter='*miss*.hdr',$
path='/Users/shellierose/Desktop')
```

```
;truncates hdr filename to get img name
infile=strmid(hdr_file,0, strlen(hdr_file)-4)

;opens file and writes to img array
dims = VJR_READ_ENVI(hdr_file)
img = VJR_READ_IMAGE(infile, dims)

END
```

A.4 VJR_READ_ENVI.PRO

```
;+
;  NAME:
;         VJR_READ_ENVI
;
;  PURPOSE:
;         Read an ENVI header file from disk and return the
;         image dimensions in a structure
;
;  CATAGORY:
;         File I/O
;
;  CALLING SEQUENCE:
;         dims = VJR_READ_ENVI(file, HEAD=hdrfile, MAP=mapinfo)
;
;  INPUT:
;         file:     name of the ENVI header file that is to be read
;
;  OUTPUT:
;         dims:   dimension structure {ns, nl, nb, offset, form, org, order}
;                           dims = -1 if there is are any read errors.
;
;         OPTIONAL OUTPUT:
;         head: string array of entries in the header file.
;         map:  array of map information values [pixel easting, pixel northing, x pixel size, y pixel
size]
;
;  COMMON BLOCKS:
;         None.
;
```

```
;  SIDE EFFECTS:
;          None.
;
;  RESTRICTIONS:
;          Must have write access to disk.
;
;  MODIFICATION HISTORY
;          Written for Win NT January 1997, VJR
;          byte order keyword added July 1997, VJR
;          Last Update:    16 November 2002, VJR
;-


PRO SEARCH_LIST, buf, key, value

;          search routine for keywords

index = WHERE(STRPOS(buf, key) NE -1, count)

IF (count NE 1) THEN value = 'BAD HEADER' ELSE BEGIN

          pos = STRPOS(buf[index], '=')
          value = STRMID(buf[index], pos[0]+1, 15)

ENDELSE

RETURN
END




PRO SEARCH_MAPINFO, buf, value

;          search routine for map info keyword

index = WHERE(STRPOS(buf, 'map info') NE -1, count)

IF (count NE 1) THEN value = -9999 ELSE BEGIN

          ;          find the positions of all commas in the "map info" string

          comma = INTARR(10)
          pos = 0
          idx = 0
```

```
    comma_loop:

        test = STRPOS(buf[index], ',', pos)

        IF test NE -1 THEN BEGIN

            comma[idx] = test
            pos = test + 1
            idx = idx + 1
            GOTO, comma_loop

        ENDIF

    ;   extract the map information

    value=FLTARR(4)

    FOR idx = 0, 3 DO value[idx] = FLOAT(STRMID(buf[index], comma[idx+2]+1,
    $
    comma[idx+3]-comma[idx+2]-1))

ENDELSE

RETURN
END




FUNCTION VJR_READ_ENVI, file, HEAD=hdrbuf, MAP=map

;   read image dimension information from
;   ENVI header file and return dimensions
;   in structure format

ON_ERROR, 2             ; return to caller upon error

hdrbuf = (gulp = STRING(0))
OPENR, unit1, file, /GET_LUN, ERROR=err

IF (err EQ 0) THEN BEGIN

    READF, unit1, hdrbuf
    WHILE NOT EOF(unit1) DO BEGIN

        READF, unit1, FORMAT='(A)', gulp
```

```
        hdrbuf = [hdrbuf, gulp]

    ENDWHILE
  FREE_LUN, unit1

;   search for keywords

    SEARCH_LIST, hdrbuf, 'samples', ns
    IF (ns[0] eq 'BAD HEADER') THEN BEGIN
        dummy = DIALOG_MESSAGE('BAD SAMPLES KEYWORD!', /ERROR)
        RETURN, -1
    ENDIF

    SEARCH_LIST, hdrbuf, 'lines', nl
    IF (nl[0] EQ 'BAD HEADER') THEN BEGIN
        dummy = DIALOG_MESSAGE('BAD LINES KEYWORD!', /ERROR)
        RETURN, -1
    ENDIF

    SEARCH_LIST, hdrbuf, 'bands', nb
    IF (nb[0] EQ 'BAD HEADER') THEN BEGIN
        dummy = DIALOG_MESSAGE('BAD BANDS KEYWORD!', /ERROR)
        RETURN, -1
    ENDIF

    SEARCH_LIST, hdrbuf, 'header offset', offset
    IF (offset[0] EQ 'BAD HEADER') THEN BEGIN
        dummy  = DIALOG_MESSAGE('BAD HEADER OFFSET KEYWORD!',
/ERROR)
        RETURN, -1
    ENDIF

    SEARCH_LIST, hdrbuf, 'data type', form
    IF (form[0] EQ 'BAD HEADER') THEN BEGIN
        dummy = DIALOG_MESSAGE('BAD DATA TYPE KEYWORD!', /ERROR)
        RETURN, -1
    ENDIF

    SEARCH_LIST, hdrbuf, 'interleave', org
    IF (org[0] EQ 'BAD HEADER') THEN BEGIN
        dummy = DIALOG_MESSAGE('BAD INTERLEAVE KEYWORD!', /ERROR)
        RETURN, -1
    ENDIF ELSE org[0] = STRUPCASE(org[0])

    SEARCH_LIST, hdrbuf, 'byte order', order
    IF (order[0] EQ 'BAD HEADER') THEN BEGIN
```

```
                dummy = DIALOG_MESSAGE('BAD BYTE ORDER KEYWORD!',
/ERROR)
                RETURN, -1
        ENDIF

        IF KEYWORD_SET(map) THEN SEARCH_MAPINFO, hdrbuf, map

;       create structure and exit

        dims = {ns:LONG(ns[0]), nl:LONG(nl[0]), nb:LONG(nb[0]), $
                        offset:LONG(offset[0]), form:FIX(form[0]), $
                        org:STRTRIM(org[0],2), order:FIX(order[0])}

        RETURN, dims

ENDIF ELSE BEGIN
        dummy = DIALOG_MESSAGE('ERROR READING '+file, /ERROR)
        RETURN, -1
ENDELSE

END
```

A.5 VJR_READ_IMAGE.PRO

```
;+
;  NAME:
;       VJR_READ_IMAGE
;
;  PURPOSE:
;       Open image file, check dimensions vs. those defined in dim structure.
;       Redefine dim structure (and write new header file) if necessary.
;       Read image file into data buffer and return buffer to user.
;
;  CATAGORY:
;       File I/O
;
;  CALLING SEQUENCE:
;       buf = VJR_READ_IMAGE(fname, dims)
;
;  INPUT:
;       fname: name of image file to be opened and read. Character string.
```

```
;
;       dims:   dimension structure {ns, nl, nb, offset, form, org, order}.
;                       A new structure is returned if original dims is found
;                       to be wrong.
;
;  OUTPUT:
;        buf:    Data buffer filled with data from image file. Value of
;                       -1 returned if data format or file organization is
;                       not supported.
;
;
;  COMMON BLOCKS:
;       None
;
;  SIDE EFFECTS:
;       A new header file is written to disk if necessary.
;
;  RESTRICTIONS:
;       Multiband files must be in BSQ format. Complex and string data types
;       are not supported.
;
;  MODIFICATION HISTORY:
;       Written January 1997, VJR
;       Last Update:    15 NOVEMBER 2002, VJR
;-

FUNCTION VJR_READ_IMAGE, fname, dims

;       catch errors

CATCH, errors
IF (errors NE 0) THEN BEGIN

        FREE_LUN, iunit
        dummy = DIALOG_MESSAGE(['Source: VJR_READ_IMAGE', !ERR_STRING],
/ERROR)
        RETURN, -1

ENDIF


;       determine the size of the image file (in bytes)

OPENR, iunit, fname, /BINARY, /NOAUTO, /GET_LUN
a = FSTAT(iunit)
```

```
;       check the reported dimensions against the file size

CASE dims.form OF
        1: nbytes = 1L                  ; byte format
        2: nbytes = 2L                  ; integer format
        3: nbytes = 4L                  ; long integer format
        4: nbytes = 4L                  ; floating point format
        5: nbytes = 8L                  ; double precision floating point format
ENDCASE

chk_siz = (dims.ns*dims.nl*nbytes*dims.nb)+dims.offset

IF (chk_siz GT a.size) THEN BEGIN
        dummy = DIALOG_MESSAGE('REVISE HEADER INFORMATION!')
        CHANGE_DIMS, fname, a.size, dims
ENDIF

CASE STRUPCASE(dims.org) of

        'BSQ': BEGIN

        CASE dims.form OF

                1: buf = BYTARR(dims.ns, dims.nl, dims.nb)
                2: buf = INTARR(dims.ns, dims.nl, dims.nb)
                3: buf = LONARR(dims.ns, dims.nl, dims.nb)
                4: buf = FLTARR(dims.ns, dims.nl, dims.nb)
                5: buf = DBLARR(dims.ns, dims.nl, dims.nb)

                ELSE: BEGIN
                        dummy = DIALOG_MESSAGE('!DATA FORMAT NOT
SUPPORTED!', /ERROR)
                        RETURN, -1
                END

        ENDCASE
        END

        'BIL': BEGIN

        CASE dims.form OF

                1: buf = BYTARR(dims.ns, dims.nb, dims.nl)
                2: buf = INTARR(dims.ns, dims.nb, dims.nl)
                3: buf = LONARR(dims.ns, dims.nb, dims.nl)
                4: buf = FLTARR(dims.ns, dims.nb, dims.nl)
```

```
        5: buf = DBLARR(dims.ns, dims.nb, dims.nl)

        ELSE: BEGIN
            dummy = DIALOG_MESSAGE('!DATA FORMAT NOT
SUPPORTED!', /ERROR)
            RETURN, -1
        END

    ENDCASE
    END

    'BIP': BEGIN

    CASE dims.form OF

        1: buf = BYTARR(dims.nb, dims.ns, dims.nl)
        2: buf = INTARR(dims.nb, dims.ns, dims.nl)
        3: buf = LONARR(dims.nb, dims.ns, dims.nl)
        4: buf = FLTARR(dims.nb, dims.ns, dims.nl)
        5: buf = DBLARR(dims.nb, dims.ns, dims.nl)

        ELSE: BEGIN
            dummy = DIALOG_MESSAGE('!DATA FORMAT NOT
SUPPORTED!', /CONTINUE)
            RETURN, -1
        END

    ENDCASE
    END

ENDCASE

POINT_LUN, iunit, dims.offset       ; skip over VICAR hdr (if present)
READU, iunit, buf
FREE_LUN, iunit

;   test if swapping is required

;family = !VERSION.OS_FAMILY
family = !VERSION.ARCH

IF (((family EQ 'x86') OR (family EQ 'x86_64') OR (family EQ 'i386') OR (family EQ 'i686'))
AND (dims.order EQ 1)) THEN BEGIN
    buf = SWAP_ENDIAN(buf)
    dims.order = 0
ENDIF
```

```
IF ((family EQ 'ppc') AND (dims.order EQ 0)) THEN BEGIN
        buf = SWAP_ENDIAN(buf)
        dims.order = 1
ENDIF

RETURN, buf

END
```

A.6 SWIR_READER.PRO

```
PRO SWIR_reader, SWIR_img

;reads in aster SWIR IMG data and returns an array

;read in the hdr file
hdr_file=dialog_pickfile(title='Select the solar corrected SWIR radiance file',
filter='*adiance*.hdr', $
path='/Users/shellierose/Desktop')

;truncates hdr filename to get img name
infile=strmid(hdr_file,0, strlen(hdr_file)-4)

;opens file and writes to img array
dims = VJR_READ_ENVI(hdr_file)
SWIR_img = VJR_READ_IMAGE(infile, dims)

END
```

A.7 ASTER_IMG_READER_TIRRAD.PRO

```
PRO ASTER_img_reader_TIRrad, img, dims

;reads in aster IMG data and returns an array
```

```
;read in the hdr file
hdr_file=dialog_pickfile(title= 'Select the TIR radiance file', filter='*adiance*.hdr',$
path='/Users/shellierose/Desktop')

;truncates hdr filename to get img name
infile=strmid(hdr_file,0, strlen(hdr_file)-4)

;opens file and writes to img array
dims = VJR_READ_ENVI(hdr_file)
img = VJR_READ_IMAGE(infile, dims)

END
```

A.8 SWIR_PIXEL_RETRIEVER.PRO

```
PRO SWIR_pixel_retriever, temp_thresh, band_no, gain_setting, hot_pixel, swir_img,
mixed_radiance, wavelen, radiance, true_mixed, img

;takes location of TIR hot/slopey pixel identified in mixel_locator_E.pro
;and extracts 9 x 6 array of SWIR radiance for that pixel.

;takes the x and y position of the TIR image and extracts the
;relevant 9 SWIR pixels




;set mixed_radiance as a flag for the instance when no hot pixels are found in the SWIR.
mixed_radiance=fltarr(5)
mixed_radiance(*)=-2
radiance=fltarr(5)
radiance(*)=img[hot_pixel[0],hot_pixel[1],*]
;This should display a -2.00 for the pixels that are not changed in the un-mixing process.


;get upper left and lower right co-ords of the SWIR pixels
swir_pix=[hot_pixel*3, (hot_pixel*3)+2] ;converts the TIR coordinates to SWIR coordinates
tir_pix=[hot_pixel, hot_pixel]

;choose band > add user prompts later
;read, band_no, prompt='Enter the SWIR band used for analysis:'
```

```
;band_no=4
;gain_setting=''
;read, gain_setting, prompt='Enter the gain setting (L2, L1, N, or H)'
;gain_setting='L2'

;define gain setting in context of rad_thresh_array
if gain_setting eq 'L2' then rad_thresh_subs=0
if gain_setting eq 'L1' then rad_thresh_subs=1
if gain_setting eq 'N' then rad_thresh_subs=2
if gain_setting eq 'H' then rad_thresh_subs=3

;define maximum radiance thresholds for different band/gain setting combos
max_rad_thresh_array=fltarr(4,6)
max_rad_thresh_array(0,*)=[73.3, 103.5, 98.7, 83.8, 62.0, 67.0]
max_rad_thresh_array(1,*)=[73.3, 23.4, 21.0, 20.1, 14.06, 10.72]
max_rad_thresh_array(2,*)=[55.0, 17.6, 15.8, 15.1, 10.55, 8.04]
max_rad_thresh_array(3,*)=[27.5, 8.8, 7.9, 7.55, 5.27, 4.02]

;define minimum radiance thresholds for different band/gain setting combos
min_rad_thresh_array=fltarr(4,6)
min_rad_thresh_array(0,*)=[1.55, 2.16, 2.03, 1.80, 1.33, 1.44]
min_rad_thresh_array(1,*)=[1.55, 0.47, 0.43, 0.41, 0.29, 0.22]
min_rad_thresh_array(2,*)=[1.16, 0.36, 0.32, 0.30, 0.22, 0.16]
min_rad_thresh_array(3,*)=[0.58, 0.18, 0.16, 0.15, 0.11, 0.08]

;relate band number to array position
band_subs=band_no-4

;picks correct hot radiance threshold
rad_thresh_max=max_rad_thresh_array(rad_thresh_subs, band_subs)

;picks correct cool radiance threshold
rad_thresh_min=min_rad_thresh_array(rad_thresh_subs, band_subs)

;converts to 9 co-ords
SWIR_hot_pixels=SWIR_img(swir_pix(0):swir_pix(2), swir_pix(1):swir_pix(3), band_subs)
;extracts the nine SWIR values within one TIR pixel area in a specified band.

;gets total radiance in each band for 9 SWIR pixel subset
band4 = TOTAL(SWIR_img(swir_pix(0):swir_pix(2), swir_pix(1):swir_pix(3), 0))
band5 = TOTAL(SWIR_img(swir_pix(0):swir_pix(2), swir_pix(1):swir_pix(3), 1))
band6 = TOTAL(SWIR_img(swir_pix(0):swir_pix(2), swir_pix(1):swir_pix(3), 2))
band7 = TOTAL(SWIR_img(swir_pix(0):swir_pix(2), swir_pix(1):swir_pix(3), 3))
band8 = TOTAL(SWIR_img(swir_pix(0):swir_pix(2), swir_pix(1):swir_pix(3), 4))
band9 = TOTAL(SWIR_img(swir_pix(0):swir_pix(2), swir_pix(1):swir_pix(3), 5))
;**********************************************************************
```

```
********************************************************
print, "--------------------------------------------------------------"
print, "SWIR radiance values for the identified TIR mixels"
print, SWIR_hot_pixels ;prints all 9 SWIR radiance values
print, "SWIR pixel coordinates"
print, swir_pix ;prints the SWIR pixel coordinates
print, " "
print, "TIR pixel coordinates"
print, tir_pix
;****************************************************************************
********************************************************
;;;;;;;;;;;;;;;;;;;;;;;;;;;;;;;;;;;;;;;;;;;;;;;;;;;;;;;;;;;;;;;;;;;;;;;;;;;;;;;;;;;;;;;;;;;;;;;;;;;;;;;;;;;;;;
;This portion of the code calculates the average SWIR radiance for the 9 SWIR pixels and
;prints it out on the screen.



cool_area = TOTAL(SWIR_hot_pixels lt rad_thresh_min)/9 ;find the average radiance of the
cool SWIR pixels
hot_area = TOTAL(SWIR_hot_pixels gt rad_thresh_min)/9 ;find the average radiance of the hot
SWIR pixels
number_cool_pix = cool_area * 9 ;determines the number of cool pixels in the 3 x 3 array
number_hot_pix = hot_area * 9 ;determines the number of hot pixels in the 3 x 3 array.
;The following prints the number of cool and hot SWIR pixels in the 3 x 3 array to the screen.
;****************************************************************************
********************************************************
print, "The number of cool SWIR pixels is", number_cool_pix, "  The cool area % is", cool_area
print, "The number of hot SWIR pixels is ", number_hot_pix, "   The hot area & is", hot_area
;****************************************************************************
********************************************************
;define mean cool radiance
radiance_cool=0.0 ;This will allow the following scenarios to be dealt with.
CASE band_no OF
  4: SWIR_length = 1.656
  5: SWIR_length = 2.167
  6: SWIR_length = 2.209
  7: SWIR_length = 2.262
  8: SWIR_length = 2.336
  9: SWIR_length = 2.400
ENDCASE
bkd_temp = temp_thresh-10.0
radiance_cool = planck(SWIR_length, bkd_temp) ;calls planck.pro to calculate the radiance of
the background temperature
bkd_radiance=radiance_cool
```

```
; 1. no hot pixels > jump to next one
if cool_area eq 1.0 then begin
  print, '    no hot SWIR pixels found'
  radiance=img[hot_pixel[0],hot_pixel[1],*]    ;The radiance is set to the original TIR radiance
  mixed_radiance=img[hot_pixel[0],hot_pixel[1],*]  ;The mixed radiance is set to the original
TIR radiance.
  goto, jump1
endif

;We now know that we have a mixed pixel so we set true_mixed to 1.00
true_mixed=1

;; 2. at least one cool pixel
;if cool_area ne 0.0 then begin
;  radiance_cool=bkd_radiance ;mean(swir_hot_pixels[where(swir_hot_pixels le
rad_thresh_min)])
;endif
;
;; 3. mean cool radiance lt 0.0 (from solar correction)
;if radiance_cool lt rad_thresh_min then radiance_cool=bkd_radiance ;In the event that solar
radiance correction produces negative radiance values
;;this will set all negative radiance values to 0.0001

; 4. hot pixels
radiance_hot = mean(swir_hot_pixels[where(swir_hot_pixels gt rad_thresh_min)])

; 5. Saturated SWIR pixels
if (mean(swir_hot_pixels) gt rad_thresh_max) then begin
  print, 'Saturated SWIR pixels have been found'
  radiance=img[hot_pixel[0],hot_pixel[1],*]
  mixed_radiance=img[hot_pixel[0],hot_pixel[1],*]
  ;not a mixed pixel
  true_mixed=0
  goto, jump1
endif

;6. All hot pixels equal each other (not a true mixed TIR pixel)
if stddev(swir_hot_pixels) eq 0.00 then begin
print, 'All SWIR pixels are the same. This TIR area is not thermally mixed.'
  radiance=img[hot_pixel[0],hot_pixel[1],*]
  mixed_radiance=img[hot_pixel[0],hot_pixel[1],*]
  ;not a mixed pixel
  true_mixed=0
```

```
  goto, jump1
endif

; 7.  All of the SWIR pixels are above the min rad array.
;A new cool value needs to be determined by averaging the values below the mean of the 9
pixels
if hot_area eq 1.0 then begin
  avg = mean(swir_hot_pixels)
  ;just in case a pixel = avg, put it as a hot pixel to put it somewhere....
  radiance_hot = mean(swir_hot_pixels[where(swir_hot_pixels ge avg)])
  radiance_cool = mean(swir_hot_pixels[where(swir_hot_pixels lt avg)])
endif




print, "The mean radiance of cool SWIR pixels is", radiance_cool
print, "The mean radiance of hot SWIR pixels is ", radiance_hot

;;;;;;;;;;;;;;;;;;;;;;;;;;;;;;;;;;;;;;;;;;;;;;;;;;;;;;;;;;;;;;;;;;;;;;;;;;;;;;;;;;;;;;;;;;;;;;;;;;;;;;;;;;;;;;;;
;The average radiance value for the hot and cool portion are then put into the plkinv.pro function
to determine
;the associated temperatures for each.  Then the planck.pro function is called to determine the
new radiance
;values for the mixed temperatures for each TIR band.
;Finally, the original and newly calculated TIR radiance values are ratioed to determine the true
;emissivity for each TIR band.

wavlen_array=[1.656, 2.167, 2.209, 2.262, 2.336, 2.400]
wavelen_SWIR = wavlen_array(band_subs)  ;Defines the wavelengths for the SWIR
print, 'band' + string(band_no)

;   status = self->PromptUsertext('Enter a radiance value', $
;   radiance, TITLE = 'Input Radiance')                ;The radiance band should be entered by the
user

print, "-------------------------------------------------------------"
temperature=plkinv(wavelen_SWIR, radiance_cool, radiance_hot, temperature_cool,
temperature_hot)                ;Calls the plkinv function to calculate a temperature

print, temperature_cool-273.15, " = Cool temperature derived by SWIR radiance in º Celsius"
print, temperature_hot-273.15, " = Hot temperature derived by SWIR radiance in º Celsius"
print, "-------------------------------------------------------------"
print, " "
```

```
temp_low = temperature_cool
temp_high = temperature_hot
temp = temperature
wavelen = [8.291, 8.634, 9.075, 10.657, 11.318]
mixed_radiance=mixed_planck(wavelen, temp_low, temp_high, cool_area, hot_area,
mixed_radiance)           ;Calls the planck function to calculate radiance based
                              ;on the temp from plkinv for TIR bands.

print, "New TIR radiance values in W/m^2/µm/sr"
print, "     Band 10      Band 11      Band 12      Band 13      Band 14"
print, "radiance: "
print, radiance
print, "mixed radiance: "
print, mixed_radiance
emissivity = radiance/mixed_radiance
print, "emissivity: "
print, emissivity
print, "--------------------------------------------------------------"


jump1:

END
```

A.9 PLANCK.PRO

```
;
;+
; NAME:
;      PLANCK
;
; PURPOSE:
;      calculate planck function, input wavelength and temperature
;      can be arrays
;
; CATEGORY:
;      ????
;
; CALLING SEQUENCE:
;      radiance = planck(wavelength,temperature)
;
```

```
; INPUTS:
;       Wavelength:     wavelength in microns (scalar or array)
;       Temperature:    temperature in degrees Kelvin (scalar)
;
; OUTPUTS:
;       Radiance:       radiance in W/(m*m*sr*um)
;                               scalar if wavelength is scalar,
;                               array if wavelength is array
;
; OPTIONAL OUTPUT PARAMETERS:
;       none
;
; COMMON BLOCKS:
;       none
;
; SIDE EFFECTS:
;       none
;
; RESTRICTIONS:
;       no negative or zero wavelengths
;       negative or zero temperatures cause zero radiance on output
;       IDL !pi is good to 7 places
;
; EXAMPLE:
;
; MODIFICATION HISTORY:
;       written  march 93
;          modified 22 March 1997, vjr
;
;-
;

FUNCTION PLANCK, SWIR_length, bkd_temp

s = SIZE(SWIR_length)

IF (s(s(0)+1) NE 5) THEN BEGIN          ; single-precision input
        c1 = 3.74151e-16
        c2 = 0.0143879e
        fact = 1.0e-6
        pi = FLOAT(!pi)
        limit = 88.0                    ; limit prevents floating overflows in EXP

ENDIF ELSE BEGIN                        ; double-precision input
        c1 = 3.74151d-16
        c2 = 0.0143879d
```

```
        fact = 1.0d-6
        pi = DOUBLE(!pi)
        limit = 700.0d                  ; limit prevents floating overflows in EXP
ENDELSE

tmp = bkd_temp > fact                       ; prevent divide by zero

wave = SWIR_length * fact                   ; convert um to m

a = wave ^ 5.0
b = EXP((c2/(wave*tmp)) < limit)
bkd_radiance = c1 / (a * (b-1.0))
bkd_radiance = (bkd_radiance * fact) / pi   ; convert W/(m*m*m) to W/(m*m*sr*um)

RETURN, bkd_radiance
END
```

A.10 PLANCKINV.PRO

```
;
;+
; NAME:
;     PLKINV
;
; PURPOSE:
;     use planck functionto calculate temperature from input wavelength
;     and radiance
;
; CATEGORY:
;     ????
;
; CALLING SEQUENCE:
;     temperature = plkinv(wavelength,radiance)
;
; INPUTS:
;     Wavelength:   wavelength in microns
;     Radiance:     radiance in W/(m*m*sr*um)
;
; OUTPUTS:
;     Temperature:  temperature in degrees Kelvin
;
```

```
; OPTIONAL OUTPUT PARAMETERS:
;       none
; COMMON BLOCKS:
;       none
; SIDE EFFECTS:
;       none
; RESTRICTIONS:
;       no negative or zero wavelengths allowed
;       negative or zero radinaces cause zero temperature on output
;       IDL !pi is good to 7 places
; EXAMPLE:
;
; MODIFICATION HISTORY:
;       written  march 93
;
;-
;--------------------------------------------------------------------------
FUNCTION PLKINV, wavelen, radiance_cool, radiance_hot, temperature_cool, temperature_hot

  s = SIZE(wavelen)

  IF (s(s(0)+1) NE 5) THEN BEGIN                    ; check if input is double precision
    c1 = 3.74151e-16
    c2 = 0.0143879e
    fact = 1.0e-6
    pi = FLOAT(!pi)
    temperature_cool = radiance_cool * 0.0
    temperature_hot = radiance_hot * 0.0
  ENDIF ELSE BEGIN
    c1 = 3.74151d-16
    c2 = 0.0143879d
    fact = 1.0d-6
    pi = DOUBLE(!pi)
    temperature_cool = radiance_cool * 0.0d
    temperature_hot = radiance_hot * 0.0d
  ENDELSE

  index_cool = WHERE(radiance_cool GT 0.0,count)
  index_hot = WHERE(radiance_hot GT 0.0,count)

  IF (count GT 0) THEN BEGIN
    b = temperature_cool
    c = temperature_hot
    wave = wavelen * fact                ; convert um to m
    a = wave ^ 5.0
```

```
    rad_cool = pi * radiance_cool / fact            ;  W/(m*m*sr*um) to W/(m*m*m)
    rad_hot = pi * radiance_hot / fact

    b(index_cool) = c1 / (a(index_cool) * rad_cool(index_cool))
    c(index_hot) = c1 / (a(index_hot) * rad_hot(index_hot))
    temperature_cool(index_cool) = c2 /(wave(index_cool) * alog(b(index_cool)+1.0));
    temperature_hot(index_hot) = c2 /(wave(index_hot) * alog(c(index_hot)+1.0));

  ENDIF

RETURN, temperature_cool
RETURN, temperature_hot

END
```

A.11 MIXED_PLANCK.PRO

```
FUNCTION MIXED_PLANCK, wavelen, temp_low, temp_high, cool_area, hot_area,
mixed_radiance

s = SIZE(wavelen)

IF (s(s(0)+1) NE 5) THEN BEGIN    ; single-precision input
  c1 = 3.74151e-16
  c2 = 0.0143879e
  fact = 1.0e-6
  pi = FLOAT(!pi)
  limit = 88.0            ; limit prevents floating overflows in EXP

ENDIF ELSE BEGIN      ; double-precision input
  c1 = 3.74151d-16
  c2 = 0.0143879d
  fact = 1.0d-6
  pi = DOUBLE(!pi)
  limit = 700.0d       ; limit prevents floating overflows in EXP
ENDELSE

tmp_low = temp_low > fact     ; prevent divide by zero
tmp_high = temp_high > fact
```

```
wave = wavelen * fact       ; convert um to m

a = wave ^ 5.0
b = EXP((c2/(wave*tmp_low)) < limit)
c = EXP((c2/(wave*tmp_high)) < limit)
radiance_cool = c1 / (a * (b-1.0))
radiance_hot = c1 / (a * (c-1.0))
mixed_radiance = (cool_area * (radiance_cool * fact) / pi) + (hot_area * (radiance_hot * fact) /
pi)   ; convert W/(m*m*m) to W/(m*m*sr*um)
;too_high=where(mixed_radiance gt 35.0)
;if (too_high[0] ne -1) then read, pauseval, prompt='STOP'
RETURN, mixed_radiance
END
```

A.12 VJR_WRITE_ENVI.PRO

```
PRO VJR_WRITE_ENVI, dims, file

;+
;  NAME:
;          VJR_WRITE_ENVI
;
;  PURPOSE:
;          Write an ENVI header file to disk.
;
;  CATAGORY:
;          File I/O
;
;  CALLING SEQUENCE:
;          VJR_WRITE_ENVI(dims, file)
;
;  INPUT:
;          dims:   Structure containing image dimensions
;                          dims = {nl, ns, nb, offset, form, org, order}
;
;          file:    Name of ENVI header file that will be written.
;                          Character string.
;
;  OUTPUT:
;          None.
;
```

```
;  COMMON BLOCKS:
;          None.
;
;  SIDE EFFECTS:
;          ENVI header written to disk
;
;  MODIFICATION HISTORY:
;          Written 1/97  VJR
;          Last Update:   16 August 2000
;-

ON_ERROR, 2                    ; return to caller upon error

;
;          determine byte ordering
;
;IF (!version.os EQ 'Win32') THEN dims.order = 0 ELSE dims.order = 1
;This changes the byte order to 0 because above IF command was writing out byte order = 1 and
the image
;was unable to be read into ENVI without producing bin size max/min errors.
dims.order = 0
;
;          write keyword pairs to file
;
OPENW, unit1, file, /GET_LUN

PRINTF, unit1, 'ENVI'
PRINTF, unit1, 'samples = ' + STRTRIM(dims.ns, 2)
PRINTF, unit1, 'lines = ' + STRTRIM(dims.nl, 2)
PRINTF, unit1, 'bands = ' + STRTRIM(dims.nb, 2)
PRINTF, unit1, 'header offset = ' + STRTRIM(dims.offset, 2)
PRINTF, unit1, 'file type = IDL'
PRINTF, unit1, 'data type = ' + STRTRIM(dims.form, 2)
PRINTF, unit1, 'interleave = ' + dims.org
PRINTF, unit1, 'byte order = ' + STRTRIM(dims.order, 2)

FREE_LUN, unit1

END
```

A.13 VJR_WRITE_IMAGE.PRO

```
PRO VJR_WRITE_IMAGE, dims, buf, fname

;+
;  NAME:
;         VJR_WRITE_IMAGE
;
;  PURPOSE:
;         Write data buffer to disk.
;
;  CATAGORY:
;         File I/O
;
;  CALLING SEQUENCE:
;         VJR_WRITE_IMAGE, dims, buf, fname
;
;  INPUT:
;         dims:   structure containing image dimensions
;
;         buf:    Data buffer that is to be written to disk.
;
;         fname: name of image file to be opened and written to. Character string.
;
;  OUTPUT:
;          None.
;
;  COMMON BLOCKS:
;         None
;
;  SIDE EFFECTS:
;         None.
;
;  RESTRICTIONS:
;         Must have write access to current directory.
;
;  MODIFICATION HISTORY:
;         Written January 1997, VJR
;         Last Update: 16 August 2000, VJR
;-

ON_ERROR, 2                 ; return to calling program upon error

;
;         write image to file
```

```
;
OPENW, iunit, fname, /BINARY, /NOAUTO, /GET_LUN
WRITEU, iunit, buf
FREE_LUN, iunit

;
;         write ENVI header to file
;
VJR_WRITE_ENVI, dims, fname+'.hdr'

END
```

BIBLIOGRAPHY

Abrams, M.J., Glaze, L.S., Sheridan, M., 1991. Monitoring Colima volcano, Mexico, using satellite data. Bulletin of Volcanology, Vol. 53, pp. 571-574.

Abrams, M., Bianchi, R. and Pieri, D., 1996. Revised mapping of lava flows on Mount Etna, Sicily. Photogrammetric Engineering and Remote Sensing 62, pp. 1353–1359.

Abrams, M.J., 2000. The Advanced Spaceborne Thermal Emission and Reflection Radiometer (ASTER): data products for the high spatial resolution imager on NASA's Terra Platform, International Journal of Remote Sensing, Vol. 21, No. 5. pp. 847-859.

Abtahi, A.A., Kahle, A.B., Abbott, E.A., Gillespie, A.R., Sabol, D., Yamada, G., and Pieri, D., 2002. Emissivity changes in basalt cooling after eruption from Pu'u O'o, American Geophysical Union, Fall Meeting, Abstract #V71A-1263.

Adams, J.B., Smith, M.O., Johnson, P.E., 1986. Spectral mixture modeling: A new analysis of rock and soil types at the Viking Lander I site. Journal of Geophysical Research. 91: 8098-8112.

Advanced Spaceborne Thermal Emission and Reflection Radiometer (ASTER) Higher Level Product User Guide v. 2.1, 2001. (http://asterweb.jpl.nasa.gov/content/03_data/04_Documents/ASTERHigherLevelUserGuideVer2May01.pdf). Cited May 2010.

Bandfield, J.L., Hamilton, V.E., and Christensen, P.R., 2000. A global view of Martian surface compositions from MGS-TES. Science, Vol. 285(5458), pp. 1626-1630.

Bates, P.D., Horritt, M.S., Smith, C.N., and Mason, D., 1997. Integrating remote sensing observations of flood hydrology and hydraulic modeling. Hydrological Processes, Vol. 11, No. 14, pp. 1777-1795.

Byrnes, J.M., Ramsey, M.S., and Crown, D.A., 2004. Surface unit characterization of the Mauna Ulu flow field, Kilauea Volcano, Hawai'i, using integrated field and remote sensing analyses. Journal of Volcanology and Geothermal Research, Vol. 135, No. 1-2, pp. 169-193.

Carter, A.J., Girina, O., Ramsey, M.S., Demyanchuk, Y.V., 2008. ASTER and field observations of the 24 December 2006 eruption of Bezymianny Volcano, Russia. Remote Sensing of Environment. 112 (5): 2569-2577.

Carter, A.J., Ramsey, M.S., Durant, A.J., Skilling, I.P., and Wolfe, A.L., 2009. Micron-scale roughness of volcanic surfaces from thermal infrared spectroscopy and scanning electron microscopy, Journal of Geophysical Research, Vol. 114, B02213.

Carter, A.J., and Ramsey, M.S., 2010. Long-term volcanic activity at Shiveluch Volcano: Nine years of ASTER Spaceborne thermal infrared observations, Remote Sensing, Vol. 2, pp. 2571-2583.

Casadevall, T.J., 1993. Volcanic ash and airports – Discussion and recommendations from the workshop on impacts of volcanic ash on airport facilities. U.S. Geological Survey Open-File Report. 93-518, pp. 52.

Casadevall, T.J., 1994. The 1980-90 eruption of Redoubt volcano, Alaska: Impacts on aircraft operations. Journal of Volcanology and Geothermal Research (Special Issue). 62 (1-4): 301-316.

Chebrov, V., 2008. Complex seismological and geophysical investigation of Kamchatka and Commander Islands. Annual report of KB GS RAS. Ed. V. Chebrov. pp. 268. (in Russian).

Christensen, P.R., 2000. A thermal emission spectral library of rock-forming minerals, Journal of Geophysical Research, Vol. 105, No. E4, pp. 9735-9739.

Christensen, P.R., McSween, Jr, H.Y., Bandfield, J.L., Ruff, S.W., Rogers, A.D., Hamilton, V.E., Gorelick, N., Wyatt, M.B., Jakosky, B.M., Kieffer, H.H., Malin, M.C., and Moersch, J. E., 2005. Evidence for magmatic evolution and diversity on Mars from infrared observations, Nature, Vol. 436, pp. 504-509, doi:10.1038/nature03639.

Crisp, J, Kahle, A.B., and Abbott, E.A., 1990. Thermal Infrared Spectral Character of Hawaiian Basaltic Glasses, Journal of Geophysical Research, Vol. 95, No. B13, pp. 21657-21669.

Dehn, J., Dean, K., Engle, K., 2000. Thermal monitoring of North Pacific volcanoes from space. Geology (Boulder), Vol. 28, No. 8, pp. 755-758.

Dehn, J., Dean, K., Engle, K., Izbekov, P., 2002. Thermal precursors in satellite images of the 1999 eruption of Shishaldin Volcano. Bulletin of Volcanology. 64 (8): 525-534.

Dozier, J., 1981. A method for satellite identification of surface temperature fields of subpixel resolution. Remote Sensing of Environment., Vol. 11, pp. 221-229.

Duda, K.A., & Abrams, M., 2005. ASTER and USGS EROS disaster response: emergency imaging after hurricane Katrina. Photogrammetric Engineering and Remote Sensing. 71: 1346-50.

Duda, K.A., Ramsey, M., Wessels, R., and Dehn, J., 2009. Optical satellite volcano monitoring: A multi-sensor rapid response system, in: P.P. Ho, (ed.), Geoscience and Remote Sensing, IN-TECH Press, Vukovar, Croatia, ISBN 978-953-307-003-2, 473-496.

Eggleton, R.A., Foudoulis, C., and Farkevisser, D., 1987. Weathering of basalt: Changes in rock chemistry and mineralogy. Clays Clay Minerals Vol. 35, pp. 161–169.

Fedotov, S.A., Khrenov, A.P., Zharinov, N.A., 1987. Kliuchevskoi Volcano, its activity in 1952-1986 and possible evolution. Volcanology and Seismology. 6: 3-17 (in Russian).

Fedotov, S.A., Masurenkov, Y.P., 1991. Active volcanoes of Kamchatka vol. 1, Nauka, Moscow. pp. 713.

Feely, K.C., and Christensen, P.R., 1999. Quantitative compositional analysis using thermal emission spectroscopy: Application to igneous and metamorphic rocks, Journal of Geophysical Research, Vol. 104, No. E10, pp. 24,195-24,210.

Flynn, L.P., Mouginis-Mark, P.J., Horton, K.A., 1994. Distribution of thermal areas on an active lava flow field: Landsat observations of Kilauea, Hawaii, July 1991. Bulletin of Volcanology, Vol. 56, pp. 284-296.

Giammanco, S., Valenza, M., Pignato, S., and Giammanco, G., 1996. Mg, Mn, Fe, and V Concentrations in the ground waters of Mount Etna (Sicily), Water Resources, Vol. 30, No. 2, pp. 378-386.

Gillespie, A.R., 1985. Lithologic mapping of silicate rocks using TIMS. The TIMS Data Users' Workshop. JPL Publication 86-38, Jet Propulsion Laboratory, Pasadena, CA, (pp. 29-44).

Gillespie, A., 1992. Spectral mixture analysis of multispectral thermal infrared images. Remote Sensing of Environment. 42: 137-145.

Gillespie, A.R., Rokugawa, S., Matsunaga, T., Cothern, J.S., Hook, S., and Kahle, A.B., 1998. A Temperature and emissivity separation algorithm for Advanced Spaceborne Thermal Emission and Reflection Radiometer (ASTER) images. IEEE Transactions on Geoscience and Remote Sensing, 36, pp. 1113-1126.

Giglio, L., Descoitres, J., Justice, C.O., and Kaufman, Y.J., 2003. An Enhanced Contextual Fire Detection Algorithm for MODIS. Remote Sensing of Environment, Vol. 87, pp. 273–282.

Glaze, L.S., Francis, P.W., Rothery, D.A., 1989. Measuring thermal budgets of active volcanoes by satellite remote sensing. Nature, Vol. 338, pp. 144-146.

Gorbatov, A., Kostoglodov, V., Suarez, G., and Gordeev, E., 1997. Seismicity and structure of the Kamchatka subduction zone. Journal of Geophysical Research. 102: 17883-17898.

Gushchenko I.I., 1979. Eruptions of volcanoes of the world: A Catalog. Nauka, Moscow. Academy of Science USSR Far Eastern Science Center. pp. 474, (in Russian).

Hamilton, V.E., Christensen, P.R., McSween Jr., H.Y., 1997. Determination of Martian meteorite lithologies and mineralogies using vibrational spectroscopy, Journal of Geophysical Research, Vol.102, pp. 25,593-25,603.

Hamilton, V.E., Wyatt, M.B., McSween, H.Y., and Christensen, P.R., 2001. Analysis of terrestral and Martian volcanic compositions using thermal emission spectroscopy 2. Application to Martian surface spectra from the Mars Global Surveyor Thermal Emission Spectrometer, Journal of Geophysical Research, Vol. 106, No. 7, pp. 14,733-14,746.

Hapke, B., 1993. Theory of Reflectance and Emittance Spectroscopy, Cambridge Univ. Press, Cambridge, 1993.

Harris, A.J.L., and Stevenson, D.S., 1997. Thermal observations of degassing open conduits and fumaroles at Stromboli and Vulcano using remotely sensed data, Journal of Volcanology and Geothermal Research, Vol. 76, pp. 175-198.

Harris, A.L., Flynn, L.P., Keszthelyi, L., Mouginis-Mark, P.J., Rowland, S.K., and Resing, J.A., 1998. Calculation of lava effusion rates from Landsat TM data, Bulletin of Volcanology, Vol. 60, pp. 52-71.

Heiken, G., Casadevall, T.J., Newhall, C., 1992. First international symposium on volcanic ash and aviation safety. Bulletin of Volcanology. 54 (3): 250-251.

Hook, S., Dmochowski, J., Howard, K., Rowan, L., Karlstrom, K., and Stock, J., 2005. Mapping weight percent silica variation from remotely acquired multispectral thermal infrared data with examples from the Hiller Mountains, Nevada, USA and Tres Virgenes-La Reforma, Baja California Sur, Mexico. Remote Sensing of Environment. 95: 273-289.

Hughes, C.G. and Ramsey, M.S., 2010. Super-resolution of THEMIS thermal infrared data: Creating radiometrically-accurate, sub-100 meter resolution images of Mars, Icarus, Vol. 208, No. 2, pp. 704-720, doi:10.1016/ j.icarus.2010.02.023.

Iwasaki, A, and Tonooka, H., 2005. Validation of a crosstalk correction algorithm for ASTER/SWIR, IEEE Transactions on Geoscience and Remote Sensing. 43 (12): 2747-2751.

Iwasaki, A., and Fujisada, H., 2005. ASTER Geometric Performance. IEEE Transactions on Geoscience and Remote Sensing, Vol. 43, No. 12, pp. 2700-2706.

Johnson, P.E., Smith, M.O., and Adams, J.B., 1992. Simple algorithms for remote determination of mineral abundances and particle sizes from reflectance spectra. Journal of Geophysical Research. 97: 2649-2657.

Kahle, A.B., Madura, D.P., and Soha, J.M., 1980. Middle infrared multispectral aircraft scanner data: analysis for geological applications. Applied Optics. 19: 2279-2290.

Kahle, A.B., Gillespie, A.R., Abbott, E.A., Abrams, M.J., Walker, R.E., and Hoover, G., 1988. Relative Dating of Hawaiian Lava Flows Using Multispectral Thermal Infrared Images: A New Tool for Geologic Mapping of Young Volcanic Terranes, Journal of Geophysical Research, Vol. 93, No. B12, pp. 15239-15251.

Kahle, A., Palluconi, F., Hook, S., Realmuto, V., Bothwell, G., 1991. The Advanced Spaceborne Thermal Emission and Reflectance Radiometer (ASTER). International Journal of Systematic Technology. 3: 144-156.

Kamchatka Volcanic Eruption Response Team (KVERT) Report, 2005. Kliuchevskoi Volcano, 14 January through 13 May 2005. (http://www.avo.alaska.edu/activity/avo-report.php?view=kaminfo&id=&month=January&year=2005). Cited January 2007.

Kirianov, V.Y., Neal, C.A., Gordeev, E.I., and Miller, T.P., 2002. KVERT (Kamchatkan Volcanic Eruptions Response Team): U.S. Geological Survey Fact Sheet. 064-02 (in English and Russian). Also online (http://geopubs.wr.usgs.gov/fact-sheet/fs064-02/).

Krasheninnikov, S.P., 1949. Description of Kamchatka Land. Moscow-Leningrad: Glavmorsevput, pp. 841. (In Russian).

Lee, R., King, P.L., and Ramsey, M.S., 2010. Spectral analysis of synthetic quartzofeldspathic glasses using laboratory thermal infrared spectroscopy, Journal of Geophysical Research, Vol. 115, B06202.

Lopez, T., 2006. Volcanic Gas Analysis at Cerro Negro Volcano, Nicaragua : Chemical, Spatial, and Thermal Trends of Cerro Negro’s Fumarolic Gases, Using New and Existing Gas Sampling Techniques, M.S. Thesis, Michigan Technological University, Houghton, pp. 168.

Li, Z.L., Becker, F., Stoll, M.P., and Wan, Z., 1999. Evaluation of Six Methods for Extracting Relative Emissivity Spectra from Thermal Infrared Images, Remote Sensing of Environment, 69, pp. 197-214.

LPDAAC, 2009. https://lpdaac.usgs.gov/lpdaac/products/aster_products_table/on_demand/surface_radiance_vnir_crosstalk_corrected_swir/v1/ast_09xt

Lyon, R.P., 1964. Evaluation of infrared spectrophotometry for compositional analysis of lunar and planetary soils, II, Rough and powdered surfaces, NASA Contract Rep., CR-100.

Lyon, R.P., 1965. Analysis of rocks by spectral infrared emission (8–25microns), Economic Geology, Vol. 60, pp. 715–736.

Mansor, S.B., Cracknell, A.P., Shilin, B.V., and Gornyi, V.I., 1994. Monitoring of underground coal fires using thermal infrared data: International Journal of Remote Sensing, Vol. 15, no. 8, pp. 1675-1685.

Matson, M, and Dozier, J., 1981. Identification of subresolution high temperature sources using a thermal IR sensor. Photogrammetric Engineering and Remote Sensing, Vol. 47, pp.1311-1318.

McAdoo, B.G., Richardson, N., Borreo, J., 2007. Inundation distances and run-up measurements from ASTER, QuickBird and SRTM data, Aceh coast, Indonesia. International Journal of Remote Sensing. 28 (13-14): 2961-2975.

McKnight, S.B., 1995, Geology and Petrology of Cerro Negro Volcano, Nicaragua, M.S. Thesis, Arizona State University.

McKnight S.B. and S.N. Williams, 1997, Old cinder cone or young composite volcano?: The nature of Cerro Negro, Nicaragua, Geology, V. 25, pp. 339-342.

Metternicht, G., Hurni, L., and Gogu, R., 2005. Remote sensing of landslides: An analysis of the potential contribution to geo-spatial systems for hazard assessment in mountainous environments. Remote Sensing of Environment, Vol. 98, No. 2-3, pp. 284-303.

Miller, T.P., Kirianov, V.Y., Kelley, H.L., 1994. Kliuchevskoi Fact Sheet. U.S. Geological Survey Fact Sheet. 94-067, pp. 4. Also online (http://eq.giseis.alaska.edu/volcanoes/klyu/klyufact.html).

Miller, T.P., and Casadevall, T.J., 2000. Volcanic Ash Hazards to Aviation. In: Sigurdsson, H., Houghton, B., McNutt, S.R., Rymer, H. and Stix, J., Editors, 2000. Encyclopedia of Volcanoes, Academic Press, San Diego, CA, pp. 915–930.

Morisette, J.T., Giglio, L., Csiszar, I., & Justice, C.O., 2005. Validation of the MODIS active fire product over southern Africa with ASTER data. International Journal of Remote Sensing. 26 (19): 4239–4264.

Oppenheimer, C.M., and Rothery, D.A., 1991. Infrared monitoring of volcanoes by satellite. Journal of the Geological Society of London, Vol. 148, pp. 563-569.

Oppenheimer, C.M., 1991. Lava flow cooling from Landsat Thematic Mapper infrared data: the Lonquimay eruption (Chile, 1989). Journal of Geophysical Research, Vol. 96, No. B13, pp. 21865-21878.

Oppenheimer, C.M., 1993. Infrared surveillance of crater lakes using satellite data. Journal of Volcanology and Geothermal Research, Vol. 55, pp. 117-128.

Oppenheimer C.M., Francis, P.W., Rothery, D.A., Carlton, R.T., 1993. Infrared image analysis of volcanic thermal features: Lascar volcano, Chile, 1984-1992. Journal of Geophysical

Research, Vol. 98, pp. 4269-4286.

Ouzounov, D., and Freund, F., 2004. Mid-infrared emission prior to strong earthquakes analyzed by remote sensing data. Advances in Space Research, Vol. 33, No. 3, pp. 268-273.

Ozerov, A., Ariskin, A., Kyle, P., Bogoyavlenskaya, G., and Karpenko, S., 1997. Petrological-Geochemical Model for Genetic Relationships between Basaltic and Andesitic Magmatism of Klyuchevskoi and Bezymiannyi Volcanoes, Kamchatka. Petrology. 5 (6): 550-569.

Palluconi, F., Hoover, G., Alley, R., Jentoft-Nilsen, M., and Thompson, T., 1996. An atmospheric correction method for ASTER Thermal radiometry over land, revision 2: ASTER standard data product AST09, Level 2 Radiance—TIR, land-leaving. Jet Propul. Lab., Pasadena, CA, http://asterweb.jpl.nasa.gov/asterhome/atbd/ATBD-AST-04.doc.

Pieri, D.C., Glaze, L.S., and Abrams, M.J., 1990. Thermal radiance observations of an active lava flow during the June 1984 eruption of Mount Etna. Geology, Vol. 18, pp. 1018-1022.

Pieri, D.C., and Abrams, M., 2004. ASTER watches the world's volcanoes: a new paradigm for volcanological observations from orbit. Journal of Volcanology and Geothermal Research, Vol. 135, No. 1-2, pp. 13-28.

Pinkerton, H., James, M., and Jones, A., 2002. Surface temperature measurements of active lava flows on Kilauea volcano, Hawai'i. Journal of Volcanology and Geothermal Research, Vol. 113, No. 1-2, pp. 159-176.

Prabhakara, C., and Dalu, G., 1976. Remote sensing of surface emissivity at 9 µm over the globe. Journal of Geophysical Research, Vol. 81, No. 21, pp. 3719-3724.

Prata, F., Stohl, A., Torseth, K., Clarisse, L., Carn, S., Pavalonis, S.C., Merucci, L., and Piscini, A., 2010. Satellite detection of volcanic ash from Eyjafjallajökull and the threat to aviation, Geophysical Research Abstracts, EGU General assembly, Vol., 12, EGU2010-15732.

Przedpelski, Z.J, and Casadevall, T.J., 1994. Volcanic Ash and Aviation Safety: Proceeding of the First International Symposium on Volcanic Ash and Aviation Safety. Casadevall, T.J., Editor. U.S. Geological Survey Bulletin. 2047: 129-136.

Ramsey, M.S., Howard, D.S., Christensen, P.R., Lancaster, N., 1993. Mineralogic variability of the Kelso Dunes, Mojave Desert, California derived from thermal infrared multispectral scanner (TIMS) data, in Summaries of the Fourth Annual Airborne Earth Science Workshop, Vol. 2, edited by Realmuto, V.J., JPL Publication, 93-26, pp. 9-12.

Ramsey, M.S., 1996. Quantitative analysis of geological surfaces: A deconvolution algorithm for midinfrared remote sensing data, Ph.D. dissertation, Arizona State University, Tempe, pp. 276.

Ramsey, M.S., and Fink, J.H., 1997. Remote determination of lava vesicularity: Technique preparation for the upcoming spaceborne ASTER instrument. Geological Society of America Cordilleran Section Abstract with Programs, Vol. 29, No. 5, p. A58.

Ramsey, M.S., and Christensen, P.R., 1998. Mineral abundance determination: Quantitative deconvolution of thermal emission spectra. Journal of Geophysical Research, 103, pp. 577-596.

Ramsey, M.S., and Fink, J.H., 1999. Estimating silicic lava vesicularity with thermal remote sensing: A new technique for volcanic mapping and monitoring. Bulletin of Volcanology, 61, pp. 32-39.

Ramsey, M.S., Christensen, P.R., Lancaster, N., and Howard, D.A., 1999. Identification of sand sources and transport pathways at the Kelso Dunes, California, using thermal infrared remote sensing, Geological Society of America Bulletin, Vol. 111, No. 5, pp. 646-662.

Ramsey, M.S., 2002. Ejecta distribution patterns at Meteor Crater, Arizona: On the applicability of lithologic end-member deconvolution for spaceborne thermal infrared data of Earth and Mars. Journal of Geophysical Research, 107(E8), 3.1-3.14.

Ramsey, M.S., and Flynn, L.P., 2004. Strategies, insights, and the recent advances in volcanic monitoring and mapping with data from NASA's Earth Observing System, J. Volc. Geotherm. Res., Vol. 135, No. 1-2, 1-11.

Ramsey, M.S., and Dehn, J., 2004. Spaceborne observations of the 2000 Bezymianny, Kamchatka eruption: the integration of high-resolution ASTER data into near real-time monitoring using AVHRR. Journal of Volcanology and Geothermal Research, Vol. 135, No. 1-2, pp. 127-146.

Ramsey, M.S., and Kuhn, S., 2004. Fusion of parametric and thematic data to characterize the Soufrière Hills volcanic dome. Abstract of the General Assembly, IAVCEI.

Ramsey, M.S., Dehn, J., Wessels, R., Byrnes, J., Duda, K., Maldonado, L., and Dwyer, J., 2004. The ASTER emergency scheduling system: A new project linking near-real-time satellite monitoring of disasters to the acquisition of high-resolution remote sensing data. Eos Transactions AGU. 85 (47), Fall Meeting Supplement, Abstract SF23A-0026.

Ramsey, M.S., 2006. The critical need for moderate to high resolution thermal infrared data for volcanic hazard mitigation and process monitoring from the micron to the kilometer scale, Eos Transactions AGU. 87: Fall Meeting Supplement, Abstract H32D-06s.

Realmuto, V.J., 1990. Separating the effects of temperature and emissivity: emissivity spectrum normalization. In Proceedings of the Second TIMS Workshop, JPL Publication 90-55, Jet Propulsion Laboratory, Pasadena, CA, pp. 23-27.

Realmuto VJ, Hon, K., Kahle, A.B., Abbott, E.A., and Pieri, D.C., 1992. Multispectral thermal infrared mapping of the 1 October 1988 Kupaianaha flow field, Kilauea Volcano, Hawaii, Bulletin of Volcanology, Vol. 55, pp. 33-44.

Realmuto, V.J., Abrams, M.J., Buongiorno, M.F., 1994. The use of multispectral thermal infrared image data to estimate the sulfur dioxide flux from volcanoes: A case study from Mount Etna, Sicily, July 29, 1986. Journal of Geophysical Research. 99 (B1): 481–488.

Realmuto, V.J., Sutton, A.J. and Elias, T., 1997. Multispectral thermal infrared mapping of sulfur dioxide plumes: a case study from the East rift zone of Kilauea volcano, Hawaii. Journal of Geophysical Research. 102 (B7): 15057–15072.

Ripepe, M., Harris, A.L., Carniel R., 2002. Thermal, seismic and infrasonic evidences of variable degassing rates at Stromboli volcano. Journal of Volcanology and Geothermal Research. 118: 285–297.

Roach, A.L., Benoit, J.P., Dean, K.G., McNutt, S.R., 2004. The combined use of satellite and seismic monitoring during the 1996 eruption of Pavlof volcano, Alaska. Bulletin of Volcanology. 62 (6-7): 385-399.

Robinson, J., 1991. Fire from space: Global fire evaluation using infrared remote sensing. International Journal of Remote Sensing, Vol. 12, No. 1, pp. 3–24.

Roggensack, K., 2001. Sizing up crystals and their melt inclusions: a new approach to crystallization studies, Earth and Planetary Science Letters, Vol. 187, pp. 221-237.

Rose, S., Ramsey, M.S., 2008. The Eruptive Behavior of Kliuchevskoi Volcano, Russia, American Geophysical Union, Fall Meeting 2008, abstract #V43A-2141.

Rose, S., Ramsey, M., 2009. The 2005 Eruption of Kliuchevskoi Volcano: Chronology and Processes Derived From ASTER Spaceborne and Field-based Data, Journal of Volcanology and Geothermal Research, Vol. 184, pp. 367-380.

Rose, S., and Ramsey, M., in review-a. Spectral Deconvolution and Extraction of Compositional and Textural Variations of the Tephra Plain and a'a Lava Flows at Cerro Negro Volcano, Nicaragua Using the ASTER Spaceborne Instrument.

Rose, S.R. and Ramsey, M.S., in review-b. The 2005 and 2007 eruptions of Kliuchevskoi Volcano, Russia: Behavior and effusion mechanisms, in Dean, K. and Dehn, J., (eds.), Volcanic Atlas of the North Pacific, Springer-Verlag Press.

Rose, S.R., Watson, I.M., Ramsey, M.S., and Hughes, C.G., in review-c. Accurate retrieval of multispectral infrared emissivity from thermally-mixed volcanic surfaces, Journal of Geophysical Research.

Rothery, D.A., Francis, P.W., and Wood, C.A., 1988. Volcano Monitoring Using Short Wavelength Infrared Data from Satellites. Journal of Geophysical Research, Vol. 93, No. B7, pp. 7993-8008.

Rothery, D., 1989. Volcano monitoring by satellite. Geology Today. 5 (4): 128 –132.

Ruff, S.W., Christensen, P.R., Barbera, P.W., and Anderson, D.L., 1997. Quantitative thermal emission spectroscopy of minerals: A laboratory technique for measurement and calibration, Journal of Geophysical Research, Vol. 102, pp. 14899 –14913.

Sabol, D.E., Adams, J.B., Smith, M.O., 1992. Quantitative subpixel spectral detection of targets in multispectral images. Journal of Geophysical Research. 97: 2659-2672.

Saraf, A.K., and Choudhury, S., 2005. Thermal Remote Sensing Technique in the Study of Pre-Earthquake Thermal Anomalies. Journal of Indian Geophysical Union, Vol. 9, No. 3, pp. 197-207.

Saraf, A.K., Rawat, V., Banerjee, P., Choudhury, S., Panda, S.K., Dasgupta, S., and Das, J.D., 2008. Satellite detection of earthquake thermal infrared precursors in Iran. Natural Hazards, Vol. 47, No. 1, pp. 119-135.

Singer, R.B., and McCord, T.B., 1979. Mars: Large scale mixing of bright and dark surface materials and implications for analysis of spectral reflectance, Proceedings of Lunar and Planetary Science Conference, 10th, pp. 1835-1848.

Self, S., & Walker, G.L., 1994. Volcanic Ash and Aviation Safety: Proceeding of the First International Symposium on Volcanic Ash and Aviation Safety. In: Casadevall, T.J., Editor, U.S. Geological Survey Bulletin. 2047: 65-74.

Searcy, C.K., Dean, K., and Stringer, B., 1998. PUFF: A volcanic ash tracking and prediction model. Journal of Volcanology and Geothermal Research. 40: 1-16.

Smithsonian National Museum of Natural History Global Volcanism Program (GVP), 2008. Kliuchevskoi Volcano Eruptive History. (http://www.volcano.si.edu/world/volcano.cfm-?vnum=1000-26=&volpage=erupt).

Taylor, B.W., 1963. An outline of the vegetation of Nicaragua, Journal of Ecology, Vol. 51, No. 1, pp. 27-54.

Thomson, J.L., and Salisbury, J.W., 1993. The mid-infrared reflectance of mineral mixtures (7-14 µm), Remote Sensing of Environment, Vol. 45, pp. 1-13.

Tralli, D.M., Blom, R.G., Zlotnicki, V., Donnellan, A., and Evans, D.L., 2005. Satellite remote sensing of earthquake, volcano, flood, landslide and coastal inundation hazards, ISPRS Journal of Photogrammetry and Remote Sensing. 59 (4): 185-198.

Urai, M., Fukui, K., Yamaguchi, Y., and Pieri, D.C., 1999. Volcano observation potential and global volcano monitoring plan with ASTER. Bulletin of the Volcanological Society of Japan. 44 (3): 131-141.

Vaughan, R.G., Hook, S.J., Ramsey, M.S., Realmuto, V.J., and Schneider, D.J., 2005. Monitoring eruptive activity at Mount Saint Helens with TIR image data. Geophysical Research Letters. 32, L10305.

Viramonte, J., and Di Scala, L., 1970. Summary of the 1968 eruption of Cerro Negro, Nicaragua, Bulletin of Volcanology, Vol. 34, pp. 347-351.

Walker, J., and Carr, M., 1986. Compositional variations caused by phenocryst sorting at Cerro Negro volcano, Nicaragua, Geological Society of America Bulletin, Vol. 97, pp. 1156-1162.

Watson, I.M., Oppenheimer, C., Voight, B., Francis, P.W., Clarke, A., Stix, J., Miller, A., Pyle, D.M., Burton, M.R., Young, S.R., Norton, G., Loughlin, S., Darroux, B., MVO Staff, 2000. The relationship between degassing and ground deformation at Soufriere Hills Volcano, Montserrat, Journal of Volcanology and Geothermal Research, Vol. 98, pp. 117-126.

Watson, I.M., Realmuto, V.J., Rose, W.I., Prata, A.J., Bluth, G.S., Gu, Y., Bader, C.E., and Yu, T., 2004. Thermal infrared remote sensing of volcanic emissions using the moderate resolution imaging spectroradiometer, Journal of Volcanology and Geothermal Research, Vol. 135, No. 1-2, pp. 75-89.

Wooster, M.J., and Rothery, D.A., 1997. Thermal monitoring of Lascar Volcano, Chile, using infrared data from the along-track scanning radiometer: a 1992-1995 time series, Bulletin of Volcanology, Vol. 58, No. 7, pp. 566-579.

Wooster, M.J., and Kaneko, T., 2001. Testing the accuracy of solar-reflected radiation corrections applied during satellite shortwave infrared thermal analysis of active volcanoes, Journal of Geophysical Research, Vol. 106, No. 13, pp. 13381-13393.

Wright, R., Flynn, L.P., 2003. On the retrieval of lava-flow surface temperatures from infrared satellite data, Geology, Vol. 31, No. 10, pp. 893-896.

Wright, R., Flynn, L.P., Garbeil, H., Harris, A.J.L., and Pilger, E., 2004. MODVOLC: near-real-time thermal monitoring of global volcanism. Journal of Volcanology and Geothermal Research, Vol. 135, pp. 29-49.

Wright, R., Carn, S.A., and Flynn, L.P., 2005. A satellite chronology of the May-June 2003 eruption of Anatahan volcano, Journal of Volcanology and Geothermal Research, Vol. 146, No. 1-3, pp. 102-116.

Wright, S.P., and Ramsey, M.S., 2006. Thermal infrared data analyses of Meteor Crater, Arizona: Implications for Mars Spaceborne data from the Thermal Emission Imaging System. Journal of Geophysical Research, Vol. 111(E8), pp. 16.

Yamaguchi, Y., Kahle, A., Tsu, H., Kawakami, T., Pniel, M., 1998. Overview of the Advanced Spaceborne Thermal Emission and Reflectance Radiometer (ASTER). IEEE Transactions on Geoscience and Remote Sensing. 36: 1062-1071.

Zorn, N.V., Ramsey, M.S., 2002. An automated spectral deconvolution algorithm: application to thermal infrared studies of Earth and Mars. Solar System Remote Sensing, LPI Contribution, No. 1129, pp. 93-94.